EFFICIENT AND ROBUST APPROACHES TO THE STABILITY ANALYSIS AND OPTIMAL CONTROL OF LARGE-SCALE MULTIBODY SYSTEMS

A Thesis
Presented to
The Academic Faculty

by

Jielong Wang

In Partial Fulfillment
of the Requirements for the Degree
Doctor of Philosophy in the
School of Aerospace Engineering

Georgia Institute of Technology
August 2007

EFFICIENT AND ROBUST APPROACHES TO THE STABILITY ANALYSIS AND OPTIMAL CONTROL OF LARGE-SCALE MULTIBODY SYSTEMS

Approved by:

Professor Olivier A. Bauchau,
Committee Chair
School of Aerospace Engineering
Georgia Institute of Technology

Professor Erian A. Armanios
School of Aerospace Engineering
Georgia Institute of Technology

Professor Olivier A. Bauchau, Adviser
School of Aerospace Engineering
Georgia Institute of Technology

Professor Massimo Ruzzene
School of Aerospace Engineering
Georgia Institute of Technology

Professor Dewey H. Hodges
School of Aerospace Engineering
Georgia Institute of Technology

Assistant Professor Yingjie Liu
School of Mathematics
Georgia Institute of Technology

Date Approved: 6 June 2007

To my parents and my elder sister

ACKNOWLEDGEMENTS

I would like to express my most profound gratitude and appreciation to Dr. Olivier Bauchau, my thesis advisor. Without his ideas and suggestions, the completion of this thesis would not have been possible. For the past four years, he has guided me through this research work, selected challenging topics and problems for this thesis, and provided an excellent environment for research. I especially thank him for his patience and constant availability to answer my numerous questions day by day. I have also benefited from Dr. Bauchau's excellent software expertise and his experience in writing large finite element programs.

I am grateful to Dr. Dewey Hodges for his unselfish help. His papers in the area of rotorcraft dynamics widened my interest when I was studying in Tsinghua University for my Master degree. I truly appreciate him for recommending me to be a graduate research assistant of Dr. Bauchau.

I thank Dr. Erian Armanios, Dr. Massimo Ruzzene and Dr. Yingjie Liu for taking the time to read the manuscript of my thesis, and suggesting valuable ways to improve it.

A good thesis is not answering a question, a good thesis is asking a question.

Dr. Olivier A. Bauchau

TABLE OF CONTENTS

LIST OF TABLES

LIST OF FIGURES

SUMMARY

Linearized stability analysis methodologies, system identification algorithms and optimal control approaches that are applicable to large scale, flexible multibody dynamic systems are presented in this thesis.

For stability analysis, two classes of closely related algorithms based on a partial Floquet approach and on an autoregressive approach, respectively, are presented in a common framework that underlines their similarity and their relationship to other methods. The robustness of the proposed approach is improved by using optimized signals that are derived from the proper orthogonal modes of the system. Finally, a signal synthesis procedure based on the identified frequencies and damping rates is shown to be an important tool for assessing the accuracy of the identified parameters; furthermore, it provides a means of resolving the frequency indeterminacy associated with the eigenvalues of the transition matrix for periodic systems. Unlike classical stability analysis methodologies, it does not require the linearization of the equations of motion of the system.

As an extension of the stability evaluation approaches, a robust system identification algorithm is developed to construct subspace plant models. The proposed system identification algorithm uniquely combines the methods of minimum realization and subspace identification. The proposed approach bypasses the computation of Markov parameters because the free impulse response of the system can be directly computed in the present computational environment. Minimum realization concepts were applied to identify the stability and output matrices. On the other hand, subspace identification algorithms construct a state space plant model of linear system by

using computationally expensive oblique matrix projection operations. The proposed algorithm avoids this burden by computing the Kalman filter gain matrix and model dependency on external inputs in a small sized subspace. Balanced model truncation and similarity transformation form the theoretical foundation of proposed stability analysis approaches and system identification algorithms. The proposed stability analysis approaches and identification algorithms are all based on the assumption that the plant is a linear system. Numerically stable mathematical tools, singular value decomposition and least-square regression, are applied to improve the robustness of the system identification algorithms. Finally, a forward innovation model is constructed and estimates the input-output behavior of the system within a specified level of accuracy. The proposed stability and system identification algorithms are computationally inexpensive and consist of purely post processing steps that can be used with any multi-physics computational tool or with experimental data.

Optimal control methodologies that are applicable to comprehensive large-scale flexible multibody systems are presented. The classical linear quadratic Gaussian controller, a combination of the linear quadratic regulator and Kalman filter, is designed, including subspace plant model identification, the evaluations of linear quadratic regulator feedback gain and Kalman filter gain matrices and online control implementation. The controller is applied to control of large-scale flexible multibody systems. The online control uses a time adaptive scheme to compute the control inputs at a very low computational cost.

CHAPTER I

INTRODUCTION

In this chapter, the background, previous work, objective of present work, and present approaches for stability analysis, system identification and optimal control will be introduced. The relationships among stability analysis, system identification and optimal control are summarized.

1.1 Stability Analysis of Multibody Dynamical Systems

An important aspect of the dynamic response of flexible multibody systems is the potential presence of instabilities. The instability of a cantilevered beam subjected to a tip, compressive follower force [21], or the instabilities appearing in rotor dynamics [42, 65] are two well-known types instabilities that can occur in dynamical systems and flexible multibody systems. If the equations of motion of the system can be formulated in the form of linear, ordinary differential equations with constant coefficients, classical stability evaluation methodologies based on the characteristic exponents of the system can be used. On the other hand, when the equations of motion of the system are cast in the form of linear, ordinary differential equations with periodic coefficients, Floquet's theory [47, 77] is the preferred approach.

1.1.1 Background

Stability analysis is typically performed on simplified models with the smallest number of degrees of freedom required to capture the physical phenomenon that causes the instability. Due to the variety of problems encountered, stability analysis methods can be classified into three categories. When the stability characteristics of a

dynamical system extracted from the analytical expression of its governing differential equations, *analytical methods* are used. As the number of degrees of freedom used to represent the system increases, these methods become increasingly cumbersome, and quickly unmanageable. On the other hand, due to increased available computer power, the analysis of flexible multibody systems relies on increasingly complex, large scale models. Full finite element analysis codes are now routinely used for this purpose [27, 28, 9] and, more often than not, multibody models are coupled to other codes to capture multi-physics phenomena. For instance, the analysis of the ride quality of a road vehicle might require the coupling of a multibody representation of the suspension system to an engine model. For aeroelastic problems, the structural dynamics model of the flight vehicle must be coupled to a fluid dynamics code that predicts the aerodynamic forces acting on the structure. *Numerical methods*, often based on their analytical counterparts, extract stability characteristics from numerical models that represent, as accurately as possible, the behavior of the dynamical system. Finally, *experimental methods* extract stability characteristics of the system from measured test data, such as signals from sensors that measure the response of the dynamical system.

1.1.2 Previous Work

Bauchau and Wang [16], have reviewed several approaches to stability analysis and their applicability to large scale multibody systems. They pointed out that one of the most general analytical method for stability evaluation is Lyapunov's function method that gives information about *nonlinear stability*, the other two methods, the characteristic exponent method and Floquet's theory, are classical approaches to solve the problem of *linearized stability*. When extracting damping rates and stability information from experimental measurements, Ibrahim's time domain method [50, 34], the complex exponential method [34] and moving block technique [44, 23] are

often used. Furthermore, they point out that Lyapunov's function method can not directly be applied to large dimensional numerical models. Hence, the problem of linearized stability is addressed in this thesis, *i.e.* the stability of small perturbations about a nonlinear equilibrium configuration that could be periodic. Based on the assumption of linear systems, Bauchau and Wang [17] have developed efficient and robust numerical approaches to extract the stability characteristics of flexible multi-physics systems. The advantages and range of applicability of these approaches will be discussed in details in this thesis.

1.1.3 Objective of Present Work

For large scale multibody models, a formal linearization is difficult and costly to obtain for constant in time systems, and virtually impossible in the case of periodic systems. This is particularly true when multi-physics models are coupled to multibody simulations. Hence, the only option is to study the response of the system to small perturbations about an equilibrium configuration using a fully nonlinear, coupled simulation tool. This means, in effect, that the complex dynamic model is used as a virtual prototype of the actual dynamical system, and the analyst is running a set of "experiments" to determine the stability characteristics of the system. A similar approach was taken by other researchers [76, 105, 94, 69] for systems modeled by simple analytical models featuring a few degrees of freedom.

1.1.4 Present Approaches

In this framework, the actual sensors that experimentally measure the response of a physical system are replaced by "sensors" that extract from the numerical model the predicted response of the system. In an experimental setting, the number of available sensors is typically limited because the complexity and cost of the experiment will dramatically increase with the number of sensors. Hence, the location and nature of the sensors will be carefully selected so as to obtain high quality measurements

that are most relevant to the phenomenon under scrutiny. On the other hand, in a numerical setting, the very nature of computational simulations implies that the response of each degree of freedom is available at no additional cost. The analyst could select a small number of these signals to perform stability analysis, mimicking the process used in an experimental setting, but it is also possible to use all the available data in an effort to obtain more accurate predictions.

In an experimental setting, stability analysis methods must be robust enough to deal with experimental noise. Numerical implementation also involves noise associated with the time discretization and inaccuracies of the solution. Another source of noise is the fact that the computed response is not that of a linear system, but rather that of a nonlinear system acted upon by small perturbations. In practice, this is a major hurdle: if the perturbation is too large, the nonlinearity in the response is pronounced and linearized stability tools give erroneous stability characteristics; on the other hand, if the perturbation is too small, the response has a small amplitude that becomes indistinguishable from the numerical noise, leading once again to erroneous predictions. If all the predictions produced by the numerical simulation are used for stability analysis, the data set will be highly redundant: the important information is a small subset of the large, noisy, highly redundant data set. This discussion clearly indicates that noise is as much a problem for numerical methods as it is for experimental methods.

In this thesis, two algorithms are presented for stability analysis based on techniques that are widely used in model reduction, damage detection, system identification, optimal control, and signal processing. In broad terms, these methods [1] are based on two techniques: the singular value decomposition and polynomial or moment matching concepts. The first type of algorithms are directly derived from linear time-invariant state space models. The polynomial based methods are generated from autoregressive moving average models [33], an approach which is equivalent to that

used for linear, time-invariant state space models. When impulse responses are solely considered, the autoregressive moving average model reduces to the autoregressive formulation. Bauchau and Wang [16] have proved that Prony's method is, in effect, an autoregressive method, although it is often presented as a curve fitting procedure.

To eliminate the effect of the noise in the measured signals, numerous modifications of autoregressive methods have been developed [59, 38]. A widely used approach to noise filtering is based on the singular values truncation technique. It has been proved that singular value decomposition associated with Hankel-norm model reduction [39], is equivalent to finite impulse response filtering [100]. On the other hand, the proper orthogonal decomposition [83, 97, 110], often performed via singular value decomposition, is also an efficient noise filtering technique that has been widely applied to fluid problems [98, 96, 72]; it also forms the basis for model reduction techniques in solid mechanics [6, 19], nonlinear control [66, 67], and others [60, 63, 4]. The physical interpretation of the proper orthogonal modes is discussed in refs. [35, 5]

1.2 System Identification for Linearized Dynamical Systems

As an extension of the two stability analysis algorithms discussed above, a robust system identification algorithm is developed, which forms the second part of this thesis.

1.2.1 Background

The problem of system realization or system identification for linear, time-invariant models has received considerable attention in numerous engineering applications such as dynamic simulation and control of flight vehicle [55], identification of vibrational modes of large-scale flexible structures, health monitoring and damage detection of civil engineering structures [106], or electrical circuits and imaging processes [1]. In general, system identification aims at creating a mathematical model of a dynamical

system from measurements of its input and output. In past decades, identification tools for the construction of state space representation of linear systems have been developed. However, more work is needed to develop identification procedures for complex, nonlinear systems such as large-scale, flexible multibody system. Many review papers have been presented on the subject of system identification: Kim and Arora [61] focused on linear and nonlinear dynamical systems, and a number of authors [108, 95, 107] provide comprehensive reviews of subspace-based identification methods.

1.2.2 Previous Work

The seminal work Kalman [57] introduced the concepts of controllability and observability, which are important prerequisites to identification. A state space approach was subsequently provided by the Ho-Kalman algorithm [46], and a minimum realization was obtained from Markov parameters. This algorithm is widely used as an identification algorithm, but it also contributed to the development of state space models [75] presenting balanced properties. When used in conjunction with numerically stable tool such as the singular value decomposition, the Ho-Kalman algorithm has been further explored [103] and extended to the eigensystem realization algorithm [55]. To decrease the effects of noise and nonlinearities, the eigensystem realization algorithm with data correlation [53] was developed. Furthermore, eigensystem realization algorithm combined with observer/Kalman filter identification [81] became an optimal procedure to construct a minimum order plant and compute Kalman filter gain matrix from input-output data. However, the computation of Markov parameters by observer/Kalman filter identification remains complex and determines the accuracy of the system realization. If a poor approximation of Markov parameters is obtained, the system identification might be meaningless, prompting the development of methods aimed at improving the accuracy of these parameters. System realization

methods based on Ho-Kalman algorithms and its extensions are known as minimum realization procedures.

Another system identification approach is based on subspace identification methods [95, 107, 80]. In these methods, a state space representation of linear system is found by matrix projection operations, and eliminating the effects of noise is a major concern. For stochastic system, Peeters and de Roeck [84, 85] have used Kalman filters to eliminate the effect of white noise with zero mean. For more general cases, Overschee and De Moor [80] have reviewed subspace methods and algorithms for the identification of linear time-invariant systems from given input-output data. Robust identification procedures have been developed for deterministic, stochastic, and combined deterministic-stochastic systems. Because matrix projection operations are computationally expensive, these methods are most suitable for solving small sized problems.

1.2.3 Objective

As discussed above, neither minimum realization nor subspace system identification algorithms can be applied to solve the identification problem for the large-scale flexible multibody system. In the framework of this thesis, a forward innovation model is required to estimate the input-output relationship satisfying a specified level of accuracy for a large-scale nonlinear flexible multibody dynamical system. A linearized model about a possibly time dependent equilibrium configuration of the nonlinear system will be extracted without performing a formal linearization of the governing nonlinear equations of motion of the system. The reason is that constructing nonlinear model plant is very difficult, and the formal linearization for a large-scale system is nearly impossible. The goal of this work is to develop robust identification algorithms to construct linearized plant models from archived control inputs data and

sensed system outputs data. The identified plant models will be used for solving optimal control problems from archived control inputs data and sensed system outputs. The identified linearized plant models must be suitable for the solution of optimal control problems.

1.2.4 Present Approach

The second part of this thesis focuses on a modified minimum realization approach combined with least-square techniques, to construct linear reduced order models of nonlinear, flexible multibody systems. The linearized realization is valid for small perturbations about an equilibrium configuration of nonlinear systems. Similarity transformation and balanced truncation form the theoretical basis for the proposed identification algorithm. Similarity transformations, clearly, do not affect system input-output behavior. This implies that the linear time-invariant model of the system is not unique. Balanced truncations [75, 67] dramatically decrease the order of high-dimensional systems; the modes of the reduced model form a subset of the modes of the original system and remain invariant in this reduction procedure.

The proposed algorithms can be applied to one or multiple time signals, and are equally applicable to experimental measurements or numerically computed responses. For linear systems, the signals are directly extracted from the system's dynamic response; for nonlinear systems, the signals are computed as the difference between the sensed responses under external perturbations and those of the equilibrium configuration. The proposed system identification algorithm uniquely combines the methods of minimum realization and subspace identification. For minimum realization, as pointed out in section 1.2.2, the computation of Markov parameters remains complex and determines the accuracy of the system realization. The proposed approach bypasses the computation of Markov parameters because the free impulse response of the system can be directly computed in the present computational environment. As

proposed by Bauchau and Wang [16, 17] for stability analysis, minimum realization concepts were applied to identify the stability and output matrices. The singular value decomposition, a numerically stable mathematical tool, is used to filter noise. On the other hand, subspace identification algorithms construct a state space plant model of linear systems by using computationally expensive oblique matrix projection operations. The proposed algorithm avoids this burden by computing the Kalman filter gain matrix and model dependency on external inputs based on a small sized subspace. A Kalman filter is used to minimize the effects of white noise on the identification process; the filter is computed by solving the associated discrete time algebraic Riccati equations directly. Both deterministic or combined deterministic-stochastic systems can be treated. Finally, the least squares technique is applied to compute the model dependency on external inputs. The simplicity and robustness of the proposed identification algorithm will be demonstrated.

1.3 Optimal Control of Flexible Dynamical Systems

Once a subspace plant model has been identified, it is possible to apply optimal control theory to flexible multibody systems. This will be developed in the last part of this thesis.

1.3.1 Background and Previous Work

Optimal control, building on the optimal filtering work of Wiener, reached maturing in the 1960's with what is now call linear quadratic Gaussian or LQG controller [3]. Aerospace problems, such as rocket maneuvering with minimum fuel consumption, could be easily formulated with these tools, which have now found wide application in many engineering disciplines. However, implementation of these methodologies requires accurate plant models to be developed and furthermore, the assumption of white noise disturbance is not always meaningful in practical applications.

As previously mentioned, the availability of increased computer power enables increasingly complex, large-scale plant model to be developed, often based on multibody dynamic models. However, these increasingly high order models represent a challenge for optimal control methodologies [31], which typically require low order plant models to be effective. The reason is obvious: for high order models, the computation of control actions is increasing challenging. In most cases, practical application of control algorithms requires a dimensional reduction of the plant model. A first approach to dimensional reduction is modal truncation: the eigenmodes of the system associated with high natural frequencies are eliminated from the plant model, resulting in a dramatic dimensional reduction, and the optimal controller only deals with the physically meaningful, low frequencies of the system. However, in the presence of time dependent or nonlinear systems, eigenmodes are not easily extracted. Another possible approach is the proper orthogonal decomposition, as discussed above, which has found increased application in the last decade. Proper orthogonal decomposition projects the large-scale plant into an orthogonal subspace to condense the large amount of redundant data. Robust optimal control then becomes an iterative procedure involving proper orthogonal decomposition, plant reduction and application of linear quadratic Gaussian controller, a well known adaptive control procedure [92, 58]. But the evaluation of the proper orthogonal modes remains a computational burden for large-scale, time-variant plants.

1.3.2 Present Approach

The third part of this thesis presents a new approach to this problem. At first, a plant model is identified, which accurately captures the input-output behavior of the system. The proposed robust system identification algorithm is used for this purpose; it is based on sensing the time history of both input and output signals of the system. A linearized model about a possibly time dependent equilibrium configuration of the

nonlinear system is then easily extracted without performing a formal linearization of the governing nonlinear equations of motion of the system. This approach is ideally suited for the analysis of large-scale, multibody dynamics based multi-physics problems. The classical linear quadratic optimal controller is then designed based on the identified plant model. The time adaptive controller is then applied to minimize output perturbations, or to drive the system to desired output target values.

1.4 Chapter Summary

In summary, the two stability analysis algorithms presented in this thesis are closely related and will be introduced through Floquet's theory for the first and autoregressive concepts for the second. Because singular value decomposition is a powerful tool for dealing with noise, both approaches make use of this technique. The proposed stability analysis algorithms can be applied to one or multiple time signals, and are able to deal with time constant or periodic systems. For linear systems, the signals are measured from the dynamic responses directly; for nonlinear systems, the signals are computed as the difference between the sensed responses under external perturbations and those of the equilibrium configuration. The algorithms are equally applicable to experimental measurements or numerically computed responses. If all signals are used, *i.e.* if the time histories of all the degrees of freedom of the system are used, the computational burden associated with these algorithms becomes large. One option is to retain a few signals only to reduce the computational cost, but at the expense of loosing potentially relevant information contained in the discarded signals. In this thesis, a different approach is taken. First, the proper orthogonal decomposition technique is applied to the full set of all degrees of freedom of selected substructures and other components of the comprehensive multibody system. The few proper orthogonal modes associated with the largest amount of energy contained in the responses of all degrees of freedom are retained and visualized to explore the

physical reasons that cause the instability. The optimized signals, from which noise was filtered out by the selection of proper orthogonal modes, are used as an input to the stability analysis algorithms. This approach is computationally efficient, while retaining accuracy and requiring minimum user input.

As a combination of methods of minimum realization and subspace identification, the proposed robust system identification technique bypasses the computation of Markov parameters and avoids the computational burden of oblique matrix projection operations, which are widely used in subspace identification algorithms. In the proposed approach, minimum realization concepts are applied to identify the stability and output matrices after the free impulse response of the system was directly computed. Note that computing the Kalman filter gain matrix is an user option. Finally, the least-square regression is applied to determine input dependency. Furthermore, the proposed identification approach is combined with the proper orthogonal decomposition to filter out noise and create optimized signals that can be used to construct subspace based plant models. For optimal control, two discrete time algebraic Riccati equations must be solved: one is associated with the linear quadratic regulator, the other with the Kalman filter if not determined in the process of the system identification. Applications of the proposed methodology are presented that demonstrate its robustness and efficiency. Both stability analysis and optimal control are based on a unified framework, system identification. Typically, stability analysis of a system is a prerequisite to its control.

Chapter 2 of this thesis is an overview of the numerical models, which form the foundation for stability analysis, system identification and optimal control; then, chapter 3 reviews a number of existing tools for stability analysis, in an attempt to identify the methods that are most suitable for the stability analysis of complex multibody systems. Chapter 4 details the proposed robust numerical stability analysis methods; numerical examples are presented in chapter 5. Two types of system

identification algorithms are reviewed in chapter 6, which also presents the proposed, minimum realization approach. The design of optimal control is presented in chapter 7. Finally, conclusions of this work and recommendations for future work are summarized in chapter 8.

CHAPTER II

SYSTEM MODELS

The systems to be investigated here are assumed to be linear models featuring constant or periodic coefficients. Discrete mechanical models of such a dynamic system are introduced at first, then reformulated in the state space framework. Discrete time model are constructed, that reflect the numerical process used to solve the governing equations of motion, or the digital sampling of system response in experimental settings. The autoregressive moving average model often used in signal process is introduced. Finally, system modal parameters are defined.

2.1 Mechanical Model

When the finite element method is applied to compute the response of dynamical systems, the behavior of discrete mechanical systems is described by a set of second order differential equations

$$M\underline{\ddot{x}}(t) + C_\zeta \underline{\dot{x}}(t) + K\underline{x}(t) = \underline{f}(t), \tag{2.1}$$

where M, C_ζ and K are the mass, damping and stiffness matrices, $\underline{f}(t)$ the array of external excitations, and $\underline{x}(t)$ the array of displacements; the notation $()^{\cdot}$ indicates a derivative with respect to time. For systems with distributed parameters, these equations are obtained as the finite element approximation of the system with only N degrees of freedom.

2.2 Continuous Time Model

To reduce the second order equations to a first order, state space system, the following notations are defined

$$\underline{u}(t) = \left| \begin{array}{c} \underline{x}(t) \\ \dot{\underline{x}}(t) \end{array} \right|, \quad A = \left[\begin{array}{cc} 0 & I \\ -M^{-1}K & -M^{-1}C_\zeta \end{array} \right] \quad \text{and} \quad B = \left[\begin{array}{c} 0 \\ M^{-1} \end{array} \right], \tag{2.2}$$

and eqs. (2.1) then become

$$\dot{\underline{u}}(t) = A\underline{u}(t) + B\underline{f}(t), \tag{2.3}$$

where $\underline{u}(t)$ is the state vector of dimension $2N$, A the system characteristic matrix, often called the *"stability matrix."* Eqs. (2.3) could represent the first order form of the equations of motion of a multibody system, in which case the state vector would store the displacements and velocities of all degrees of freedom of the model. For multi-physics models, the state vector would include additional information; for instance, fluid pressures and velocities in the case of an aeroelastic simulation.

The corresponding eigenvalue problem is $\Psi\Lambda = A\Psi$, where $\Lambda = \text{diag}(\lambda_j)$ is a diagonal matrix containing the stability characteristics of the system, and Ψ contains the $2N$ eigenvectors of the system. Generally, for damped systems, Λ and Ψ have the following structure

$$\Lambda = \left[\begin{array}{cc} \Lambda_c & 0 \\ 0 & \bar{\Lambda}_c \end{array} \right] \quad \text{and} \quad \Psi = \left[\begin{array}{cc} \Psi_c & \bar{\Psi}_c \\ \Psi_c\Lambda_c & \bar{\Psi}_c\bar{\Lambda}_c \end{array} \right]. \tag{2.4}$$

In these notations, Ψ_c is a matrix the columns of which are the system eigenmodes, and the diagonal elements of Λ_c the poles of the dynamical system defined by eqs. (2.1). Matrices $\bar{\Psi}_c$ and $\bar{\Lambda}_c$ are complex conjugates; the eigenvalue decomposition of the matrix A can be rewritten as $A = \Psi\Lambda\Psi^{-1}$.

Output signals are arbitrarily selected from the response of the discrete mechanical system. The array of output signals can be written as a linear combination of system

displacements $\underline{x}$, velocities $\dot{\underline{x}}$ and accelerations $\ddot{\underline{x}}$

$$\underline{y} = L_d\underline{x} + L_v\dot{\underline{x}} + L_a\ddot{\underline{x}}, \tag{2.5}$$

where matrices L_d, L_v and L_a defined the desired mapping. Solving for the accelerations, $\ddot{\underline{x}}$, from eqs. (2.1), yields $\ddot{\underline{x}} = M^{-1}(-C_\zeta\dot{\underline{x}} - K\underline{x} + \underline{f})$, assuming that M is nonsingular, and introducing this result into eqs. (2.5), the output array, $\underline{y}$, becomes function of displacements, velocities and external excitations

$$\underline{y} = L_d\underline{x} + L_v\dot{\underline{x}} + L_aM^{-1}(\underline{f} - C_\zeta\dot{\underline{x}} - K\underline{x}). \tag{2.6}$$

Array $\underline{y}$ can now be written in a compact form as

$$\underline{y}(t) = C\underline{u}(t) + D\underline{f}(t), \tag{2.7}$$

where matrices C and D are defined as

$$C = \begin{bmatrix} L_d - L_aM^{-1}K & L_v - L_aM^{-1}C_\zeta \end{bmatrix} \quad \text{and} \quad D = L_aM^{-1}. \tag{2.8}$$

Finally, the complete continuous time model consists of eqs. (2.3) and (2.7)

$$\begin{cases} \dot{\underline{u}}(t) = A\underline{u}(t) + B\underline{f}(t); \\ \underline{y}(t) = C\underline{u}(t) + D\underline{f}(t). \end{cases} \tag{2.9}$$

2.3 Discrete Time Model

In numerical applications, the response of the system will typically be computed at a set of discrete times by using the numerical iteration techniques, then, a discrete time model can be constructed to capture the dynamic properties of the system in a discrete way.

2.3.1 Discrete Time Model With Constant Coefficient

Consider first a system featuring constant coefficients, *i.e.* matrix A is constant. Given initial conditions, $\underline{u} = \underline{u}(t_0)$ at time t_0, the continuous time solution of the

system, eqs. (2.3), is given in textbooks [47] as

$$\underline{u}(t) = e^{A(t-t_0)}\underline{u}(t_0) + \int_{t_0}^{t} e^{A(t-\tau)}B\underline{f}(\tau)\mathrm{d}\tau. \tag{2.10}$$

The discrete time response of the system will be computed with the help of numerical methods at a set of discrete times $t_k = k\Delta t$, where Δt is the time step size and k a positive integer. Without loss of generality, the initial time can be assumed to be zero, *i.e.*, $t_0 = 0$. The discrete solution $\underline{u}(k\Delta t)$, denoted $\underline{u}(k\Delta t) = \underline{u}_k$, at time t_k now writes

$$\underline{u}_k = e^{Ak\Delta t}\underline{u}_0 + \int_{0}^{k\Delta t} e^{A(k\Delta t-\tau)}B\underline{f}(\tau)\mathrm{d}\tau, \tag{2.11}$$

and at time step $k+1$, $\underline{u}_{k+1}$ is

$$\underline{u}_{k+1} \;=\; e^{A\Delta t}\underline{u}_k + \int_{k\Delta t}^{(k+1)\Delta t} e^{A((k+1)\Delta t-\tau)}B\underline{f}(\tau)\mathrm{d}\tau. \tag{2.12}$$

It will be assumed that all discrete quantities, say $\underline{f}(t)$, remain constant over a time step, *i.e.* $\underline{f}(t) = \underline{f}_k$ for $t \in [k\Delta t,\ (k+1)\Delta t]$. The discrete solution at time $k+1$ now becomes

$$\underline{u}_{k+1} = e^{A\Delta t}\underline{u}_k + (e^{A\Delta t} - I)A^{-1}B\underline{f}_k, \tag{2.13}$$

where I is the identity matrix. Introducing the following notations

$$A_s = e^{A\Delta t} \quad \text{and} \quad B_s = (e^{A\Delta t} - I)A^{-1}B, \tag{2.14}$$

the discrete time state space model with constant coefficients can be expressed in a compact form as

$$\begin{cases} \underline{u}_{k+1} = A_s\underline{u}_k + B_s\underline{f}_k; \\ \underline{y}_k = C\underline{u}_k + D\underline{f}_k. \end{cases} \tag{2.15}$$

It is well known that the stability characteristics of the system can be determined from its characteristic matrix; hence, when focusing on stability analysis, the sole homogeneous problem is considered. If $\underline{f}(k) = 0$, the discrete time model can now be

cast in the following compact form

$$\begin{cases} \underline{u}_{k+1} = A_s \underline{u}_k; \\ \underline{y}_k = C\underline{u}_k. \end{cases} \tag{2.16}$$

2.3.2 Discrete Time Model With Periodic Coefficients

Next, consider a system with periodic coefficients, *i.e.* matrix A is a periodic function of time, $A(t) = A(t+T)$, where T is the period of the system. Here again, the solution of the homogeneous problem, $\dot{\underline{u}}(t) = A\underline{u}(t)$, is found in textbooks [47], and given a set of initial conditions, the solution becomes

$$\underline{u}(t) = P(t)e^{\Lambda(t-t_0)}P(t_0)^{-1}\underline{u}(t_0), \tag{2.17}$$

where $\Lambda = \mathrm{diag}(\lambda_j)$ is a diagonal matrix of characteristic exponents of the periodic system and $P(t)$ a periodic matrix, $P(t) = P(t+T)$.

When a full set of initial conditions $\underline{u}^{(i)}(t_0)$, $i = 1, 2, \ldots, 2N$, is given, the fundamental solutions $U(t)$ is constructed from a full set of linearly independent solutions $\underline{u}^{(i)}(t)$

$$U(t) = [\underline{u}^{(1)}(t), \underline{u}^{(2)}(t), \ldots, \underline{u}^{(2N)}(t)]. \tag{2.18}$$

The explicit expression for $U(t)$ is

$$U(t) = P(t)e^{\Lambda(t-t_0)}P(t_0)^{-1}U(t_0), \tag{2.19}$$

where $U(t_0)$ stores all the initial conditions, $U(t_0) = [\underline{u}^{(1)}(t_0), \underline{u}^{(2)}(t_0), \ldots, \underline{u}^{(2N)}(t_0)]$. The solutions of eqs. (2.3) with periodic coefficients in textbooks [47] are recast of

$$\underline{u}(t) = U(t)U(t_0)^{-1}\underline{u}(t_0) + \int_{t_0}^{t} U(t)U(\tau)^{-1}B\underline{f}(\tau)\ \mathrm{d}\tau; \tag{2.20}$$

Note that $U(t)$ is nonsingular, the explicit expression of the solutions $\underline{u}(t)$ becomes

$$\underline{u}(t) = P(t)e^{\Lambda(t-t_0)}P(t_0)^{-1}\underline{u}(t_0) + \int_{t_0}^{t} P(t)e^{\Lambda(t-\tau)}P(\tau)^{-1}B\underline{f}(\tau)\ \mathrm{d}\tau. \tag{2.21}$$

At discrete time, $t = k\Delta t$, with zero initial time, discrete solutions are reformulated as

$$\underline{u}_k = P_k e^{\Lambda k\Delta t} P_0^{-1} \underline{u}_0 + \int_0^{k\Delta t} P_k e^{\Lambda(k\Delta t-\tau)} P(\tau)^{-1} B \underline{f}(\tau)\ \mathrm{d}\tau, \tag{2.22}$$

after shifting $\underline{u}_k$ forward one time step, the relationship between $\underline{u}_{k+1}$ and $\underline{u}_k$ can be found

$$\underline{u}_{k+1} = P_{k+1} e^{\Lambda\Delta t} P_k^{-1} \underline{u}_k + \int_{k\Delta t}^{(k+1)\Delta t} P_{k+1} e^{\Lambda((k+1)\Delta t-\tau)} P(\tau)^{-1} B \underline{f}(\tau)\ \mathrm{d}\tau. \tag{2.23}$$

Under the assumption that excitation $\underline{f}(t)$ is constant within the k^{th} sampling period, and making the same assumption concerning matrix $P(t)^{-1}$, it is possible to approximately evaluate the integral as

$$\int_{k\Delta t}^{(k+1)\Delta t} P_{k+1} e^{\Lambda((k+1)\Delta t-\tau)} P(\tau)^{-1} B \underline{f}(\tau)\ \mathrm{d}\tau = P_{k+1}(e^{\Lambda\Delta t} - I)\Lambda^{-1} P_k^{-1} B \underline{f}_k. \tag{2.24}$$

It then becomes possible to express $\underline{u}_{k+1}$ as $\underline{u}_{k+1} = A_k \underline{u}_k + B_k \underline{f}_k$, where matrices A_k and B_k are defined as

$$A_k = P_{k+1} e^{\Lambda\Delta t} P_k^{-1} \quad \text{and} \quad B_k = P_{k+1}(e^{\Lambda\Delta t} - I)\Lambda^{-1} P_k^{-1} B. \tag{2.25}$$

Because the system is periodic, it follows that $A_k = A_{k+p}$ and $P_k = P_{k+p}$, where p is the number of time steps per period, $p = T/\Delta t$, assumed to be an integer. Finally, the discrete time model is recast in a compact form as

$$\begin{cases} \underline{u}_{k+1} = A_k \underline{u}_k + B_k \underline{f}_k, \\ \underline{y}_k = C \underline{u}_k + D \underline{f}_k. \end{cases} \tag{2.26}$$

For the homogeneous problem, $\underline{f}_k = 0$, the discrete time model description is given by

$$\begin{cases} \underline{u}_{k+1} = A_k \underline{u}_k, \\ \underline{y}_k = C \underline{u}_k \end{cases} \tag{2.27}$$

2.3.3 Autoregressive Moving Average Model

The autoregressive moving average model [33], typically applied to the sequence of discrete time data, is equivalent to the linear model, eqs. (2.15). As a highly flexible technique, the autoregressive moving average is used to parameterize and represent the dynamics of linear system. To illustrate the basic issues associated with autoregressive moving average, a single input-single output model will be presented using this modeling approach in this section.

Combining the two equations of the linear model, eqs. (2.15), and performing a backward recursion, the outputs, $\underline{y}_k$, can be expressed by the following convolution

$$\underline{y}_k = CA_s^k\underline{u}_0 + CA_s^{k-1}B_s\underline{f}_0 + CA_s^{k-2}B_s\underline{f}_1 + \ldots + CB_s\underline{f}_{k-1} + D\underline{f}_k. \tag{2.28}$$

If a single input-single output model is considered, matrix C reduces to a row vector, the control inputs, $\underline{f}_i$, for $i = 0, 1, \ldots, k$, are presented by a data sequence, f_i, and matrix D reduces to a real number. The single output, h_k, can be expressed as

$$h_k = \sum_{j=1}^{2N} a_j e^{\lambda_j k\Delta t} + \sum_{i=0}^{k} b_i f_i, \tag{2.29}$$

where $\exp(\lambda_j\Delta t)$ are the eigenvalues of the stability matrix, A_s, associated with eigendecomposition, $A_s = \Psi\exp(\lambda_j\Delta t)\Psi^{-1}$, and a_j are defined as, $a_j = \ell_j\psi_j$, ℓ_j and ψ_j are the elements of products, $C\Psi$ and $\Psi^{-1}\underline{u}_0$, respectively; b_i are the products, $b_i = CA_s^{k-i-1}B_s$ for $i = 0, 1, \ldots, k-1$, and $b_k = D$. The characteristic exponents of the system, $\exp(\lambda_j\Delta t)$, have been assumed to be distinct in this discussion. A complete discussion of the general case of repeated eigenvalues is found in textbooks [47].

Consider a set of unkown coefficients β_k for $k = 0, 1, \ldots, 2N-1$, and the following linear combination of the discrete data points

$$\beta_0 h_0 + \beta_1 h_1 + \ldots + \beta_{2N-1}h_{2N-1} + h_{2N} = \sum_{j=1}^{2N} a_j \left[\sum_{k=0}^{2N-1} \beta_k q_j^k + q_j^{2N}\right] + \sum_{i=0}^{2N} c_i f_i, \tag{2.30}$$

where $q_j = \exp(\lambda_j\Delta t)$, coefficients $c_i = b_i\left[\sum_{k=i}^{2N-1}\beta_k + 1\right]$ for $i = 0, 1, \ldots, 2N-1$,

and $c_{2N} = b_{2N}$. If the unknown coefficients, β_k, satisfy the following polynomial

$$\beta_0 + \beta_1 q_j + \beta_2 q_j^2 + \ldots + \beta_{2N-1} q_j^{2N-1} + q_j^{2N} = 0, \tag{2.31}$$

the linear combination of the sampling points will formulate the autoregressive moving average model

$$h_{2N} + \beta_0 h_0 + \beta_1 h_1 + \ldots + \beta_{2N-1} h_{2N-1} = c_0 f_0 + c_1 f_1 + \ldots + c_{2N-1} f_{2N-1} + c_{2N} f_{2N}. \tag{2.32}$$

Without loss of generality, the autoregressive moving average model [52, 85] with order (p, r) for the time series data, h_k, can be written as

$$h_k + \beta_0 h_{k-p} + \beta_1 h_{k-p+1} + \ldots + \beta_{p-1} h_{k-1} = c_0 f_{k-r} + c_1 f_{k-r+1} + \ldots + c_{r-1} f_{k-1} + c_r f_k. \tag{2.33}$$

In this formulation, the left hand side is called as the autoregressive part and the right hand side the moving average part. Especially, the model characterized by eq. (2.32) is of order $2N$ for both autoregressive and moving average part. If the control inputs, f_i, are zero, the autoregressive moving average model reduces to the autoregressive model

$$h_k + \beta_0 h_{k-p} + \beta_1 h_{k-p+1} + \ldots + \beta_{p-1} h_{k-1} = 0, \tag{2.34}$$

which is widely used for stability analysis.

The canonical form of the autoregressive moving average model will be defined under the assumption $p = r$. It is easy to verify that the following set of equations is equivalent to the autoregressive moving average model, eq. (2.33),

$$\begin{cases} z_k^{(1)} = -\beta_{p-1} z_{k-1}^{(1)} + z_{k-1}^{(2)} + (c_{r-1} - c_r \beta_{p-1}) f_{k-1}; \\ z_{k-1}^{(2)} = -\beta_{p-2} z_{k-2}^{(1)} + z_{k-2}^{(3)} + (c_{r-2} - c_r \beta_{p-2}) f_{k-2}; \\ \vdots \\ z_{k-p+2}^{(p-1)} = -\beta_1 z_{k-p+1}^{(1)} + z_{k-p+1}^{(p)} + (c_1 - c_r \beta_1) f_{k-r+1}; \\ z_{k-p+1}^{(p)} = -\beta_0 z_{k-p}^{(1)} + (c_0 - c_r \beta_0) f_{k-r}; \\ h_k = z_k^{(1)} + c_r f_k. \end{cases} \tag{2.35}$$

The canonical form is recast as

$$\begin{cases} \underline{z}_{k+1} = \tilde{A}\underline{z}_k + \tilde{B}f_k; \\ h_k = \tilde{C}\underline{z}_k + \tilde{D}f_k, \end{cases} \tag{2.36}$$

using the following notations

$$\begin{aligned} \underline{z}_k &= \begin{bmatrix} z_k^{(1)} \\ z_k^{(2)} \\ \vdots \\ z_k^{(p-1)} \\ z_k^{(p)} \end{bmatrix}, \quad \tilde{A} = \begin{bmatrix} -\beta_{p-1} & 1 & 0 & \dots & 0 \\ -\beta_{p-2} & 0 & 1 & \dots & 0 \\ \vdots & \vdots & \vdots & \ddots & \vdots \\ -\beta_1 & 0 & 0 & \dots & 1 \\ -\beta_0 & 0 & 0 & \dots & 0 \end{bmatrix}, \quad \tilde{B} = \begin{bmatrix} c_{r-1} - c_r\beta_{r-1} \\ c_{r-2} - c_r\beta_{r-2} \\ \vdots \\ c_1 - c_r\beta_1 \\ c_0 - c_r\beta_0 \end{bmatrix}, \\ \tilde{C} &= \begin{bmatrix} 1 & 0 & \dots & 0 \end{bmatrix}, \quad \tilde{D} = \begin{bmatrix} c_r \end{bmatrix}. \end{aligned} \tag{2.37}$$

Comparing the canonical form, eqs. (2.36), and the deterministic model, eqs. (2.15), both of them describe the input-output behavior of a single input and single output system. In fact, the canonical form can be directly obtained from the linear model, eqs. (2.15), by similarity transformation. It means the formulation of linear model, eqs. (2.15), is not unique, a fundamental observation for stability analysis and system identification that will be further explored in section 6.1.1. The proper way to determine the unknown coefficients, β_k, c_i and b_r will be discussed in section 4.4 and the physical meaning of the coefficients β_k will also be investigated.

2.3.4 Modal Parameters of the Discrete Time Model

With the help of eigenvalue decomposition of the stability matrix, $A = \Psi\Lambda\Psi^{-1}$, the eigenvalue decomposition of the exponential characteristic matrix A_s can be found from the definition, $A_s = \exp(A\Delta t)$. Indeed,

$$A_s = e^{A\Delta t} = e^{\Psi\Lambda\Psi^{-1}\Delta t} = \Psi e^{\Lambda\Delta t}\Psi^{-1}, \tag{2.38}$$

where the Mc Laurin series expansion of the exponential function, $e^X = \sum_{n=0}^{\infty} X^n/n!$, is used to obtain the expression

$$e^{\Psi\Lambda\Psi^{-1}\Delta t} = \sum_{n=0}^{\infty} \frac{1}{n!} \left(\Psi\Lambda\Psi^{-1}\Delta t\right)^n = \sum_{n=0}^{\infty} \frac{1}{n!} \Psi \left(\Lambda\Delta t\right)^n \Psi^{-1} = \Psi e^{\Lambda\Delta t}\Psi^{-1}. \tag{2.39}$$

The eigenvalues of A_s are written as $\exp(\lambda_j \Delta t) = r_j \exp(\pm \mathbf{i}\phi_j)$, and the characteristic exponents as $\lambda_j = \omega_j \left(\zeta_j \pm \mathbf{i}\sqrt{1-\zeta_j^2}\right)$, where ω_j and ζ_j are the frequency and damping, respectively, associated with this characteristic exponent and $\mathbf{i} = \sqrt{-1}$; it then follows that

$$\zeta_j = \frac{c_j}{\sqrt{1+c_j^2}}; \quad \omega_j = \frac{\phi_j}{\Delta t}\sqrt{1+c_j^2}, \quad j = 1, 2, \ldots, N, \tag{2.40}$$

where $c_j = (\ln r_j)/\phi_j$.

The mode shapes Ψ of the system are shown to be the same as those of matrix A_s in eq. (2.38). Hence, all the modal parameters of the linear system with constant coefficients can be determined from the eigenvalue decomposition of matrix A_s. For systems with periodic coefficients, matrix $A_k = P_{k+1} e^{\Lambda\Delta t} P_k^{-1}$ still contains the valuable information about the characteristic exponents, Λ, and the physical meaning of matrix P_k is explained by the Floquet's theory [47, 77]. The columns of matrix P_k are the eigenvectors of the transition matrix, and its determinant is unity, $\det(P_k) = 1$. This property is used to extract the frequencies and damping rates of the periodic coefficient system from the eigenvalues of A_k because

$$\det(A_k) = \det(P_{k+1}) \det(e^{\Lambda\Delta t}) \det(P_k^{-1}) = \det(e^{\Lambda\Delta t}). \tag{2.41}$$

2.4 Chapter Summary

The linearized models to be used for stability evaluation, system identification and optimal control of nonlinear flexible multibody systems were presented in this chapter. Discrete mechanical model were constructed using the finite element approximation, discretized with N degrees of freedom. When N is a large number, this process leads

to a complex, large-scale, time continuous linear model in state space. Once the solution of the constant or periodic coefficient systems has been obtained, three types of discrete time models were defined: constant coefficient deterministic model, periodic coefficient deterministic model and autoregressive moving average model. Finally, the modal parameters of linear systems were defined for both constant coefficient and periodic coefficient systems.

CHAPTER III

TOOLS FOR STABILITY ANALYSIS

Tools for stability analysis can be classified into three categories in general. First, *analytical tools* asses the stability characteristics of a dynamical system from the analytical expression of its governing differential equations. These methods are also the fundamental of *numerical tools* that extract stability characteristics from numerical models that represent, as accurately as possible, the behavior of the dynamical system. Finally, *experimental tools* extract stability characteristics of the system from measured experimental data. Since comprehensive multibody models in numerical simulation are "virtual prototypes" of actual systems, the experimental tools can be also applied to numerical models.

This chapter reviews existing methods belong to the analytical and experimental tools. The advantages, shortcomings, limitations and range of application of the various approaches are discussed. Two types of numerical tools for stability analysis will be discussed in next chapter, the first applies Floquet's theory, an analytical tool, to numerical model; the second uses the autoregressive methodology.

3.1 Analytical Tools for Stability Analysis

In this section, an overview of several analytical tools for stability analysis is introduced. The Lyapunov direct method enables assessing the stability property of the general dynamical system; the characteristic exponent method is widely used for systems with constant coefficients; Floquet's theory considers more general dynamical systems with periodic coefficients. Finally, the Lyapunov exponents characterizes the chaotic motion of nonlinear system.

3.1.1 Lyapunov Direct Method

It is well known that Lyapunov direct method [47] is the most general method for stability analysis of a nonlinear dynamic system

$$\dot{\underline{u}} = \underline{F}(\underline{u}(t)), \tag{3.1}$$

where $\underline{F}$ an arbitrary function of $\underline{u}$. Without loss of generality, it always assume that the equilibrium solution is $\underline{u}(t) = 0$, so that $\underline{F}(0) = 0$. With this simplification, the stability criteria are defined.

1. A system is said to be *Lyapunov stable* if, for all small amplitude perturbation $\epsilon > 0$, there exists a $\delta > 0$ such that if $\|\underline{u}(0)\| < \delta$, then $\|\underline{u}(t)\| < \epsilon$ for $t \geq 0$.

2. A system is said to be *asymptotically stable* if it is Lyapunov stable and there exists a $\delta > 0$ such that if $\|\underline{u}(0)\| < \delta$, then $\underline{u}(t) \to 0$ at $t \to \infty$.

3. The system is *unstable* if it is not Lyapunov stable,

To assess the stability characteristics using the above definition of stability criterion, the Lyapunov direct method involves a positive definite scalar function $V(\underline{u})$ with initial condition $V(0) = 0$ and $V(\underline{u}) > 0$ for $\underline{u} \neq 0$, called the *Lyapunov function* such that its first derivative with respect to time, $\dot{V}(u)$, is continuous. If the following condition is satisfied,

$$\dot{V}(\underline{u})\ \underline{F}(\underline{u}) \leq 0, \tag{3.2}$$

then the solution $\underline{u}(t) = 0$ is Lyapunov stable. If this condition is changed to

$$\dot{V}(\underline{u})\ \underline{F}(\underline{u}) < 0, \tag{3.3}$$

then the solution is asymptotically stable. The proof of this theorem can be found in ref. [47].

Lyapunov direct method enables assessing the stability characteristics of general dynamical systems. Unfortunately, the choice of Lyapunov function is not always

easy; in fact, there exists no general method of constructing this function for nonlinear or time-dependent dynamical systems. So Lyapunov direct method is rarely used in practice, although it is an important theoretical tool. In fact, Lyapunov direct method can not be applied to numerical models or experimental data.

3.1.2 Characteristic Exponent Method

The characteristic exponent method [47] deals with the special case of dynamical systems defined by a set of linear, ordinary differential equations with constant coefficients. In first order form the dynamical system is governed by $2N$ homogeneous equations

$$\dot{\underline{u}} = A\ \underline{u}, \tag{3.4}$$

where A is a matrix of constant coefficients. Given initial conditions, $\underline{u} = \underline{u}_0$ at time $t = 0$, the solution of this system is given in textbooks [47] as

$$\underline{u}(t) = e^{At}\underline{u}_0. \tag{3.5}$$

When matrix A is factorized as $A = \Psi\Lambda\Psi^{-1}$, where $\Lambda = \mathrm{diag}(\lambda_j)$, and λ_j are distinct characteristic exponents, the solution can be rewritten as

$$\underline{u}(t) = \Psi e^{\Lambda t}\Psi^{-1}\underline{u}_0 = \sum_{j=1}^{2N} \hat{c}_j \underline{\psi}_j e^{\lambda_j t}, \tag{3.6}$$

where $\hat{c}_j$ is the j^{th} entry of array $\Psi^{-1}\underline{u}_0$, $\underline{\psi}_j$ the j^{th} column of orthogonal matrix Ψ. The stability characteristics of the system can be computed from the eigenvalues, $\lambda_j,\ j = 1, 2, \ldots, 2N$. The damping ζ_j and frequency ω_j associated with each eigenvalue are defined by eqs. (2.40). The system is stable if all the damping values are negative or zero, *i.e.* $\zeta_j \leq 0,\ j = 1, 2, \ldots, 2N$.

An alternative formulation of the solution of linear time-invariant system is known to be in the form of

$$\underline{u}(t) = \bar{\underline{u}}\ e^{\lambda t}, \tag{3.7}$$

and direct substitution into the governing equations leads to an eigenvalue problem $A\ \underline{\bar{u}} = \lambda\ \underline{\bar{u}}$; the eigenvalues are the roots of characteristic equation

$$\det(A - \lambda I) = a_0\lambda^{2N} + a_1\lambda^{2N-1} + \ldots + a_{2N-1}\lambda + a_{2N} = 0. \tag{3.8}$$

Instead of actually computing the eigenvalues of the system, the Routh-Hurwite criterion [64] gives necessary and sufficient conditions for stability assessment of the system. It requires all the roots of characteristic equation to have non-positive real part for the case of system is stable. The so called *Hurwite determinants* is defined as the diagonal minors of the following matrix D_N

$$D_N = \begin{bmatrix} a_1 & a_3 & a_5 & \ldots & 0 & 0 \\ a_0 & a_2 & a_4 & \ldots & 0 & 0 \\ 0 & a_1 & a_3 & \ldots & 0 & 0 \\ 0 & a_0 & a_2 & \ldots & 0 & 0 \\ 0 & 0 & a_1 & \ldots & 0 & 0 \\ 0 & 0 & a_0 & \ldots & 0 & 0 \\ \vdots & \vdots & \vdots & \ddots & \vdots & \vdots \\ 0 & 0 & 0 & \ldots & a_{2N-1} & 0 \\ 0 & 0 & 0 & \ldots & a_{2N-2} & a_{2N} \end{bmatrix}. \tag{3.9}$$

Equivalently, when the system is stable, the Hurwite determinants should be non-negative.

The characteristic exponent approach is an analytical method that can be used for systems featuring a very small number of degrees of freedom; it is also used for numerical problem since the resulting eigenproblem is easily solved numerically for larger dimensional problems. The characteristic exponent method can be applied to study the stability of small perturbations about an equilibrium configuration of the nonlinear system. First, the system is linearized about one of its nonlinear equilibrium solution, then, the characteristic exponent method is applied to the resulting linear

system. For small sized systems, the linearization process can be carried out analytically; for large sized systems, finite difference concepts are used for the linearization, but the computational cost becomes overwhelming as the size of the system, $2N$, increases.

3.1.3 Floquet's Theory

Floquet's theory [47, 77] considers more general dynamical systems described by a set of $2N$ linear, ordinary differential equations with periodic coefficients of the form

$$\dot{\underline{u}}(t) = A(t)\ \underline{u}(t), \tag{3.10}$$

where $A(t+T) = A(t)$ is a periodic matrix and T the period of the system. Note that constant coefficient systems, $A(t) = A$, are a special case where the period is arbitrary. Let $U(t)$, defined by eq.(2.18), be a full set of linearly independent solutions which satisfies the differential equations

$$\dot{U}(t) = A(t)\ U(t). \tag{3.11}$$

With the help of the periodic nature of matrix A, it is true that

$$\dot{U}(t+T) = A(t+T)\ U(t+T) = A(t)\ U(t+T). \tag{3.12}$$

It means that $U(t+T)$ is a fundamental matrix solution of the same equations. Two fundamental matrix solutions $U(t)$ and $U(t+T)$ should be uniquely dependent. Consequently, the so called *transition matrix*, $\Phi(t,T)$ exists, that relates the states of the system at two consecutive periods, t and $t+T$,

$$\underline{u}(t+T) = \Phi(t,T)\ \underline{u}(t) \quad \text{and} \quad U(t+T) = \Phi(t,T)\ U(t). \tag{3.13}$$

It then follows that $\Phi(t,T) = U(t+T)\ U(t)^{-1}$. The eigenvalues of the transition matrix are denoted $\exp(\lambda_j T),\ j = 1, 2, \ldots, 2N$, and assumed to be distinct in this discussion; a complete discussion of the general case of repeated eigenvalues is found

in ref. [47]. The stability criterion can now be stated as: the periodic system is stable if and only if the norms of all eigenvalues are smaller than unity: $|\exp(\lambda_j T)| < 1$, for $j = 1, 2, \ldots, 2N$. Alternatively, the general solution of the periodic system, eq. (2.17), can be rewritten as

$$\underline{u}(t) = \sum_{j=1}^{2N} \underline{A}_j(t)\ e^{\lambda_j t}, \tag{3.14}$$

where $\underline{A}_j(t)$ contains the orthogonal modes.

This approach has been widely used for the stability evaluation of systems with periodic coefficients: general systems [21, 48, 49], rotor dynamics problems [42, 65], and rotorcraft problems [88, 37]. This discussion clearly shows the difficulties associated with the application of Floquet's theory for stability assessment. Analytical applications are nearly impossible except for system featuring a very small number of degrees of freedom. In numerical applications, the evaluation of the transition matrix can become an overwhelming task as it requires one integration of the system of equations for an entire period, for each degree of freedom of the system. As the number of degrees of freedom of the system increases, this computational effort becomes prohibitive. In experimental application, it is not possible, in practice, to excite the system with N independent initial conditions, and it is impossible to measure all the states in the response. Hence, Floquet's theory is not used in experimental applications.

To remedy this situations, the implicit Floquet's theory [11, 12] was developed. In this approach, the dominant eigenvalues of the transition matrix are computed using the Arnoldi algorithm, *without the explicit computation of this matrix*. This implicit method yields stability information at a far lower computational cost than that of the classical approach, and is ideally suited for stability computations of systems involving a large number of degrees of freedom.

To alleviate the computational or experimental burden associated with the application of Floquet's theory, approximation to the transition matrix can be constructed,

based on a small set of excitations, E, and responses (computed or measured), R, of the system; typically these matrices are rectangular because few excitations and measurements are available. Selection of the excitation and measurement variables is critical to the success of this methodology. Excitations and responses are related to the transition matrix, $R = \Phi(t, T)\ E$. However, this relationship does not allow the computation of the transition matrix because E is, in general, not invertible. Various strategies can be used to extract an approximation to the transition matrix based on least square techniques or the singular value decomposition [109, 90, 94]. Such an approach is applicable to both numerical and experimental studies.

3.1.4 Lyapunov Exponents

The Lyapunov exponents [99] characterized the chaotic motion of nonlinear system. For the general nonlinear dynamical system, eq. (3.1), a Poincaré map [91] is defined as

$$\underline{u}_{k+1} = \underline{G}(\underline{u}_k), \tag{3.15}$$

where $\underline{u}_k$ and $\underline{u}_{k+1}$ are consecutive states of the system at discrete times. The Jacobian matrix of the map will be computed

$$\nabla \underline{G}(\underline{u}_k) = \left(\frac{\partial G_i(\underline{u})}{\partial u_j} \right) |_{\underline{u}=\underline{u}_k}, \tag{3.16}$$

then the matrix J_n is defined

$$J_n = \left[\prod_{k=1}^{n} \nabla \underline{G}(\underline{u}_k) \right]^{\frac{1}{n}}, \tag{3.17}$$

After the eigenvalues of J_n are computed as $\Lambda_j(J_n)$, the Lyapunov exponents are

$$\lambda_j = \ln \left\{ \lim_{n \to \infty} |\Lambda_j(J_n)| \right\}, \tag{3.18}$$

It is clear that the Lyapunov exponents depend on the initial conditions $\underline{u}_0$ and are invariant under coordinate transformations. These exponents can be interpreted as the average factors by which the distance between the adjacent points is stretched

after one application of the Poincaré map. Physically, the Lyapunov exponents also measure the loss of information about the initial configuration averaged over all $\underline{u}_k$.

3.2 Experimental Tools for Stability Analysis

Three experimental tools are discussed in this section. It will be shown that Ibrahim's time-domain method is based on the same approximate techniques as those used in partial Floquet theory. The complex exponential method, generally viewed as curve fitting procedure, is also equivalent to the partial Floquet method, whereas the moving block method is essentially curve fitting procedure.

3.2.1 Ibrahim's Time-domain Method

Ibrahim's time domain method [50, 34] is used to extract damping rates and stability information from experimental measurements. In the process of this approach, the system is excited and response is measured so that a large number of measurements in the time domain are available. Then, the discrete time responses of the system, $\underline{u}(kT)$ and $\underline{u}((k+1)T)$, serve as k^{th} excitation and measurement, respectively, in the framework of partial Floquet theory, T is the period of system. Hence, Ibrahim's time-domain method is a special case of the partial Floquet approach. The excitations and responses matrices are assembled

$$E = C\left[\underline{u}(0)\ \underline{u}(T)\dots\underline{u}((m-1)T)\right] \quad \text{and} \quad R = C\left[\underline{u}(T)\ \underline{u}(2T)\dots\underline{u}(mT)\right], \tag{3.19}$$

where matric C is matrix of measured states, defined by the first equation of eqs. (2.8). The transition matrix will be approximated

$$\Phi = R\ E^{+}, \tag{3.20}$$

where E^{+} is the Moore-Penrose inverse [41] of E. It can be seen that the quality of the approximation relies on the proper choice of initial excitations, and the length of time history of the response that should provide enough information to extract the system stability properties.

3.2.2 Complex Exponential Method

The complex exponential method [34], also known as Prony's method or autoregressive method, is generally viewed as a curve fitting procedure because the measured response of a linear periodic system is fitted to the form of eq. (3.14), as predicted by Floquet's theory. This approach will be further developed in this thesis, and the close relationship between the autoregressive method, Floquet's theory and partial Floquet's theories has been proved by Bauchau and Wang [16]. In this section, the basic procedure of complex exponential method is simply described.

The measurement of impulse response of a degree of freedom of a time-invariant system can be written as

$$h_k = \sum_{j=1}^{2N} a_j e^{\lambda_j k \Delta t}, \tag{3.21}$$

which is exactly the first item of eq. (2.29) due to the fact that external excitation is zero, $f_j = 0$. With the notation of $q_j = e^{\lambda_j \Delta t}$, the discrete data set reduces to

$$h_k = \sum_{j=1}^{2N} a_j q_j^k, \tag{3.22}$$

where the unknown parameters a_j and q_j can be determined by autoregressive approach. For impulse response, the autoregressive moving average model, eq. (2.33), reduces to autoregressive model

$$h_k + \beta_0 h_{k-p} + \beta_1 h_{k-p+1} + \ldots + \beta_{p-1} h_{k-1} = 0, \tag{3.23}$$

where coefficients β_k satisfy the algebraic equations

$$\sum_{k=0}^{p} \beta_k q^k = \prod_{j=1}^{p} (q - q_j) = 0, \tag{3.24}$$

and $\beta_p = 1$. The coefficients $\beta_0, \beta_1, \ldots, \beta_{p-1}$ are computed by solving a set of linear

equations, a successive application of eq. (3.23)

$$\begin{bmatrix} h_0 & h_1 & \dots & h_{p-1} \\ h_1 & h_2 & \dots & h_p \\ \vdots & \vdots & \ddots & \vdots \\ h_{m-1} & h_m & \dots & h_{m+p-2} \end{bmatrix} \begin{vmatrix} \beta_0 \\ \beta_1 \\ \dots \\ \beta_{p-1} \end{vmatrix} = - \begin{vmatrix} h_p \\ h_{p+1} \\ \vdots \\ h_{p+m-1} \end{vmatrix} \tag{3.25}$$

In general $m > p$, a least-square approximation of this system yields the coefficients β_k. In turns, the unknown parameters, q_j, solved from the algebraic equation, eq. (3.24). Finally, the frequencies and damping of the system can be extracted from experimental characteristics q_j.

3.2.3 The Moving Block Method

The moving block method [44, 23] is another curve-fitting technique that is widely used for experimental data reduction. This method appears to be a pure curve fitting method and does not seem to be related to the other approaches described earlier. Although it can yield useful stability information, the results are quite sensitive to many of the parameters of the methods and details of its implementation. It allows the determination of modal damping and frequency from the measurement of the transient response of a single degree of freedom of the system. The impulse response for a degree of freedom system can be rewritten as that of a damped sinusoid

$$h(t) = Ae^{-\zeta\omega_n t}\sin(\omega t + \phi), \tag{3.26}$$

where ζ is the damping, ω_n the natural frequency and $\omega = \omega_n\sqrt{1-\zeta^2}$ the damped frequency. The finite Fourier transform of response $h(t)$ is

$$H(\omega, \tau) = \int_{\tau}^{T_n+\tau} Ae^{-\zeta\omega_n t}\sin(\omega t + \phi)e^{-\mathbf{i}\ \omega t}\ \mathrm{d}t, \tag{3.27}$$

where $H(\omega, \tau)$ is a function of τ at the frequency ω. For lightly damped system, it is reasonable to assume $\zeta \ll 1$, it follows that $\omega_n \approx \omega$, and the terms involving higher

powers of ζ can be neglected. Consequently, the natural logarithm of the moving block function is found to be

$$\ln|H(\omega,\tau)| = -\zeta\omega\tau + \ln\left(\frac{A}{2\omega}\right) + \frac{1}{2}\ln\left(\frac{1+f(\zeta)}{\zeta^2}\right), \tag{3.28}$$

where

$$f(\zeta) = -2e^{-\zeta\omega T_n} + e^{-2\zeta\omega T_n} + (1-e^{-\zeta\omega T_n})\zeta\sin 2(\omega t+\phi)$$
$$-e^{-\zeta\omega T_n}(1-e^{-\zeta\omega T_n})\zeta\sin 2(\omega t+\omega\ T_n+\phi).$$

Thus a plot of $\ln|H(\omega,\tau)|$ as a function of τ consists of the superposition of a straight line with a slope of $-\zeta\omega$ and an additional oscillatory function of frequency 2ω. When T_n is defined as an integral multiple of the basic period of oscillation, $T_n = n2\pi/\omega$, the logarithm simplifies to

$$\ln|H(\omega,\tau)| = -\zeta\omega\tau + \frac{1}{2}\zeta\sin 2(\omega\tau+\phi) + C_n, \tag{3.29}$$

where the constant, C_n, is determined by $C_n = \ln\left(\frac{A}{2\omega}\right) + \ln(\omega T_n) - \frac{1}{2}\zeta\omega T_n$. The damping ζ can be obtained by a simple curve-fitting technique applied to eq. (3.29). To obtain accurate results, the frequency ω must be accurately evaluated. For sampled data, the frequencies of interested are determined by using a fast Fourier transform algorithm, eq. (B.4), on the entire signal. Blocks of size n_b are selected, which size must be less than the sample length n and usually set as $n_b = n/2$; the first block starts at $\tau = 0$, and the others are shifted a sample step accordingly. The natural logarithm of the moving block function is calculated for all the data blocks, and $\ln|H(\omega,\tau)|$ is recomputed, where $\tau = i\Delta t$ for $i = 1, 2, \ldots, n-n_b$. Finally the least-square technique is applied to extract the slope, the damping of the system, which is fitted to the resulting curve.

The procedure described here only deals with the response of a signal degree of freedom. Actually, it is possible to determine the frequency and damping for each of modes in the multi-mode response signal, which is a summation of several single

degree of freedom responses. When all frequencies of interested are determined by the fast Fourier transform, the moving block technique can be repeatedly applied to each of them to obatin the associated damping.

3.3 Chapter Summary

The approaches used to evaluate the stability characteristics of dynamical systems from the analytical expression of their governing equations or experimental measurements were presented. The possibilities, advantages and limitations of applying these methods to numerical model have been investigated. Lyapunov's function method, the only approach that gives information about nonlinear stability, clearly can not be applied to the large dimensional numerical models because there exists no general procedure to generate Lyapunov function. The characteristic exponent method and Floquet's theory are used to extract stability information of linear system with constant and periodic coefficients, respectively. But the computational cost becomes overwhelming when assessing the stability characteristics of large scale numerical models. The complex exponential method or the partial Floquet's theory are good choices for stability evaluation of numerical models. The reason is that if the complex dynamic model is used as a virtual prototype of the actual dynamical system, experimental methods are also applicable to numerical models. Furthermore, Ibrahim's time-domain method, Prony's method and the autoregressive method are good candidates to extract system characteristics from numerical multi-physics models.

CHAPTER IV

APPLICATION OF NUMERICAL TOOLS FOR STABILITY ANALYSIS

It has been mentioned earlier that the modeling of flexible multibody systems becomes increasingly complex with increasing available computer power. Multi-physics phenomena can be captured by coupling full finite element commercial codes to other codes that model the relevant aspects of the problem. The stability analysis of large-scale *multi-physics numerical models* is truly a challenge. As pointed out in chapter 3, many of the classical analytical tools become difficult to use when evaluating the stability characteristics of large dimensional model; some methods result in heavy computational cost, which prevents their routine application.

In this chapter, the application of partial Floquet's theory and autoregressive method to linear time-invariant numerical model is further developed. These two methods are shown to be closely related and even identical to each other under certain conditions. The discrete numerical models described in chapter 2 are the starting point for these two approaches to stability analysis. These methods are also widely used in the fields of model reduction, undamage detecting, system identification, optimal control, and signal processing.

Numerical implementation of these two approaches must be robust enough to filter the noise associated with the time discretization, nonlinearity and inaccuracies of the solution. To eliminate the effect of noise, the approaches have been combined with the singular value decomposition. Another approach for noise filtering is the proper orthogonal decomposition, also is performed via singular value decomposition. In the current framework of this thesis, Lanczos algorithm is specially developed to compute

the larger r proper orthogonal modes, reducing the numerical cost to a reasonable level. Signals reconstruction and the discrepancy between the reconstructed and original signals are two important accuracy indicators of stability evaluation, also discussed in this chapter.

Since stability analysis of numerical models is the focus of current work, the sampled signal is described in section 4.1; the application of Floquet's theory for numerical model and its limitation are discussed at first in sections 4.2 and then partial Floquet's theory in sections 4.3. The autoregressive concept is introduced in section 4.4. Proper orthogonal decomposition is presented in section 4.5, and Lanczos algorithm is introduced in section 4.5.3; the signal synthesis is described in section 4.6. Finally, the entire procedure proposed for stability analysis is summarized in section 4.7.

The proposed approaches for stability analysis will be presented for periodic systems only, because constant coefficient systems are a particular case of periodic systems featuring an arbitrary period.

4.1 The Sampled Data

Since the methods developed in this work are inherited from experimental techniques, they are based on "sampled data" obtained from experimental measurements or numerical simulation of the system. Consider a linear system featuring coefficients that are periodic in time with a period T. According to eq. (2.17), the solution of the homogeneous equations, the response of a single degree of freedom of the system can be written as

$$h(t) = L(t)e^{\Lambda t}P(0)^{-1}\underline{u}(0), \tag{4.1}$$

where array $L(t)$ represents a single line of matrix $P(t)$, and hence, $L(t) = L(t+T)$; finally, the response, $h(t)$, can be expressed in terms of the characteristic exponents as $h(t) = \sum_{j=1}^{2N} \ell_j(t) \exp(\lambda_j t) p_j$, where $\ell_j(t)$ and p_j are the j^{th} elements of arrays $L(t)$

and $\underline{p} = P(0)^{-1}\underline{u}(0)$, respectively. This expression is further simplified by defining $a_j(t) = \ell_j(t)p_j$, to find

$$h(t) = \sum_{j=1}^{2N} a_j(t)e^{\lambda_j t}, \tag{4.2}$$

where $2N$ is the order of the system, λ_j its characteristic exponents, and $a_j(t) = a_j(t+T)$ are periodic functions. Eq. (4.2) assumes that the characteristic exponents of the system are all distinct. In the presence of multiple exponents, the response of the system can still be written in closed form, see ref. [47], but the present developments assume that the system features distinct exponents.

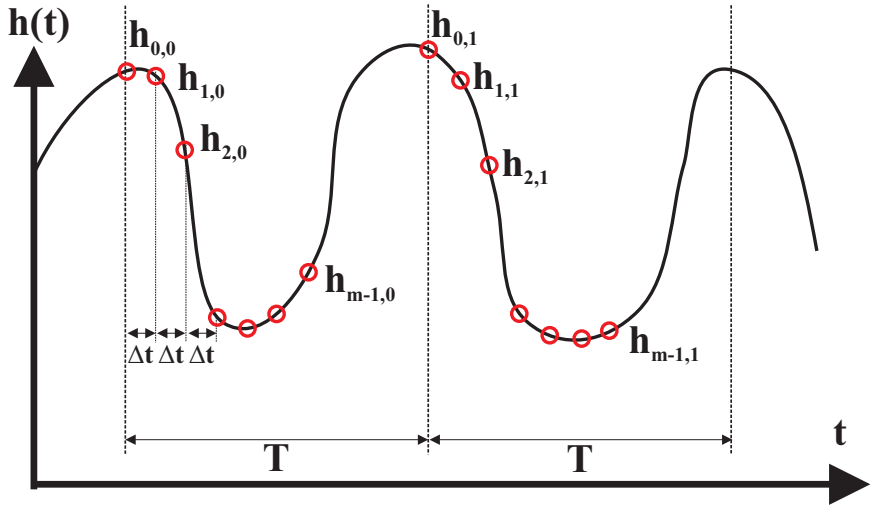

Figure 4.1: Sampling the output of a periodic system.

A signal $h(t)$ can be viewed as a "sensor" output such as the time history generated by a strain gauge or accelerometer attached to the system. When the response of the system is sampled at a constant rate Δt, such that $T = p\ \Delta t$, where p is the number of time steps per period, assumed to be an integer. The following notation is used to identify the sampled data points

$$h_{k,\ell} = h(t = k\Delta t + \ell T), \tag{4.3}$$

and this convention is illustrated in fig. 4.1. In the following developments, it will be necessary to work with sequences of m consecutive data points starting at time

$t = \ell T$, that will be stored in the following array

$$\underline{h}_\ell^T = \lfloor h_{0,\ell}, h_{1,\ell}, h_{2,\ell}, \ldots, h_{m-1,\ell} \rfloor. \tag{4.4}$$

Let μ be an integer such that $0 < \mu < p$ and ν an integer such that $\nu > 1$. Array $\underline{h}_\ell$ lists a sequence of data points spanning less than one period of the system if $m = p - \mu$, spanning exactly one period if $m = p$, spanning more than one period if $m = p + \mu$, or even several periods if $m = \nu p + \mu$. The so called *output Hankel matrix* will play an important role in subsequent developments

$$H_k = \left[\underline{h}_k, \underline{h}_{k+1}, \underline{h}_{k+2}, \ldots, \underline{h}_{k+n-1} \right], \tag{4.5}$$

Each column of these matrices stores an array $\underline{h}_\ell$, as defined by eq. (4.4), *i.e.* a sequence of m consecutive data points.

If the sampled data is the response of a linear periodic system, it must be in the form of eq. (4.1) or eq. (4.2), implying that

$$h_{k,\ell} = L_k e^{\Lambda(k\Delta t + \ell T)} P_0^{-1} \underline{u}_0, \quad \text{or} \quad h_{k,\ell} = \sum_{j=1}^{2N} a_{j,k} e^{\lambda_j (k\Delta t + \ell T)}. \tag{4.6}$$

where $L_k = L(k\Delta t + \ell T) = L(k\Delta t)$; the last equality follows from the periodic nature of $L(t)$. The periodicity of the function $a_i(t)$ implies that $a_{j,k} = a_j(k\Delta t + \ell T) = a_j(k\Delta t)$. With the help of the following notations, $q_j = e^{\lambda_j \Delta t}$ and

$$\mathcal{Q}_j = e^{\lambda_j T} = q_j^p, \tag{4.7}$$

the second expression of eq. (4.6) is alternatively represented as

$$h_{k,\ell} = \sum_{j=1}^{2N} q_j^k \mathcal{Q}_j^\ell a_{j,k}, \tag{4.8}$$

One approach to stability analysis is to determine the characteristic exponents, λ_j, of the system from the knowledge of sampled data points, $h_{k,\ell}$. If a sufficient number of data points are available, eq. (4.8) could be used to compute those characteristic exponents. This task is, however, difficult because the equations are nonlinear, and because of the noise that will be undoubtable present in the sampled data.

4.2 Floquet's Theory

As discussed in section 3.1.3, Floquet's theory [47, 77] assesses the stability characteristics of general dynamical systems described by eq. (3.10) with periodic coefficients. This approach involves the *transition matrix*, $\Phi(t)$, that relates the states of the system at time t and $t+T$, $\underline{u}(t+T) = \Phi(t)\underline{u}(t)$. When $t = k\Delta t$, the discrete relationship becomes

$$\underline{u}_{k+p} = \Phi_k \underline{u}_k. \tag{4.9}$$

The relationship between matrices Φ_k and A_k is found from the first equation of discrete time model, eq. (2.27), as

$$\Phi_k = A_{k+p-1} A_{k+p-2} \dots A_k. \tag{4.10}$$

From the definition of matrix, $A_k = P_{k+1} e^{\Lambda \Delta t} P_k^{-1}$, and applied the periodic properties, $P_k = P_{k+p}$, an explicit expression for Φ_k is obtained

$$\Phi_k = P_k e^{\Lambda p \Delta t} P_k^{-1}, \tag{4.11}$$

where p is the number of sampling points per period. The eigenvalues of the transition matrix are $\exp(\lambda_j p \Delta t)$, $j = 1, 2, \dots, 2N$, and assumed to be distinct in this discussion. The periodic system will be stable if and only if the norms of all eigenvalues are smaller than unity: $|\exp(\lambda_j p \Delta t)| < 1,\ j = 1, 2, \dots, 2N$.

In practice, the transition matrix is constructed by a full set of linearly independent solutions $\underline{u}_p^{(i)}$, $i = 1, 2, \dots, 2N$, when initial conditions are given by identity matrix,

$$\Phi_0 = \left[\underline{u}_p^{(1)}, \underline{u}_p^{(2)}, \dots, \underline{u}_p^{(2N)}\right]; \tag{4.12}$$

This discussion clearly shows the difficulties associated with the application of Floquet's theory for stability assessment. In numerical applications, the evaluation of the transition matrix becomes an overwhelming task as it requires the integration of the system of equations for an entire period, for each degree of freedom of the system. As

the number of degrees of freedom of the system increases, this computational effort becomes prohibitive. Furthermore, for larger systems, the transition matrix becomes increasingly ill conditioned.

The last step of Floquet's theory involves the determination of the characteristic exponents of the system from the eigenvalues of the transition matrix. A typical eigenvalue is written as $\exp(\lambda_j p\Delta t) = r_j \exp(\pm \mathbf{i}\phi_j)$, where $\mathbf{i} = \sqrt{-1}$, and a characteristic exponent as $\lambda_j = \omega_j \left(\zeta_j \pm \mathbf{i}\sqrt{1-\zeta_j^2}\right)$, where ω_j and ζ_j are the frequency and damping, respectively, associated with this characteristic exponent; it then follows that

$$\zeta_j = \frac{c_j}{\sqrt{1+c_j^2}}; \quad \omega_j = \frac{\phi_j}{p\Delta t}\sqrt{1+c_j^2}, \quad j = 1, 2, \ldots, N, \tag{4.13}$$

where $c_j = (\ln r_j)/\phi_j$. For constant coefficient system, the period is usually selected as the time step size; so the number of time steps per period will be $p = 1$, and eq. (4.13) will recover to eq. (2.40).

4.3 The Partial Floquet Approach

In view of the high computational cost associated with the application of Floquet's theory, it is desirable to construct an approximation of the transition matrix. In partial Floquet's theory [109, 90], information about the dynamics of the system is extracted from the response of a small number of degrees of freedom.

According to eq. (4.4), array $\underline{h}_\ell$ is assembled by m consecutive data points of the discretized signal starting in the ℓ^{th} period. Matrix R is now defined

$$R = \begin{bmatrix} L_0 \\ L_1 e^{\Lambda \Delta t} \\ \vdots \\ L_{m-1} e^{\Lambda (m-1)\Delta t} \end{bmatrix}. \tag{4.14}$$

With the help of this notation and first formulation of eqs. (4.6) , it is clear that $\underline{h}_\ell = R\ e^{\Lambda \ell T} P_0^{-1} \underline{u}_0$. The relationship between arrays $\underline{h}_{\ell+1}$ and $\underline{h}_\ell$ is now written in

terms of the *transition matrix*, Q, as

$$\underline{h}_{\ell+1} = Q\ \underline{h}_{\ell} \quad \text{and} \quad Q = R\ e^{\Lambda T} R^{+}, \tag{4.15}$$

where R^{+} is the Moore-Penrose inverse [41] of R; the superscript $()^{+}$ will be used here to denote Moore-Penrose inverses. According to eq. (4.5), when setting k as 0 and 1, the following two matrices are now defined

$$H_{0(m\times n)} = \left[\underline{h}_0 \quad \underline{h}_1 \quad \ldots \quad \underline{h}_{n-1}\right], \quad \text{and} \quad H_{1(m\times n)} = \left[\underline{h}_1 \quad \underline{h}_2 \quad \ldots \quad \underline{h}_{n}\right]. \tag{4.16}$$

Since eq. (4.15) holds for each column of these matrices, it follows that

$$H_1 = Q\ H_0. \tag{4.17}$$

This relationship does not allow the exact computation of the transition matrix, Φ_k, defined by eq. (4.9). Indeed, complete knowledge of this matrix requires the responses of all degrees of freedom to $2N$ linearly independent initial conditions, as expressed by eq. (4.12); if this information was available, matrices H_0 and H_1 of size $2N \times 2N$ could be constructed and $\Phi_0 = H_1 H_0^{-1}$ would yield the transition matrix. In view of the limited information available, an approximation to the transition matrix is evaluated as $Q = H_1 H_0^{+}$, where the Moore-Penrose inverse [41] of H_0 is evaluated using the singular value decomposition as $H_0^{+} = V_r \Sigma_r^{-1} U_r^T$, see Appendix A, where r is the estimated rank of H_0. The estimated transition matrix becomes

$$Q_{(m\times m)} = H_1 V_r \Sigma_r^{-1} U_r^T. \tag{4.18}$$

In view of its definition in eq. (4.16), matrix H_0 will store highly redundant data and it is not unexpected that, more often than not, $r < m$. It follows that of the m eigenvalues of Q in eq. (4.18), r only are expected to be physically meaningful, whereas the remaining $m - r$ eigenvalues are related to noise in the data. Consequently, it makes sense to project matrix Q in the subspace defined by the r proper orthogonal modes of H_0, stored in U_r, to find

$$\hat{Q}_{(r\times r)} = U_r^T Q\ U_r = U_r^T H_1 V_r \Sigma_r^{-1}. \tag{4.19}$$

The stability characteristics of the system are then extracted from the eigenvalues of the approximate transition matrices, Q or $\hat{Q}$, using eq. (4.13).

The method presented thus far is based on the information extracted from a single signal, see eq. (4.6). In practice, if N_s signals are available, the following matrices are constructed

$$\mathbb{H}_0 = \begin{bmatrix} H_0^{(1)} \\ H_0^{(2)} \\ \vdots \\ H_0^{(N_s)} \end{bmatrix}, \quad \mathbb{H}_1 = \begin{bmatrix} H_1^{(1)} \\ H_1^{(2)} \\ \vdots \\ H_1^{(N_s)} \end{bmatrix}; \tag{4.20}$$

where matrices $H_0^{(k)}$ and $H_1^{(k)}$ are constructed with the data of the k^{th} signal, as defined in eq. (4.16). The analysis then proceeds as before, with matrices $\mathbb{H}_0$ and $\mathbb{H}_1$ replacing matrices H_0 and H_1, respectively.

4.4 The Autoregressive Approach

The autoregressive method will be presented here as a modification of the partial Floquet approach. When the sole case of impulse response considered, it can be proved that autoregressive moving average approach will be reduced to autoregressive approach, which is equivalent to Prony's method [34].

4.4.1 The Procedure of Autoregressive Approach

In fact, Prony's method is a procedure that determines the characteristic exponents, λ_j, of a periodic system, based on the knowledge of a set of data points, see eq. (4.3), sampled from the system outputs. To that effect, a linear combination of the data points, similar to eq. (2.30), is formed

$$\begin{aligned} \sum_{\ell=0}^{2N-1} \beta_\ell h_{k,\ell} + h_{k,2N} &= \sum_{\ell=0}^{2N-1} \beta_\ell \sum_{j=1}^{2N} q_j^k \mathcal{Q}_j^\ell a_{j,k} + \sum_{j=1}^{2N} q_j^k \mathcal{Q}_j^{2N} a_{j,k}, \\ &= \sum_{j=1}^{2N} q_j^k a_{j,k} \left[\sum_{\ell=0}^{2N-1} \beta_\ell \mathcal{Q}_j^\ell + \mathcal{Q}_j^{2N} \right], \end{aligned} \tag{4.21}$$

where the coefficients β_ℓ are as yet unknown coefficients. The linear combination of the data points defined by eq. (4.21) can be made to vanish if the bracketed terms in the last expression all vanish, *i.e.* if

$$\beta_0 + \beta_1 \mathcal{Q}_j + \beta_2 \mathcal{Q}_j^2 + \ldots + \beta_{2N-1} \mathcal{Q}_j^{2N-1} + \mathcal{Q}_j^{2N} = 0, \quad j = 1, 2, \ldots, 2N. \tag{4.22}$$

These conditions are satisfied if and only if the $\mathcal{Q}_j$ are the $2N$ roots of the $2N^{\text{th}}$ order polynomial defined by the coefficients β_ℓ,

$$\beta_0 + \beta_1 \mathcal{Q} + \beta_2 \mathcal{Q}^2 + \ldots + \beta_{2N-1} \mathcal{Q}^{2N-1} + \mathcal{Q}^{2N} = 0. \tag{4.23}$$

With this choice of the $\mathcal{Q}_j$, the linear combination defined in eq. (4.21) then reduces to $\sum_{\ell=0}^{2N-1} \beta_\ell h_{k,\ell} + h_{k,2N} = 0$. The same reasoning can be made for any value of index $k = 0, 1, 2, \ldots, m-1$. Collecting all results then yields

$$\sum_{\ell=0}^{2N-1} h_{k,\ell} \beta_\ell = -h_{k,2N}, \quad k = 0, 1, \ldots, m-1. \tag{4.24}$$

These equations form a *set of linear equations* for the unknown coefficients β_ℓ. With the help of the following notation

$$\underline{\beta}^T = \lfloor \beta_0, \beta_1, \beta_2, \ldots, \beta_{2N-1} \rfloor \tag{4.25}$$

the system of linear equations, eq. (4.24), can be recast as

$$H_0 \, \underline{\beta} = -\underline{h}_{2N}, \tag{4.26}$$

where matrix H_0 was defined in eq. (4.5) and $\underline{h}_{2N}$ in eq. (4.4). In general $m > 2N$, and this system is an over determined set of linear equations that could be solved using the least-square technique [41], for instance.

Autoregressive method can be summarized as a three steps process. First, using the sampled data, form the array $\underline{h}_{2N}$ and matrix H_0 defined by eqs. (4.4) and (4.5), respectively. Next, solve the linear system defined by eq. (4.26) to find the $2N$ coefficients β_ℓ. If necessary, *i.e.* if $m > 2N$, use an appropriate method to determine

an approximate solution of the over determined linear system. Finally, determine the $2N$ roots, $\mathcal{Q}_j$, of the polynomial defined by eq. (4.23). The characteristic exponents of the system are then obtained from the definition of $\mathcal{Q}_j$, see eq. (4.7).

The second step of the procedure can present difficulties: as the order of the system increases, so does the order of the polynomial defined by eq. (4.23) and the extraction of its root becomes an increasingly arduous task. One of the most reliable manners of computing the roots of a polynomial [29, 93] is to recast the problem as an eigenvalue problem. To that effect, the following matrix relationship is constructed

$$\lfloor 1, \mathcal{Q}, \mathcal{Q}^2, \ldots, \mathcal{Q}^{2N-1} \rfloor \begin{bmatrix} 0 & 0 & \ldots & 0 & -\beta_0 \\ 1 & 0 & \ldots & 0 & -\beta_1 \\ 0 & 1 & \ldots & 0 & -\beta_2 \\ 0 & 0 & \ddots & \vdots & \vdots \\ 0 & 0 & \ldots & 0 & -\beta_{2N-2} \\ 0 & 0 & \ldots & 1 & -\beta_{2N-1} \end{bmatrix} = \mathcal{Q} \lfloor 1, \mathcal{Q}, \mathcal{Q}^2, \ldots, \mathcal{Q}^{2N-1} \rfloor, \quad (4.27)$$

where the first $2N-1$ equations are identities, whereas the last equation is identical to the polynomial defined by eq. (4.23). The following notations are introduced

$$B_H = \begin{bmatrix} 0 & 0 & \ldots & 0 & -\beta_0 \\ 1 & 0 & \ldots & 0 & -\beta_1 \\ 0 & 1 & \ldots & 0 & -\beta_2 \\ 0 & 0 & \ddots & \vdots & \vdots \\ 0 & 0 & \ldots & 0 & -\beta_{2N-2} \\ 0 & 0 & \ldots & 1 & -\beta_{2N-1} \end{bmatrix} \quad \text{and} \quad \underline{q} = \begin{vmatrix} 1 \\ \mathcal{Q} \\ \mathcal{Q}^2 \\ \vdots \\ \mathcal{Q}^{2N-1} \end{vmatrix}, \quad (4.28)$$

where B_H is an upper Hessenberg matrix known as the *companion matrix to a polynomial*. Eq. (4.27) now simply writes

$$B_H^T \, \underline{q} = \mathcal{Q} \, \underline{q}. \quad (4.29)$$

This is clearly a standard eigenvalue problem; the eigenvalues, $\mathcal{Q}$, of matrix B_H are also the roots of the polynomial defined by eq. (4.23). The eigenvalues of B_H

are, in general, complex conjugate numbers, since all β_ℓ are real numbers. It will be convenient to write $\mathcal{Q}_j = r_j e^{\pm \mathbf{i}\phi_j}$. The last step of Prony's method involves the determination of the characteristic exponents of the system from the eigenvalues, $\mathcal{Q}_j$, of matrix B_H. Then the frequency and damping associated with the characteristic exponent will be determined using eqs. (4.13).

4.4.2 Relationship to Floquet's Theory

The linear system defined by eq. (4.26) can be expanded to form the following matrix relationship

$$\left[\underline{h}_0, \underline{h}_1, \underline{h}_2, \ldots, \underline{h}_{2N-1}\right] \begin{bmatrix} 0 & 0 & \ldots & 0 & -\beta_0 \\ 1 & 0 & \ldots & 0 & -\beta_1 \\ 0 & 1 & \ldots & 0 & -\beta_2 \\ 0 & 0 & \ddots & \vdots & \vdots \\ 0 & 0 & \ldots & 0 & -\beta_{2N-2} \\ 0 & 0 & \ldots & 1 & -\beta_{2N-1} \end{bmatrix} = \left[\underline{h}_1, \underline{h}_2, \underline{h}_3, \ldots, \underline{h}_{2N}\right]. \tag{4.30}$$

Note that the first $2N-1$ equations implied by this relationship are identities, $\underline{h}_1 = \underline{h}_1$, $\underline{h}_2 = \underline{h}_2$, etc., whereas the last equation is identical to the linear system of eq. (4.26). Using the notations defined in eqs. (4.5) and (4.28), this matrix equation simply writes

$$H_0 B_H = H_1. \tag{4.31}$$

Clearly, matrix B_H and the transition matrix Q are closely related since

$$Q = H_0 B_H H_0^+. \tag{4.32}$$

As was the case for the partial Floquet method, too little information is contained in matrices H_0 and H_1 to afford an exact evaluation of B_H. Hence, the Moore-Penrose inverse of matrix H_0 is used here again to evaluate the approximation of similar transform. In fact, if $2N$ linearly independent excitations are available, H_0 is an

invertible matrix and this relationship would yield the Floquet transition matrix of the system. A fundamental result of Floquet's theory [47, 77] is that the eigenvalues of this transition matrix are the $\mathcal{Q}_i$ defined by eq. (4.7). This result is identical to that obtained in the derivation of autoregressive approach: the $\mathcal{Q}_i$ are the eigenvalues of the companion matrix B_H. This proves that autoregressive approach is not simply a curve fitting method; rather, it is closely related to Floquet's theory, a rigorous tool for the stability analysis of linear periodic systems.

Since autoregressive and partial Floquet methods are equivalent, it is not unexpected that both methods require the inverse of the same matrix H_0, as implied by eqs.(4.26) and (4.31), respectively. Since H_0 is not necessarily a square matrix, and not necessarily of full rank, its inverse does, in general, not exist, a problem that is closely related to the noise and redundancy in the sampled data. A practical implementation of autoregressive approach requires the identification of array $\underline{\beta}$; the other alternative implementation is the identification of the transition matrix B_H directly. When applied singular value decomposition, the second is more elegant and strong way. Hence, the practical implementation of the sole autoregressive method will be addressed next.

4.4.3 Practical Implementation of Autoregressive Approach

To be effective in the stability analysis of large scale multibody systems, the details of the implementation of the method described in the previous section must be carefully considered. In applications of autoregressive approach to experimental set-ups, a limited number of signals are available, because each signal requires a physical sensor, adding to the cost and complexity of the experiment. On the other hand, in numerical applications, comprehensive dynamical models typically involve a large number of degrees of freedom and hence, a large number of "sensors" are available at no cost. This fact is a double edged sword; as the number of sensors increases, more robust

predictions should be obtained because more data is readily available, but the highly redundant data leads to an increasingly ill conditioned and rank deficient system of equations (4.31). So Moore-Penrose inverse of matrix H_0 is used here again to evaluate an approximation as $B_H = H_0^+ H_1$, and finally,

$$B_{H(n\times n)} = V_r \Sigma_r^{-1} U_r^T H_1; \tag{4.33}$$

In view of highly redundant nature of the data stored in matrix H_0, it should be expected that, in general, $r < n$, and hence, only r eigenvalues of B_H should be physically meaningful. Consequently, it makes sense to project matrix B_H in the subspace defined by V_r, to find

$$\hat{B}_{H(r\times r)} = V_r^T B_H V_r = \Sigma_r^{-1} U_r^T H_1 V_r. \tag{4.34}$$

The stability characteristics of the system are then extracted from the eigenvalues of the approximate transition matrices, B_H or $\hat{B}_H$, using eq. (4.13).

The stability analysis algorithms presented in this section produce estimates of r characteristic exponents of the system. The analyst is now faced with the following dilemma: how reliable are these estimates? Poor estimates are due to two broad categories of errors. First, if the excitation of the system is chosen inappropriately, some relevant modes might not be excited, and no matter what signals are used for stability analysis, the dynamics associated with such modes cannot possibly be extracted by any algorithm. Exact evaluation of the characteristic exponents requires the response of all modes to $2N$ linearly independent initial conditions, *i.e.* all modes must be excited to obtain the exact solution. Second, assuming that all relevant modes have sufficient excitation, the noise in the data or a poor choice of signals might lead to inaccurate estimates of system dynamics. Error from the first source cannot be remedied by better algorithms, rather, a better judgement is required of the analyst. Note that this problem is also present when running an experiment: the

excitation device must be properly designed to provide enough energy to all relevant modes.

Errors from the second source can be alleviated by better algorithms; two complementary approaches are presented here. The first method eliminates the need to select specific signals as input to the stability analysis by using all the available data, *i.e.* the responses of all degrees of freedom of the system. While this approach certainly eliminates the guesswork, it will require the singular value decomposition of very large matrices, resulting in large computational costs. The proper orthogonal decomposition method is proposed as a solution of this problem, as discussed in section 4.5. The second method relies on the reconstruction or synthesis of the signals associated with the estimates of r characteristic exponents of the system. If the reconstructed signals are in close agreement with the original signals, it is likely that the identified characteristic exponents are reliable estimates. This method is presented in section 4.6. The combination of these two methods is expected to yield more reliable estimates of stability characteristics, and warn the analyst when poor predictions are obtained.

If N_s signals are used for stability analysis, the arrays $\mathbb{H}_0$ and $\mathbb{H}_1$, eq. (4.20), are constructed. The autoregressive approach now involves the solution of the following linear system

$$\mathbb{H}_0 \; B_H = \mathbb{H}_1, \tag{4.35}$$

where $\mathbb{H}_0$ and $\mathbb{H}_1$ are matrices of size $mN_s \times n$.

The main difficulty of practical implementations of autoregressive method, also together with the partial Floquet approach, is the determination of the order, $2N$, of the system. From a theoretical standpoint, the order of the system equals its number of degrees of freedom, typically a very large number for comprehensive multibody models. However, the available data is unlikely to be sufficient to identify all the characteristic exponents of the system. Indeed, Floquet's theory implies that the

determination of the $2N$ characteristic exponents requires a complete knowledge of the transition matrix, which in turns, requires the evaluation of the system response to $2N$ linearly independent initial conditions. If such data were to available, autoregressive and partial Floquet approaches would become identical, and would both yield all the characteristic exponents of the system. In practical situations, it is reasonable to ask the following question: given the sampled data available for the analysis, how many characteristic exponents can be accurately computed?

Let n denote a preliminary estimate of the observable order of the system that will be evaluated based on two criteria. First, the system of equations (4.35) should be over determined, *i.e.* $mN_s = \alpha n$, where $\alpha > 1$ is a user defined parameter. Second, it is desirable to use as much of the available data as possible, *i.e.* $p\,n+m-1 = N_d-1$, where N_d is the total number of data points in a signal. Solving these two equations yields

$$n = \frac{N_s N_d}{\alpha + pN_s}, \quad m = \frac{\alpha N_d}{\alpha + pN_s}. \tag{4.36}$$

With this choice, system (4.35) represents an over determined system of linear equations that could be solved using the least square method [41], for instance. This approach, however, does not guarantee an accurate solution because $\mathbb{H}_0$ could still be rank deficient due to the redundant nature of the sampled data. Hence, the singular value decomposition technique [41] is used to first determine the rank of $\mathbb{H}_0$ by the condition, eq. (A.2).

4.5 Use of Proper Orthogonal Modes

When applying the stability algorithms described in above sections 4.3 and 4.4 to numerical systems, the responses of all degrees of freedom of the system are available as a result of the computation. This contrasts with experimental applications where only a small number of signals are available. To extract the most accurate predictions, it is logical to use all available data, *i.e.* in eq. (4.20), the number of signals equals the

number of degrees of freedom of the system, $N_s = 2N$. Clearly, the required singular value decomposition of matrix $\mathbb{H}_{0(2Nm\times n)}$ will be very expensive in view of its size.

To bypass this high cost, a preprocessing step, based on the proper orthogonal decomposition, is used to condense the available data. This technique provides a unique decomposition of system response in terms of a set of orthogonal modes associated with decreasing energy content. The few proper orthogonal modes with the highest energy content are then selected to span the orthogonal subspace. The projections of the system response onto this subspace are used as "generalized" or "optimized" sensors to drive the stability analysis.

4.5.1 Construction of Optimal Signals

To implement this approach, the following matrix is assembled from the time histories of all degrees of freedom

$$T_0 = \begin{bmatrix} \underline{u}_0 & \underline{u}_1 & \dots & \underline{u}_{n-1} \end{bmatrix}, \tag{4.37}$$

where array $\underline{u}_k$ stores all the degrees of freedom of the system at time $k\Delta t$. Here again, the singular value decomposition is used to compute the proper orthogonal modes of T_0 as $T_0 = U_r \Sigma_r V_r^T$, where U_r stores the proper orthogonal modes, and r is the estimated rank of T_0. The system response $\underline{u}(t)$ is then projected onto the subspace spanned by the proper orthogonal modes through the definition

$$\underline{u}(t) = U_r \underline{\hat{u}}(t), \tag{4.38}$$

where $\underline{\hat{u}}(t)$ is r states vector. With the help of the orthogonal properties of U_r, $U_r^T U_r = I$, the projected solution becomes $\underline{\hat{u}}(t) = U_r^T \underline{u}(t)$, and the original system, eq. (3.10), reduced to

$$\dot{\underline{\hat{u}}}(t) = \hat{A}(t)\ \underline{\hat{u}}(t), \quad \hat{A}(t)_{(r\times r)} = U_r^T A(t) U_r; \tag{4.39}$$

where the periodic property $\hat{A}(t) = \hat{A}(t+T)$ still holds. The optimal signals can be assembled by the time history of response of r degrees of freedom $\underline{\hat{u}}(t)$

$$\left[\underline{\hat{u}}_0 \quad \underline{\hat{u}}_1 \quad \dots \quad \underline{\hat{u}}_{n-1}\right] = U_r^T T_0 = \Sigma_r V_r^T, \tag{4.40}$$

or

$$\underline{\mathfrak{h}}_i = \sigma_i \underline{v}_i, \quad i = 1, 2, \dots, r, \tag{4.41}$$

where $\underline{v}_i$ is the i^{th} column of V_r. The r signals, $\underline{\mathfrak{h}}_i$, are generalized, or optimized signals: while they are not the response of any specific degree of freedom of the system, they form a set of r orthogonal signals containing most of the energy of the system, as measured by the index defined in eq. (A.3).

4.5.2 Application of Lanczos Algorithm to Singular Value Decomposition

In view of eq. (4.37), matrix T_0 consists of the time histories of all the degrees of freedom of selected substructures or objects of a complex multibody system. This matrix is of size $2N \times n$ and hence, the singular value decomposition of this matrix will be an expensive operation, the cost of which is estimated to be $\mathcal{O}(4N^2n + n^3)$, see refs. [30, 104]. However, in the present application, it is not necessary to extract all the singular values of T_0, rather, only the r dominant singular values are necessary. Several algorithms [36, 62] have been proposed for this task, but the most effective tool is the Lanczos algorithm [41] that operates on the following real symmetric matrix

$$\mathbb{T} = \begin{bmatrix} 0 & T_0 \\ T_0^T & 0 \end{bmatrix}. \tag{4.42}$$

If the compact form of the singular value decomposition for matrix T_0 is $T_0 = U\Sigma V^T$, the eigenproblem for matrix $\mathbb{T}$ becomes

$$\begin{bmatrix} 0 & T_0 \\ T_0^T & 0 \end{bmatrix} \begin{bmatrix} U & U \\ V & -V \end{bmatrix} = \begin{bmatrix} U & U \\ V & -V \end{bmatrix} \begin{bmatrix} \Sigma & 0 \\ 0 & -\Sigma \end{bmatrix}. \tag{4.43}$$

The desired factors of the singular value decomposition are the eigenvector of $\mathbb{T}$. If the eigenproblem is truncated to r eigenvectors, matrices U_r and V_r are readily obtained. Numerical practice shows that the Lanczos algorithm produces the r dominant singular values and the matrices U_r and V_r at a very reasonable computational cost.

4.5.3 Lanczos Algorithm

The Lanczos algorithm is one of the most reliable methods of extracting the eigenvalues of a general symmetric matrix $\mathbb{T}$ of size $n_{\mathbb{T}} \times n_{\mathbb{T}}$, and $n_{\mathbb{T}} = n + 2N$. The algorithm starts from the iterated constructing the krylov subspace

$$\mathcal{K}_j(\mathbb{T}, \underline{b}) = \text{span}\{\underline{b}, \mathbb{T}\underline{b}, \mathbb{T}^2\underline{b}, \ldots, \mathbb{T}^{j-1}\underline{b}\}, \tag{4.44}$$

where $\underline{b}$ is an arbitrary vector. The orthogonal basis vectors for subspace $\mathcal{K}_j$ are defined by Ritz vectors

$$Q_j = \left[\underline{q}_1, \underline{q}_2, \ldots, \underline{q}_j\right], \tag{4.45}$$

The basic idea is to use this subspace decomposition to transform the symmetric matrix $\mathbb{T}$ to a tridiagonal matrix T_j

$$T_j = \begin{bmatrix} \alpha_1 & \beta_2 & 0 & \ldots & 0 & 0 \\ \beta_2 & \alpha_2 & \beta_3 & \ldots & 0 & 0 \\ 0 & \beta_3 & \alpha_3 & \ldots & 0 & 0 \\ \vdots & \vdots & \vdots & \ddots & \vdots & \vdots \\ 0 & 0 & 0 & \ldots & \alpha_{j-1} & \beta_{j-1} \\ 0 & 0 & 0 & \ldots & \beta_{j-1} & \alpha_j \end{bmatrix}. \tag{4.46}$$

A new vector $\underline{q}_{j+i}$ will be constructed using the following three terms recurrence relationship

$$\beta_{j+1}\ \underline{q}_{j+i} = \mathbb{T}\ \underline{q}_j - \alpha_j\ \underline{q}_j - \beta_j\ \underline{q}_{j-1} = \underline{r}_j, \tag{4.47}$$

where the coefficients α_j and β_j are selected to enforce the orthogonality, *i.e.* $\underline{q}_j^T \underline{q}_j = 1$ and $\underline{q}_j^T \underline{q}_{j+1} = 0$. Finally, α_j and β_{j+1} are determined as

$$\beta_{j+1} = \sqrt{\underline{r}_j^T \underline{r}_j} \quad \text{and} \quad \alpha_j = \underline{q}_j^T \mathbb{T}\ \underline{q}_j. \tag{4.48}$$

For each time step, a new vector $\underline{q}_{j+1}$ is added to the Ritz vectors, Q_{j+1}, such that $Q_{j+1} = [\underline{q}_1, \underline{q}_2, \ldots, \underline{q}_{j+1}]$, the basic recurrence relationship, eq. (4.47), is fundamental

$$\mathbb{T}\ \underline{q}_j = \beta_j\ \underline{q}_{j-1} + \alpha_j\ \underline{q}_j + \beta_{j+1}\ \underline{q}_{j+i} = \left[\underline{q}_{j-1}, \underline{q}_j, \underline{q}_{j+1}\right] \left| \begin{array}{c} \beta_j \\ \alpha_j \\ \beta_{j+1} \end{array} \right|, \tag{4.49}$$

Combining the recurrence relationships, eq. (4.49), at all steps, the fundamental relationships of Lanczos algorithm are conveniently written in a matrix form

$$\mathbb{T}\ Q_j = Q_j\ T_j + \beta_{j+1}\ \underline{q}_{j+1} \underline{e}_j^T \tag{4.50}$$

where $\underline{e}_j = \lfloor 0 \quad 0 \quad \ldots \quad 0 \quad 1 \rfloor^T$.

Considering the eigenvalue problem

$$\mathbb{T}\ \underline{w} = \lambda\ \underline{w}. \tag{4.51}$$

An approximate solution of this problem is sought within the Krylov subspace Q_j obtained after j steps. Defining the transformation $\underline{w} = Q_j\ \underline{s}$ which yields the reduced problem in the form

$$T_j\ \underline{s} = \hat{\lambda}\ \underline{s}, \tag{4.52}$$

where tridiagonal matrix, $T_j = Q_j^T \mathbb{T} Q_j$, is obtained from eq. (4.50) together with the orthogonality of $\underline{q}_{j+1}$ to all previous $\underline{q}_j$, and $\hat{\lambda}$ are the eigenvalues of this reduced eigen-problem. In summary, the eigenvalues of matrix T_j approximate those of the original matrix $\mathbb{T}$, *i.e.* $\hat{\lambda} \approx \lambda$.

The procedure of Lanczos algorithm is summarized as:

1. Choose an initial vector $\underline{q}_1$ with $\|\underline{q}_1\| = 1$, set $\beta_1 = 0$, $\underline{q}_0 = 0$;

2. **for** $j = 1,\ 2,\ \ldots,\ n$ do

   (a) $\underline{r}_j = \mathbb{T}\ \underline{q}_j - \beta_j\ \underline{q}_{j-1}$;

   (b) $\alpha_j = \underline{r}_j^T \underline{q}_j$;

   (c) $\underline{r}_j = \underline{r}_j - \alpha_j \underline{q}_j$;

   (d) $\beta_{j+1} = \sqrt{\underline{r}_j^T \underline{r}_j}$;

   (e) $\underline{q}_{j+1} = \underline{r}_j / \beta_{j+1}$;

3. **end**

After j steps, the QR algorithm [41] is used to extract the roots $\hat{\lambda}_i$ and the corresponding eigenvectors $\underline{s}_i$ of the tridiagonal matrix T_j, which are increasingly accurate approximations to the eigenvalues of $\mathbb{T}$, *i.e.* $\hat{\lambda}_i \approx \lambda_i$ and $\underline{w}_i = Q_j\ \underline{s}_i$. The quality of this approximation can be readily evaluated. With the help of eqs. (4.50) and (4.52), it can be shown that

$$\|\mathbb{T}\ Q_j\ \underline{s}_i - \hat{\lambda}_i\ Q_j\ \underline{s}_i\| = |\beta_{j+1}|\ |s_{ij}|, \tag{4.53}$$

where s_{ij} is the bottom element of the eigenvector $\underline{s}_i$. The accuracy of the eigenvalue evaluation can be assessed by

$$|\lambda_i - \hat{\lambda}_i| \leq |\beta_{j+1}|\ |s_{ij}|. \tag{4.54}$$

It is clear that error bound of Lanczos algorithm can be evaluated without even calculating the eigenvectors $\underline{w}_i$. The most important feature of the Lanczos algorithm is that matrix $\mathbb{T}$ which eigenvalues are being computed is not explicitly manipulated. In the algorithm, matrix $\mathbb{T}$ only appears in the operation $\underline{r}_j = \mathbb{T}\ \underline{q}_j - \beta_j\ \underline{q}_{j-1}$. In other words, extracting the eigenvalues of $\mathbb{T}$ with the Lanczos algorithm, only requires the ability to perform the matrix multiplication. This feature makes the Lanczos algorithm ideally suited to the extraction of dominant eigenvalues of large, sparse matrices.

4.6 Signal Synthesis

Because of noise in the data or the possibility of a poor choice of signals, the stability analysis algorithms described above can lead to inaccurate estimates of system dynamics. To detect eventual problems, it is important to reconstruct or synthesize the signals associated with the r estimated characteristic exponents of the system. Let h_k and $\hat{h}_k$ be the original and reconstructed signals, respectively; the discrepancy between the two is quantified by the following index

$$\epsilon = \sqrt{\frac{1}{n}\sum_{k=1}^{n}(\hat{h}_k - h_k)^2}. \tag{4.55}$$

If the reconstructed signals are in close agreement with the original signals, *i.e.* if ϵ is small, it is likely that the identified characteristic exponents are reliable estimates.

The response of a degree of freedom of the system, $h(t)$, can be expressed in terms of the characteristic exponents as $h(t) = \sum_{j=1}^{2N} a_j(t)\exp(\lambda_j t)$, eq. (4.2). Note that for the actual signal, the summation extents over all $2N$ characteristic exponents of the system; on the other hand, the estimated signal is $\hat{h}(t) = \sum_{j=1}^{r} \hat{a}_j(t)\exp(\hat{\lambda}_j t)$, where the summation extends over the r estimated characteristic exponents, $\hat{\lambda}_j$. Among the r estimated exponents, a null exponent often occurs, corresponding to an offset of the signal, n_r real exponents might appear, and finally, $2n_c$ complex conjugate exponents are also likely to occur. When the characteristic exponents are written as $\exp(\hat{\lambda}_j \Delta t) = r_j \exp(\mathbf{i}\phi_j)$ and the coefficients of the expansion as $\hat{a}_j(t) = \alpha_j(t) + \mathbf{i}\beta_j(t)$, the estimated signal becomes

$$\hat{h}(t) = \alpha_0(t) + \sum_{j=1}^{n_r} \alpha_j(t)\ r_j^{t/\Delta t} + \sum_{j=n_r+1}^{n_r+n_c} \left[2r_j^{t/\Delta t} \left(\alpha_j(t)\cos(\phi_j \frac{t}{\Delta t}) - \beta_j(t)\sin(\phi_j \frac{t}{\Delta t}) \right) \right]. \tag{4.56}$$

At time $t = k\Delta t$, the discrete value of the estimated signal is

$$\hat{h}_k = \alpha_{0,k} + \sum_{j=1}^{n_r} \alpha_{j,k}\ r_j^k + \sum_{j=n_r+1}^{n_r+n_c} \left[2\alpha_{j,k}\ r_j^k \cos(k\phi_j) - 2\beta_{j,k}\ r_j^k \sin(k\phi_j) \right] = \underline{q}_k^T \underline{a}_k, \tag{4.57}$$

where the subscript k indicates a quantity computed at time $k\Delta t$, and the two arrays $\underline{a}_k$ and $\underline{q}_k$ are defined as

$$\underline{a}_k = \begin{vmatrix} \alpha_{0,k} \\ \alpha_{1,k} \\ \vdots \\ \alpha_{n_r,k} \\ \alpha_{n_r+1,k} \\ \beta_{n_r+1,k} \\ \vdots \\ \alpha_{n_r+n_c,k} \\ \beta_{n_r+n_c,k} \end{vmatrix} \quad \text{and} \quad \underline{q}_k = \begin{vmatrix} 1 \\ r_1^k \\ \vdots \\ r_{n_r}^k \\ 2r_{n_r+1}^k \cos(k\phi_{n_r+1}) \\ -2r_{n_r+1}^k \sin(k\phi_{n_r+1}) \\ \vdots \\ 2r_{n_r+n_c}^k \cos(k\phi_{n_r+n_c}) \\ -2r_{n_r+n_c}^k \sin(k\phi_{n_r+n_c}) \end{vmatrix}, \tag{4.58}$$

respectively, and $\alpha_{j,k} = \alpha_j(k\Delta t)$. Array $\underline{q}_k$ stores known quantities related to the estimated exponents and $\underline{a}_k$ the unknown coefficients of the expansion of the estimated signal. Floquet's theory implies that $a_j(t)$ is a periodic function and hence, $\underline{a}_k = \underline{a}_{k+p}$. The unknown coefficients of the expansion are now computed by matching the actual and estimated signals at discrete time steps $t_{k+\ell p}$, $h_{k+\ell p} = \hat{h}_{k+\ell p}$, $\ell = 0, 1, \ldots, m$, to find

$$\begin{vmatrix} h_k \\ h_{k+p} \\ \vdots \\ h_{k+mp} \end{vmatrix} = \begin{bmatrix} \underline{q}_k^T \\ \underline{q}_{k+p}^T \\ \vdots \\ \underline{q}_{k+mp}^T \end{bmatrix} \underline{a}_k = \mathcal{Q}_k \, \underline{a}_k. \tag{4.59}$$

This set of linear equations is solved using the least square method, such that

$$\underline{a}_k = (\mathcal{Q}_k^T \mathcal{Q}_k)^{-1} \mathcal{Q}_k \begin{vmatrix} h_k \\ h_{k+p} \\ \vdots \\ h_{k+mp} \end{vmatrix}. \tag{4.60}$$

Solving this linear system for $k = 0, 1, 2, \ldots p-1$, will yield discrete values of the

periodic coefficients of the expansion, $\hat{a}_j(t)$, over one period. Of course, for constant coefficient systems, the procedure simplifies considerably, since the coefficients of the expansion become constants. Once the coefficients of the expansion are evaluated, the estimated signal, $\hat{h}$, follows from eq. (4.57) and the quality of the estimation can be assessed with the help of eq. (4.55). The evaluation of the estimated signal is particularly important for periodic systems: if the sole information available is the characteristic exponent, an indeterminacy remains concerning the corresponding system frequency. Indeed, the contribution of the exponent to system response is of the form $a_j(t)\exp(\lambda_j)$, where $a_j(t)$ is a periodic function. Expanding a_j in Fourier series yields $a_j(t) = \sum_k g_{jk}\exp(\mathbf{i}k\Omega t)$, where ϕ_k is phase angle, $\Omega = 2\pi/T$, and hence, the frequency of the system becomes $\omega_j\sqrt{1-\zeta_j^2} + k\Omega$, where k is an undetermined integer. If the estimated signal is evaluated, $a_j(t)$ is known in discrete form and so are its Fourier coefficients, g_{jk}. The non vanishing coefficients g_{jk} determine the integers k.

4.7 Stability Analysis Procedure

The algorithms described in the last two sections are combined to provide a robust approach to the stability analysis of complex systems. The overall procedure involves the following steps.

1. Determine the dynamic response of the system to a given excitation.
2. Construct matrices T_0 and $\mathbb{T}$ defined in eq. (4.37) and eq. (4.42), respectively.
3. Evaluate $r_{\mathbb{T}}$ proper orthogonal modes from matrix $\mathbb{T}$ by using Lanczos algorithm.
4. Compute the $r_{\mathbb{T}}$ optimal signals defined by eq. (4.41).
5. From these signals, assemble matrices $\mathbb{H}_0$ and $\mathbb{H}_1$ defined by eq. (4.16) the size of the matrices is determined by eq. (4.36).

6. Perform the singular value decomposition of $\mathbb{H}_0$.

7. Evaluate matrix $\hat{Q}$ or $\hat{B}$ using eq. (4.19) or (4.34), and compute its eigenvalues.

8. Compute the associated system frequencies and dampings using eq. (4.13).

9. Compute the coefficients of the expansion, $\underline{a}_k$, using eq. (4.60).

10. Evaluate the estimated signal, $\hat{h}_k$, using eq. (4.57), and compute the discrepancy using eq. (4.55).

The above procedure calls for the following remarks.

1. The procedure presented above is equally applicable for constant and periodic coefficient systems. In the former case, many of the steps of the procedure considerably simplify.

2. The first step of the procedure is critical as it involves the selection of the suitable excitations. The excitation should provide an adequate amount of energy for the modes of interest, typically, the least damped modes of the system. Clearly, this step requires the understanding of the dynamic behavior of the system.

3. Steps 2, 3 and 4 can be bypassed and replaced by a choice of suitable signals, typically the response of specific degrees of freedom of the system. The computation of the proper orthogonal decomposition and associated optimal signals relieves the analyst from having to select suitable signals, leading to a more robust procedure.

4. Steps 3 and 7 involve the estimations of the rank of matrices $\mathbb{T}$ and $\mathbb{H}_0$, respectively; these are crucial steps of the procedure. The energy index, defined in Appendix A, eq. (A.3), is conveniently used for this estimation by requiring

$E_{r_{\mathbb{T}}} > 1 - \epsilon$ and $E_{r_{\mathbb{H}_0}} > 1 - \epsilon$, where ϵ is a small, user defined number. It is sometimes convenient to let $r_{\mathbb{T}}$ and $r_{\mathbb{H}_0}$ be user specified inputs.

4.8 Chapter Summary

The robust and efficient approaches for linearized stability analysis of numerical multi-physics models were presented in this chapter. The partial Floquet approach was proved to be equivalent to the autoregressive method, both approaches were derived from the discrete time linear model. Consequently, the stability characteristics of the dynamic system were computed with the help of singular value decomposition. An alternative way to filter noise is the use of proper orthogonal modes. The signal synthesis was used to estimate the accuracy of the approximation of the stability characteristics. Finally, the entire stability analysis procedure was summarized.

CHAPTER V

NUMERICAL EXAMPLES FOR STABILITY ANALYSIS

The chapter presents numerical applications of proposed stability analysis approaches. Applications to classical problems are provided at first in section 5.1 to validate the methodology. The results have been compared with those of the existing techniques. The section 5.2 demonstrates the application of proposed approaches to aeroelastic fixed wing problem, the sections 5.3 and 5.4 show the whole procedure of proposed approach to solve the multibody problem. The other sections validate the proposed approaches to experimental and nonlinear problems.

5.1 Classical Application

Two examples will be treated in this section, illustrating the various methods described in this thesis. The performance of various methods described in chapter 3 will be contrasted with the proposed approaches.

5.1.1 The Follower Force Problem

The first numerical example deals with a cantilevered beam of length $L = 2.4$ m subjected to a tip compressive follower force P. This example will be used to validate the proposed methodology, since an exact solution is available for this problem [21]. The beam has a bending stiffness $EI = 23$ kN·m^2, and a mass per unit span $m = 1.6$ kg/m. The equation of force equilibrium in transverse direction will be

$$p_y = -P\frac{\mathrm{d}^2 w}{\mathrm{d}^2 x}, \tag{5.1}$$

where p_y is the distributed force in transverse direction. To solve this problem, a two mode approximation for the cantilevered beam response is given

$$w(x,t) = \gamma_1(x)\ q_1(t) + \gamma_2(x)\ q_2(t), \tag{5.2}$$

the modes γ_1 and γ_2 to be used are specified as the lowest two bending modes of the cantilevered beam

$$\gamma_i(x) = \left[\cosh\left(k_i\frac{x}{L}\right) - \cos\left(k_i\frac{x}{L}\right)\right] - \alpha_i\left[\sinh\left(k_i\frac{x}{L}\right) - \sin\left(k_i\frac{x}{L}\right)\right], \quad \text{for} \quad i = 1, 2. \tag{5.3}$$

The coefficients $k_1 = 1.8751$, $k_2 = 4.6941$, and $\alpha_1 = 0.7341$, $\alpha_2 = 1.0185$. Application of the Lagrange equation leads to following equations of motion

$$\frac{mL^4}{EI}\begin{bmatrix} 1 & 0 \\ 0 & 1 \end{bmatrix}\begin{vmatrix} \ddot{q}_1 \\ \ddot{q}_2 \end{vmatrix} + \begin{bmatrix} k_1^4 & 0 \\ 0 & k_2^4 \end{bmatrix}\begin{vmatrix} q_1 \\ q_2 \end{vmatrix} + \frac{PL^2}{EI}\begin{bmatrix} 0.8582 & -11.74 \\ 1.874 & -13.30 \end{bmatrix}\begin{vmatrix} q_1 \\ q_2 \end{vmatrix} = 0 \tag{5.4}$$

Solution of these equations is in the form $q_i = \bar{q}_i \exp(pt)$, where p is the characteristic exponent. The non-dimensional magnitude of the follower force, and characteristic exponent, denote λ and $\bar{p}$, are defined as

$$\lambda = \frac{PL^2}{EI} \quad \text{and} \quad \bar{p} = p\sqrt{\frac{mL^4}{EI}}, \tag{5.5}$$

and they will satisfy the following characteristic polynomial

$$\bar{p}^4 + \bar{p}^2(497.9 - 12.44\lambda) + (12.36 + 0.8582\lambda)(485.5 - 13.30\lambda) + 22.00\lambda^2 = 0 \tag{5.6}$$

For small magnitude of the follower force, the characteristic exponents of the system are purely imaginary and yield the frequencies of oscillation of the beam. At the critical magnitude $P_{cr} = 20.0509$ EI/L^2, the characteristic exponent presents a positive real part, and the system is unstable. Figs. 5.1 shows the analytical frequencies and dampings of the system, as a function of the follower force magnitude.

These analytical results will now be compared with the predictions of autoregressive approach. The finite element based multibody formulation [8] was used to

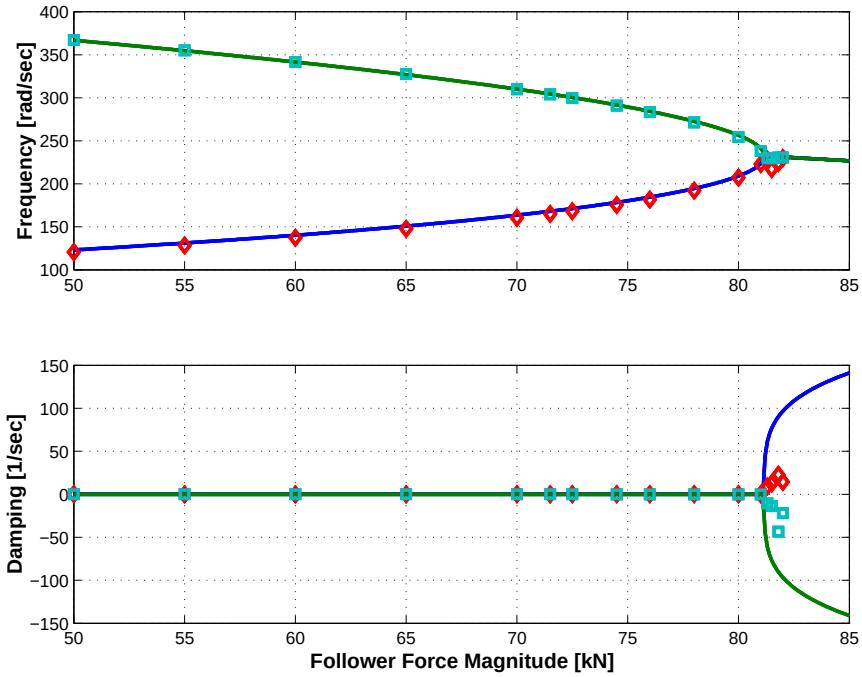

Figure 5.1: The frequencies and dampings of the cantilevered beam subjected to a follower force. Solid line: exact solution; ♢ and □: present predictions for the two lowest frequencies.

simulate the dynamic response of the cantilevered beam modeled with eight cubic beam elements. The beam model included both shearing deformation and rotary inertia effects. To compare the predictions with the analytical solution which neglect these effects, a very large shearing stiffness $GK = 2.8$ GN was selected, and the rotary inertia was set to zero. To excite the system, a small impulsive load was applied at the tip of the beam: the triangular pulse reached a maximum value of 30 N at time $t = 10$ msec, then ramps back to a zero value at time $t = 20$ msec. A constant time step of $\Delta t = 0.5$ msec was used to simulate a 1 sec period of the response. A single signal was extracted from this response: the beam three-quarter span transverse deflection. Figs. 5.1 compares the analytical frequencies and damping rates of the system with the prediction of autoregressive approach as extracted from the characteristic exponents using eqs. (4.13). Excellent correlation is observed between the analytical solution and the predictions extracted from autoregressive method.

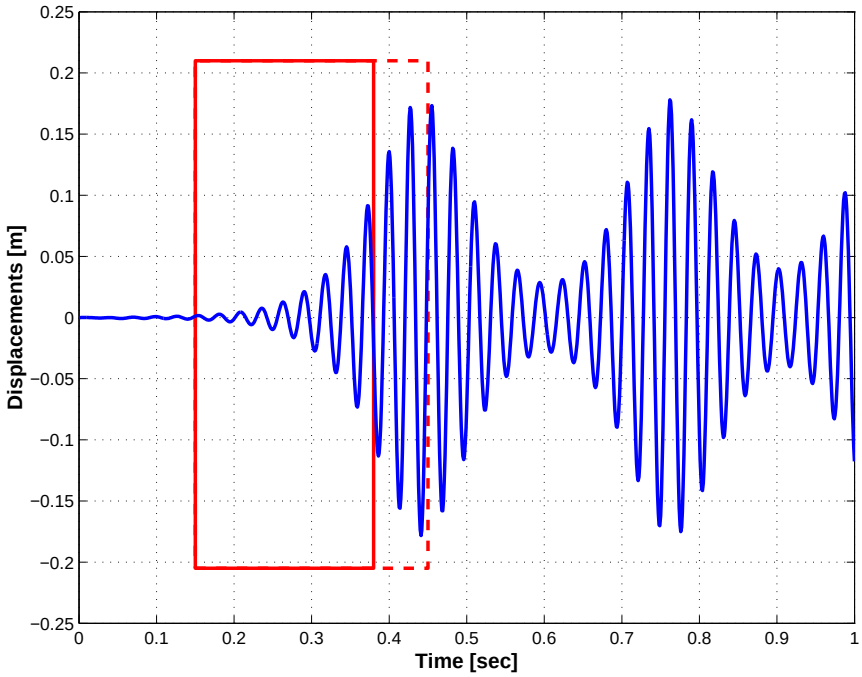

Figure 5.2: Time history of the transverse displacement of the beam at three-quarter span, for to tip compressive load $P = 82$ kN. Window $0.15 < t < 0.45$ sec: dashed line; window $0.15 < t < 0.38$ sec: solid line.

It should be noted, however, that the proposed approach encounters difficulties when the system is unstable. Fig. 5.2 shows the transverse displacement of the beam at quarter-span, for a tip compressive load $P = 82$ kN, *i.e.* in the unstable regime. Clearly, the behavior is nonlinear since the exponential growth predicted by the linear theory, see eq. (3.14), is replaced by a beating phenomenon that involves large transverse deflections. To obtain good predictions, it is important to select the signal appropriately: if a longer window is selected, the nonlinear behavior becomes more pronounced and poor results should be expected; of course, if the window is too short, the response of the system will be difficult to identify. For instance, the two windows illustrated in fig. 5.2 yield the following results: for window $0.15 < t < 0.45$ sec, $\omega_{1,2} = 184,\ 238$ rad/sec and $\zeta_{1,2} = 102,\ -31$ sec^{-1}, whereas for window $0.15 < t < 0.38$ sec, $\omega_{1,2} = 230,\ 231$ rad/sec and $\zeta_{1,2} = 14,\ -22$ sec^{-1}.

A detailed view of the predictions near the instability boundary are shown in

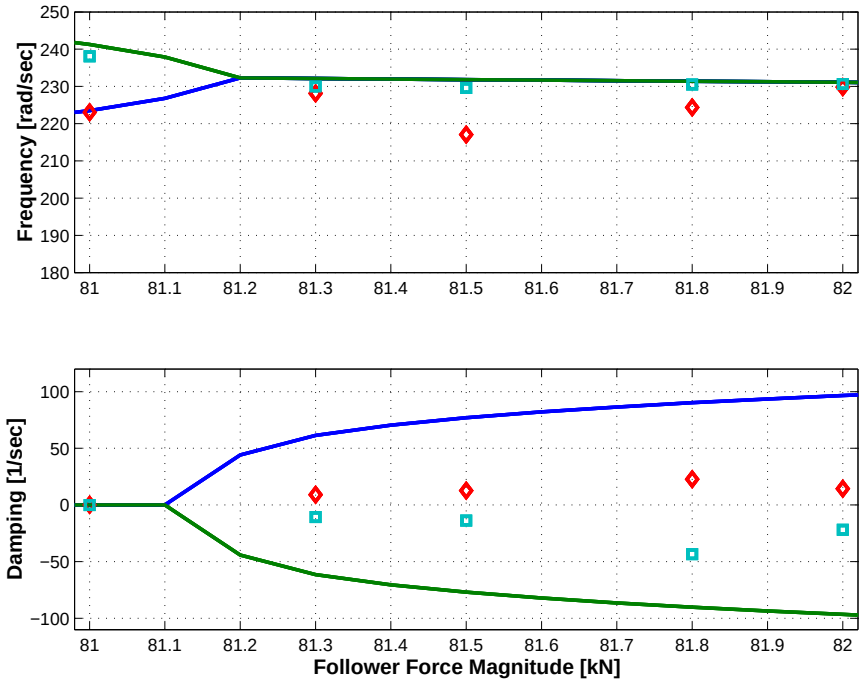

Figure 5.3: The frequencies and dampings of the cantilevered beam subjected to a follower force. Solid line: exact solution; ♢ and □: present predictions for the two lowest frequencies. Detailed view near instability boundary.

figs. 5.3. Although the predicted stability boundary is in good agreement with its analytical counterpart, the growth rates in the unstable regime do not match closely. This is probably due to the fact that the numerical model captures the nonlinear behavior of the system, whereas the analytical solution is derived for the linearized problem.

While the above difficulties are encountered in the unstable regime, predictions are much easier to obtain when the system is stable. It should be noticed that accurate predictions are most important in the stable regime: the designer want to accurately predict damping rates of the system. In most cases, unstable regimes are to be avoided, and accurate predictions of growth rates are not important.

5.1.2 Parametric Excitation of a Beam

The second example deals with a uniform, simply supported beam of length $\ell = 1$ m subjected to an end compressive load of harmonically varying amplitude, $P = P_0 + P_1 \cos(\omega_p t)$, as depicted in fig.5.4. The physical properties of the beam are: bending stiffness, $EI = 6.57$ kN·m^2 and mass per unit span, $m = 3.24$ kg/m.

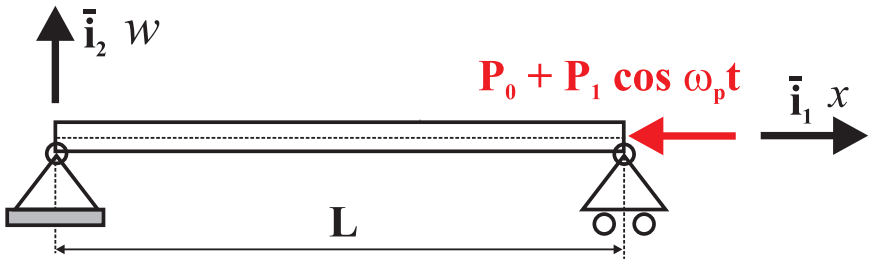

Figure 5.4: The parametric excitation of a beam.

The governing equation of the problem is readily derived with the help of the Euler-Bernoulli assumptions to find

$$EI\frac{\partial^4 w}{\partial x^4} + (P_0 + P_1 \cos\omega_p t)\frac{\partial^2 w}{\partial x^2} + c\frac{\partial w}{\partial t} + m\frac{\partial^2 w}{\partial t^2} = 0, \tag{5.7}$$

where w is the transverse displacement of the beam, c is damping coefficient. Analytical solutions of the problem are obtained with the help of the variable separation method [21]. The transverse displacement of the beam is expanded as

$$w(x,t) = q_k(t)\sin\frac{k\pi x}{\ell}, \tag{5.8}$$

where $k = 1, 2, \ldots, n$. Substituting this assumed solution into the governing equation then yields

$$\ddot{q}_k + \epsilon\,\dot{q}_k + \Omega_k^2\,(1 - \frac{P_0 + P_1\cos\omega_p t}{P_k})\,q_k = 0 \tag{5.9}$$

where Ω_k, the k^{th} natural frequency of the beam, P_k, the k^{th} Euler buckling load, and ϵ are defined as

$$\Omega_k = \frac{k^2\pi^2}{\ell^2}\sqrt{\frac{EI}{m}}, \quad P_k = \frac{k^2\pi^2 EI}{\ell^2}, \quad \epsilon = \frac{c}{m}. \tag{5.10}$$

For convenience, eq. (5.9) is rewritten as

$$\ddot{q}_k + \epsilon\ \dot{q}_k + \omega_k^2\ (1 - 2\mu_k \cos\omega_p t)\ q_k = 0, \tag{5.11}$$

where

$$\omega_k = \Omega_k \sqrt{1 - \frac{P_0}{P_k}}, \quad \mu_k = \frac{1}{2}\ \frac{P_1}{P_k - P_0}. \tag{5.12}$$

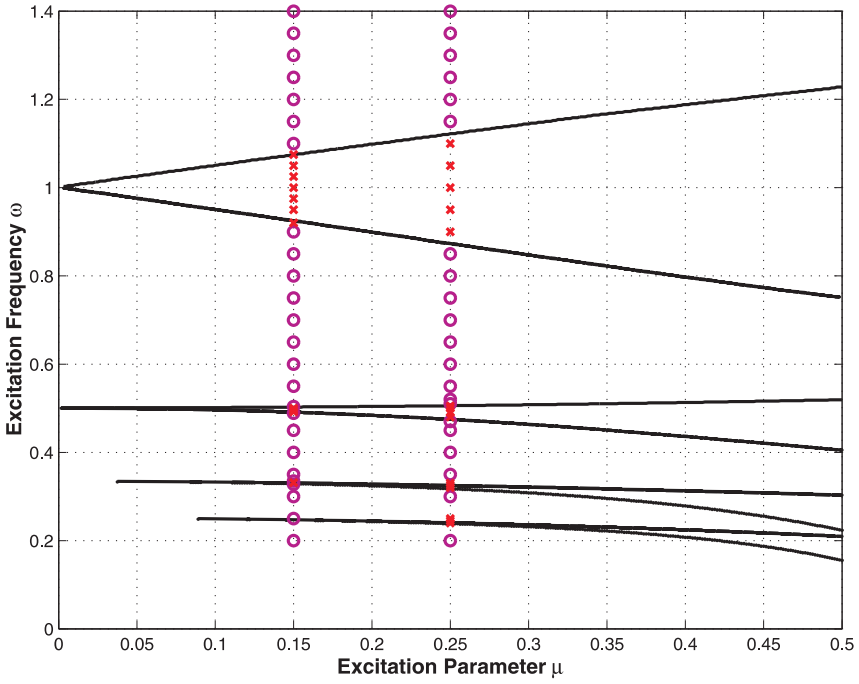

Figure 5.5: Strutt's diagram. Stability boundaries predicted by Hill's infinite determinant, solid lines. Present solutions for $\mu = 0.15$ and 0.25: stable solution, ($\circ$), unstable solution, ($\times$).

Finally, this equation is brought in the form of the well-known Mathieu equation [77] by non dimensionalizing all terms to find

$$\frac{\mathrm{d}^2 q_k}{\mathrm{d}\tau^2} + \hat{\epsilon}\ \frac{\mathrm{d}q_k}{\mathrm{d}\tau} + (a - 2\ q\cos 2\tau)\ q_k = 0, \tag{5.13}$$

where

$$\tau = \frac{\omega_p t}{2}, \quad \hat{\epsilon} = \frac{2\ \epsilon}{\omega_p}, \quad a = \left(\frac{2\omega_k}{\omega_p}\right)^2, \quad q = a\mu_k. \tag{5.14}$$

With the help of the harmonic balance method, a classical solution of this equation $q_k(t)$ is written as a superposition of harmonics of period $2T$ as

$$q_k(t) = \sum_{j=1,3}^{\infty} \left(a_j \sin \frac{j\omega_p t}{2} + b_j \cos \frac{j\omega_p t}{2} \right), \tag{5.15}$$

and of harmonics of period T as

$$q_k(t) = b_0 + \sum_{j=2,4}^{\infty} \left(a_j \sin \frac{j\omega_p t}{2} + b_j \cos \frac{j\omega_p t}{2} \right), \tag{5.16}$$

and the stability boundaries for the problem are computed via Hill's infinite determinant approach. Substituting the odd harmonic expansion into eq. (5.11), a set of homogeneous equations for the coefficients a_j and b_j will be identified; then a nontrivial solution exists if the Hill's infinite determinants vanishes, *i.e.*

$$\begin{vmatrix} \cdots & \cdots & \cdots & \cdots \\ 1 - 9\omega_p^2/(4\omega_k^2) & -\mu & 0 & -3\epsilon\omega_p/(2\omega_k^2) \\ -\mu & 1 + \mu - \omega_p^2/(4\omega_k^2) & -\epsilon\omega_p/(2\omega_k^2) & 0 \\ 0 & \epsilon\omega_p/(2\omega_k^2) & 1 - \mu - \omega_p^2/(4\omega_k^2) & -\mu \\ 3\epsilon\omega_p/(2\omega_k^2) & 0 & -\mu & 1 - 9\omega_p^2/(4\omega_k^2) \\ \cdots & \cdots & \cdots & \cdots \end{vmatrix} = 0, \tag{5.17}$$

similarly, for the even harmonics, the solution becomes

$$\begin{vmatrix} \cdots & \cdots & \cdots & \cdots & \cdots \\ 1 - 4\omega_p^2/(\omega_k^2) & -\mu & 0 & 0 & -2\epsilon\omega_p/(\omega_k^2) \\ -\mu & 1 - \omega_p^2/(\omega_k^2) & 0 & -\epsilon\omega_p/(\omega_k^2) & 0 \\ 0 & 0 & 1 & -\mu & 0 \\ 0 & \epsilon\omega_p/(\omega_k^2) & -2\mu & 1 - \omega_p^2/(\omega_k^2) & -\mu \\ 2\epsilon\omega_p/(\omega_k^2) & 0 & 0 & -\mu & 1 - 4\omega_p^2/(\omega_k^2) \\ \cdots & \cdots & \cdots & \cdots & \cdots \end{vmatrix} = 0, \tag{5.18}$$

where $\mu = \mu_k$. The roots of determinants (5.17) and (5.18) are approximated by iteration approach from the central parts of the determinant and yield the stability

boundaries for the problem. Fig. 5.5 shows Strutt's diagram that depicts the stability boundaries in the space of the excitation frequency, $\omega = \omega_p/(2\omega_k)$, versus excitation parameter, $\mu = \mu_k$, in the absence of damping.

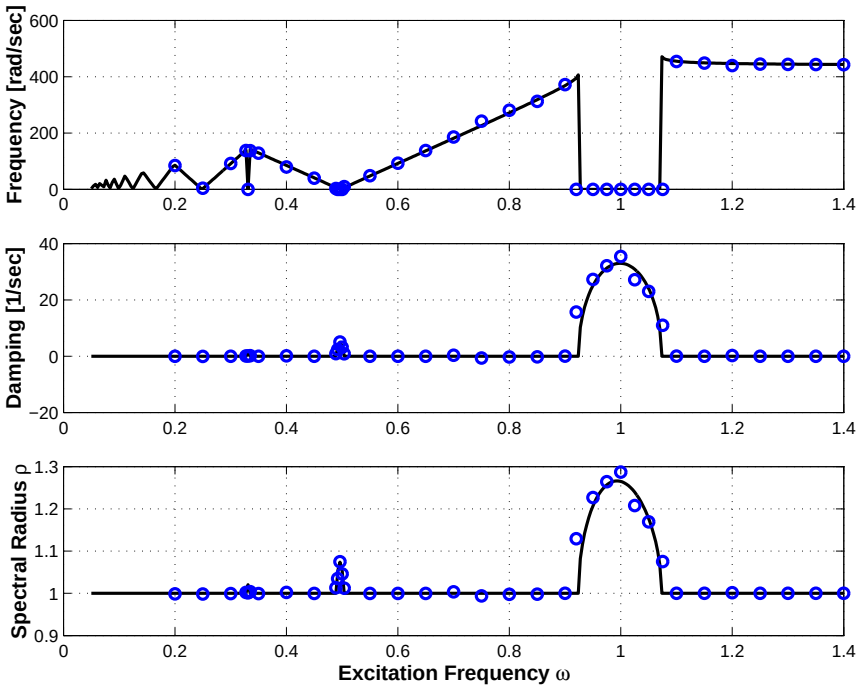

Figure 5.6: Frequency (top figure), damping (middle figure) and norm (bottom figure) of the maximum eigenvalue of the system versus excitation frequency, for $\mu = 0.15$. Floquet's classical analysis: solid line; present approach: ($\circ$).

The stability analysis method proposed in this thesis will be validated by comparing predicted stability boundaries with those obtained via Hill's infinite determinant method and predicted frequencies and damping with those extracted from a direct application of Floquet's classical theory. The beam was modeled with 4 cubic finite elements [8]; the numerical simulation was run for a total of 12 periods, $T = 2\pi/\omega_p$, with a time step $\Delta t = 1.0$ msec. For the stability analysis, the sampling period was set to $T/96$, the time histories of three proper orthogonal modes containing over 95% of the signal's energy were used as optimized signals, and the characteristics of the system were estimated using matrix $\hat{Q}$, see eq. (4.19). Fig. 5.5 shows that excellent correlation is found between the predictions of Hill's determinant and of the proposed

approach.

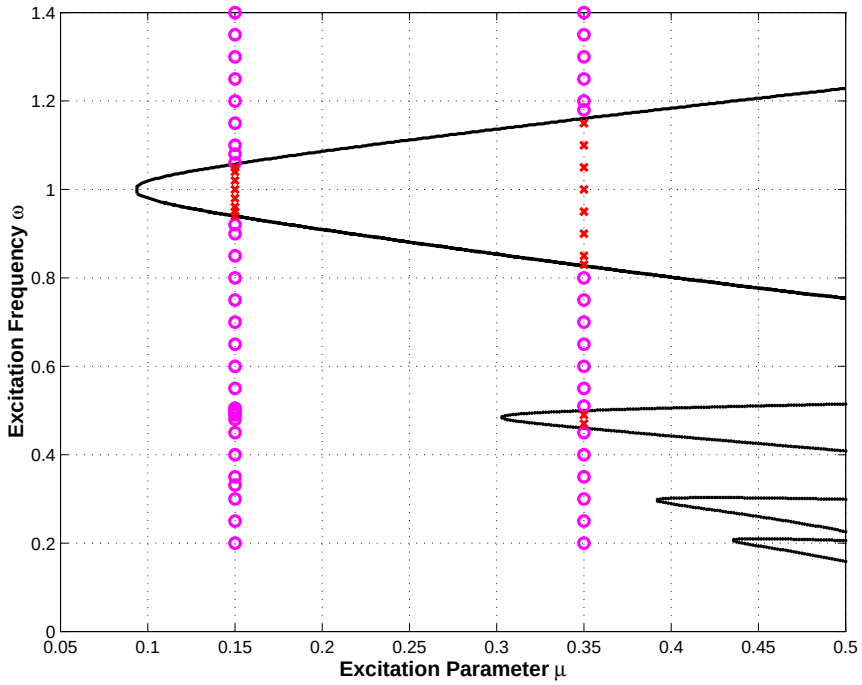

Figure 5.7: Strutt's diagram. Stability boundaries predicted by Hill's infinite determinant, solid lines. Present solutions for $\mu = 0.15$ and 0.35: stable solution, ($\circ$), unstable solution, ($\times$).

For a more quantitative comparison of the predictions, figs. 5.6 shows the frequency and damping associated with the characteristic exponent of largest magnitude as a function of excitation frequency, for an excitation parameter $\mu = 0.15$. Finally, the last part of the figure compares the norms of the maximum eigenvalue of the transition matrix. Excellent agreement is found for all results.

Next, the effect of damping on stability boundaries was investigated. Damping was modeled by adding to the simulation viscous forces proportional to the strain rates, $\underline{F}_d = \mu_s K_s \underline{\dot{e}}$, where μ_s is the damping coefficient, $\underline{e}$ the strain array, and K_s the beam cross-sectional stiffness matrix. These quantities are all measured in a cross-section attached coordinate system. Fig. 5.7 shows the stability boundaries in the presence of damping, as predicted by Hill's infinite determinant and by the present method. The damping coefficient was selected as $\mu_s = 0.2$ msec, which corresponds

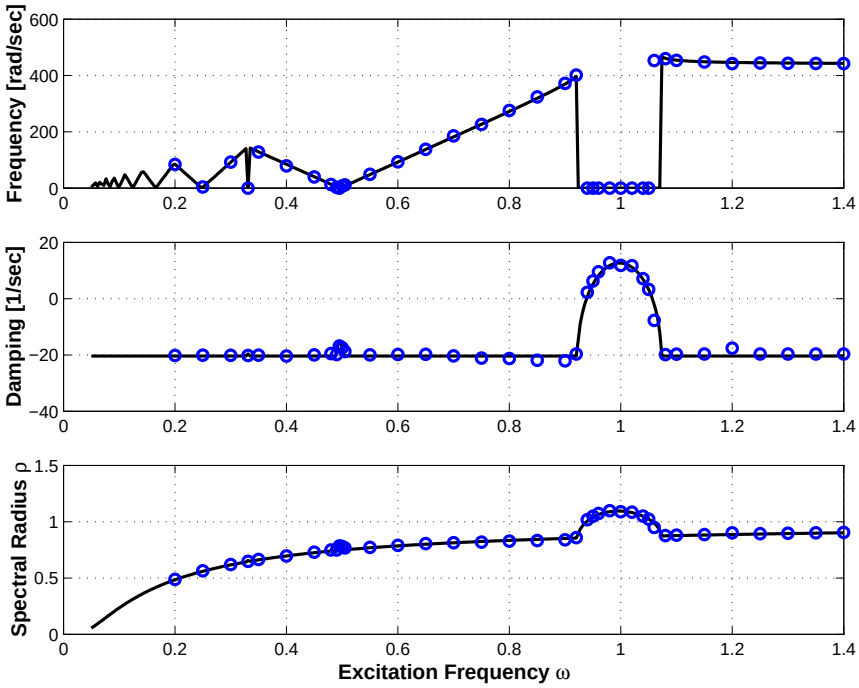

Figure 5.8: Frequency (top figure), damping (middle figure) and norm (bottom figure) of the maximum eigenvalue of the system versus excitation frequency, for $\mu = 0.15$. Floquet's classical analysis: solid line; present approach: ($\circ$).

to $\epsilon = 12.57$ sec^{-1}. Figs. 5.8 shows the frequency, damping and norm associated with the characteristic exponent of largest magnitude, for an excitation parameter $\mu = 0.15$. Excellent agreement is found for all results.

5.2 Flutter of a Rectangular Planform Wing

This example is an aeroelastic problem dealing with the symmetric flutter of a rectangular planform wing clamped at its mid-point [40]. Due to symmetry, a half configuration was modeled and proper symmetry conditions were applied. This problem involves both structural and aerodynamic states. The half wing has a rectangular planform of length $L = 20$ ft and chord length $c = 6$ ft. The flutter speed of the wing was experimentally measured as $U_F = 590$ ft/sec. The structural properties of the cantilevered wing are as follows: bending stiffness, $EI = 2.4\ 10^7$ lbs·ft^2, torsional stiffness, $GJ = 2.4\ 10^6$ lbs·ft^2, mass per unit span, $m = 0.75$ slugs/ft, polar moment

of inertia, $I = 1.95$ slugs·ft. The airfoil quarter-chord and center of mass are located 0.5 and 0.6 ft aft the elastic axis of the wing, respectively. The wing semi-span is modeled with four cubic beam elements.

The aerodynamic model combines thin airfoil theory with a three dimensional dynamic inflow model. The airfoil has a constant slope of the lift curve $a_0 = 6.28$, and the moment coefficients about the quarter-chord are zero. The inflow velocities at each span-wise location are computed using the finite state induced flow model developed by Peters *et al.* [89, 87]. The number of inflow harmonics was selected as $m = 9$, corresponding to 55 aerodynamic inflow states for this symmetric problem. Airloads were computed at 9 stations along the wing span, located at the positions corresponding to Gaussian quadrature. Selecting a larger number of aerodynamic states or airloads computation points did not significantly affect the results.

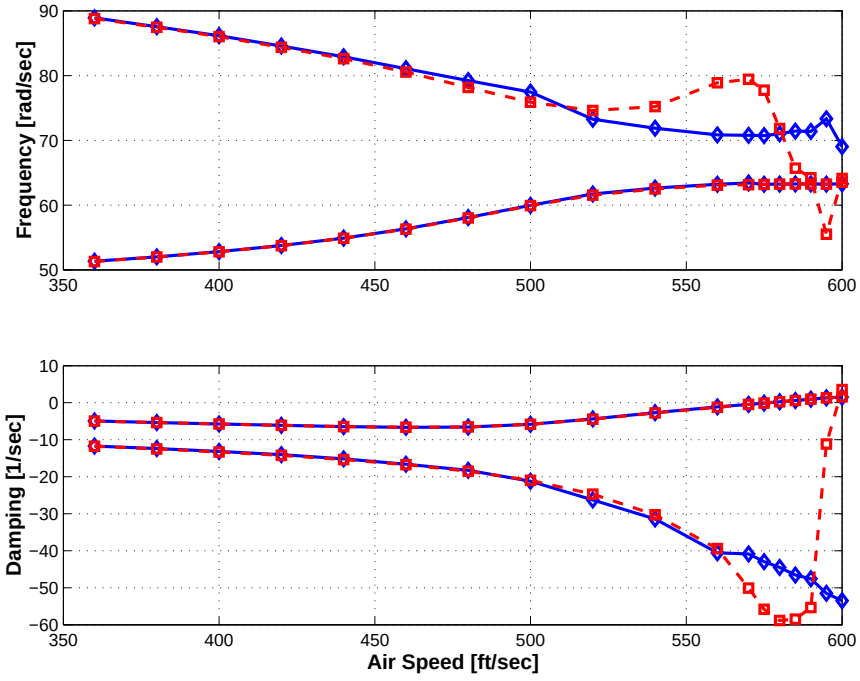

Figure 5.9: Frequencies and dampings of the cantilevered wing. *Case 1*: dashed line (⋄): *Case 2*: solid line (□).

The simulation was run for a total period of 1 sec, using a constant time step $\Delta t =$

1 msec. This example will be used to illustrate the two strategies proposed in this thesis: the use of user selected signals and the use of optimized signals based on proper orthogonal modes. The first case, denoted *case 1*, uses two signals: the three-quarter span transverse displacement, and twist of the wing. The second case, denoted *case 2*, uses optimized signals: the proper orthogonal modes of the system were first extracted from the response of all the degrees of freedom, the six displacement components at each of the 12 nodes of the structural model, and the airload components at the 9 stations. The criterion $E_{r_{\mathbb{T}}} > 0.92$, see eq. (A.3), leads to the use of 3 optimized signals based on 3 proper orthogonal modes; on the other hand, $r_{\mathbb{H}_0}$ was set to 6, corresponding to criterion $E_{r_{\mathbb{H}_0}} > 0.97$. The signals used for stability analysis spanned the response of the system for $t \in [0.30, 0.95]$ sec, with a sampling period of 2 msec.

Figs. 5.9 shows the frequency and damping of the two modes with the lowest frequencies versus far field flow velocity. This figure is similar to that obtained from the classical, two degree of freedom analysis of a wing section [20]. The lowest bending and torsional modes nearly coalesce at flutter. Note that the higher bending and torsional modes do not appear on the figure, although they are included in the model. This is due to the fact that these modes are heavily damped by the aerodynamic forces, and hence are identified as "noise" by the proposed methods. To illustrate this point, fig. 5.10 shows the normalized singular values of matrix $\mathbb{H}_0$ for *cases 1* and *2*. When only two sensors are used, six singular values only are larger than $\varepsilon_{\text{rank}}$ whereas when proper orthogonal modes are used, the additional data enables the accurate estimate of twelve singular values. This means that in *cases 1* and *2*, a system of order six and twelve, respectively, will be identified.

From figs. 5.9, the flutter speed is found to be $U_F = 585$ ft/sec, for *cases 1* and *2*; this compares favorably with the experimentally measured flutter speed of 590 ft/sec. For *case 2*, the optimized sensors obtained from the proper orthogonal modes allow a more robust determination of the frequency and damping rates: for air speeds

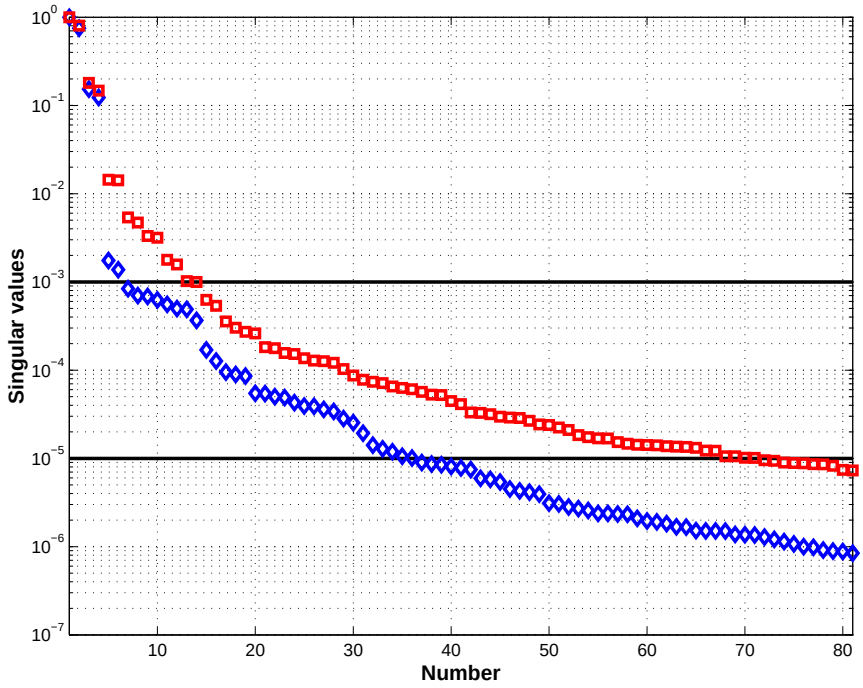

Figure 5.10: The normalized singular values of matrix $\mathbb{H}_0$ for far field velocity $U = 500$ ft/sec. *Case 1*: ($\diamondsuit$); *Case 2*: ($\square$). The horizontal lines represent the user defined tolerances: $\varepsilon_{\text{rank}} = 10^{-3}$ and $\varepsilon_{\text{noise}} = 10^{-5}$.

above 520 ft/sec, the predictions based on two signals only are no longer satisfactory for the second mode of the system. It should be noted, however, that both cases predict the same flutter speed. The predictions becomes less accurate in the unstable region, due to the nonlinear behavior associated with large deflections of the wing. Furthermore, it becomes increasingly difficult to trace the second mode because it is heavily damped.

For this example, the four stability algorithms presented in this thesis, see eqs. (4.18), (4.19), (4.33) and (4.34), were used to predict the frequencies and dampings of the system for a far field flow velocity $U = 590$ ft/sec. Identical predictions, within four significant digits, were obtained from the eigenvalues of the four matrices.

5.3 The Ground Resonance Problem

The example in this section deals with the ground resonance problem depicted in fig. 5.11.

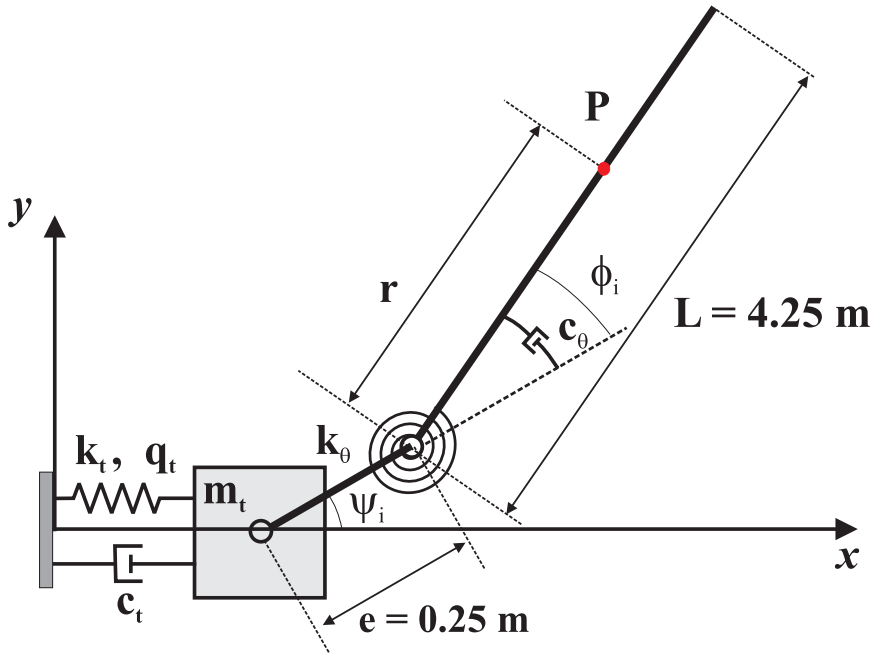

Figure 5.11: Schematic of the ground resonance problem. For clarity, a single blade of the system is shown.

A four-bladed rotor rotating at an angular velocity Ω is mounted on a rigid block of mass $m_t = 30$ kg. This block is connected to the ground by a spring of stiffness constant $k_t = 12$ kN/m and dashpot of constant $c_t = 150$ N·s/m. The four-bladed rotor is connected to the block by means of a revolute joint; each blade of length $L = 4.25$ m is connected to this joint through a root retention device of length $e = 0.25$ m and a lead-lag revolute joint that allows relative rotation of the blade with respect to the root retention in the plane of rotation of the rotor. Both root retention and blade are modeled as beams of bending stiffness $I_{22} = 545$ N·m^2, torsional stiffness $GJ = 620$ N·m^2, and mass per unit span $m = 3$ kg/m; they are modeled with one and two cubic beam elements, respectively. The blade lead-lag revolute joint features

a torsional spring of stiffness $k_\theta = 2760$ N·m/rad and a torsional damper of constant $c_\theta = 230$ N·m·s/rad.

This system is clearly a periodic system. If the blades are considered to be rigid bodies, it is possible to find an analytical solution of the problem: the governing equations with periodic coefficients are transformed to a set of equations with constant coefficients using a Fourier transformation, and classical methods are then used to predict linearized stability. As shown in fig. 5.11, the coordinates of arbitrary point P at the i^{th} blade are

$$\begin{cases} x = q_t + e\cos\psi_i + r\cos(\psi_i + \phi_i); \\ y = e\sin\psi_i + r\sin(\psi_i + \phi_i), \end{cases} \tag{5.19}$$

where q_t is the position of rigid moving block, ψ_i the azimuth angle of i^{th} blade, $\psi_i(t) = \Omega\ t + 2\pi(i-1)/4$, Ω is the angular speed of the rotor, the angle ϕ_i measures the lead-lag rotation of the i^{th} rigid blade. The motion equations of the system can be obtained by Lagrange equation

$$\begin{cases} m_0\ddot{q}_t + c_t\dot{q}_t + k_t q_t - S\dfrac{\mathrm{d}^2}{\mathrm{d}t^2}\left(\displaystyle\sum_{i=1}^{4}\phi_i\sin\psi_i\right) = 0; \\ -S\sin\psi_i\ddot{q}_t + I_\rho\ddot{\phi}_i + c_\theta\dot{\phi}_i + (k_\theta + Se\Omega^2)\phi_i = 0, \end{cases} \tag{5.20}$$

where I_ρ is the moment of inertia of blade about the lead-lag joint, S the static moment of blade about the lead-lag joint, and the total mass $m_0 = m_t + 4\ m\ L$. For a sinusoidal and cosinusoidal variation of lead-lag motion, $\phi_i(t) = a_1(t)\sin\psi_i + b_1(t)\cos\psi_i$, the non-dimensional result equations using Fourier transform are

$$S_H\ \underline{x}' = B_H\ \underline{x}, \tag{5.21}$$

where the notation $()'$ indicates a derivative with respect to non-dimensional time

$\tau = \Omega t$. The vector $\underline{x}$ and the matrix S_H are defined as

$$\underline{x} = \begin{vmatrix} q_t \\ a_1 \\ b_1 \\ q_t' \\ a_1' \\ b_1' \end{vmatrix} \quad \text{and} \quad S_H = \begin{bmatrix} 1 & 0 & 0 & 0 & 0 & 0 \\ 0 & 1 & 0 & 0 & 0 & 0 \\ 0 & 0 & 1 & 0 & 0 & 0 \\ 0 & 0 & 0 & m_0/m_t & -2S/m_t & 0 \\ 0 & 0 & 0 & -S/I_\rho & 1 & 0 \\ 0 & 0 & 0 & 0 & 0 & 1 \end{bmatrix}, \tag{5.22}$$

and matrix B_H

$$B_H = \begin{bmatrix} 0 & 0 & 0 & 1 & 0 & 0 \\ 0 & 0 & 0 & 0 & 1 & 0 \\ 0 & 0 & 0 & 0 & 0 & 1 \\ -\omega_t^2/\Omega^2 & 0 & 0 & -\zeta_t\omega_t/\Omega & 0 & 0 \\ 0 & -\omega_t^2/\Omega^2 - eS/I_\rho + 1 & \zeta_\theta\omega_b/\Omega & 0 & -\zeta_\theta\omega_b/\Omega & 2 \\ 0 & -\zeta_\theta\omega_b/\Omega & -\omega_t^2/\Omega^2 - eS/I_\rho + 1 & 0 & -2 & -\zeta_\theta\omega_b/\Omega \end{bmatrix},$$

where the natural frequencies of blade and moving block, ω_b and ω_t, and viscous damping parameters ζ_b and ζ_t are defined

$$\omega_t^2 = \frac{k_t}{m_t}, \quad \zeta_t = \frac{1}{\omega_t}\frac{c_t}{m_t}, \quad \text{and} \quad \omega_b^2 = \frac{k_\theta}{I_\rho}, \quad \zeta_\theta = \frac{1}{\omega_b}\frac{c_\theta}{I_\rho}. \tag{5.23}$$

Obviously, eq. (5.21) is a set of homogeneous, ordinary differential equations with constant coefficients. The solution of these equations is written in the form $\underline{x} = \bar{\underline{x}}\exp(p\ t)$, where p is the characteristic exponent. Introducing this solution into eq. (5.21) yields a set of homogeneous, algebraic equations, $(p\ I - S_H^{-1}B_H)\ \bar{\underline{x}} = 0$. A nontrivial solution of these equations is possible only when the determinant of the algebraic system is zero. *i.e.*

$$\det(p\ I - S_H^{-1}B_H) = 0, \tag{5.24}$$

which has the complex conjugate solution p, the damping of the system can be determined from the characteristic exponent p.

When the present approaches were applied to extract the damping of the system, the system was simulated by a finite element based multibody formulation [8, 9] using a constant time step $\Delta t = 1$ msec, for a total of 5 sec. A total of five signals were used to asses stability characteristics based on autoregressive approach: the block translation, and the four relative rotations of the blade lead-lag joints.

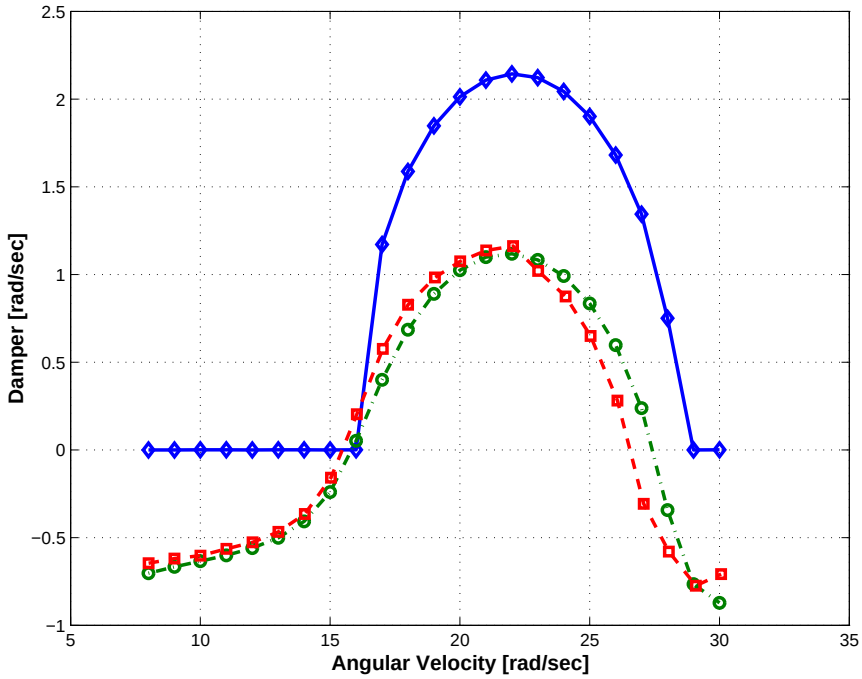

Figure 5.12: The dampings of ground resonance of windmill simple model. Analytical solution without damping: solid line (◇); analytical solution with damping: dashed-dotted line (○); present solution: dashed line (□).

Fig. 5.12 shows the results of the analysis. At first, for reference, the damping in the system is plotted against rotor speed using the analytical solution with and without dampers. As expected, in the presence of dampers, the unstable zone is reduced, and the growth rate of the instability is decreased. Next, the proposed methodology was used to predict the damping parameters of the system, as shown in fig. 5.12. Note the excellent correlation between the present results and the analytical predictions. The slight difference between the two sets of results is due to the elasticity of the blades that is ignored in the analytical solution.

5.4 The Wind Turbine Problem

This example, also the ground resonance problem, deals the modeling of the three-bladed wind turbine depicted in fig. 5.13. The physical properties of the system are tabulated in ref. [102] and will not be repeated here. In the multibody dynamics model [9], the cantilevered tower is connected to a flexible bed plate, modeled with two and one cubic beam elements, respectively. The shaft, modeled as a single cubic beam element, is connected to the bed plate by means of a revolute joint. In turns, the tip of the shaft is attached to the hub, modeled as a rigid body. Finally, the three flexible blades, each modeled by two cubic beam elements, are attached to the hub by revolute joints, called "lag hinges," that allow relative rotation of the blade with respect to the hub in the plane of rotation of the rotor and flexible root retention beams, each modeled as a single cubic beam element, connect the assemblies back to the hub.

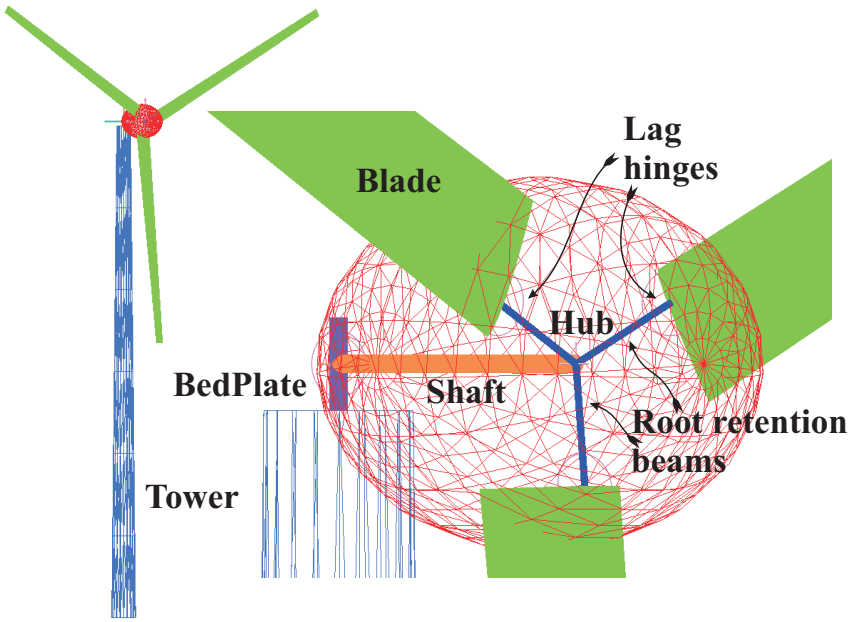

Figure 5.13: Schematic of the wind turbine problem.

As the angular speed of the rotor increases, an instability of a purely mechanical

origin is encountered in this periodic system. It is associated with a coupling between the motions of the blades in the plane of rotation of the rotor and lateral vibrations of the tower. If the blades are considered to be rigid bodies and the tower replaced by an equivalent spring-mass system, it is possible to find an analytical solution of the problem: the governing equations with periodic coefficients are transformed to a set of equations with constant coefficients using a Fourier transformation, and classical methods are then used to predict linearized stability. On the other hand, the multibody model was used to predict the dynamic response of the system for various rotor speeds. A small perturbation, in the form of a triangular impulsive moment (total duration: 0.05 sec; maximum amplitude 100 kN·m) acting at the lag hinge of the first blade, was used to excite the system. Its stability was then assessed using autoregressive method with a total of seven sensors: the two tip transverse deflections of the tower, the two root bending moments of the tower, and the three relative rotations at the lag hinges of blades.

The predicted damping in the system is shown in fig. 5.14: the unstable region extends from about 9.4 to 11.3 rad/sec rotor speed. For reference, the analytical solution obtained from the approximate, rigid body model is also shown in the figure; although the damping rates predicted by the two models are slightly different, as expected, the predicted instability boundaries are in close agreement. Two other simulations were performed by removing one and two of the lag hinge dampers, respectively; the results are also shown in fig. 5.14. It is interesting to note that the loss of one or two dampers does not significantly alter the stability characteristics of the system.

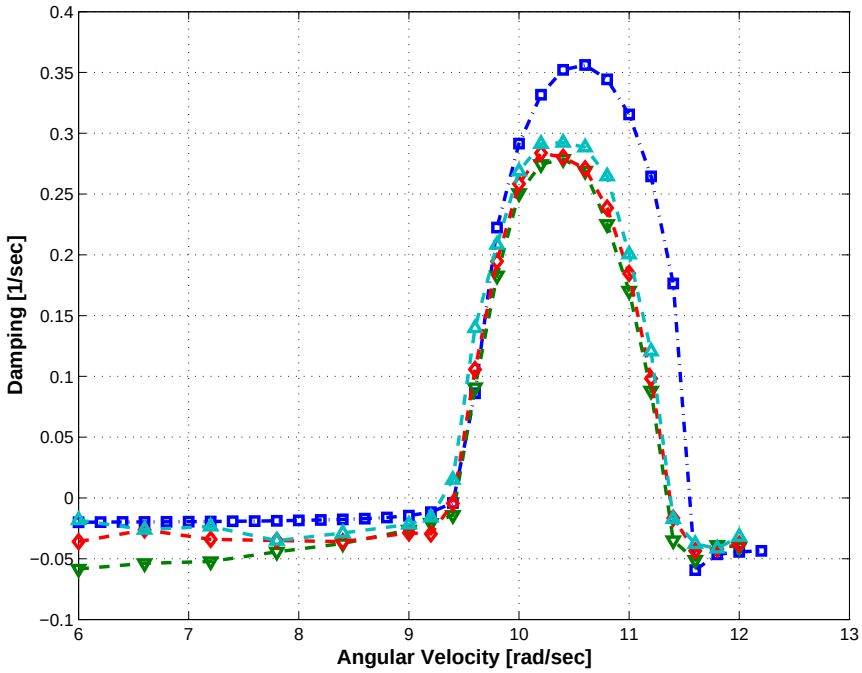

Figure 5.14: Dampings in the wind turbine problem as a function of rotor angular speed. Analytical solution (□); all three dampers active (▽); two dampers active only (◇); single damper active (△).

5.5 Stability Analysis of a Soft In-plane Tilt Rotor System

The example deals with a detailed analysis of a soft in-plane tilt rotor system [79] using a finite element based multibody dynamics code [9]. This multibody representation includes the rotor blades, pitch link, pitch horns, swash plate (rotating and non-rotating components), and hydraulic control actuators, see fig. 5.15, which are attached to an elastic wing through the pylon, see fig. 5.16. The rotor blades are modeled as elastic beams undergoing coupled flap, lag and torsion deformations.

Fig. 5.15 illustrates the key elements of the multibody model of the tilt rotor. The wing, rotor mast, and four blades are modeled as elastic beam elements featuring four parabolic, five cubic and one cubic element, respectively. The aerodynamic forces on rotor and wing are modeled using lifting line theory; rotor inflow is calculated with a three-dimensional nonlinear dynamic inflow model [87]. Aerodynamic interactions

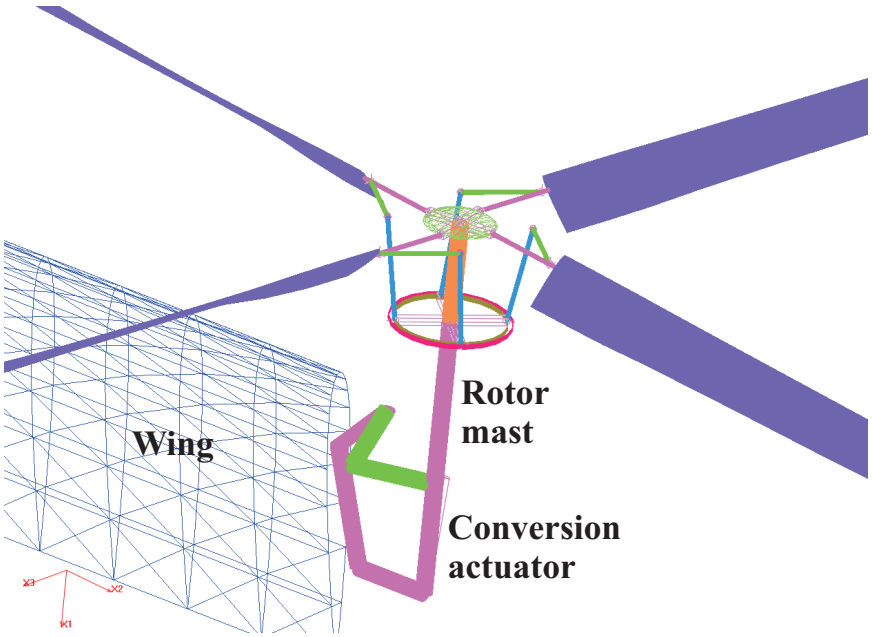

Figure 5.15: Multibody model of the soft in-plane tilt rotor system.

between the rotor and wing are ignored. The rotor hub, pitch links/horns, swash plates, and pylon are modeled as rigid bodies. The blade flap and lag hinges and torsion bearings are modeled as revolute joints; the stiffness and damping of the blade lag damper are included in the lag revolute joint element. The pylon conversion actuators are modeled as flexible joints, *i.e.* a set of concentrated springs and dampers. Two configurations of the tilt rotor in airplane mode were tested in the wind tunnel: the off-downstop configuration, which simulate the pylon conversion actuator stiffness and damping in conversion state, and the on-downstop configuration, which has higher actuator stiffness to simulate the "locked" state after conversion to airplane mode. It is important to model these two pylon conversion actuators accurately because they determine the wing chordwise/torsional mode frequency, and this mode is critical in tilt rotor aeroelastic stability.

The very complex system described above will be used to illustrate the proposed stability analysis tool in two manners. First, the *experimental measurements* will be processed to extract frequencies and damping rates using three different approaches.

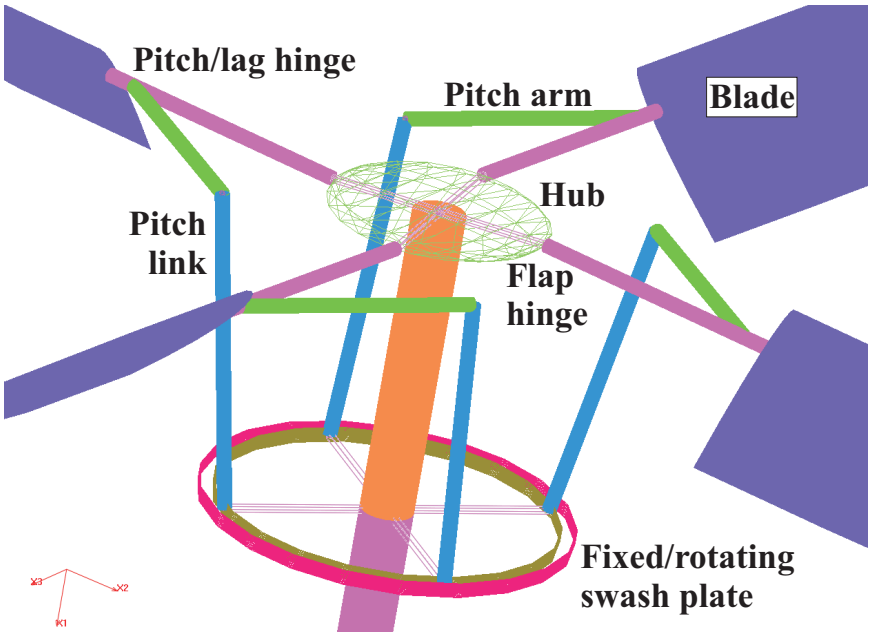

Figure 5.16: Multibody model of the soft in-plane tilt rotor system: detail of the hub.

Second, the dynamic response of the system will be predicted based on the multibody model described above. Autoregressive method will then be used to extract the frequencies and damping rates of the system from its *predicted response*; these predictions will then be compared with the experimental measurements.

Table 5.1: Frequencies, in rad/sec, (coefficient of variation, in %), extracted from experimental data using the moving block, autoregressive, and partial Floquet methods.

Experiment ID#	*Moving block*	*Autoregressive*	*Partial Floquet*
#4190	31.979 (0.49%)	32.080 (0.08%)	32.093 (0.10%)
#4191	32.139 (0.37%)	32.193 (0.11%)	32.267 (0.03%)
#4192	32.086 (0.21%)	32.108 (0.06%)	32.142 (0.04%)
#4193	32.014 (0.57%)	32.150 (0.15%)	32.128 (0.09%)
Mean Values	32.055	32.133	32.157
Coefficient of variation	0.22%	0.15%	0.24%

For nominal parameter values of 550 rpm rotor speed and 25 knot airspeed, four experiments, labeled #4190 to #4193, were run in the off-downstop configuration.

The system was excited during a short time with a shaker, and strain gauges were used to measure wing root bending moments upon completion of the excitation. This experimental signal will be used to extract frequencies and damping rates of the system using three approaches: the moving block, autoregressive and partial Floquet's methods. In each case, four window sizes were used to analyze the signal corresponding to 3/4, 4/5, 5/6 and 7/8 of the total experimental record.

Table 5.2: Damping rates, in %, (coefficient of variation, in %), extracted from experimental data using the moving block, autoregressive, and partial Floquet methods. Coefficients of variation are indicated in parentheses.

Experiment ID#	*Moving block*	*Autoregressive*	*Partial Floquet*
#4190	2.986 (1.65%)	3.070 (0.94%)	3.035 (1.03%)
#4191	3.064 (0.27%)	3.009 (1.88%)	3.006 (0.71%)
#4192	2.797 (1.11%)	2.805 (0.91%)	2.757 (1.88%)
#4193	2.956 (0.31%)	3.044 (1.00%)	3.013 (1.04%)
Mean Values	2.951	2.982	2.953
Coefficient of variation	3.79%	4.05%	4.45%

Table 5.1 lists the average frequencies and corresponding coefficients of variation extracted from this data using the three methods; system damping rates are listed in table 5.2. Note that smaller coefficients of variation were obtained when extracting frequencies with Prony's and partial Floquet methods than with the moving block approach. On the other hand, all three methods exhibit larger coefficients of variation when it comes to damping rates. This is due to the small amount of damping present in the system, of the order of 3%: a small amount of damping is inherently difficult to measure because it generates small amplitude differences from cycle to cycle that are obscured by experimental noise. For damping rates, the coefficient of variations computed based on the four nominally identical experiments are larger than those obtained for four windows of the same signal; this indicates that the experimental error is mainly due to the experimental set-up, rather than to the damping identification procedure. System characteristics identified by the three methods are in good

agreement with each other. This should be expected from Prony's and partial Floquet methods, since they are closely related to each other, as explained above. The moving block also performed satisfactorily because its main shortcomings [44, 23] did not affect its prediction for this particular experiment.

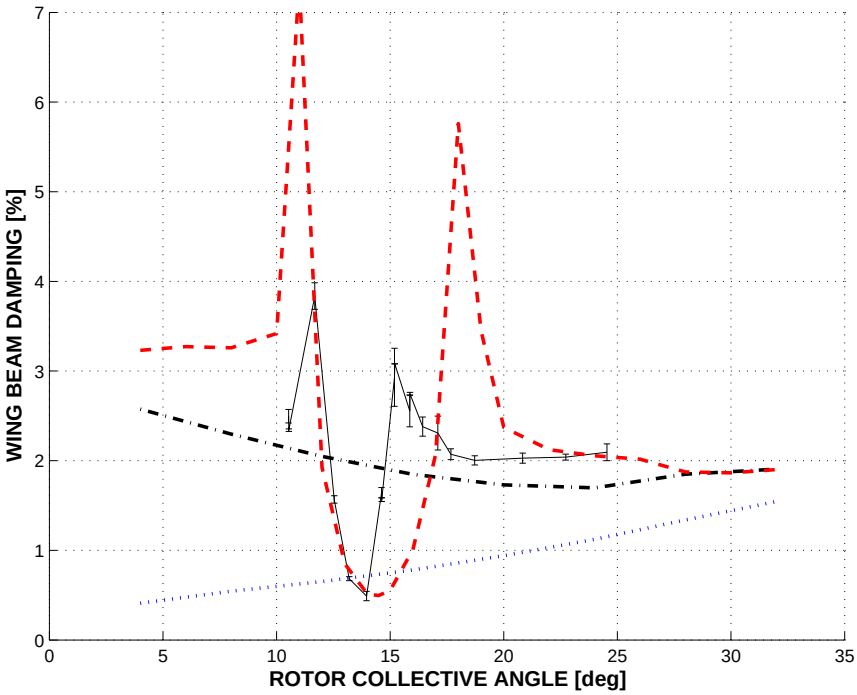

Figure 5.17: Wing beamwise dampings as a function of rotor collective angle; off-downstop configuration, 550 rpm rotor angular speed, 25 knot airspeed. Experimental measurements: solid line; *case 1*: dotted line; *case 2*: dashed-dotted line; *case 3*: dashed line.

During wind tunnel testing, the variation of wing beamwise damping in airplane-mode was investigated as a function of rotor torque, *i.e.* as a function of rotor collective angle. As shown in fig. 5.17, the test data exhibits dramatic nonlinear damping variations for rotor collective angles over the range of 10 to 15 degrees. For larger rotor collective angles, wing beamwise damping shows an expected, nearly linear increase with collective angle. In the same range of collective angles, rotor torque is known to be small, with a zero torque crossing, the so called "wind milling" case, at about 14 degrees. When rotor torque is slightly shifted from zero, in the

positive or negative directions, wing beamwise damping exhibits a sharp increase, or shoulder, well above the damping measured for larger rotor mast torque values. This nonlinear variation in wing beamwise damping for small rotor torque values may be attributed to the coupling of rotor, wing and drive train dynamics. Drive train free-play increases this coupling and renders it highly nonlinear. To prove this point, three models with different levels of fidelity were exercised, labeled *case 1* to *3*. *Case 1* ignored drive train dynamics, *i.e.* the rotor mast was modeled as a rigid body; *case 2* included an elastic rotor mast, modeled as a beam with a torsional stiffness that matches that of the drive train system; finally, in *case 3*, the rotor mast is connected to the hub by means of a revolute joint with backlash [14] featuring a ± 1 degree free-play angle.

Fig. 5.17 shows the predictions of the analysis for the three different models; in all cases, damping rates were extracted from the numerical predictions using Prony's method. The two models that ignore free-play do not capture the nonlinear relationship between collective angle and beamwise wing damping. On the other hand, with the inclusion of free-play, both lowest damping point (wind milling case) and the sharp increase in damping near the zero torque point are well captured by the model. It is interesting to note that the phenomenon under scrutiny in this example, intermittent contact due to free-play, is inherently nonlinear. On the other hand, all the methods for stability assessment presented in this work are derived based on the assumption of linearity of the system governing equations. Yet, the proposed methods performed well on both experimental and numerical signals. This is probably due to the ability of the proposed method to deal with signal noise: the nonlinear behavior is "filtered out" as if it were noise. This does not imply that autoregressive method will always adequately perform in the presence of nonlinearities, but rather that is can, in some cases, give good results.

5.6 Jeffcott Rotor with Isotropic Bearings

The Jeffcott rotor is composed of a flexible anisotropic shaft of length $L = 1$ m and of a mid-span rigid disk of mass $M = 5$ kg and radius $R = 0.18$ m, as shown in fig. 5.18. The shaft, modeled by six equally spaced cubic beam elements, is connected to end flexible couplings, represented by concentrated spring. The finite stiffness end bearings consist of revolute joints connected to the ground by concentrated springs. The relative rotation of the left hand side revolute joint was prescribed to be a constant angular velocity Ω.

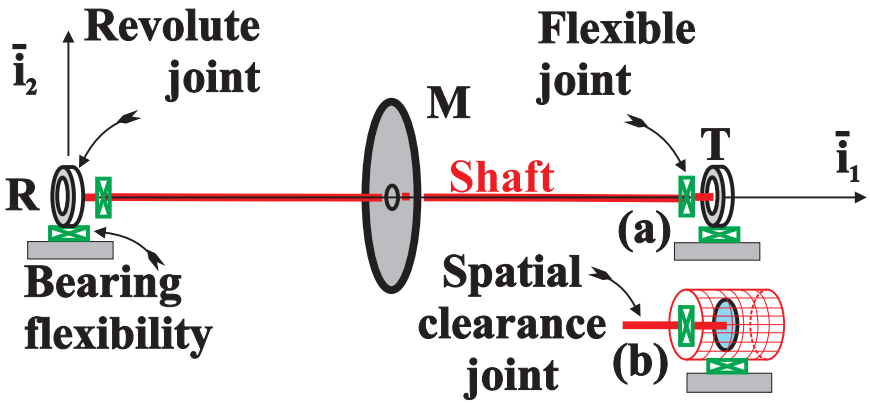

Figure 5.18: Jeffcott rotor with flexible anisotropic bearings.

The sectional properties of the shaft are as follows: bending stiffness, $EI_2 = 175$ and $EI_3 = 98.9$ N·m^2, mass per unit length $m_s = 0.00475$ kg/m, torsional stiffness $GJ = 71.9$ N·m^2, and polar moment inertial $I_\rho = 1.01\ 10^{-5}$ kg·m^2. The elastic couplings had very low axial stiffness $k_1^c = 10.0$ N/m and bending stiffness $c_2^c = c_3^c = 10.0$ N·m/rad but high transverse stiffness $k_2^c = k_3^c = 1.0\ 10^8$ N/m and torsional stiffness $c_1^c = 1.0\ 10^8$ N·m/rad; the elastic bearings have low transverse stiffness $k_2^b = k_3^b = 3.0\ 10^4$ N/m, high axial stiffness $k_1^b = 1.0\ 10^8$ N/m, and high bending stiffness $c_1^b = c_2^b = c_3^b = 1.0\ 10^8$ N·m/rad. Simulations were run for a total of 10 periods, $T = 2\pi/\Omega$, with a time step $\Delta t = 0.1$ msec, after application of an external perturbation along the $\bar{\imath}_3$ axis, $f_3 = 10\sin(20\pi t)$ for $t \in [0, 0.05]$ sec, to rigid disk.

For the stability analysis, the sampling period is $T/128$ sec and 3 proper orthogonal modes were used. System characteristics were extract from matrix $\hat{Q}$, see eq.(4.19).

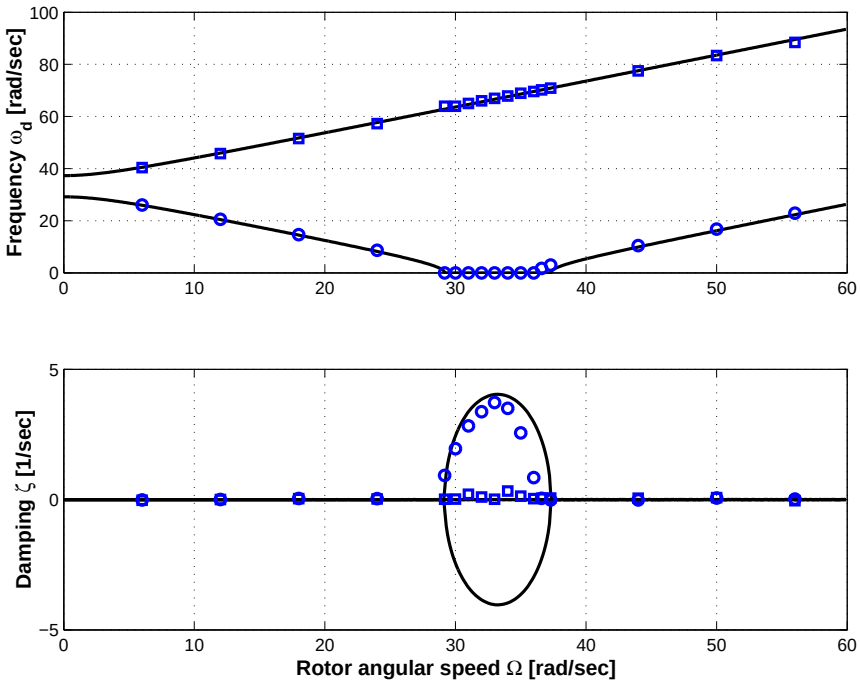

Figure 5.19: Frequencies and dampings of the two least-damped modes versus shaft angular velocity. No damping. Simplified modal solution: solid line; proposed approach: first mode, (○), second mode (□).

An simplified analytical solution of this problem was obtained based on classical modal reduction techniques. The bending flexibility of the shaft was taken into account, but its torsional flexibility was ignored. Furthermore, since the mid-span rigid disk is much more massive than the shaft, the inertial effects of the shaft were ignored. When the equations of motion for this simplified system are written in a rotating frame of reference, a set of constant coefficient equations results, and classical methods can be used to evaluate stability of the system. Figs. 5.19 compares the predictions of the simplified analytical model with those of the proposed approach. Due to the bending stiffness anisotropy of the shaft, the system is unstable for angular speeds between the two lowest bending frequencies of the shaft, *i.e.* for $29.2 < \Omega < 37.3$ rad/sec. Note the excellent agreement between the predictions of

the two approaches.

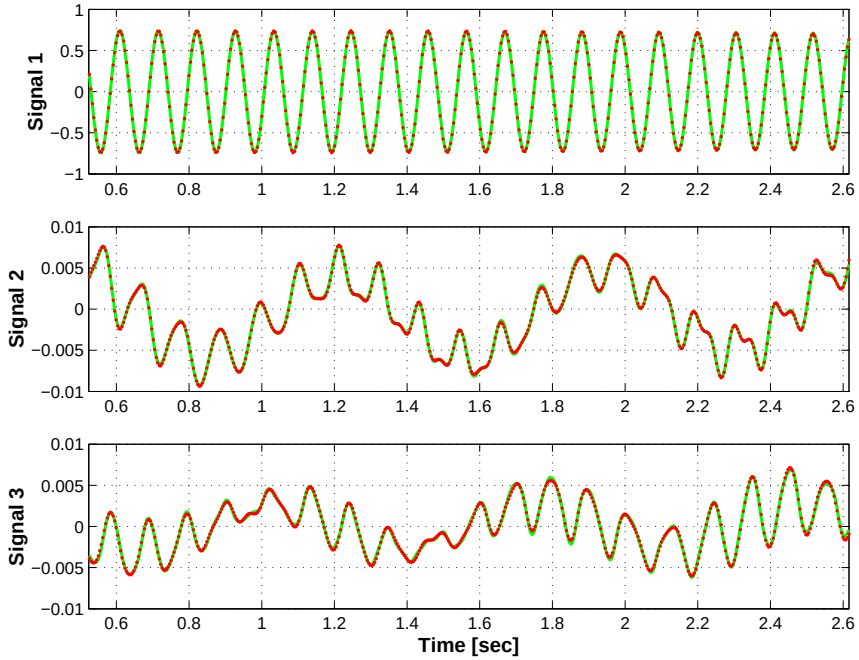

Figure 5.20: Curve fitting of three optimized signals. Original signals: dashed line; Reconstructed signals: solid line.

Figs. 5.20 shows the original and reconstructed signals for the three generalized signals corresponding to the three proper orthogonal modes selected for the stability analysis, at an angular speed $\Omega = 24$ rad/sec. The original and reconstructed are in a good agreement, $\epsilon = 3.99\ 10^{-4}$, $9.10\ 10^{-4}$ and $1.95\ 10^{-4}$ for the three signals, respectively, see eq. (4.55). Fig. 5.21 shows the coefficient of the Fourier transform of a_j associated with the frequency $\omega_j\sqrt{1-\zeta_j^2} = 8.643$ rad/sec extracted from two signals corresponding to the two transverse displacements of the rigid disk. The only non vanishing component of the Fourier transforms corresponds to $k = 1$; this means that the frequency of the system is $\omega_j\sqrt{1-\zeta_j^2} + \Omega$, removing the frequency indeterminacy.

Next, the effect of damping is investigated. Damping in the rotating system will be modeled by viscous forces proportional to the strain rates, $\underline{F}_d = \mu_s K_s \underline{\dot{e}}$, where μ_s is the damping coefficient, $\underline{e}$ the strain array, and K_s the beam cross-sectional stiffness

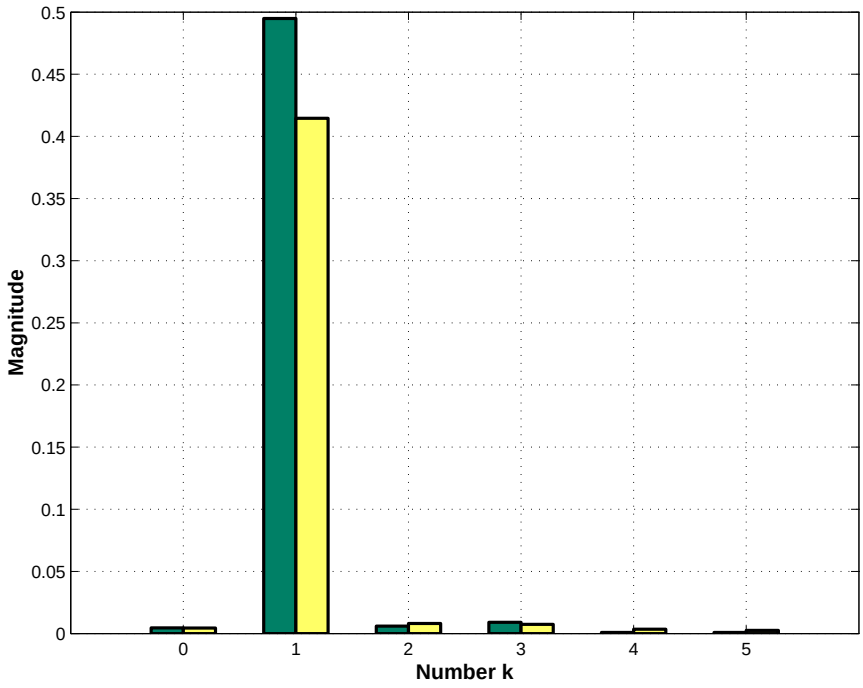

Figure 5.21: Magnitude of the Fourier coefficients of a_j for signals 1 and 2. Signal 1: deep color; signal 2: light color.

matrix. On the other hand, damping in the non-rotating system will be modeled by viscous dampers of constant μ_b in the bearing supports. Figs. 5.22 compares the predictions of the simplified analytical model and of the present approach, for damping parameters $\mu_s = 10^{-3}$ sec and $\mu_b = 3$ N·sec/m. For shaft speeds below the stability boundary, the two bending modes are now damped. The fixed and rotating system damping have a modest effect on the size of the unstable zone, $29.4 < \Omega < 37.0$ rad/sec, and do not stabilize the system at higher shaft speeds.

In a second set of simulations, the compliant bearing at the right hand side of the shaft was replaced by a spatial clearance element (SCE), see fig. 5.18(b), which models the clearance between the inner and outer races of a journal bearing, as described by Bauchau and Rodriguez [13]. Intermittent contact is allowed between a disk of radius 80 mm, representing the journal, and a cylinder, of radius 80.8 mm, representing the outer race of the bearing. When the two components are

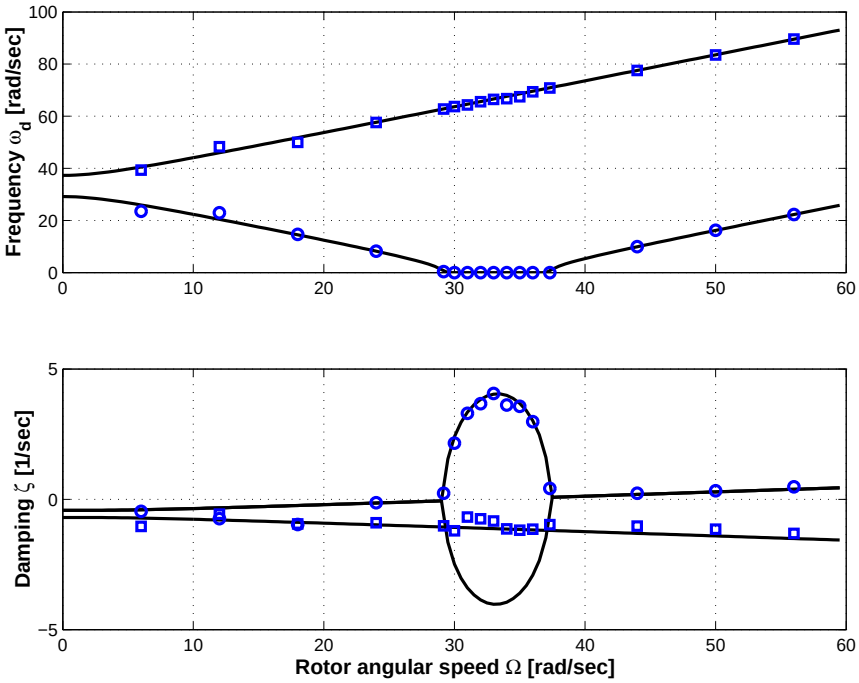

Figure 5.22: Frequencies and dampings of the two least-damped modes versus shaft angular velocity. Damping coefficients: $\mu_s = 10^{-3}$ sec and $\mu_b = 3$ N·sec/m. Simplified modal solution: solid line; proposed approach: first mode, (∘), second mode (□).

in contact, an elastic contact model is activated that consists of an elastic force, $F^e = 15\ a$ MN/m, where a is the approach between the inner and outer races, and of a dissipative force, $F^d = F^e \mu \dot{a}$, where the damping coefficient $\mu = 1.0\ 10^{-3}$ sec/m. Due to the intermittent nature of the contact between the inner and outer races, the problem presents severe nonlinearities, and a chaotic response. Clearly, an analytical solution of the problem would be difficult to obtain, and furthermore, any stability analysis approach based on linearization of the equation of motions would be unable to capture the effect of intermittent contact. Indeed, the linearization procedure could be performed about the contacting or non contacting state, but not for intermittent contact. When contact occurs, the modes of the system are those of a simply supported beam, but in the non contacting state, the modes are those of a simply supported-free beam.

Figs. 5.23 shows the frequency and damping of the lowest damped modes of the

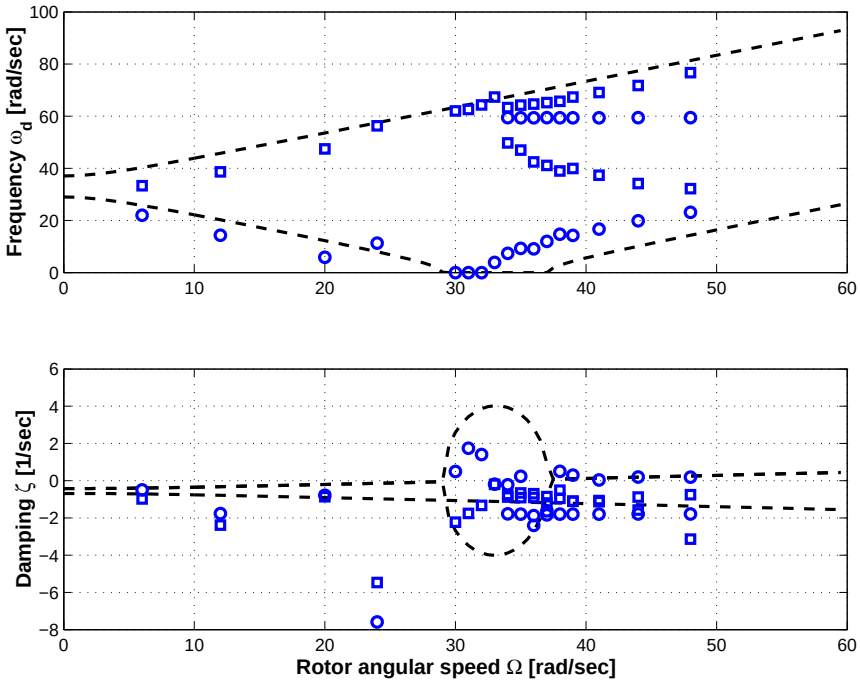

Figure 5.23: Frequencies and dampings of the least-damped modes versus shaft angular velocity. SCE and damping. Solid line: modal solution; symbols: proposed approach.

system. Since no analytical solution is available, the solution of the problem featuring two compliant bearings is presented in dotted lines, for reference. Clearly, the nonlinear behavior of the system greatly affects the stability characteristics of the system. Due to the additional modes of the system stemming from the varying boundary conditions at the spatial clearance joint, additional frequencies and associated dampings are identified for rotor speeds larger than 33 rad/sec. A larger scatter in the predictions is observed, due to the chaotic nature of the response. Note that strictly speaking, the proposed methodology does not apply to nonlinear systems since it is based on Floquet's theory. However, partial Floquet's or Prony's methods are routinely used to reduce experimental data, although they strictly apply to linear systems only. Clearly, the proposed approach closely follows the procedures used to reduce experimental data.

5.7 Aeroelastic Stability of Helicopter in Forward Flight

The last example deals with a detailed aeroelastic of the UH-60 rotor system shown in fig. 5.24. The description of the physical properties of the rotor can be found in ref. [22]. This problem involves both structural and aerodynamic states. The struc-

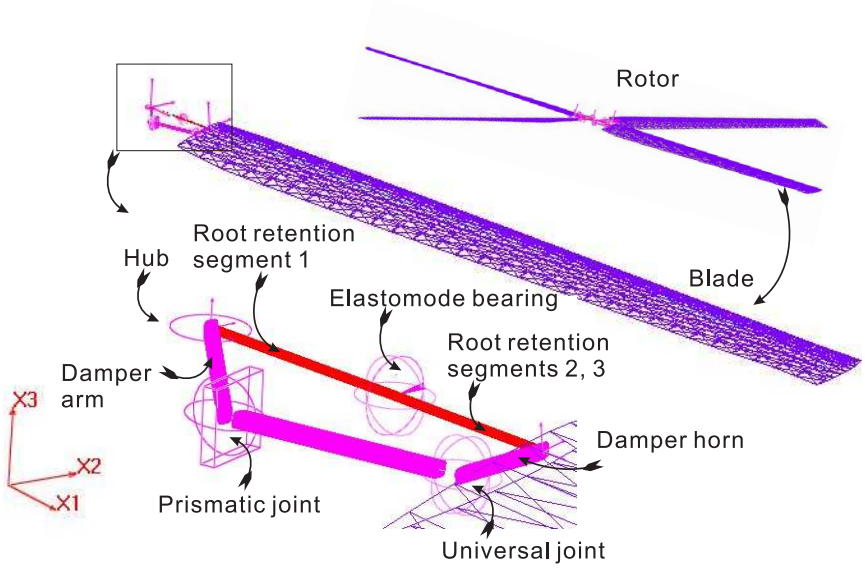

Figure 5.24: Schematic of the UH-60 rotor system.

tural model involves four blades connected to the hub through blade root retention structures and lead-lag dampers. Each blade was discretized by means of ten cubic finite elements using the finite element based multibody dynamics code described in ref. [9]. The root retention, connecting the hub to the blade, was separated into three segments and modeled by one, two and two beam elements, respectively, labeled segment 1, 2 and 3, respectively, in fig. 5.24. The flap, lead-lag and pitch hinges of the blade were described by three revolute joints connecting the first two segments of the root retention structures. Prismatic joints were used to model the lead-lag dampers, assumed to be dashpots with linear properties. The complete structural model involved 5,656 states.

The aerodynamic model combines thin airfoil theory with a three dimensional dynamic inflow model. The inflow velocities at each span-wise location were computed

using the finite state induced flow model developed by Peters *et al.* [89, 87]. The airfoil has a constant lift curve slope, $a_0 = 5.73$, drag coefficient, $c_d = 0.018$, and a vanishing moment coefficient about the quarter-chord. The number of inflow harmonics was selected as $m = 10$, corresponding to 66 aerodynamic inflow states for this problem. Airloads were computed at 81 equally spaced stations along the quarter-chord line of each blade.

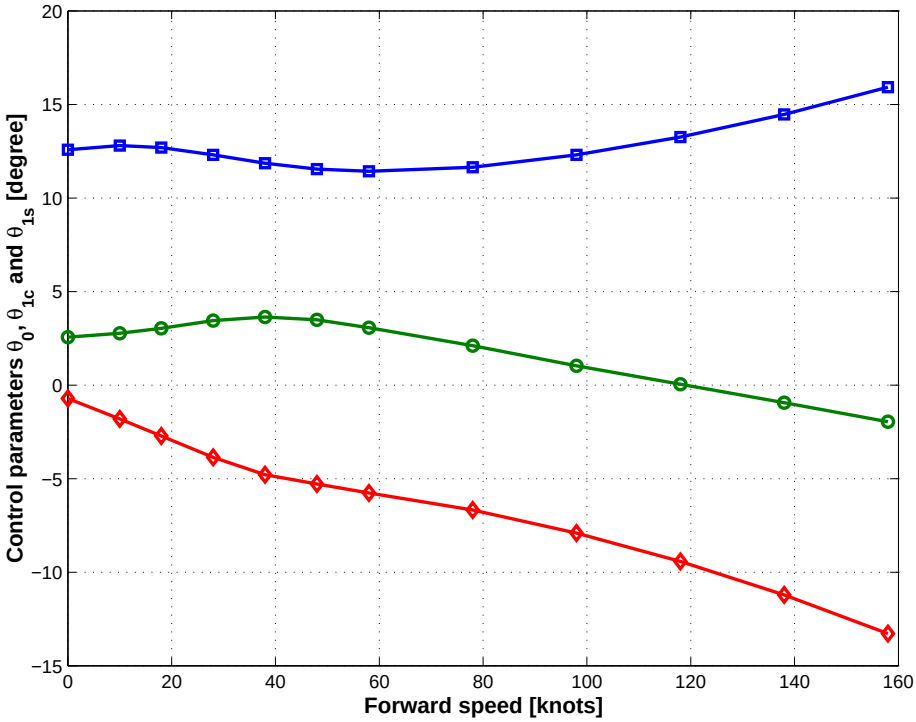

Figure 5.25: main rotor control parameters. collective θ_0:(□); lateral cyclic θ_{1c}:(○); longitudinal cyclic θ_{1s}:(◇).

Flight conditions from hover to forward flight at a speed of 158 knots were considered. An autopilot algorithm [78] was used to trim the helicopter at each speed. The constant thrust $T = 17944$ lb, and the rolling moment $M_1 = 6884$ lb·ft, the pitch moment $M_2 = -2583$ lb·ft are desired in details. The control parameters were determined and were shown in fig. 5.25. Next, the dynamic response of the rotor was computed for 15.0 sec using 128 time steps per revolution. The transverse deflection, lead-lag deflection and twist at the blade three-quarter span location and

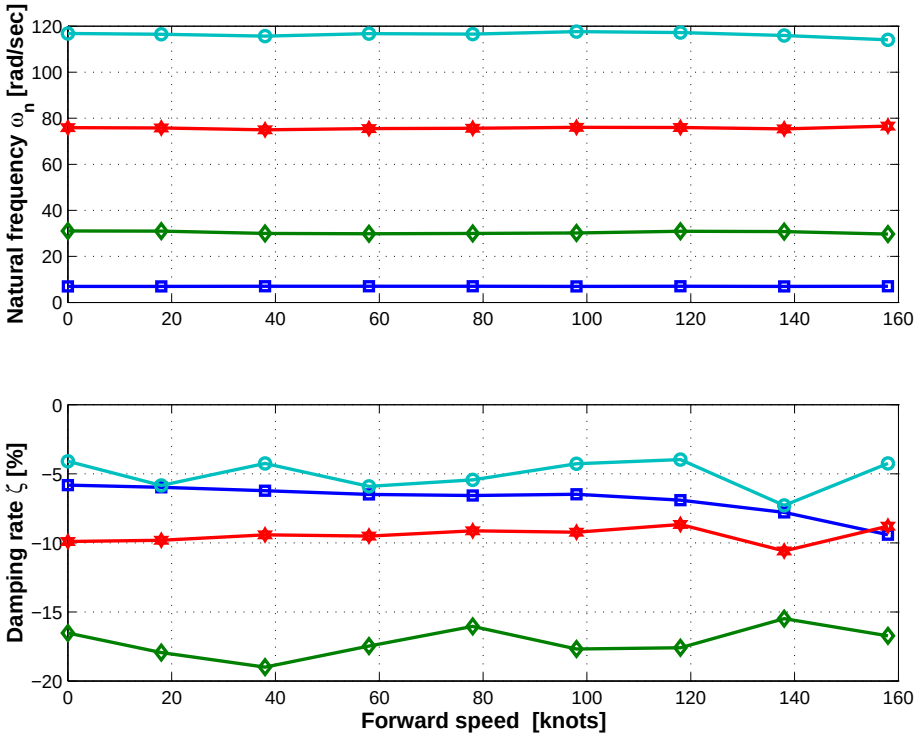

Figure 5.26: The frequencies and damping rates of the UH-60 rotor system. Lead-lag mode: (□); first flap mode: (◇); second flap mode: (⋆); torsion mode: (○).

the root flap angle were selected as input sensors; the sampling rate was 64 steps per revolution. A perturbation was then applied to the system in the form of an impulsive torsional moment of amplitude 1.0 10^4 lb·ft and duration of 0.02 sec applied at the tip of the blade. This impulse was applied to the system at time $t = 9.23$ sec. Measurements were obtained from the same sensors, and the differences between the perturbed and unperturbed measurements were selected as input signals for the stability analysis procedure with the time window $t \in [9.25, 15.0]$ sec. The proposed partial Floquet approach was applied to extract the frequencies and dampings of the system, which are shown in figs. 5.26. As expected, forward speed velocity has little effect on system frequencies, whereas damping level are more significantly affected. For the forward speed of 158 knots, the four original and reconstructed signals are shown in figs. 5.27; the rank of the Hankel matrix used in this case was

$r = 32$. Clearly, the original and reconstructed signals are in close agreement, implying the identified characteristic exponents are reliable estimates. For the results presented in figs. 5.27, the associated discrepancy indices, as defined by eq. (4.55), were $\epsilon = 6.4797\ 10^{-4}, 6.1800\ 10^{-4}, 7.2447\ 10^{-3}, 6.3253\ 10^{-4}$, respectively.

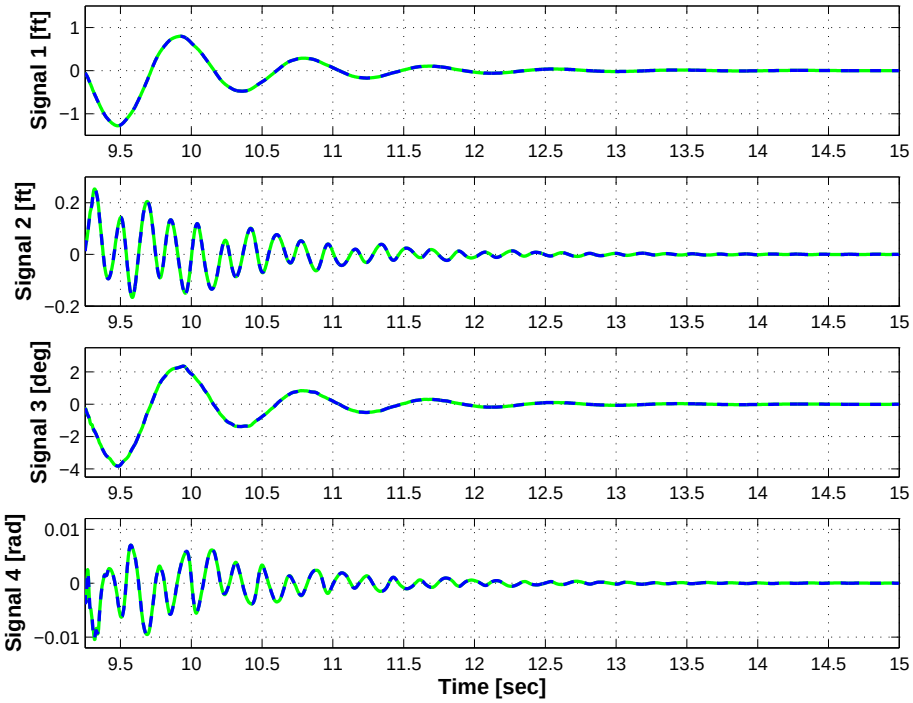

Figure 5.27: Signals 1, 2 and 3: blade three-quarter transverse deflection, lead-lag deflection and twist, respectively. Signal 4: blade root flap angle. Original signal: solid line; reconstructed signal: dashed line. Forward flight speed of 158 knots.

In an effort to improve the robustness of stability characteristic predictions, the proper orthogonal decomposition method was also exercised. The displacements of all degrees of freedom of one blade were used as input. The difference between the unperturbed and perturbed signals was used to drive the stability analysis procedure. Array T_0, defined by eq. (4.37), was constructed and the first six proper orthogonal modes were computed from the singular value decomposition of $\mathbb{T}$, see eq. (4.42), using Lanczos' algorithm. Focusing again on the case of forward flight speed at 158 knots, six optimized signals were extracted corresponding to the time histories of the six proper orthogonal modes associated with the highest energy content and used as

Table 5.3: Identified frequencies, ω_n [rad/sec], of rotor in forward flight at 158 knots. *Case 1*: four sensors are used as input signals; *case 2*: six proper orthogonal modes are used as inputs.

	Case 1: sensors				**Case 2**: P.O.M.			
Rank	Lead-lag	1^{st} Flap	2^{nd} Flap	Torsion	Lead-lag	1^{st} Flap	2^{nd} Flap	Torsion
12	7.06	29.97	73.97	111.91	7.00	30.13	75.75	115.79
18	7.08	29.69	75.32	116.58	7.08	29.87	76.66	113.51
24	7.04	29.65	76.19	113.40	7.00	29.60	75.85	113.56
32	7.11	29.63	75.85	113.09	7.02	29.45	76.76	113.28
40	7.09	29.54	76.43	113.71	7.02	29.62	77.14	114.32
48	7.07	29.56	77.04	113.64	7.01	29.63	77.46	114.25
60	7.09	29.58	76.91	112.81	7.01	29.58	76.40	113.89
mean	**7.08**	**29.66**	**75.96**	**113.59**	**7.02**	**29.70**	**76.58**	**114.08**
C.V.	**0.31%**	**0.46%**	**1.29%**	**1.18%**	**0.38%**	**0.71%**	**0.76%**	**0.69%**

inputs to the stability analysis algorithm with a time window $t \in [9.25, 15.0]$ sec. The frequencies and damping rates of the system were identified again based on these optimized signals. Table 5.3 compares the identified frequencies of the rotor system for two different cases: the first case, denoted *case 1*, uses the four sensors defined earlier, whereas the second case, denoted *case 2*, uses six optimized signals. Table 5.4 lists the corresponding damping rates. In both cases, system characteristics were identified for different rank numbers of the Hankel matrix, r = 12, 18, 24, 32, 40, 48 and 60. The last two lines in the tables list the means and coefficients of variation of the frequencies and damping rates identified with various rank numbers. System frequencies are equally well identified in both cases, whereas the use of the proper orthogonal modes and associated optimized signals clearly improves the robustness of the damping rate identifications. It should be noted here that the extracted stability characteristics remain nearly unchanged when Hankel matrix rank numbers are selected within a wide range, r = 12 to 60.

In the study presented thus far, lead-lag dampers were modeled as linear dashpots. Next, two types of nonlinear dampers will be investigated. First, the actual hydraulic

Table 5.4: Identified damping rates, ζ [%], of rotor in forward flight at 158 knots. *Case 1*: four sensors are used as input signals; *case 2*: six proper orthogonal modes are used as inputs.

	Case 1: sensors				**Case 2**: P.O.M.			
Rank	Lead-lag	1^{st} Flap	2^{nd} Flap	Torsion	Lead-lag	1^{st} Flap	2^{nd} Flap	Torsion
12	-9.18	-13.29	-7.13	-4.43	-9.40	-19.06	-9.12	-4.45
18	-9.14	-19.37	-9.12	-4.61	-8.78	-16.10	-8.16	-4.50
24	-9.47	-15.91	-8.07	-3.42	-9.52	-16.14	-8.57	-4.15
32	-9.07	-16.13	-9.01	-5.89	-9.61	-16.14	-8.60	-4.38
40	-9.14	-15.76	-8.23	-10.44	-9.49	-16.49	-8.24	-4.14
48	-9.19	-16.19	-8.04	-3.79	-9.59	-16.50	-8.89	-4.12
60	-9.15	-16.41	-8.32	-10.99	-9.51	-16.72	-9.99	-4.05
mean	**-9.19**	**-16.15**	**-8.27**	**-6.23**	**-9.41**	**-16.73**	**-8.80**	**-4.26**
C.V.	**-1.31%**	**-10.16%**	**-7.47%**	**-47.09%**	**-2.84%**	**-5.82%**	**-6.58%**	**-3.96%**

damper mounted on the UH-60 helicopter will be simulated using the modeling approach developed by Bauchau and Liu [10]. Second, a semi-active, Coulomb friction damper will be simulated using the modeling approach developed by Bauchau *et al.* [15]; in this case, it is possible to adjust the normal force at the frictional interface to modify to damping characteristics of the device. The damping rate of the lead-lag mode was identified for forward flight at 156 knots using two sensors measuring the lead-lag angle at the blade articulation and the stroke in the lead-lag damper.

Fig. 5.28 shows the identified damping rates as a function of the normal force at the frictional interface; the damping rate for the hydraulic damper is also shown. As expected, the damping rate of the semi-active friction damper increases as the normal force applied to the friction interface increases. The damping capability of the semi-active device matches, or even exceeds that of the hydraulic device for the higher normal force levels. In fig. 5.28, the average damping rates are reported, together with their maximum and minimum values when the Hankel matrix rank number took the following values: r = 12, 24, 36, 48, 60, 72, 84, 96, 108, 120. To verify the reliability of the identified system characteristics, the original and reconstructed damper stroke signals are compared in figs. 5.29, for different rank numbers of the

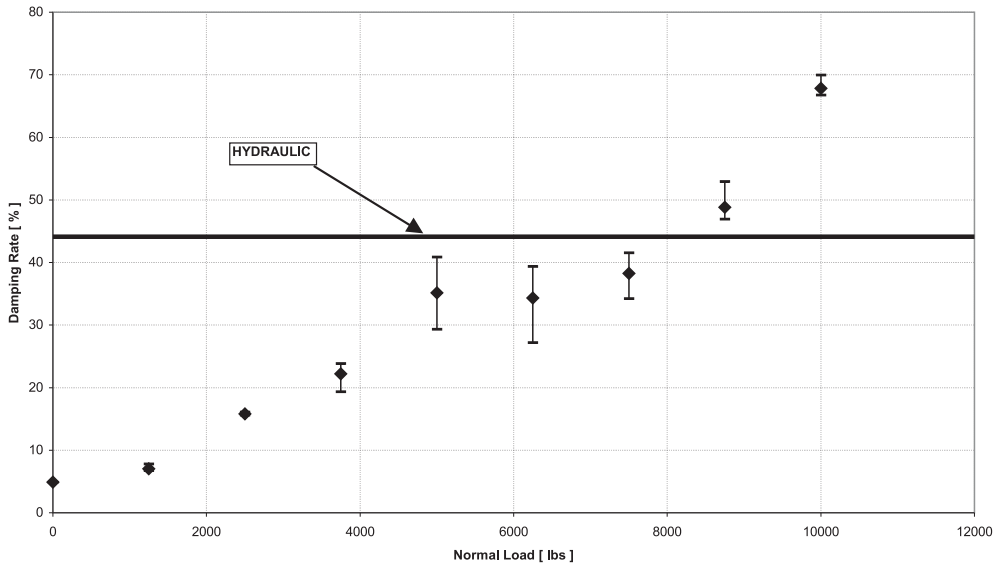

Figure 5.28: Damping rate of the lead-lag mode as a function of normal force at the friction interface of the semi-active Coulomb friction damper. The damping rate of the hydraulic damper is given for reference. Forward flight at 156 knots.

Hankel matrix, r = 12, 84 and 96, when the normal force at the friction interface is 7500 lbs. Significant discrepancies between the two signals are observed for the lower rank number, r = 12; using a higher rank number, r = 84, leads to better correlation, but further increase in rank number yields little improvement. This is probably due to the fact that the strongly nonlinear behavior of the friction damper affects the response of the system, while the algorithm used here to identify stability characteristics assumes linear behavior. In fact, the proposed approaches to stability analysis synthesize a best fit linear approximation of the observed nonlinear response of the system.

The significance of this example is that the proposed approach to stability analysis enables the approximate analysis of nonlinear systems. In fact, it closely mimics the process that would be used if system stability characteristics were to be experimentally measured. This contrasts with the classical approaches to stability analysis that require the linearization of the equations of motion as a starting point of the

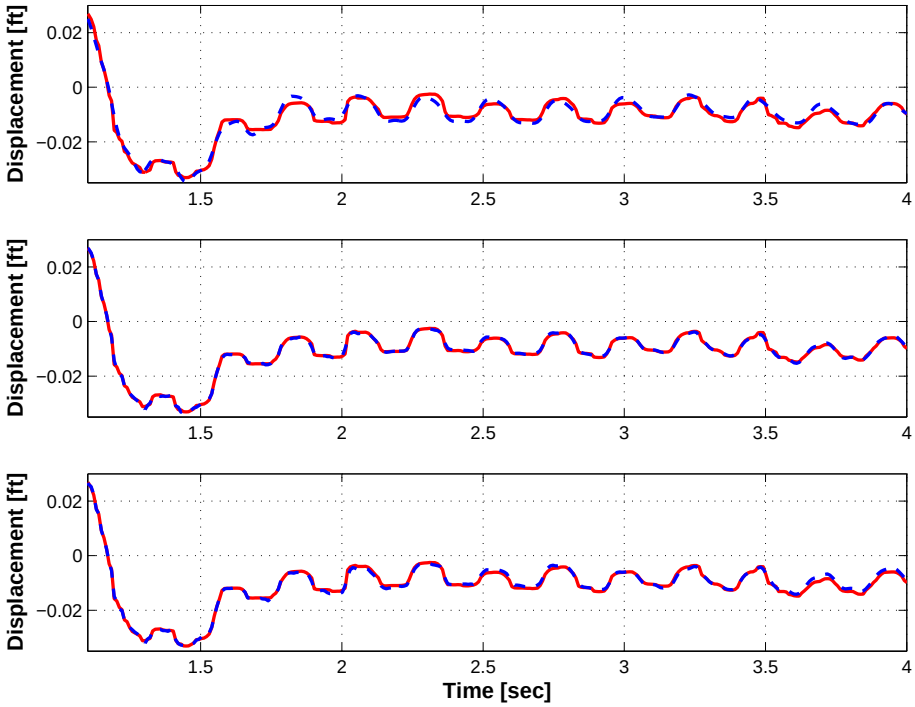

Figure 5.29: Signal synthesis of lead-lag damper stroke, friction damper for the normal force equal to 7500 lbs. For different rank number: $r = 12$, top figure; $r = 84$, middle figure; $r = 96$, bottom figure. Original signal: solid line; signal reconstruction: dashed line.

procedure. For the problem at hand, the linearization of either hydraulic or friction damper cannot be done in a meaningful manner, short of modeling either device as a linear dashpot.

CHAPTER VI

IDENTIFICATION METHODS FOR LINEAR SYSTEMS

This chapter focuses on the development of a modified minimum realization approach combining Kalman filter and least-square techniques, for the analysis of nonlinear, flexible multibody systems. The linearized realization is valid for small perturbations about an equilibrium configuration of the nonlinear systems. The goal of this work is to develop robust identification algorithms to construct the linearized plant models required for solving optimal control problems, the topics of next chapter. The starting point of the approach is the stability analysis methodology developed by Bauchau and Wang [16, 17], which determines the system frequencies and damping rates without computing the Markov parameters. A numerically stable mathematical tool, the singular value decomposition, is used to filter noise. A Kalman filter is used to minimize the effects of white noise on the identification process; the filter is computed by solving the associated discrete time algebraic Riccati equations directly. Both forward innovation model or deterministic model can be identified. The least squares technique is applied to compute the model dependency on external inputs. Furthermore, the proposed identification approach is combined with the proper orthogonal decomposition to provide additional noise filtering capability. Finally, the proper orthogonal decomposition creates optimized signals that can be used to construct subspace based plant models.

This chapter will introduce modal truncation and balanced truncation, both closely

associated with minimum realization, based on the concepts of observability and controllability. Hence, minimum realization methodologies are first reviewed; they include the observer/Kalman filter identification, the Ho-Kalman algorithm, the eigensystem realization algorithm and eigensystem realization algorithm with data correlation. Two accuracy indicators, the modal amplitude coherence and the mode singular value, are also defined. After a subspace identification approach based on oblique projection operations is introduced, the optimal procedure of Kalman filter is described in details. Then, a robust identification approach is proposed and its implementation is discussed in details. Finally, the numerical examples validate the proposed algorithm.

6.1 Truncation of Dynamical System

Due to increased computer power, numerical models of increasingly higher complexity have been constructed to capture the behavior of flexible nonlinear multibody systems and multi-physics problems. However, low dimensional models that accurately represent the behavior of dynamical systems are desirable for the solution of optimal control problems. Modal truncation [32] is usually applied to obtain a reduced order approximation of high dimensional systems. In this section, modal truncation and the balanced truncation are introduced.

6.1.1 Modal Truncation

Consider a state space transformation, $\underline{u}_k = \Psi \widetilde{u}_k$, where Ψ is a non-singular matrix of dimension $2N$. Substituting the state space transformation into eqs. (2.15), and solving for $\widetilde{u}_{k+1}$, the discrete time deterministic model becomes

$$\begin{cases} \widetilde{u}_{k+1} = (\Psi^{-1} A_s \Psi)\widetilde{u}_k + \Psi^{-1} B_s \underline{f}_k; \\ \underline{y}_k = C\Psi\widetilde{u}_k + D\underline{f}_k. \end{cases} \tag{6.1}$$

Transformation $\widetilde{A}_s = \Psi^{-1} A_s \Psi$, called a *similarity transformation* of matrix A_s, does clearly not affect the input-output behavior. This implies that the representation of a linear time-invariant model with specific input-output characteristics is not unique. This property is at the heart of system identification algorithms. Another important property is that the similarity transformation leaves the eigenvalues of exponential characteristic matrix A_s invariant.

As discussed in section 2.3.4, if Ψ stores the eigenvectors of matrix A_s, see eq. (2.38), matrix $\widetilde{A}_s$ will be the *Jordan form* of matrix A_s, which is a diagonal matrix, $\widetilde{A}_s = \exp(\Lambda \Delta t)$, containing the mode exponents of system, assuming that all eigenvalues are distinct. Using the notations $\widetilde{B}_s = \Psi^{-1} B_s$, $\widetilde{C}_s = C\Psi$ and $\widetilde{D}_s = D$, the *modal canonical state space form* is formulated

$$\begin{cases} \widetilde{u}_{k+1} = \widetilde{A}_s \widetilde{u}_k + \widetilde{B}_s \underline{f}_k; \\ \underline{y}_k = \widetilde{C}_s \widetilde{u}_k + \widetilde{D}_s \underline{f}_k. \end{cases} \tag{6.2}$$

Without loss of generality, the diagonal elements of $\widetilde{A}_s$ can be arranged in increasing order of their absolute value. The state vectors $\widetilde{u}_k$ are ordered accordingly and partitioned into two components as, $\widetilde{u}_k^T = \lfloor \hat{\underline{u}}_k^T \quad \check{\underline{u}}_k^T \rfloor$: the first entries, $\hat{\underline{u}}_k$, are associated with the lowest frequencies of the system, whereas the last entries, $\check{\underline{u}}_k$, corresponds to the highest frequencies. The system matrices are partitioned in a similar manner

$$\widetilde{A}_s = \begin{bmatrix} \hat{A}_s & 0 \\ 0 & \check{A}_s \end{bmatrix}, \quad \widetilde{B}_s = \begin{bmatrix} \hat{B}_s \\ \check{B}_s \end{bmatrix}, \quad \widetilde{C}_s = \begin{bmatrix} \hat{C}_s & \check{C}_s \end{bmatrix}. \tag{6.3}$$

If the dimension of $\hat{\underline{u}}_k$ is r, then the r^{th} order modal truncation of eqs. (6.2) defines a linear model in subspace

$$\begin{cases} \hat{\underline{u}}_{k+1} = \hat{A}_s \hat{\underline{u}}_k + \hat{B}_s \underline{f}_k; \\ \underline{y}_k = \hat{C}_s \hat{\underline{u}}_k + \widetilde{D}_s \underline{f}_k. \end{cases} \tag{6.4}$$

This truncation is usually called as *modal truncation*. The modes of the r^{th} order model, eqs. (6.4), form a subset of the modes of the original system, eqs. (2.15), and

remain invariant in this reduction procedure. This modal reduction is a foundation of the proposed stability evaluation approaches in subspace, eqs. (4.19) and (4.34), and proposed subspace identification algorithm. In particular, the r^{th} order truncation defines a stable system if the system, eqs. (2.15), is stable.

6.1.2 Balanced Truncation

Another popular procedure for model reduction is the balanced truncation [75, 67], which is a minimum realization of a system represented in balanced state space. This representation requires both *controllability Gramian* and *observability Gramian* to become diagonal and identical to each other. In a balanced realization, the state components are as well "observable" in the outputs as they are "excitable" from the inputs. In other words, the easy controllable state components will coincide with the easily observable state components; on the contrary, components that are difficult to control are also difficult to observe.

In this section, the definitions of *controllability matrix*, *observability matrix* and *Hankel matrix* will be introduced at first; then, the output signal energy is investigated to explore the physical properties of *controllability Gramian* and *observability Gramian*. Finally, the process to realize a balanced truncation is described.

A good starting point for the analysis of balanced truncation is to study how signal energy is transferred, because the concepts of both controllability and observability are closely associated with energy transfer. First, the energy transferred from the past inputs to the current states is investigated. Without loss of generality, assuming initial conditions are zero, $\underline{u}_0 = 0$, and substituting the external excitations $\underline{f}_i$, $i = 0, 1, 2, \ldots, k$, and $\underline{f}_i \neq 0$, into the first equation of linear model, eqs. (2.15), the forced state response at time step $k+1$ is represented by the following convolution

$$\underline{u}_{k+1} = B_s \underline{f}_k + A_s B_s \underline{f}_{k-1} + \ldots + A_s^{k-1} B_s \underline{f}_1 + A_s^k B_s \underline{f}_0, \tag{6.5}$$

or in a compact form

$$\underline{u}_{k+1} = \left[B_s, A_s B_s, \ldots, A_s^{k-1} B_s, A_s^k B_s\right] \left| \begin{array}{c} \underline{f}_k \\ \underline{f}_{k-1} \\ \vdots \\ \underline{f}_1 \\ \underline{f}_0 \end{array} \right| . \tag{6.6}$$

When k goes to infinite, the *controllability matrix* M_c is defined as

$$M_c = \left[B_s, A_s B_s, \ldots, A_s^{k-1} B_s, A_s^k B_s, \ldots\right] . \tag{6.7}$$

Second, the signal energy transferred from current states $\underline{u}_{k+1}$ to the future outputs is explored. If there are no external excitations, $f_{k+1} = 0$, the free impulse response is obtained from eqs. (2.15) as a regression process

$$\left| \begin{array}{c} \underline{y}_{k+1} \\ \underline{y}_{k+2} \\ \vdots \\ \underline{y}_{k+m} \end{array} \right| = \left[\begin{array}{c} C \\ CA_s \\ \vdots \\ CA_s^{m-1} \end{array} \right] \underline{u}_{k+1}, \tag{6.8}$$

where m is an arbitrary number. The *observability matrix*, M_o, is defined when m tends to infinity

$$M_o = \left[\begin{array}{c} C \\ CA_s \\ \vdots \\ CA_s^{m-1} \\ \vdots \end{array} \right] . \tag{6.9}$$

The properties of matrices M_c and M_o can be described as follow. A linear time-invariant system is controllable if it is possible to find a control sequence, $\underline{f}_k$, such that the origin can be reached from any initial state in finite time steps. For finite-dimensional system, a system is controllable if and only if the controllability matrix

M_c has rank $2N$, equal to the order of the system [53]. Furthermore, stabilizability of system answers that a system is stabilizable if the only uncontrollable states decay to the origin. The strict definition of stabilizability can be found in textbooks [32]. On the other hand, the system is completely observable if all states of system are observable. The finite-dimensional system is observable if and only if the rank of observability matrix M_o is equal to the order of the system. If the unobservable states decay to the origin, the system is detectable, which defines detectability of the system.

Third, the combination of eqs. (6.6) and (6.8) leads to the relationship between past inputs and future outputs

$$\begin{vmatrix} \underline{y}_{k+1} \\ \underline{y}_{k+2} \\ \vdots \\ \underline{y}_{k+m} \end{vmatrix} = \begin{bmatrix} CB_s & CA_sB_s & \dots & CA_s^kB_s \\ CA_sB_s & CA_s^2B_s & \dots & CA_s^{k+1}B_s \\ \vdots & \vdots & \ddots & \vdots \\ CA_s^{m-1}B_s & CA_s^mB_s & \dots & CA_s^{m+k-1}B_s \end{bmatrix} \begin{vmatrix} \underline{f}_k \\ \underline{f}_{k-1} \\ \vdots \\ \underline{f}_1 \\ \underline{f}_0 \end{vmatrix}. \tag{6.10}$$

Let $k = n - 1$, n an arbitrary integer; the following *output block Hankel matrix* of infinite dimension is now assembled

$$H_0 = \begin{bmatrix} CB_s & CA_sB_s & \dots & CA_s^{n-1}B_s & \dots \\ CA_sB_s & CA_s^2B_s & \dots & CA_s^nB_s & \dots \\ \vdots & \vdots & \ddots & \vdots & \dots \\ CA_s^{m-1}B_s & CA_s^mB_s & \dots & CA_s^{m+n-2}B_s & \dots \\ \vdots & \vdots & \vdots & \vdots & \ddots \end{bmatrix}. \tag{6.11}$$

In view of eqs. (6.6) and (6.8), it is readily verified that

$$H_0 = M_oM_c. \tag{6.12}$$

The stability evaluation procedure previously investigated in this thesis has demonstrated that this Hankel matrix contains valuable information about the stability

characteristics of the system. It will be shown in section 6.2.2 that this Hankel matrix can be directly assembled from the system free impulse response. Comparing the definitions of Hankel matrix, eq. (4.5) in pseudo space and (6.11) in block form, it can be concluded that when a single signal is used, eq. (6.11) is identical to eq. (4.5). When multiple signals are used, matrices, eqs. (4.20) and (6.11) are still identical, although rows and columns ordering are different.

Finally, the detailed analysis of the signal energy transferred from past inputs to future outputs will lead to the definitions of controllability and observability Gramians. With the help of following notations

$$\underline{y}_f = \begin{vmatrix} \underline{y}_{k+1} \\ \underline{y}_{k+2} \\ \vdots \end{vmatrix} \quad \text{and} \quad \underline{f}_p = \begin{vmatrix} \underline{f}_{k-1} \\ \underline{f}_{k-2} \\ \vdots \end{vmatrix}, \tag{6.13}$$

the total signal power of future outputs, p_t, defined as the summation of inner product of output sensors, can be expressed as a function of the past inputs as

$$p_t = \sum_{i=1}^{\infty} \underline{y}_{k+i}^T \underline{y}_{k+i} = \underline{y}_f^T \underline{y}_f = \underline{f}_p^T H_0^T H_0 \underline{f}_p. \tag{6.14}$$

The next step is to maximize the output power under the constraint of constant total input power, $\underline{f}_p^T \underline{f}_p = 1$. The method of Lagrangian multipliers is applied to solve this constrained optimization problem. This approach transforms the constrained problem into an unconstrained optimization formulated as

$$p_t(\underline{f}_p) = \underline{f}_p^T H_0^T H_0 \underline{f}_p + \lambda(1 - \underline{f}_p^T \underline{f}_p). \tag{6.15}$$

The maximum power is found by imposing the vanishing of the derivative of this expression

$$\frac{\partial p_t(\underline{f}_p)}{\partial \underline{f}_p} = 2H_0^T H_0 \underline{f}_p - 2\lambda \underline{f}_p = 0. \tag{6.16}$$

This leads to the following eigenvalue problem

$$H_0^T H_0 \underline{f}_p = \lambda \underline{f}_p, \tag{6.17}$$

where λ and $\underline{f}_p$ are eigenvalues and eigenvectors of matrix $H_0^T H_0$, respectively. Matrix $H_0^T H_0$ is known as the *snapshot matrix,* whereas matrix $H_0 H_0^T$ is called the *data correlation matrix.* If matrix H_0 is factorized with the help of the singular value decomposition, see Appendix A, as $H_0 = U\Sigma V^T$, the eigenvalue decomposition of snapshot matrix becomes $H_0^T H_0 = V\Sigma^2 V^T$, whereas the eigenvalue decomposition of data correlation is $H_0 H_0^T = U\Sigma^2 U^T$. Assuming the controllability matrix, M_c, to be nonsingular, pre- and post multiplication of the snapshot matrix, $H_0^T H_0$, by M_c and M_c^{-1}, respectively, leads to the following eigenproblem

$$M_c M_c^T M_o^T M_o = M_c V \ \Sigma^2 \ (M_c V)^{-1}, \tag{6.18}$$

where diagonal elements of Σ^2 are the eigenvalues, and $M_c V$ the eigenvectors. The matrix product, $M_c M_c^T M_o^T M_o$, consists of the product of two Gramians. The first is called the *"controllability Gramian"*

$$P_c = M_c M_c^T = \sum_{k=0}^{\infty} A_s^k B_s B_s^T A_s^{kT}, \tag{6.19}$$

the other is *"observability Gramian"*

$$P_o = M_o^T M_o = \sum_{k=0}^{\infty} A_s^{kT} C^T C A_s^k. \tag{6.20}$$

From these definitions, it is easily verified that both P_c and P_o satisfy the Lyapunov equations

$$\begin{cases} A_s P_c A_s^T - P_c = -B_s B_s^T; \\ A_s^T P_o A_s - P_o = -C^T C. \end{cases} \tag{6.21}$$

If the system matrices A_s, B_s and C are known, P_c and P_o can be found by solving the associated Lyapunov equations.

It now becomes possible to introduce the concept of the *balanced transformation* which is closely related to the controllability and observability Gramians, P_c and P_o, respectively. If a similarity transformation, $\widetilde{u}_{k+1} = \Psi \underline{u}_k$, exists, such that the

controllability and observability Gramians both become diagonal and identical each other

$$\widetilde{P}_c = \Psi^{-1} P_c \Psi^{-T} = \widetilde{P}_o = \Psi^T P_o \Psi = \Sigma = \text{diag}(\sigma_i), \tag{6.22}$$

the transformed state space model is said to be "balanced." The diagonal elements of Σ, σ_i, known as the *Hankel singular values*, are the singular values of the Hankel matrix H_0. If the dimension of Hankel matrix is $m \times n$, the singular values, σ_i, can be arranged in decreasing order: $\sigma_1 > \sigma_2 > \ldots > \sigma_n$, where σ_1 and σ_n are the maximum and minimum gains of the system, respectively. The largest singular value σ_1 is also called as the *Hankel norm* of the system. With this decreasing ordering, the state component of the system associated with σ_1 is both easy to observe and control, whereas state component associated with σ_n is both difficult to observe and control.

The name "balanced state space representation" has its root in the balance between controllability and observability of the states. In the balanced truncation, the elimination of the small singular values corresponds to the elimination of the states that are both difficult to observe and control. The process is a very similar approach to that of modal truncation discussed in section 6.1.1. The selection of a truncated similarity transformation matrix, Ψ, to construct a balanced state space model is not unique. The eigensystem realization algorithm, will be introduced in section 6.2.3 and gives a systematic process to construct similarity transformations that will lead to balanced representations of a minimum order.

6.2 The Minimum Realization

The process of constructing a state space representation from experimental data is called *system realization*, see Juang and Pappa [55]. Among all system realizations, the *minimum realization* reproduces input-output relationships within a specified degree of accuracy with a model of minimum dimension. Minimum realization algorithms, including the Ho-Kalman algorithm, the observer/Kalman filter identification,

and the eigensystem realization algorithm, have been developed and will be presented in this section. The complete procedure for minimum realization is summarized into following computational stages.

1. Calculate the observer Markov parameters and observer gain by observer/Kalman filter identification. Furthermore, evaluate the system Markov parameters.

2. Identify the state matrices, A_s, B_s, C and D of the linear time-invariant system, eqs. (2.15), by one of the following approaches: the Ho-Kalman algorithm, the eigensystem realization algorithm, or the eigensystem realization algorithm with data correlation.

3. Find the eigensolutions of identified exponential characteristic matrix, A_s, and compute the frequencies and damping rates using eqs. (2.40). Transform the identified model to *modal canonical state space form*.

4. Compute the accuracy indicators, the modal amplitude coherence and the mode singular values, to differentiate the actual system modes and those that result from noise. Finally, a reduced model is obtained through modal truncation.

This section will detail the four steps identified above. At first, the algorithms for observer/Kalman filter identification, for evaluation of the Markov parameters and observer gain are discussed. Second, minimum realization methodologies such as the Ho-Kalman algorithm, the eigensystem realization algorithm, and the eigensystem realization algorithm with data correlation, are investigated in details. Finally, two accuracy indicators, the modal amplitude coherence and mode singular values, are defined after the modal parameters are computed.

6.2.1 Observer/Kalman Filter Identification

Since most minimum realization algorithms require the knowledge of the system Markov parameters, evaluation of these parameters from the forced system response

is very important. In general, the Fourier transform, see Appendix B, is applied to the input-output data, and the associated inverse Fourier transform is used to compute the Markov parameters. But the shortcomings of this approach are apparent: first, the computational cost is heavy, because the Fourier transform requires long time history of input-output data; second, it is sensitive to numerical ill-conditioning which is often the case in system identification. Consequently, inaccurate Markov parameters are often obtained. A better approach is the observer/Kalman filter identification [53, 73] and its modifications [54]. Observer/Kalman filter identification computes the system Markov parameters from the forced response of system by introducing an "observer."

If the external excitations, $\underline{f}_k$, do not vanish for $k = 0, 1, 2, \ldots$, substitution of the first equation of the linear system, eqs. (2.15), into the second leads to a backward regression for the outputs, $\underline{y}_k$, which can be written as a convolution

$$\underline{y}_k = CA_s^k \underline{u}_0 + \sum_{j=0}^{k-1} CA_s^{k-1-j} B_s \underline{f}_j + D\underline{f}_k. \tag{6.23}$$

Without loss of generality, the initial conditions are select as zero, $\underline{u}_0 = 0$. The outputs, $\underline{y}_k$, for $k = 0, 1, \ldots, m+n-1$, are then recast in a matrix form, $Y = M_p F$, where matrix $M_p \in \mathbb{R}^{N_s \times N_c(m+n)}$ contains the *system Markov parameters*, a sequence of measured output of free impulse responses, $M_p = [D,\ CB_s,\ CA_sB_s,\ \ldots,\ CA_s^{m+n-2}B_s]$. Matrix $Y \in \mathbb{R}^{N_s \times (m+n)}$ and upper triangular matrix $F \in \mathbb{R}^{N_c(m+n)\times(m+n)}$ collect the input and output data, respectively,

$$Y = \left[\underline{y}_0, \underline{y}_1, \underline{y}_2, \ldots, \underline{y}_{m+n-1}\right] \quad \text{and} \quad F = \begin{bmatrix} \underline{f}_0 & \underline{f}_1 & \underline{f}_2 & \cdots & \underline{f}_{m+n-1} \\ & \underline{f}_0 & \underline{f}_1 & \cdots & \underline{f}_{m+n-2} \\ & & \underline{f}_0 & \ddots & \vdots \\ & & & \ddots & \underline{f}_1 \\ & & & & \underline{f}_0 \end{bmatrix}. \tag{6.24}$$

In the case of multi-inputs systems, $N_c > 1$, the number of unknown Markov parameters, $N_s \times N_c(m+n)$, is much larger than the number of equations, $N_s \times (m+n)$. Hence, the system Markov parameters will not be unique, which is contrary to the fact that M_p must be uniquely determined for a finite-dimensional linear system. Even in the case of single input systems, $N_c = 1$, if the external excitations have zero initial values, matrix F will become ill-conditioned, and the system Markov parameters, $M_p = YF^{-1}$, still cannot be accurately computed. An approximate solution for the Markov parameters can only be found when the system is asymptotically stable, $A_s^k \approx 0$ for $k \geq r$, when r is sufficiently large. The outputs, Y, can be represented approximately, $Y \simeq \hat{M}_p \hat{F}$, where the truncated matrix, $\hat{M}_{p(N_s \times N_c r)}$, is defined as

$$\hat{M}_p = \left[D, CB_s, CA_sB_s, \ldots, CA_s^{r-1}B_s \right], \tag{6.25}$$

and $\hat{F}_{N_c r \times (m+n)}$ as

$$\hat{F} = \begin{bmatrix} \underline{f}_0 & \underline{f}_1 & \underline{f}_2 & \cdots & \underline{f}_{r-1} & \cdots & \underline{f}_{m+n-1} \\ & \underline{f}_0 & \underline{f}_1 & \cdots & \underline{f}_{r-2} & \cdots & \underline{f}_{m+n-2} \\ & & \underline{f}_0 & \ddots & \vdots & \vdots & \vdots \\ & & & \ddots & \underline{f}_1 & \cdots & \underline{f}_{m+n-r} \\ & & & & \underline{f}_0 & \cdots & \underline{f}_{m+n-1-r} \end{bmatrix}. \tag{6.26}$$

The truncated system Markov parameters, $\hat{M}_p$, will be solved from a redundant set of equations, $Y \simeq \hat{M}_p \hat{F}$, using the least-square regression as, $\hat{M}_p \simeq Y\hat{F}^T(\hat{F}\hat{F}^T)^{-1}$.

When the least-square regression is used to compute the Markov parameters of unstable or lightly damped system, artificial damping is added to stabilize the system. Introducing an unknown gain matrix G_d into the linear model, eqs. (2.15), the first equation becomes

$$\underline{u}_{k+1} = A_s\underline{u}_k + B_s\underline{f}_k + G_d(\underline{y}_k - \underline{y}_k) = (A_s + G_dC)\underline{u}_k + (B_s + G_dD)\underline{f}_k - G_d\underline{y}_k, \tag{6.27}$$

or, in a compact form, $\underline{u}_{k+1} = \bar{A}_s \underline{u}_k + \bar{B}_s \bar{\underline{f}}_k$, where

$$\bar{A}_s = (A_s + G_d C), \quad \bar{B}_s = [(B_s + G_d D), -G_d] \quad \text{and} \quad \bar{\underline{f}}_k = \begin{vmatrix} \underline{f}_k \\ \underline{y}_k \end{vmatrix}. \tag{6.28}$$

The output convolution is now rewritten as

$$\underline{y}_k = C\bar{A}_s^k \underline{u}_0 + \sum_{j=0}^{k-1} C\bar{A}_s^{k-1-j} \bar{B}_s \bar{\underline{f}}_j + D\underline{f}_k. \tag{6.29}$$

When r is pre-determined to satisfy the conditions for asymptotic stability, $\bar{A}_s^k \approx 0$ for $k \geq r$, the truncated matrix form of eq. (6.29) is represented as $Y \simeq \bar{M}_p \bar{F}$, where the *observer Markov parameters*, $\bar{M}_p$, a sequence of observed output data, is defined

$$\bar{M}_p = \left[D, C\bar{B}_s, C\bar{A}_s\bar{B}_s, \ldots, C\bar{A}_s^{r-1}\bar{B}_s \right], \tag{6.30}$$

and matrix, $\bar{F}$, as

$$\bar{F} = \begin{bmatrix} \underline{f}_0 & \underline{f}_1 & \underline{f}_2 & \cdots & \underline{f}_{r-1} & \cdots & \underline{f}_{m+n-1} \\ & \bar{\underline{f}}_0 & \bar{\underline{f}}_1 & \cdots & \bar{\underline{f}}_{r-2} & \cdots & \bar{\underline{f}}_{m+n-2} \\ & & \bar{\underline{f}}_0 & \ddots & \vdots & \vdots & \vdots \\ & & & \ddots & \bar{\underline{f}}_1 & \cdots & \bar{\underline{f}}_{m+n-r} \\ & & & & \bar{\underline{f}}_0 & \cdots & \bar{\underline{f}}_{m+n-1-r} \end{bmatrix}, \tag{6.31}$$

and the observer Markov parameters, $\bar{M}_p$, are computed by least-square regression. Alternatively, instead of truncating the controller inputs, $\bar{\underline{f}}_k$, $\bar{M}_p$ can be computed by the truncation of current outputs, $\underline{y}_k$. The alternative formulation of outputs convolution at time steps, $k + r$, is presented

$$\underline{y}_{k+r} = C\bar{A}_s^r \underline{u}_k + \sum_{j=0}^{r-1} C\bar{A}_s^{r-1-j} \bar{B}_s \bar{\underline{f}}_{k+j} + D\underline{f}_{k+r}, \tag{6.32}$$

and rewritten in the matrix form, $\bar{Y} = C\bar{A}_s^r \bar{U} + \bar{M}_p \bar{F}_0$, where the output array, $\bar{Y}$, and state array, $\bar{U}$, are assembled

$$\bar{Y} = \left[\underline{y}_r, \underline{y}_{r+1}, \ldots, \underline{y}_{m+n-1} \right], \quad \bar{U} = \left[\underline{u}_0, \underline{u}_1, \ldots, \underline{u}_{m+n-r-1} \right], \tag{6.33}$$

and $\bar{F}_0$ is cast as

$$\bar{F}_0 = \begin{bmatrix} \underline{f}_{r-1} & \underline{f}_r & \cdots & \underline{f}_{m+n-1} \\ \underline{\bar{f}}_{r-2} & \underline{\bar{f}}_{r-1} & \cdots & \underline{\bar{f}}_{m+n-2} \\ \vdots & \vdots & \ddots & \vdots \\ \underline{\bar{f}}_0 & \underline{\bar{f}}_1 & \cdots & \underline{\bar{f}}_{m+n-1-r} \end{bmatrix}. \tag{6.34}$$

The conditions for asymptotic stability, $\bar{A}_s^r \approx 0$, are applied again to find, $\bar{Y} \simeq \bar{M}_p \bar{F}_0$.

In summary, the observer Markov parameters, $\bar{M}_p$, can be approximated by the following two least-square regressions

$$\bar{M}_p \simeq Y\bar{F}^T(\bar{F}\bar{F}^T)^+ \quad \text{or} \quad \bar{M}_p \simeq \bar{Y}\bar{F}_0^T(\bar{F}_0\bar{F}_0^T)^+. \tag{6.35}$$

The observer Markov parameters, $\bar{M}_p$, consist of system Markov parameters, $\hat{M}_p$, and observer gain, G_d, see eq. (6.30). Once the observer Markov parameters are evaluated, $\hat{M}_p$ and G_d can be computed from $\bar{M}_p$. For this purpose, the observer and system Markov parameters both need to be partitioned

$$\bar{M}_p = \left[\bar{Y}_0, \bar{Y}_1, \ldots, \bar{Y}_r\right] \quad \text{and} \quad \hat{M}_p = \left[Y_0, Y_1, \ldots, Y_r\right], \tag{6.36}$$

such that, $\bar{Y}_0 = Y_0 = D$, $\bar{Y}_k = C\bar{A}_s^{k-1}\bar{B}_s$, and $Y_k = CA_s^{k-1}B_s$ for $k = 1, 2, \ldots, r$. Matrix D is already determined, and matrix Y_k will be computed from $\bar{Y}_k$. With the help of definition of matrix $\bar{B}_s$, see eqs. (6.28), a partition of $\bar{Y}_k$ is written as

$$\bar{Y}_k = C\bar{A}_s^{k-1}\bar{B}_s = \left[C\bar{A}_s^{k-1}\left(B_s + G_d D\right), -C\bar{A}_s^{k-1}G_d\right] = \left[\bar{Y}_k^{(1)}, -\bar{Y}_k^{(2)}\right],$$

where $\bar{Y}_k^{(1)} = C\bar{A}_s^{k-1}\left(B_s + G_d D\right)$, and $\bar{Y}_k^{(2)} = C\bar{A}_s^{k-1}G_d$. The relationship of Y_k, $\bar{Y}_k^{(1)}$ and $\bar{Y}_k^{(2)}$ is found to be

$$\begin{bmatrix} I & & & & \\ \bar{Y}_1^{(2)} & & & & \\ \bar{Y}_2^{(2)} & \bar{Y}_1^{(2)} & I & & \\ \vdots & \vdots & \vdots & \ddots & \\ \bar{Y}_{r-1}^{(2)} & \bar{Y}_{r-2}^{(2)} & \bar{Y}_{r-3}^{(2)} & \ldots & I \end{bmatrix} \begin{bmatrix} Y_1 \\ Y_2 \\ Y_3 \\ \vdots \\ Y_r \end{bmatrix} = \begin{bmatrix} \bar{Y}_1^{(1)} - \bar{Y}_1^{(2)}D \\ \bar{Y}_2^{(1)} - \bar{Y}_2^{(2)}D \\ \bar{Y}_3^{(1)} - \bar{Y}_3^{(2)}D \\ \vdots \\ \bar{Y}_r^{(1)} - \bar{Y}_r^{(2)}D \end{bmatrix}. \tag{6.37}$$

The unknowns of system Markov parameters, Y_k, can be solved from this set of linear equations since parameters $\bar{Y}_k^{(1)}$, $\bar{Y}_k^{(2)}$, and D are already determined. Consequently, the minimum realization algorithms are applied to identify the system state matrices A_s, B_s and C, the entire procedure will be summarized in following section. Finally, the unknowns of observer gain G_d will be evaluated from $\bar{Y}_k^{(2)}$. For $k = 1, 2, \ldots, r$, a data sequence is defined, $Y_k^{(0)} = CA_s^{k-1}G_d$. With the help of definition of observability matrix, M_o, eq. (6.9), $Y_k^{(0)}$ can be written as a function of G_d; in matrix form, it will be

$$\begin{bmatrix} Y_1^{(0)} \\ Y_2^{(0)} \\ \vdots \\ Y_r^{(0)} \end{bmatrix} = \begin{bmatrix} C \\ CA_s \\ \vdots \\ CA_s^{r-1} \end{bmatrix} G_d = M_o G_d. \tag{6.38}$$

Furthermore, $Y_k^{(0)}$ and $\bar{Y}_k^{(2)}$ must satisfy the following linear equations

$$\begin{bmatrix} I & & & & \\ \bar{Y}_1^{(2)} & & & & \\ \bar{Y}_2^{(2)} & \bar{Y}_1^{(2)} & I & & \\ \vdots & \vdots & \vdots & \ddots & \\ \bar{Y}_{r-1}^{(2)} & \bar{Y}_{r-2}^{(2)} & \bar{Y}_{r-3}^{(2)} & \ldots & I \end{bmatrix} \begin{bmatrix} Y_1^{(0)} \\ Y_2^{(0)} \\ Y_3^{(0)} \\ \vdots \\ Y_r^{(0)} \end{bmatrix} = \begin{bmatrix} \bar{Y}_1^{(2)} \\ \bar{Y}_2^{(2)} \\ \bar{Y}_3^{(2)} \\ \vdots \\ \bar{Y}_r^{(2)} \end{bmatrix}, \tag{6.39}$$

which allow the evaluation of $Y_k^{(0)}$. If A_s and C have already been identified using the minimum realization algorithms, G_d can be approximated from eq. (6.38) using the least-square regression

$$G_d = \left(M_o^T M_o\right)^{-1} M_o^T \begin{bmatrix} Y_1^{(0)} \\ Y_2^{(0)} \\ \vdots \\ Y_r^{(0)} \end{bmatrix}. \tag{6.40}$$

As a starting point, the conditions for asymptotic stability, $\bar{A}_s^k \approx 0$ for $k \geq r$, have been used when computing the observer and system Markov parameters, where r is

pre-determined number. First, if r is small, $\bar{A}_s$ should be heavily artificial damped by introducing matrix, G_d, to satisfy the asymptotically stable conditions; on the other hand, if r is large, $\bar{A}_s$ may be lightly artificial damped. In this sense, the gain matrix, G_d, will not be unique and will be determined by r. Second, Juang [53] proved the observer gain G_d produces the same input-output map as a Kalman filter gain matrix, K, does, and $K = -G_d$. Finally, the computation of Markov parameters by observer/Kalman filter identification remains complex and determines the accuracy of minimum realizations. If a poor approximation of Markov parameters is obtained, the system identification might be meaningless.

6.2.2 Ho-Kalman Algorithm

The seminal work of Kalman [46] contributed to the development of minimum realization theory. A state space approach is provided by the Ho-Kalman algorithm, and a minimum realization is obtained from system Markov parameters. If a set of control inputs, $f_k^b \in \mathbb{R}^{N_c \times N_c}$, is applied to the system, $f_0^b = I$ and $f_k^b = 0$ for $k = 1, 2, \ldots$, where I the identity matrix, and N_c the number of control inputs, the free impulse response of linear system, eqs. (2.15), is obtained as

$$y_k^b = \left[\underline{y}_k^{(1)}, \underline{y}_k^{(2)}, \ldots, \underline{y}_k^{(N_c)}\right] = \begin{cases} D, \text{ for } k = 0; \\ CA_s^{k-1}B_s, \text{ for } k = 1, 2, \ldots, \end{cases} \tag{6.41}$$

and the system Markov parameters, $\hat{M}_p$, eq. (6.25), will be directly written as

$$\hat{M}_p = \left[y_0^b, y_1^b, y_2^b, \ldots, y_k^b\right]. \tag{6.42}$$

This simple approach yields the system Markov parameters without applying the observer/Kalman filter identification. Consequently, the Ho-Kalman algorithm will identify the system state matrices, A_s, B_s and C, for a deterministic system, eqs. (2.15), using the system Markov parameters. From the definition of free impulse response, eq. (6.41), the finite-dimensional output block Hankel matrix, $H_0 \in \mathbb{R}^{mN_s \times nN_c}$, eq. (6.11),

can be assembled as

$$H_0 = \begin{bmatrix} y_1^b & y_2^b & \cdots & y_n^b \\ y_2^b & y_3^b & \cdots & y_{n+1}^b \\ \vdots & \vdots & \ddots & \vdots \\ y_m^b & y_{m+1}^b & \cdots & y_{m+n-1}^b \end{bmatrix}, \tag{6.43}$$

where N_s is the number of control outputs. Based on eq. (6.12), H_0 can be factorized as, $H_0 = M_o M_c$, where $M_o \in \mathbb{R}^{mN_s \times 2N}$ and $M_c \in \mathbb{R}^{2N \times nN_c}$ are finite-dimensional observability and controllability matrices, respectively. As discussed in section 6.1.1, the similarity transformation implies that if any full-rank factorization of matrix H_0 is given as $H_0 = M_o M_c$, M_o and M_c can be selected as observability and controllability matrices, respectively. Furthermore, if M_o and M_c have full rank and H_0 is of rank r, the minimum realization theory indicates the rank r is equal to the order of identified system, $2N$. The Ho-Kalman algorithm utilizes a truncated singular value decomposition to factorize matrix H_0 as $H_0 = U_r \Sigma_r V_r^T$. The observability and controllability matrices are then selected as,

$$M_o = U_r \Sigma_r^{1/2} \quad \text{and} \quad M_c = \Sigma_r^{1/2} V_r^T. \tag{6.44}$$

Matrices B_s and C are extracted from M_c, eq. (6.7), the first N_c columns, and M_o, eq. (6.9), the first N_s rows, respectively. Finally, two sub-matrices, $M_o^{(0)}$ and $M_o^{(1)}$, are constructed by deleting the last and the first N_s rows of matrix M_o, respectively

$$M_o^{(0)} = \begin{bmatrix} C \\ CA_s \\ \vdots \\ CA_s^{m-2} \end{bmatrix}, \quad M_o^{(1)} = \begin{bmatrix} CA_s \\ CA_s^2 \\ \vdots \\ CA_s^{m-1} \end{bmatrix}. \tag{6.45}$$

It is the clear that $M_o^{(1)} = M_o^{(0)} A_s$. If $M_o^{(0)}$ is not singular and its Moore-Penrose inverse denoted ${M_o^{(0)}}^+$, matrix A_s is evaluated as

$$A_s = {M_o^{(0)}}^+ M_o^{(1)}. \tag{6.46}$$

The Ho-Kalman algorithm can be summarized by the following three steps.

1. Assemble outputs block Hankel matrix H_0; factorize H_0 using singular value decomposition as $H_0 = U_r \Sigma_r V_r^T$; select the observability and controllability matrices as $M_o = U_r \Sigma_r^{1/2}$ and $M_c = \Sigma_r^{1/2} V_r^T$, respectively.

2. Extract matrices B_s and C from M_c, the first N_c columns, and M_o, the first N_s rows, respectively.

3. Construct matrices $M_o^{(0)}$ and $M_o^{(1)}$, compute the exponential characteristic matrix as $A_s = {M_o^{(0)}}^{+} M_o^{(1)}$.

6.2.3 Eigensystem Realization Algorithm

Juang and Pappa [55, 53] proposed an extension of the Ho-Kalman algorithm, denoted the eigensystem realization algorithm, which constructs a minimum order state space representation using the system Markov parameters. At first, a generic formulation of output block Hankel matrix, eq. (6.11), is defined for time step k as

$$H_k = \begin{bmatrix} CA_s^k B_s & CA_s^{k+1} B_s & \dots & CA_s^{k+n-1} B_s \\ CA_s^{k+1} B_s & CA_s^{k+2} B_s & \dots & CA_s^{k+n} B_s \\ \vdots & \vdots & \ddots & \vdots \\ CA_s^{k+m-1} B_s & CA_s^{k+m} B_s & \dots & CA_s^{k+m+n-2} B_s \end{bmatrix}. \tag{6.47}$$

Juang and Pappa [55] indicated that H_k can be factorized as

$$H_k = M_o A_s^k M_c. \tag{6.48}$$

For $k = 0$, the factorization reduces to, $H_0 = M_o M_c$, eq. (6.12). The eigensystem realization algorithm evaluates this factorization using singular value decomposition, $H_0 = U_r \Sigma_r V_r^T$, where r, the truncated rank of H_0, is equal to the order of identified system. The observability and controllability matrices are selected as $M_o = U_r \Sigma_r^{1/2}$ and $M_c = \Sigma_r^{1/2} V_r^T$, respectively, the same choice as that of the Ho-Kalman algorithm.

System matrices B_s and C are extracted from the first N_c columns of M_c, see eq. (6.7), and the first N_s rows of M_o, see eq. (6.9), respectively. For $k = 1$, the factorization, eq. (6.48), becomes $H_1 = M_o A_s M_c$. Once the observability and controllability matrices are determined, H_1 is rewritten as, $H_1 = U_r \Sigma_r^{1/2} A_s \Sigma_r^{1/2} V_r^T$, and the exponential characteristic matrix A_s can be computed from matrix H_1 as

$$A_s = \Sigma_r^{-1/2} U_r^T H_1 V_r \Sigma_r^{-1/2}, \tag{6.49}$$

where the orthogonal properties, $U_r^T U_r = I$ and $V_r^T V_r = I$, were used. Note that the observability and controllability Gramians, eqs. (6.19) and (6.20), can also be determined

$$P_o = M_o^T M_o = \Sigma_r^{1/2} U_r^T U_r \Sigma_r^{1/2} = \Sigma_r \quad \text{and} \quad P_c = M_c M_c^T = \Sigma_r^{1/2} V_r^T V_r \Sigma_r^{1/2} = \Sigma_r. \tag{6.50}$$

Clearly, both become diagonal and identical each other. It means the model, eqs. (2.15), identified by eigensystem realization algorithm, is said to be balanced and truncated, more details about balanced truncation can be found in section 6.1.2.

In summary, the eigensystem realization algorithm consists of the following steps.

1. Assemble output block Hankel matrices H_0 and H_1, perform the singular value decomposition of Hankel matrix H_0, $H_0 = U_r \Sigma_r V_r^T$. Compute the observability matrix $M_o = U_r \Sigma_r^{1/2}$ and the controllability matrix $M_c = \Sigma_r^{1/2} V_r^T$.

2. Extract matrices B_s and C from the first N_c columns of M_c and the first N_s rows of M_o, respectively.

3. Compute the exponential characteristic matrix, $A_s = \Sigma_r^{-1/2} U_r^T H_1 V_r \Sigma_r^{-1/2}$.

6.2.4 Eigensystem Realization Algorithm with Data Correlation

The minimum realization algorithm should be robust enough to deal with the numerical noise associated with time discretization and solution inaccuracy. In this section,

data correlation is combined with the eigensystem realization algorithm to handle the effects of the noise. The data correlation matrix is computed as $R_k = H_k H_0^T$, where H_k, $k = 0, 1, \ldots$, is output block Hankel matrix defined by eq. (6.47). If the Hankel matrices H_0 and H_k are factorized as $H_0 = M_o M_c$, see eq. (6.12), and $H_k = M_o A_s^k M_c$, see eq. (6.48), respectively, the data correlation matrix can be written as, $R_k = M_o A_s^k M_c M_c^T M_o^T = M_o A_s^k M_r$, where $M_r = M_c M_c^T M_o^T$. When the data correlation Hankel matrix is assembled

$$\mathcal{H}_k = \begin{bmatrix} R_k & R_{k+\tau} & \ldots & R_{k+(n-1)\tau} \\ R_{k+\tau} & R_{k+2\tau} & \ldots & R_{k+(n)\tau} \\ \vdots & \vdots & \ddots & \vdots \\ R_{k+(m-1)\tau} & R_{k+(m)\tau} & \ldots & R_{k+(m+n-2)\tau} \end{bmatrix}, \tag{6.51}$$

where τ is an integer selected to prevent significant overlap of adjacent blocks, Juang [53] found that the data correlation Hankel matrix, $\mathcal{H}_k$, can be factorized as

$$\mathcal{H}_k = \mathcal{M}_o A_s^k \mathcal{M}_r, \tag{6.52}$$

by substituting the equation, $R_k = M_o A_s^k M_r$, into the definition of $\mathcal{H}_k$, eq. (6.51), where matrices $\mathcal{M}_o$ and $\mathcal{M}_r$ are defined as

$$\mathcal{M}_o = \begin{bmatrix} M_o \\ M_o A_s^\tau \\ \vdots \\ M_o A_s^{m\tau} \end{bmatrix} \quad \text{and} \quad \mathcal{M}_r = \left[M_r, A_s^\tau M_r, \ldots, A_s^{n\tau} M_r \right]. \tag{6.53}$$

For $k = 0$, the factorization defined by eq. (6.52) reduces to $\mathcal{H}_0 = \mathcal{M}_o \mathcal{M}_r$. When the singular value decomposition of $\mathcal{H}_0$ with rank r is performed, $\mathcal{H}_0 = U_r \Sigma_r V_r^T$, matrices $\mathcal{M}_o$ and $\mathcal{M}_r$ can be selected as $\mathcal{M}_o = U_r \Sigma_r^{1/2}$ and $\mathcal{M}_r = \Sigma_r^{1/2} V_r^T$, respectively. Consequently, the observability matrix, M_o, is extracted from the first mN_s rows of matrix $\mathcal{M}_o$, whereas the controllability matrix, M_c, is computed from the Hankel matrix, H_0, as $M_c = M_o^+ H_0$, where M_o^+ is the Moore-Penrose inverse of M_o.

System matrices B_s and C will be extracted from the first N_c columns of M_c, see eq. (6.7), and the first N_s rows of M_o, see eq. (6.9), respectively. For $k = 1$, the factorization, eq. (6.52), reduces to $\mathcal{H}_1 = \mathcal{M}_o A_s \mathcal{M}_r$. If $\mathcal{M}_o$ and $\mathcal{M}_r$ are determined, the characteristic matrix, A_s, can be computed from data correlation Hankel matrix, $\mathcal{H}_1$, as

$$A_s = \Sigma_r^{-1/2} U_r^T \mathcal{H}_1 V_r \Sigma_r^{-1/2}, \tag{6.54}$$

where the orthogonal properties, $U_r^T U_r = I$ and $V_r^T V_r = I$ were used.

In summary, the procedure of eigensystem realization algorithm consists of the following steps.

1. Compute the data correlation R_k; assemble the data correlation Hankel matrices $\mathcal{H}_0$ and $\mathcal{H}_1$; perform the singular value decomposition of $\mathcal{H}_0$, $\mathcal{H}_0 = U_r \Sigma_r V_r^T$; compute matrices, $\mathcal{M}_o = U_r \Sigma_r^{1/2}$ and $\mathcal{M}_r = \Sigma_r^{1/2} V_r^T$, respectively.

2. Extract the observability matrix M_o from the first mN_s rows of $\mathcal{M}_o$; compute the controllability matrix, $M_c = M_o^+ H_0$.

3. Extract matrix B_s from the first N_c columns of M_c, and matrix C from the first N_s rows of M_o, respectively.

4. Compute the exponential characteristic matrix, A_s, as $A_s = \Sigma_r^{-1/2} U_r^T \mathcal{H}_1 V_r \Sigma_r^{-1/2}$.

6.2.5 Modal Amplitude Coherence and Mode Singular Value

When the deterministic model, eqs. (2.15), has been identified, the modes of the system are computed; the modal canonical state space form, eqs. (6.2), is then formulated. Unfortunately, practical applications show that modes associated with noise typically appear among the identified modes of the system. In numerical simulations, noise is generated mainly by numerical discretization, inaccuracy of the solution process, and nonlinearity of the system. In this section, two accuracy indicators, the

modal amplitude coherence and the *mode singular value*, are defined to distinguish physical modes from those associated with noise.

The coherence between the actual time history of a modal amplitude and its predicted counterpart is called as *modal amplitude coherence*. The actual time history of a modal amplitude is extracted from the observability matrix, and that of the identified modal amplitude is computed by extrapolating the initial value of an identified modal amplitude to later points using the identified eigenvalue. For example, if the deterministic model, eqs.(2.15), is identified by Ho-Kalman algorithm, the observability and controllability matrices are determined by eq. (6.44). In modal canonical formulation, the observability matrix becomes $\Psi^{-1}M_c \in \mathbb{R}^{2N\times nN_c}$, where Ψ are the eigenvectors of the deterministic model; the actual time histories of modal amplitudes, $\underline{q}_j$ for $j = 1, 2, \ldots, 2N$, are then extracted from the observability matrix as

$$\Psi^{-1}M_c = \left[\underline{q}_1, \underline{q}_2, \ldots, \underline{q}_{2N}\right]^T. \tag{6.55}$$

The identified modal amplitudes, $\underline{b}_j$, for $j = 1, 2, \ldots, 2N$, are defined as the row partition results of identified matrix, $\widetilde{B}_{s(2N\times N_c)}$,

$$\widetilde{B}_s = \Psi^{-1}B_s = [\underline{b}_1 \quad \underline{b}_2 \quad \ldots \quad \underline{b}_{2N}]^T, \tag{6.56}$$

the time histories of the identified modal amplitudes, $\bar{\underline{q}}_j$, for $j = 1, 2, \ldots, 2N$, are extrapolated as

$$\bar{\underline{q}}_j^T = \left[\underline{b}_j^T, e^{\lambda_j \Delta t}\underline{b}_j^T, \ldots, e^{\lambda_j (n-1)\Delta t}\underline{b}_j^T\right], \tag{6.57}$$

where $\exp(\lambda_j \Delta t)$ is the j^{th} eigenvalue of the characteristic matrix A_s.

The modal amplitude coherence for the j^{th} mode, γ_j, is defined as

$$\gamma_j = \frac{\left|\bar{\underline{q}}_j^T \underline{q}_j\right|}{\sqrt{\left|\bar{\underline{q}}_j^T \bar{\underline{q}}_j\right| \ \left|\underline{q}_j^T \underline{q}_j\right|}}, \tag{6.58}$$

which satisfies the condition, $\gamma_j \in [0, 1]$. If γ_j is close to 1, the identified system eigenvalues, λ_j, and modal amplitude, $\underline{b}_j$, are very close to their actual values for the

j^{th} mode of the system. On the contrary, if γ_j is close to 0, the identified j^{th} mode can be viewed as a noise related mode.

The mode singular value characterizes the contribution of each identified mode to the free impulse response of dynamic system. With the help of the modal decomposition, eq. (2.38), the free impulse response, eqs. (6.42), is written as

$$y_k^b = \sum_{j=1}^{2N} \underline{c}_j \underline{b}_j^T e^{\lambda_j (k-1)\Delta t} \quad \text{for} \quad k = 1, 2, \ldots, \tag{6.59}$$

where $\underline{c}_j$ is the j^{th} column of matrix $C\Psi$, and $\underline{b}_j$ is defined by eq. (6.56). Each identified mode will be associated with a sequence of modal Markov parameters

$$\left[\underline{c}_j \underline{b}_j^T, \underline{c}_j q_j \underline{b}_j^T, \ldots, \underline{c}_j q_j^{n-1} \underline{b}_j^T\right], \tag{6.60}$$

where $q_j = \exp(\lambda_j \Delta t)$. The *mode singular value* of j^{th} mode, κ_j, is defined as

$$\kappa_j = \sqrt{\left|\underline{c}_j\right| \left(1 + |q_j| + \ldots + \left|q_j^{n-1}\right|\right) \left|\underline{b}_j^T\right|}. \tag{6.61}$$

Finally, the ratio, $\kappa_j / \sum_{i=1}^{2N} \kappa_i$, indicates the contribution of each mode to the free impulse response of the dynamical system.

The modal amplitude coherence and mode singular value describe the relative participation of each identified mode to the minimum realization. Modes associated with noise can be distinguished their physical counterparts and truncated. This truncation is markedly different from modal truncation. For modal truncation, the modes associated with high frequencies are eliminated. However, if it is possible to identify the modes associated with noise, truncation now becomes based on the physics of the problem, rather than a simple frequency ranking.

6.3 Subspace Identification Approach

This section will introduce the subspace identification approach, which constructs an accurate subspace model for dynamical system from the forced input-output data

using orthogonal projection. The basic issues associated with this approach will be discussed and a deterministic model, eqs. (2.15), will be constructed.

Hankel matrices again play an important role in the process of subspace identification. The output Hankel matrix, Y_k, is assembled by using the output data of deterministic model, eqs. (2.15), as

$$Y_k = \begin{bmatrix} \underline{y}_k & \underline{y}_{k+1} & \cdots & \underline{y}_{k+n-1} \\ \underline{y}_{k+1} & \underline{y}_{k+2} & \cdots & \underline{y}_{k+n} \\ \vdots & \vdots & \ddots & \vdots \\ \underline{y}_{k+m-1} & \underline{y}_{k+m} & \cdots & \underline{y}_{k+m+n-2} \end{bmatrix}, \tag{6.62}$$

and the input Hankel matrix, F_k, by using the input data

$$F_k = \begin{bmatrix} \underline{f}_{k+m-1} & \underline{f}_{k+m} & \cdots & \underline{f}_{k+m+n-2} \\ \underline{f}_{k+m-2} & \underline{f}_{k+m-1} & \cdots & \underline{f}_{k+m+n-3} \\ \vdots & \vdots & \ddots & \vdots \\ \underline{f}_k & \underline{f}_{k+1} & \cdots & \underline{f}_{k+n-1} \end{bmatrix}. \tag{6.63}$$

The deterministic model, eqs. (2.15), will be recast in a matrix form by defining the following notations: the state array, U_k,

$$U_k = \begin{bmatrix} \underline{u}_k & \underline{u}_{k+1} & \cdots & \underline{u}_{k+n-1} \end{bmatrix}, \tag{6.64}$$

and the lower triangular Toeplitz matrix, T_0,

$$T_0 = \begin{bmatrix} 0 & 0 & \ldots & 0 & 0 & D \\ 0 & 0 & \ldots & 0 & D & CB_s \\ 0 & 0 & \ldots & D & CB_s & CA_sB_s \\ \vdots & \vdots & \ddots & \vdots & \vdots & \vdots \\ D & CB_s & \ldots & CA_s^{m-4}B_s & CA_s^{m-3}B_s & CA_s^{m-2}B_s \end{bmatrix}. \tag{6.65}$$

Eqs. (2.15) are now written as

$$Y_0 = M_o U_0 + T_0 F_0; \tag{6.66a}$$

$$Y_m = M_o U_m + T_0 F_m; \tag{6.66b}$$

$$U_m = A_s^m U_0 + M_c F_0, \tag{6.66c}$$

where $M_{o(mN_s \times 2N)}$ and $M_{c(2N \times nN_c)}$ are the finite-dimensional observability and controllability matrices, respectively. From eq. (6.66a), the state array, U_0, is found as $U_0 = M_o^+ Y_0 - M_o^+ T_0 F_0$, where M_o^+ is the Moore-Penrose inverse of M_o. Substituting this solution into eq. (6.66c), the state array, U_m, is found to be

$$U_m = A_s^m M_o^+ Y_0 + (M_c - A_s^m M_o^+ T_0) F_0. \tag{6.67}$$

Introducing this result in eq. (6.66b) yields

$$Y_m = M_o A_s^m M_o^+ Y_0 + M_o (M_c - A_s^m M_o^+ T_0) F_0 + T_0 F_m. \tag{6.68}$$

Next, the geometric operator that projects the row space of a matrix onto the orthogonal complement of the row space of matrix F_m is defined

$$F_m^\perp = I - F_m^T (F_m F_m^T)^{-1} F_m, \tag{6.69}$$

to satisfy the orthogonal property, $F_m F_m^\perp = 0$. In view of eqs. (6.66b) and (6.68), the projection, $Y_m F_m^\perp$, can be computed as

$$Y_m F_m^\perp = M_o U_m F_m^\perp = M_o A_s^m M_o^+ Y_0 F_m^\perp + M_o (M_c - A_s^m M_o^+ T_0) F_0 F_m^\perp, \tag{6.70}$$

in compact form

$$Y_m F_m^\perp = M_o U_m F_m^\perp = \begin{bmatrix} M_o (M_c - A_s^m M_o^+ T_0) & M_o A_s^m M_o^+ \end{bmatrix} W_0 F_m^\perp, \tag{6.71}$$

where W_0 is input-output Hankel matrix, $W_0^T = \begin{bmatrix} F_0^T & Y_0^T \end{bmatrix}$. If $\left(W_0 F_m^\perp\right)^+$ is the Moore-Penrose inverse of $W_0 F_m^\perp$, it then follows that $W_0 F_m^\perp \left(W_0 F_m^\perp\right)^+ W_0 = W_0$. Post-multiplying eq. (6.71) by $\left(W_0 F_m^\perp\right)^+ W_0$ then yields

$$O_0 = M_o U_m = Y_m F_m^\perp \left(W_0 F_m^\perp\right)^+ W_0. \tag{6.72}$$

For a generic time step, $m+1$, eq. (6.66b) becomes, $Y_{m+1} = M_o U_{m+1} + T_0 F_{m+1}$. Next, the first equation of eqs. (2.15) implies $U_{m+1} = A_s U_m + B_s[\underline{f}_m \quad \underline{f}_{m+1} \quad \dots \quad \underline{f}_{m+n-1}]$; introducing this result in the previous equation yields

$$Y_{m+1} = M_o A_s U_m + \widetilde{T}_0 \widetilde{F}_m, \tag{6.73}$$

where matrix, $\widetilde{T}_0$, is defined as

$$\widetilde{T}_0 = \begin{bmatrix} 0 & 0 & \dots & 0 & 0 & D & CB_s \\ 0 & 0 & \dots & 0 & D & CB_s & CA_sB_s \\ 0 & 0 & \dots & D & CB_s & CA_sB_s & CA_s^2B_s \\ \vdots & \vdots & \ddots & \vdots & \vdots & \vdots & \vdots \\ D & CB_s & \dots & CA_s^{m-4}B_s & CA_s^{m-3}B_s & CA_s^{m-2}B_s & CA_s^{m-1}B_s \end{bmatrix}, \tag{6.74}$$

and input Hankel matrix, $\widetilde{F}_m$, as

$$\widetilde{F}_m = \begin{bmatrix} \underline{f}_{2m} & \underline{f}_{2m+1} & \dots & \underline{f}_{2m+n-1} \\ \underline{f}_{2m-1} & \underline{f}_{2m} & \dots & \underline{f}_{2m+n-2} \\ \underline{f}_{2m-2} & \underline{f}_{2m-1} & \dots & \underline{f}_{2m+n-3} \\ \vdots & \vdots & \ddots & \vdots \\ \underline{f}_m & \underline{f}_{m+1} & \dots & \underline{f}_{m+n-1} \end{bmatrix}. \tag{6.75}$$

With the help of eq. (6.67), the output Hankel matrix, Y_{m+1}, eq. (6.73), is rewritten as

$$Y_{m+1} = M_o A_s^{m+1} M_o^+ Y_0 + M_o A_s (M_c - A_s^m M_o^+ T_0) F_0 + \widetilde{T}_0 \widetilde{F}_m. \tag{6.76}$$

Operator $\widetilde{F}_m^\perp$, defined as $\widetilde{F}_m^\perp = I - \widetilde{F}_m^T (\widetilde{F}_m \widetilde{F}_m^T)^{-1} \widetilde{F}_m$, projects onto the space orthogonal to $\widetilde{F}_m$. Post-multiplying eqs. (6.73) and (6.76) by this projector yields

$$Y_{m+1} \widetilde{F}_m^\perp = M_o A_s U_m \widetilde{F}_m^\perp = \begin{bmatrix} M_o A_s (M_c - A_s^m M_o^+ T_0) & M_o A_s^{m+1} M_o^+ \end{bmatrix} W_0 \widetilde{F}_m^\perp. \tag{6.77}$$

Finally, post-multiplying eq. (6.77) by $\left(W_0 \widetilde{F}_m^\perp\right)^+ W_0$ leads to

$$O_1 = M_o A_s U_m = Y_{m+1} \widetilde{F}_m^\perp \left(W_0 \widetilde{F}_m^\perp\right)^+ W_0, \tag{6.78}$$

where the property of Moore-Penrose inverses, $W_0\widetilde{F}_m^{\perp}\left(W_0\widetilde{F}_m^{\perp}\right)^{+}W_0 = W_0$, was used. Eqs. (6.72) and (6.78) show that O_0 and O_1 can be computed from the input-output data, meanwhile, O_0 is represented by the factorization, $O_0 = M_o U_m$. If a truncated factorization of matrix O_0 is evaluated by means of the singular value decomposition to find $O_0 = U_r \Sigma_r V_r^T$, where r is the estimated rank of O_0, then the controllability matrix, M_o, is selected as $M_o = U_r \Sigma_r^{1/2}$, and state array, U_m, as $U_m = \Sigma_r^{1/2} V_r^T$. The exponential characteristic matrix, A_s, is now computed from eq. (6.78) as

$$A_s = \Sigma_r^{-1/2} U_r^T O_1 V_r \Sigma_r^{-1/2}. \tag{6.79}$$

Next, matrix C is determined from the controllability matrix, M_o, the first N_s rows.

The last step of subspace identification approach includes the determination of matrices B_s and D. Once all the other unknowns are found, the problem becomes linear in the unknowns B_s and D. The least-square regression is used to solve a redundant of linear equations for rest of the unknowns. The convolution of outputs, eq. (6.23), is reformulated as a linear functions of $\underline{u}_0$, B_s and D

$$\underline{y}_k = CA_s^k \underline{u}_0 + \left(\sum_{j=0}^{k-1} \underline{f}_j^T \otimes CA_s^{k-1-j}\right) \mathrm{vec}(B_s) + \left[\underline{f}_k^T \otimes I\right] \mathrm{vec}(D). \tag{6.80}$$

where $\otimes$ denotes the Kronecker product, and $\mathrm{vec}(A)$ indicates the operation that construct an array from a stacking the columns of an arbitrary matrix A, note the identity, $\mathrm{vec}(AXB) = (B^T \otimes A)\mathrm{vec}(X)$, where A, X and B are arbitrary matrices [24]. Finally, the remaining unknowns, B_s, D and $\underline{u}_0$, if initial conditions are not zero, are obtained from a least squares approximation as

$$\arg \min_{\underline{u}_0, B_s, D} \sum_{k=0}^{n} \left[\underline{y}_k - CA_s^k \underline{u}_0 - \left(\sum_{j=0}^{k-1} \underline{f}_j^T \otimes CA_s^{k-1-j}\right) \mathrm{vec}B_s - \left[\underline{f}_k^T \otimes I\right] \mathrm{vec}D\right]^2 \tag{6.81}$$

In summary, the procedure for subspace identification algorithm involves the following steps.

1. Assemble the Hankel matrices, F_m, $\widetilde{F}_m$, Y_m, Y_{m+1}, and W_0, and compute oblique projections, $O_0 = Y_m F_m^{\perp}\left(W_0 F_m^{\perp}\right)^{+} W_0$ and $O_1 = Y_{m+1}\widetilde{F}_m^{\perp}\left(W_0\widetilde{F}_m^{\perp}\right)^{+} W_0$.

2. Perform the singular value decomposition of O_0, $O_0 = U_r \Sigma_r V_r^T$. Compute the observability matrix, $M_o = U_r \Sigma_r^{1/2}$, and state array, $U_m = \Sigma_r^{1/2} V_r^T$.

3. Compute the exponential characteristic matrix, $A_s = \Sigma_r^{-1/2} U_r^T O_1 V_r \Sigma_r^{-1/2}$. Matrix C is extracted as the first N_s rows of the observability matrix.

4. Compute matrices B_s and D by the least-square technique, see eqs. (6.81).

Note that the orthogonal projection operator is applied to compute the data correlation matrices O_0 and O_1, then the exponential characteristic matrix, A_s, and output matrix C are extracted from the input-output data. If the input Hankel matrices, F_m and $\widetilde{F}_m$, are ill-conditioned, the data correlation matrices, $F_m F_m^T$ and $\widetilde{F}_m \widetilde{F}_m^T$, will be even more ill-conditioned. The projection operators, $F_m^{\perp}$ and $\widetilde{F}_m^{\perp}$, will then be very inaccurate.

6.4 Kalman Filter

The Kalman filter, named after Rudolph E. Kalman, is one of the most well-known and often used tools for stochastic estimation. In 1960, Kalman [56] described a recursive solution to the discrete time linear filtering problem. A review of the many aspects of Kalman filtering was given by Unger [106]. Kalman filters implement a predictor-corrector estimator that is optimal in the sense that it minimizes the estimated error covariance under the assumption that the noise is Gaussian and white with a zero mean. The entire process for the determination of Kalman filters will be outlined in this section. The evaluation of the Kalman filter involves the solution of algebraic Riccati equations.

A combined deterministic-stochastic linear model is considered and modeled by the following equations

$$\begin{cases} \underline{u}_{k+1} = A_s \underline{u}_k + B_s \underline{f}_k + \underline{w}_k; \\ \underline{y}_k = C \underline{u}_k + D \underline{f}_k + \underline{v}_k, \end{cases} \tag{6.82}$$

where vector $\underline{w}_k$ represents noise in the state vector, assumed to be Gaussian with a zero mean, stationary and white, whereas vector $\underline{v}_k$ represents measurement noise, assumed to share the same characteristics. The covariance matrices are defined as

$$E\left(\left|\begin{array}{c}\underline{w}_i\\ \underline{v}_i\end{array}\right|\left\lfloor\begin{array}{cc}\underline{w}_j^T & \underline{v}_j^T\end{array}\right\rfloor\right)=\left[\begin{array}{cc}E_w & E_s\\ E_s^T & E_v\end{array}\right]\delta_{ij}, \tag{6.83}$$

where δ_{ij} is the Kronecker delta. In view of the above assumptions, $E(\underline{w}_k)=0$, and $E(\underline{v}_k)=0$.

If the best estimation of the deterministic-stochastic model, $\bar{\underline{u}}_k$, is expected, it is logical to minimize the following quantity

$$\underline{e}_k=\underline{u}_k-\bar{\underline{u}}_k. \tag{6.84}$$

The estimation will be cast in a recursive form, $\bar{\underline{u}}_{k+1}=F_k\bar{\underline{u}}_k+K_k\underline{y}_k+H_k^f\underline{f}_k$, where F_k is the closed loop characteristic matrix and K_k the Kalman filter gain. Hence, at generic time step $k+1$, the error, $\underline{e}_{k+1}=\underline{u}_{k+1}-\bar{\underline{u}}_{k+1}$, becomes

$$\underline{e}_{k+1}=(A_s-K_kC)\underline{e}_k+(A_s-F_k-K_kC)\bar{\underline{u}}_k+(B_s-K_kD-H_k^f)\underline{f}_k-K_k\underline{v}_k+\underline{w}_k. \tag{6.85}$$

Because the mean value of noise is zero, the mean value of the error, $E(\underline{e}_k)$, simplifies to

$$E(\underline{e}_{k+1})=(A_s-K_kC)E(\underline{e}_k)+(A_s-F_k-K_kC)E(\bar{\underline{u}}_k)+(B_s-K_kD-H_k^f)E(\underline{f}_k). \tag{6.86}$$

It can be proved that the estimated error will have a zero mean, $E(\underline{e}_{k+1})=0$, if and only if

$$\begin{cases}\underline{u}_0=0,\\ F_k=A_s-K_kC,\\ H_k^f=B_s-K_kD.\end{cases} \tag{6.87}$$

Once these conditions are satisfied, the error can be written as $\underline{e}_{k+1}=(A_s-K_kC)\underline{e}_k-K_k\underline{v}_k+\underline{w}_k$. Assuming the instantaneous error to be independent of the instantaneous

noise, $E(\underline{e}_k \underline{w}_k^T) = 0$ and $E(\underline{e}_k \underline{v}_k^T) = 0$, and the error covariance matrix becomes

$$\begin{aligned} P_{k+1} &= E(\underline{e}_{k+1}\underline{e}_{k+1}^T) = (A_s - K_k C)E(\underline{e}_k \underline{e}_k^T)(A_s - K_k C)^T \\ &+ K_k E(\underline{v}_k \underline{v}_k^T)K_k^T + E(\underline{w}_k \underline{w}_k^T) - K_k E(\underline{v}_k \underline{w}_k^T) - E(\underline{w}_k \underline{v}_k^T)K_k^T. \end{aligned} \quad (6.88)$$

With the help of the definition, eq. (6.83), the error covariance matrices can be manipulated to find

$$P_{k+1} = (A_s - K_k C)P_k(A_s - K_k C)^T + K_k E_v K_k^T + E_w - K_k E_s^T - E_s K_k^T. \quad (6.89)$$

It is now possible to minimize the 2-norm of $\underline{e}_k$, which is defined as

$$J_{k+1} = E(\underline{e}_{k+1}^T \underline{e}_{k+1}) = \mathrm{tr}(E(\underline{e}_{k+1}\underline{e}_{k+1}^T)) = \mathrm{tr}(P_{k+1}). \quad (6.90)$$

The error is minimized by selecting the appropriate Kalman filter gain matrix. To that effect, the derivative of the error with respect to the filter gain matrix must vanish, *i.e.*

$$\frac{\partial \mathrm{tr}(P_{k+1})}{\partial K_k} = -2(A_s - K_k C)P_k C^T + 2K_k E_v - 2E_s = 0. \quad (6.91)$$

This yields the Kalman filter gain matrix as

$$K_k = (A_s P_k C^T + E_s)(C P_k C^T + E_v)^{-1}. \quad (6.92)$$

Substituting K_k into eq. (6.89), the discrete time algebraic Riccati equation is found

$$P_{k+1} = A_s P_k A_s^T + E_w - (A_s P_k C^T + E_s)(C P_k C^T + E_v)^{-1}(A_s P_k C^T + E_s)^T. \quad (6.93)$$

This process shows that the unsteady Kalman filter gain matrix, K_k, is a function of P_k, which can be obtained from the solution of the Riccati equation. When k goes to infinity, it can be shown that P_k quickly reaches a steady value, P. In the case of steady state, P is the unique solution of the following discrete time algebraic Riccati equation

$$P = A_s P A_s^T + E_w - (A_s P C^T + E_s)(C P C^T + E_v)^{-1}(A_s P C^T + E_s)^T. \quad (6.94)$$

Consequently, the steady state Kalman filter gain matrix is obtained as

$$K = (A_s P C^T + E_s)(C P C^T + E_v)^{-1}. \tag{6.95}$$

Once this gain has been determined, the following *forward innovation model* is constructed

$$\begin{cases} \underline{\bar{u}}_{k+1} = A_s \underline{\bar{u}}_k + B_s \underline{f}_k + K \underline{\epsilon}_k; \\ \underline{y}_k = C \underline{\bar{u}}_k + D \underline{f}_k + \underline{\epsilon}_k, \end{cases} \tag{6.96}$$

where $\underline{\epsilon}_k$ is the output residual white noise assumed to be of zero mean. In view of the second equations of deterministic-stochastic model, eqs. (6.82), and forward innovation model, eqs. (6.96), the relationship between the output residual noise, $\underline{\epsilon}_k$, and the estimation error, $\underline{e}_k$, is found to be

$$\underline{\epsilon}_k = C \underline{e}_k + \underline{v}_k. \tag{6.97}$$

The solution procedure for the discrete time algebraic Riccati equation in steady state will be discussed in chapter 7. A robust algorithm [70, 2] based on Schur decomposition will be introduced.

6.5 The Proposed Robust Identification Approach

The proposed robust identification approach is described in this section. To improve the robustness of this approach, the least-square and Kalman filter techniques are applied. To account for the effects of white noise, the combined deterministic-stochastic model, eqs. (6.82), is modeled. The object of system identification is to determine the system matrices, A_s, B_s, C and D, the covariance matrices, E_w, E_s and E_v, and the Kalman filter gain matrix, K, to construct the forward innovation model, eqs. (6.96).

If the control inputs are defined as the impulse perturbations

$$\underline{f}_k = \begin{cases} \underline{f}_k^d, \ k = 0, 1, \ldots, m-1; \\ \underline{0}, \ k = m, m+1, \ldots, \end{cases} \tag{6.98}$$

the system will be excited for the first m time steps, and no control inputs are applied for the subsequent time steps. After m time steps, the inputs vanish and the innovation model reduces to

$$\begin{cases} \underline{\bar{u}}_{k+1} = A_s \underline{\bar{u}}_k + K\epsilon_k; \\ \underline{y}_k = C\underline{\bar{u}}_k + \underline{\epsilon}_k. \end{cases} \tag{6.99}$$

Juang [53] has proved that $\underline{\epsilon}_k$ represents white noise with zero mean whether the state noise, $\underline{w}_k$, and measurement noise, $\underline{v}_k$, are white noise or not. System outputs, $\underline{y}_k$, could be the computed free impulse response of the linearized model obtained form a numerical simulation, or experimental data. In view of eqs. (6.99), this response can be presented by the following convolution

$$\underline{y}_k = CA_s^k \underline{\bar{u}}_0 + \sum_{j=0}^{k-1} CA_s^{k-1-j} K \underline{\epsilon}_j + \underline{\epsilon}_k. \tag{6.100}$$

This result will be recast in a matrix form by defining the following notations: the filtered state array, $\bar{U}_k$,

$$\bar{U}_k = \begin{bmatrix} \underline{\bar{u}}_k & \underline{\bar{u}}_{k+1} & \dots & \underline{\bar{u}}_{k+n-1} \end{bmatrix}, \tag{6.101}$$

and the residual noise Hankel matrix, E_k,

$$E_k = \begin{bmatrix} \underline{\epsilon}_{k+m-1} & \underline{\epsilon}_{k+m} & \cdots & \underline{\epsilon}_{k+m+n-2} \\ \underline{\epsilon}_{k+m-2} & \underline{\epsilon}_{k+m-1} & \cdots & \underline{\epsilon}_{k+m+n-3} \\ \vdots & \vdots & \ddots & \vdots \\ \underline{\epsilon}_k & \underline{\epsilon}_{k+1} & \cdots & \underline{\epsilon}_{k+n-1} \end{bmatrix}. \tag{6.102}$$

Eqs. (6.100) are now written as

$$Y_m = M_o \bar{U}_m + \mathcal{K}_0 E_m; \tag{6.103a}$$

$$\bar{U}_m = A_s^m \bar{U}_0 + M_{\mathcal{K}} E_0, \tag{6.103b}$$

where matrix $M_{\mathcal{K}}$ is defined as

$$M_{\mathcal{K}} = \begin{bmatrix} K & A_s K & A_s^2 K & \dots & A_s^{m-1} K \end{bmatrix}, \tag{6.104}$$

and the lower triangular Toeplitz matrix, $\mathcal{K}_0$,

$$\mathcal{K}_0 = \begin{bmatrix} 0 & 0 & \dots & 0 & 0 & I \\ 0 & 0 & \dots & 0 & I & CK \\ 0 & 0 & \dots & I & CK & CA_sK \\ \vdots & \vdots & \ddots & \vdots & \vdots & \vdots \\ I & CK & \dots & CA_s^{m-4}K & CA_s^{m-3}K & CA_s^{m-2}K \end{bmatrix}. \tag{6.105}$$

In view of eq. (6.103a), the data correlation matrix, $\mathcal{O}_0 = Y_m Y_0^T$, is evaluated,

$$\mathcal{O}_0 = Y_m Y_0^T = M_o \bar{U}_m Y_0^T, \tag{6.106}$$

where the last term, $\mathcal{K}_0 E_m Y_0^T$, vanishes since the white noise assumption implies $E_m Y_0^T = 0$. For time step $m+1$, eq. (6.103a) becomes $Y_{m+1} = M_o \bar{U}_{m+1} + \mathcal{K}_0 E_{m+1}$. Next, the first equation of eqs. (6.99) implies $\bar{U}_{m+1} = A_s \bar{U}_m + K\left[\underline{\epsilon}_m, \underline{\epsilon}_{m+1}, \dots, \underline{\epsilon}_{m+n-1}\right]$; introducing this result in the previous equation yields,

$$Y_{m+1} = M_o A_s \bar{U}_m + \widetilde{\mathcal{K}}_0 \widetilde{E}_m, \tag{6.107}$$

where the residual noise Hankel matrix, $\widetilde{E}_m$, is defined as

$$\widetilde{E}_m = \begin{bmatrix} \underline{\epsilon}_{2m} & \underline{\epsilon}_{2m+1} & \cdots & \underline{\epsilon}_{2m+n-1} \\ \underline{\epsilon}_{2m-1} & \underline{\epsilon}_{2m} & \cdots & \underline{\epsilon}_{2m+n-2} \\ \underline{\epsilon}_{2m-2} & \underline{\epsilon}_{2m-1} & \cdots & \underline{\epsilon}_{2m+n-3} \\ \vdots & \vdots & \ddots & \vdots \\ \underline{\epsilon}_{m} & \underline{\epsilon}_{m+1} & \cdots & \underline{\epsilon}_{m+n-1} \end{bmatrix}, \tag{6.108}$$

and the lower triangular Toeplitz matrix, $\widetilde{\mathcal{K}}_0$, as

$$\widetilde{\mathcal{K}}_0 = \begin{bmatrix} 0 & 0 & \dots & 0 & 0 & I & CK \\ 0 & 0 & \dots & 0 & I & CK & CA_sK \\ 0 & 0 & \dots & I & CK & CA_sK & CA_s^2K \\ \vdots & \vdots & \ddots & \vdots & \vdots & \vdots & \vdots \\ I & CK & \dots & CA_s^{m-4}K & CA_s^{m-3}K & CA_s^{m-2}K & CA_s^{m-1}K \end{bmatrix}. \tag{6.109}$$

Multiplying Y_0^T from right at both side of eq. (6.107), the data correlation matrix, $\mathcal{O}_1 = Y_{m+1}Y_0^T$, at time step $m+1$ is evaluated as

$$\mathcal{O}_1 = Y_{m+1}Y_0^T = M_o A_s \bar{U}_m Y_0^T, \tag{6.110}$$

where the term, $\widetilde{\mathcal{K}}_0 \widetilde{E}_m Y_0^T$, vanishes here again since the white noise assumption implies $\widetilde{E}_m Y_0^T = 0$. Eqs. (6.106) and (6.110) indicate that the data correlation matrices, $\mathcal{O}_0$ and $\mathcal{O}_1$, can be computed from the output data by using the output Hankel matrices, Y_0, Y_m and Y_{m+1}, and the data correlation matrix, $\mathcal{O}_0$, can be represented by the factorization, $\mathcal{O}_0 = M_o \bar{U}_m Y_0^T$. A truncated factorization of matrix $\mathcal{O}_0$ is evaluated by means of the singular value decomposition to find $\mathcal{O}_0 = U_r \Sigma_r V_r^T$, where r is the estimated rank of $\mathcal{O}_0$. The observability matrix, M_o, is selected as $M_o = U_r \Sigma_r^{1/2}$, and the matrix product, $\bar{U}_m Y_0^T$, as $\bar{U}_m Y_0^T = \Sigma_r^{1/2} V_r^T$. The stability characteristic matrix, A_s, is now computed from eq. (6.110) as

$$A_s = \Sigma_r^{-1/2} U_r^T \mathcal{O}_1 V_r \Sigma_r^{-1/2}. \tag{6.111}$$

Next, matrix C is determined from the first N_s rows of observability matrix, M_o.

The computation of the Kalman filter gain matrix requires the covariance matrices E_w, E_s, and E_v. At first, the matrix projection of the row space of Y_k onto the row space of Y_0 is

$$Y_k^{\parallel} = Y_k Y_0^T \left(Y_0 Y_0^T\right)^+ Y_0. \tag{6.112}$$

The theorem of stochastic subspace identification [80] states that this projection can be represented as a product of observability matrix and the filtered states, *i.e.* $Y_k^{\parallel} = M_o \bar{U}_k$, and hence, $\bar{U}_k = \Sigma_r^{-1/2} U_r^T Y_k^{\parallel}$. Expressing this latter relationship for two consecutive time steps, m and $m+1$, gives

$$\bar{U}_m = \Sigma_r^{-1/2} U_r^T Y_m^{\parallel} \quad \text{and} \quad \bar{U}_{m+1} = \Sigma_r^{-1/2} U_r^T Y_{m+1}^{\parallel}. \tag{6.113}$$

Second, the innovation model, eqs. (6.99), is recast in matrix form as

$$\begin{cases} \bar{U}_{m+1} = A_s \bar{U}_m + K\rho_v; \\ \hat{Y}_m = C\ \bar{U}_m + \rho_v, \end{cases} \tag{6.114}$$

where array $\hat{Y}_m = [\underline{y}_m \quad \underline{y}_{m+1} \quad \dots \quad \underline{y}_{m+n-1}]$ and $\rho_v = \left[\underline{\epsilon}_m \quad \underline{\epsilon}_{m+1} \quad \dots \quad \underline{\epsilon}_{m+n-1}\right]$. Since the system matrices A_s and C, and the filtered states $\bar{U}_{m+1}$, $\bar{U}_m$, and measured outputs $\hat{Y}_m$ are now known, the residuals, $K\rho_v$ and ρ_v, are easy evaluated from eqs. (6.114). Finally, the covariance matrices are estimated from the residuals

$$\begin{bmatrix} E_w & E_s \\ E_s^T & E_v \end{bmatrix} = \begin{bmatrix} K\rho_v \\ \rho_v \end{bmatrix} \left[(K\rho_v)^T \ \rho_v^T\right]. \tag{6.115}$$

It is now possible to formulate the discrete time algebraic Riccati equation (6.94), and find its solution, P, defined by eq. (6.94), and compute the Kalman filter gain matrix K, see eq. (6.95). Note that the computation of Kalman filter gain matrix is left as a user option.

The last step of proposed system identification algorithm includes the determination of matrices B_s and D. Once all the other unknowns are found, the problem becomes linear in the unknowns B_s and D. The least-square regression is used to solve a redundant of linear equations for rest of the unknowns. The innovation model, eqs. (6.96), is reformulated

$$\begin{cases} \underline{\bar{u}}_{k+1} = K\underline{y}_k + \bar{A}_s \underline{\bar{u}}_k + (B_s - KD)\,\underline{f}_k; \\ \underline{y}_k = C\underline{\bar{u}}_k + D\underline{f}_k + \underline{\epsilon}_k. \end{cases} \tag{6.116}$$

where the noise array $\underline{\epsilon}_k$ is eliminated from the first equation using the second one of eqs. (6.96), and the closed-loop exponential characteristic matrix, $\bar{A}_s = A_s - KC$. It has been proved the gain matrix, $K = -G_d$, which implies $\bar{A}_s$ is the same as that defined in section 6.2.1. The solution of innovational model can be written here again

as convolution

$$\underline{y}_k = \sum_{j=0}^{k-1} C\bar{A}_s^{k-1-j} K \underline{y}_j + C\bar{A}_s^k \underline{u}_0 + \sum_{j=0}^{k-1} C\bar{A}_s^{k-1-j} \left(B_s - KD\right) \underline{f}_j + D\underline{f}_k + \underline{\epsilon}_k. \quad (6.117)$$

Furthermore, the system outputs, $\underline{y}_k$, are reformulated as a linear functions of unknowns of $\underline{u}_0$, B_s and D, $\underline{y}_k = \underline{y}_k^K + \mathcal{A}_k \underline{\mathcal{B}} + \underline{\epsilon}_k$, the array $\mathcal{A}_k$ and vectors $\underline{y}_k^K$, $\underline{\mathcal{B}}$ are cast of

$$\begin{aligned} \mathcal{A}_k &= \left[\begin{array}{cc} C\bar{A}_s^k & \sum_{j=0}^{k-1} \underline{f}_j^T \otimes C\bar{A}_s^{k-1-j} \end{array} \quad \begin{array}{c} \underline{f}_k^T \otimes I - \sum_{j=0}^{k-1} \underline{f}_j^T \otimes C\bar{A}_s^{k-1-j} K \end{array} \right], \\ \underline{y}_k^K &= \sum_{j=0}^{k-1} C\bar{A}_s^{k-1-j} K \underline{y}_j, \quad \underline{\mathcal{B}} = \left| \begin{array}{c} \underline{u}_0 \\ \mathrm{vec}(B_s) \\ \mathrm{vec}(D) \end{array} \right|. \end{aligned} \quad (6.118)$$

Finally, the remaining unknowns, stored in array $\underline{\mathcal{B}}$, are obtained from a least squares approximation as

$$\arg \min_{\underline{u}_0, B_s, D} \sum_{k=0}^{n} \left[\underline{y}_k - \underline{y}_k^K - \mathcal{A}_k \underline{\mathcal{B}} \right]^2. \quad (6.119)$$

After the initial conditions, $\underline{u}_0$, and the input dependency matrices, B_s and D, were computed, the forward innovation model, eqs. (6.96), associated with the combined deterministic-stochastic model, are constructed.

6.6 Practical Implementation of the Robust Identification Approach

To be effective in the system identification of large multibody systems, the details of the implementation of the proposed robust identification approach must be carefully considered. It is known from control theory [55] that a system with repeated eigenvalues and independent mode shapes is not identifiable by single input and single output data. To overcome this shortage, the current work is aimed at constructing the minimum order plant from the multi-inputs and multi-outputs data. To be effective in

the system identification, the inputs block, including N_c inputs, is defined

$$f_k^b = \left[\underline{f}_k^{(1)} \quad \underline{f}_k^{(2)} \quad \cdots \quad \underline{f}_k^{(N_c)}\right] = \begin{bmatrix} f_k^{(1)} & 0 & \dots & 0 \\ 0 & f_k^{(2)} & \dots & 0 \\ \vdots & \vdots & \ddots & \vdots \\ 0 & 0 & \dots & f_k^{(N_c)} \end{bmatrix}, \tag{6.120}$$

and the inputs perturbations, to excite the interested modes of dynamic systems, are presented by the discrete time data sequences

$$f_k^b = \begin{cases} f_k^d, \ k = 0, 1, \dots, \ell - 1; \\ 0, \ k = \ell, \ell + 1, \dots, \end{cases} \tag{6.121}$$

correspondingly, the output blocks, y_k^b, consisted of N_s sensors, $\underline{y}_k^{(i)}$, measured from numerical simulation or experimental data, for $i = 1, 2, \dots, N_c$, are assembled

$$y_k^b = \left[\underline{y}_k^{(1)} \quad \underline{y}_k^{(2)} \quad \cdots \quad \underline{y}_k^{(N_c)}\right], \quad \text{where} \quad \underline{y}_k^{(i)} = \left| \begin{matrix} y_1^{(i)} \\ y_2^{(i)} \\ \vdots \\ y_{N_s}^{(i)} \end{matrix} \right|_k . \tag{6.122}$$

The output block Hankel matrices, $\mathbb{Y}_0$ and $\mathbb{Y}_k$ for $k = \ell, \ell + 1$, are constructed

$$\mathbb{Y}_0 = \begin{bmatrix} y_0^b & y_1^b & \dots & y_{n-1}^b \\ y_1^b & y_2^b & \dots & y_n^b \\ \vdots & \vdots & \ddots & \vdots \\ y_{\ell-1}^b & y_\ell^b & \dots & y_{\ell+n-2}^b \end{bmatrix}, \ \mathbb{Y}_k = \begin{bmatrix} y_k^b & y_{k+1}^b & \dots & y_{k+n-1}^b \\ y_{k+1}^b & y_{k+2}^b & \dots & y_{k+n}^b \\ \vdots & \vdots & \ddots & \vdots \\ y_{k+m-1}^b & y_{k+m}^b & \dots & y_{k+m+n-2}^b \end{bmatrix}. \tag{6.123}$$

Without loss of generality, the output block Hankel matrices, $\mathbb{Y}_0$ and $\mathbb{Y}_k$ for $k = \ell, \ell + 1$, have different dimensions, ℓN_s for $\mathbb{Y}_0$ and mN_s for $\mathbb{Y}_k$. If $\ell = m$ and $N_c = 1$, $\mathbb{Y}_0$ and $\mathbb{Y}_k$ will be recovered from the output Hankel matrices. If the input-output behavior was predicted by the innovation model, the state block array, $\bar{\mathbb{U}}_k$, and the residual block array, ρ_v^b, will be

$$\bar{\mathbb{U}}_k = \left[\bar{U}_k^b, \bar{U}_{k+1}^b, \dots, \bar{U}_{k+n-1}^b\right] \quad \text{and} \quad \rho_v^b = \left[\underline{\epsilon}_\ell^b, \underline{\epsilon}_{\ell+1}^b, \dots, \underline{\epsilon}_{\ell+n-1}^b\right], \tag{6.124}$$

where the state blocks, $\bar{U}_k^b$, and residual withe noise blocks, $\underline{\epsilon}_k^b$, are cast as

$$\bar{U}_k^b = \left[\underline{\bar{u}}_k^{(1)}, \underline{\bar{u}}_k^{(2)}, \ldots, \underline{\bar{u}}_k^{(N_c)}\right] \quad \text{and} \quad \underline{\epsilon}_k^b = \left[\underline{\epsilon}_k^{(1)}, \underline{\epsilon}_k^{(2)}, \ldots, \underline{\epsilon}_k^{(N_c)}\right]. \tag{6.125}$$

The output block data correlation matrices, $\mathbb{O}_0$ and $\mathbb{O}_1$, are defined as

$$\mathbb{O}_0 = \mathbb{Y}_\ell \mathbb{Y}_0^T \quad \text{and} \quad \mathbb{O}_1 = \mathbb{Y}_{\ell+1} \mathbb{Y}_0^T, \tag{6.126}$$

and presented by the following factorizations

$$\mathbb{O}_0 = M_o \bar{\mathbb{U}}_\ell \mathbb{Y}_0^T \quad \text{and} \quad \mathbb{O}_1 = M_o A_s \bar{\mathbb{U}}_\ell \mathbb{Y}_0^T. \tag{6.127}$$

If the truncated singular value decomposition of $\mathbb{O}_0$ is performed, $\mathbb{O}_0 = U_r \Sigma_r V_r^T$, where r is the truncated rank, the observability matrix, M_o, is selected, $M_o = U_r \Sigma_r^{1/2}$, and matrix product, $\bar{\mathbb{U}}_\ell \mathbb{Y}_0^T = \Sigma_r^{1/2} V_r^T$. The exponential characteristic matrix, A_s, can be computed from data correlation matrix $\mathbb{O}_1$, the second equation of eqs. (6.127), as

$$A_s = \Sigma_r^{-1/2} U_r^T \mathbb{O}_1 V_r \Sigma_r^{-1/2}, \tag{6.128}$$

and matrix C is determined by the observability matrix, M_o, the first N_s rows.

As discussed above, the identification approach produces estimates of r characteristic exponents of the system contained in matrix, A_s, eq. (6.128). If the available data is unlikely sufficient to identify all the characteristic exponents of the system, then r is less than the order, $2N$, of the system. The reliability of these estimates is guaranteed by applying proper external excitations to provide enough energy to all relevant modes. Note that the determination of the order, r, of the identified system, or the determination of the singular energy ratio criterion, E_r, eq. (A.3), equivalently, is left as a user definition.

In view of eq. (6.123), $\mathbb{Y}_0$ and $\mathbb{Y}_k$ are the outputs block Hankel matrices of size, $\ell N_s \times n N_c$ and $m N_s \times n N_c$, respectively, where n is the preliminary estimate of the observable order of the system. It will be evaluated from the following criteria. First, the output block Hankel matrices, $\mathbb{Y}_\ell$ and $\mathbb{Y}_{\ell+1}$, should feature more lines than

columns, *i.e.* $mN_s = \alpha\, nN_c$, where $\alpha > 1$ is a user defined parameter. Second, matrix $\mathbb{Y}_0$ is selected to be square, *i.e.* $\ell N_s = nN_c$. Third, it is desirable to use as much of the available data as possible, *i.e.* $\ell + m + n - 1 = N_d - 1$, where N_d is the total length of the output signals. Solving these equations yields

$$\ell = \frac{N_c N_d}{(1+\alpha)N_c + N_s}, \quad m = \frac{\alpha N_c N_d}{(1+\alpha)N_c + N_s}, \quad n = \frac{N_s N_d}{(1+\alpha)N_c + N_s}. \tag{6.129}$$

Matrices $\mathbb{Y}_\ell$ and $\mathbb{Y}_{\ell+1}$ could be rank deficient due to the redundant nature of the sampled data. Hence, the singular value decomposition technique [41] is used to perform a singular truncation of $\mathbb{Y}_k$ by the condition, eq. (A.2). Note that the outputs block Hankel matrices, $\mathbb{Y}_\ell$ and $\mathbb{Y}_{\ell+1}$, must be assembled by using the output data of free impulse response. When $\ell < N_i$, N_i is the total length of input signals, $\mathbb{Y}_\ell$ and $\mathbb{Y}_{\ell+1}$ will be affected by the forced response. In this case, matrices $\mathbb{Y}_\ell$ and $\mathbb{Y}_{\ell+1}$ must be reassembled to only involve the free response part of the output data, *i.e.* $m+n-1 = N_f - 1$; the starting point is N_i and N_f is the total number of data points of the free response part of a signal, $N_f = N_d - N_i$. The sizes of matrices $\mathbb{Y}_0$, $\mathbb{Y}_\ell$ and $\mathbb{Y}_{\ell+1}$ are still determined by the following conditions: $mN_s = \alpha\, nN_c$ and $\ell N_s = nN_c$. The parameters ℓ, m and n now become

$$\ell = \frac{N_c N_f}{\alpha N_c + N_s}, \quad m = \frac{\alpha N_c N_f}{\alpha N_c + N_s}, \quad n = \frac{N_s N_f}{\alpha N_c + N_s}. \tag{6.130}$$

The projections, $\mathbb{Y}_\ell^{\|}$ and $\mathbb{Y}_{\ell+1}^{\|}$, are defined as

$$\mathbb{Y}_\ell^{\|} = \mathbb{Y}_\ell \mathbb{Y}_0^T \left(\mathbb{Y}_0 \mathbb{Y}_0^T\right)^+ \mathbb{Y}_0 \quad \text{and} \quad \mathbb{Y}_{\ell+1}^{\|} = \mathbb{Y}_{\ell+1} \mathbb{Y}_0^T \left(\mathbb{Y}_0 \mathbb{Y}_0^T\right)^+ \mathbb{Y}_0, \tag{6.131}$$

and the filtered state arrays at two consecutive time steps, ℓ and $\ell+1$, are computed

$$\bar{\mathbb{U}}_\ell = \Sigma_r^{-1/2} U_r^T \mathbb{Y}_\ell^{\|} \quad \text{and} \quad \bar{\mathbb{U}}_{\ell+1} = \Sigma_r^{-1/2} U_r^T \mathbb{Y}_{\ell+1}^{\|}. \tag{6.132}$$

The state and output residual block arrays, $K\rho_v^b$ and ρ_v^b, will be computed from the following forward innovation model in matrix block form,

$$\begin{cases} \bar{\mathbb{U}}_{\ell+1} = A_s \bar{\mathbb{U}}_\ell + K\rho_v^b; \\ \hat{\mathbb{Y}}_\ell = C\bar{\mathbb{U}}_\ell + \rho_v^b, \end{cases} \tag{6.133}$$

where array $\hat{\mathbb{Y}}_\ell = [\underline{y}^b_\ell \quad \underline{y}^b_{\ell+1} \quad \dots \quad \underline{y}^b_{\ell+n-1}]$. The average of residual blocks associated with all the inputs, $K\rho^b_v$ and ρ^b_v, are computed and used to evaluate the error covariance matrices, E_w, E_s and E_v using eqs. (6.115). It is now possible to compute the Kalman filter gain matrix, K, eq. (6.95), by solving discrete time algebraic Riccati equations using a Schur-type algorithm [2]. Note that the computation of Kalman filter gain matrix is left as a user option. The unknowns B_s and D are computed by solving a redundant of linear equations. If the initial conditions are zero, $\underline{u}_0 = 0$, the system outputs, $\underline{y}^{(i)}_k$, are reformulated as a linear functions of unknowns of B_s and D, $\underline{y}^{(i)}_k = \underline{y}^{K^{(i)}}_k + \mathcal{A}^{(i)}_k \underline{\mathcal{B}}^{(i)} + \underline{\epsilon}^{(i)}_k$, the array $\mathcal{A}^{(i)}_k$ and vectors $\underline{y}^{K^{(i)}}_k$, $\underline{\mathcal{B}}^{(i)}$ are cast of

$$\begin{aligned} \mathcal{A}^{(i)}_k &= \left[\sum_{j=0}^{k-1} f^{(i)}_j C\bar{A}^{k-1-j}_s, \quad \mathrm{diag}(f^{(i)}_k) - \sum_{j=0}^{k-1} f^{(i)}_j C\bar{A}^{k-1-j}_s K\right], \\ \underline{y}^{K^{(i)}}_k &= \sum_{j=0}^{k-1} C\bar{A}^{k-1-j}_s K\underline{y}^{(i)}_j \quad \text{and} \quad \underline{\mathcal{B}}^{(i)} = \left| \begin{array}{c} \underline{bs}_i \\ \underline{d}_i \end{array} \right|, \end{aligned} \tag{6.134}$$

where $\underline{bs}_i$ and $\underline{d}_i$ are i^{th} columns of matrices B_s and D, respectively. For $k = 0, 1, \dots, N_d - 1$, a redundant of linear equations are cast and $\underline{\mathcal{B}}^{(i)}$ are solved by the least-square technology

$$\underline{\mathcal{B}}^{(i)} = \left(\left[\begin{array}{c} \mathcal{A}^{(i)}_0 \\ \mathcal{A}^{(i)}_1 \\ \vdots \\ \mathcal{A}^{(i)}_{N_d-1} \end{array} \right]^T \left[\begin{array}{c} \mathcal{A}^{(i)}_0 \\ \mathcal{A}^{(i)}_1 \\ \vdots \\ \mathcal{A}^{(i)}_{N_d-1} \end{array} \right] \right)^{-1} \left[\begin{array}{c} \mathcal{A}^{(i)}_0 \\ \mathcal{A}^{(i)}_1 \\ \vdots \\ \mathcal{A}^{(i)}_{N_d-1} \end{array} \right]^T \left| \begin{array}{c} \underline{y}^{(i)}_0 - \underline{y}^{K^{(i)}}_0 \\ \underline{y}^{(i)}_1 - \underline{y}^{K^{(i)}}_1 \\ \vdots \\ \underline{y}^{(i)}_{N_d-1} - \underline{y}^{K}_{N_d-1}{}^{(i)} \end{array} \right|. \tag{6.135}$$

The procedure is repeated for $i = 1, 2, \dots, N_c$ till all the unknowns of B_s and D are computed.

Summarily, the whole procedure is described in details as follow

1. Assemble the outputs block Hankel matrices, $\mathbb{Y}_0$, $\mathbb{Y}_\ell$ and $\mathbb{Y}_{\ell+1}$, eqs. (6.123), and compute the data correlation matrices $\mathbb{O}_0 = \mathbb{Y}_\ell \mathbb{Y}^T_0$ and $\mathbb{O}_1 = \mathbb{Y}_{\ell+1}\mathbb{Y}^T_0$.

2. Perform the singular value decomposition of data correlation matrix, $\mathbb{O}_0$, using Lanczos algorithm, $\mathbb{O}_0 = U_r \Sigma_r V_r^T$. Compute the observability matrix, $M_o = U_r \Sigma_r^{1/2}$ and matrix product, $\bar{\mathbb{U}}_\ell \mathbb{Y}_0^T = \Sigma_r^{1/2} V_r^T$.

3. Compute exponential characteristic matrix, $A_s = \Sigma_r^{-1/2} U_r^T \mathbb{O}_1 V_r \Sigma_r^{-1/2}$. Matrix C is extracted from the observability matrix, M_o, the first N_s rows.

4. Compute the projections, $\mathbb{Y}_\ell^{\parallel}$ and $\mathbb{Y}_{\ell+1}^{\parallel}$, from eqs. (6.131), and the filtered state sequences, $\bar{\mathbb{U}}_\ell$ and $\bar{\mathbb{U}}_{\ell+1}$, from eqs. (6.132).

5. Compute the covariance matrices, E_w, E_s and E_v, using eqs. (6.115), and determine the Kalman filter gain matrix, K, by solving the discrete time algebraic Riccati equations.

6. Compute matrices B_s and D by using least squares technique to solve eq. (6.135).

7. Compute accuracy indicators, modal amplitude coherence, eq. (6.58), and mode singular value, eq. (6.61).

6.7 Numerical Example

Three examples will be presented to validate the identification approaches described in this chapter.

6.7.1 Identification of Phugoid Mode

The first example deals with a hovering of the helicopter as shown in fig. 6.1 in the presence of a random wind disturbance.

Bryson and Mills [25] use a simplified rigid body system to describe the motion of the helicopter; a linear state space model is formulated, $\dot{\underline{u}}(t) = A\underline{u}(t) + B\underline{f}(t)$, the system matrices, A and B, the state vector $\underline{u}(t)$ and the control inputs $\underline{f}(t)$ are

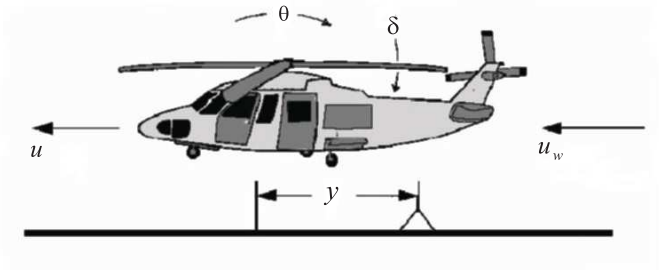

Figure 6.1: The hovering helicopter suffering a wind disturbance.

defined as

$$A = \begin{bmatrix} X_u & X_q & -0.322 & 0 \\ M_u & M_q & 0 & 0 \\ 0 & 1 & 0 & 0 \\ 1 & 0 & 0 & 0 \end{bmatrix}, \; B = \begin{bmatrix} X_\delta & -X_u \\ M_\delta & -M_u \\ 0 & 0 \\ 0 & 0 \end{bmatrix}, \; \underline{u}(t) = \begin{bmatrix} u \\ q \\ \theta \\ y \end{bmatrix}, \; \underline{f}(t) = \begin{bmatrix} \delta \\ u_w \end{bmatrix},$$

where u is the horizontal velocity of the helicopter relative to the ground, q the rate of the pitch angle, θ, of the fuselage, $q = \dot{\theta}$, y horizontal displacement; for control inputs, δ is the deflection of the longitudinal cyclic stick input and u_w the horizontal wind velocity. In the system matrices, X_u, X_q, M_u and M_q are the aerodynamic stability derivatives, X_δ and M_δ the aerodynamic control derivatives. When nominal values of these parameters are selected as, $X_u = -0.0257$, $X_q = 0.013$, $M_u = 1.26$, $M_q = -0.765$, and $X_\delta = 0.086$, $M_\delta = -0.408$, the eigenvalues of the system are $[0, -1.8891, 0.0492 \pm 0.4608\mathbf{i}]$, corresponding to a position mode, a damped pitching mode, and a slightly unstable phugoid mode, respectively.

The proposed identification approach was used to evaluate the unstable phugoid mode from input-output data. Two sensors, the horizontal velocity u and the pitch angle θ, were selected. If they are "polluted" by the stochastic inflow, u_w, the outputs can be presented by equations, $\underline{y}(t) = C\underline{u}(t) + D\underline{f}(t)$, where matrices C and D are

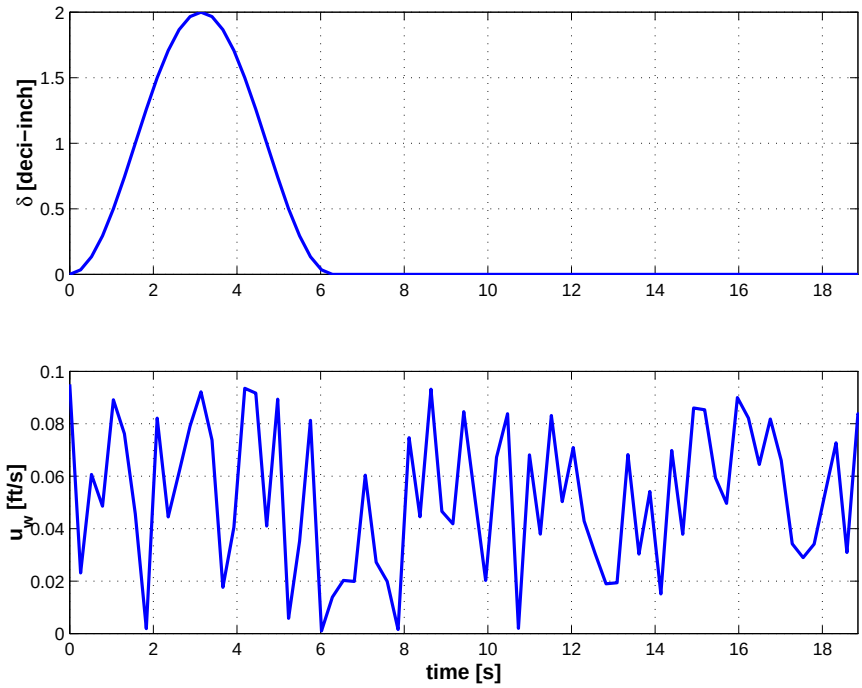

Figure 6.2: The control inputs data; top figure: control input $\delta(t)$; bottom figure: the stochastic wind $u_w(t)$.

defined as

$$C = \begin{bmatrix} 1 & 0 & 0 & 0 \\ 0 & 0 & 1 & 0 \end{bmatrix} \quad \text{and} \quad D = \begin{bmatrix} 0 & 1 \\ 0 & 1 \end{bmatrix}.$$

The time continuous state space model has been discretized by using the MATLAB function C2D with a sampling period $\Delta t = 0.2618$ sec. The control input $\delta(t)$ is defined as $\delta(t) = 1 - \cos(t)$ for $t \in [0, 6.28]$ sec, and $\delta(t) = 0$ for $t > 6.28$ sec. The stochastic wind velocity, u_w, is modeled by the MATLAB function NOISE and shown in figs. 6.2. The MATLAB function DLSIM is applied to compute the discrete time data series for the outputs $\underline{y}_k$. The sole $\delta(t)$ is selected as control input for system identification. The window of size $[0, 18.85]$ sec is selected and the associated input-output data is sampled. For various rank numbers, r, of the output block Hankel matrix, a subspace plant was identified; the phugoid mode was extracted and shown in table 6.1.

Table 6.1: Frequencies and damping rates extracted by using proposed approach.

Rank	Frequencies (rad/s)	Dampings(%)	Mode SV	Modal AC	Discrepancy
2	0.46362	10.509	1.00000	1.000	0.1696
3	0.46377	10.649	1.00000	1.000	0.0822
6	0.46353	10.648	0.89271	1.000	0.0345
12	0.46353	10.649	1.00000	1.000	0.0344
15	0.46353	10.637	1.00000	1.000	0.0369

The first column of this table lists the rank number; the next two columns show the frequency and damping rate associated with the phugoid mode. The next two columns list the mode singular value κ, see eq. (6.61), and the modal amplitude coherence γ, see eq. (6.58). The last column gives the discrepancy between the time history of measured velocity u and its reconstruction, see eq. (4.55). For a rank number $r = 3$, the singular energy ratio, see eq. (A.3), was found to be $E_r = 99.9996\%$. Good correlation is found between the extracted mode and its analytical counterpart, $\omega_p = 0.46344$ rad/sec, $\zeta_p = 10.611\%$.

The proposed identification method was applied to construct a forward innovation model, eqs. (6.96). The estimated system matrices were

$$A_s = \begin{bmatrix} 1.0108 & 0.1019 & 0.0003 \\ -0.1463 & 1.0001 & 0.0011 \\ -0.0414 & 0.0249 & 0.9359 \end{bmatrix}, \; B_s = \begin{bmatrix} 0.0085 \\ 0.0101 \\ 0.048 \end{bmatrix},$$

$$C = \begin{bmatrix} 31.341 & -36.388 & 0.6147 \\ -70.907 & -32.942 & 1.7078 \end{bmatrix}, \; D = \begin{bmatrix} 0.1658 \\ 1.1545 \end{bmatrix},$$

and the Kalman filter gain matrix

$$K = \begin{bmatrix} 0.0023 & -0.0011 \\ -0.0003 & 0.0003 \\ 0.0040 & -0.0068 \end{bmatrix}.$$

The forced responses of the system and its approximation evaluated from the above innovation model are compared in figs. 6.3, where the control input δ is depicted by figs. 6.2. Excellent correlation is found between the two predictions.

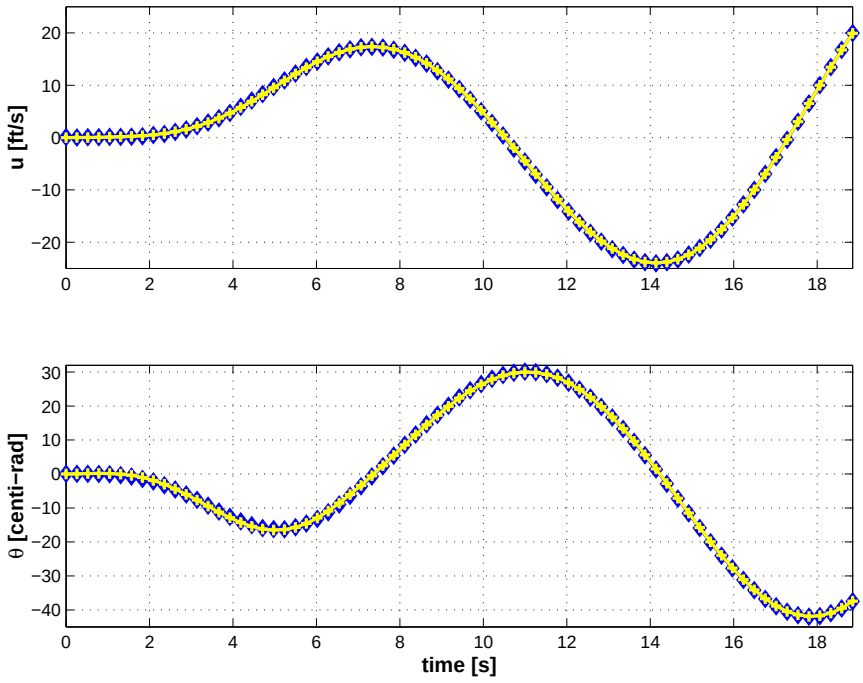

Figure 6.3: The responses of the system and associated approximations. Top figure: horizontal velocity u. Bottom figure: pitch angle of the fuselage θ. The system outputs: $\diamond$; The curve fitting: $+$.

The eigensystem realization algorithm combined with observer/Kalman filter identification and the subspace identification approach both are applied to construct a subspace model by using the same input-output data. The estimates of the phugoid mode, including the frequency and damping rate, are compared with those of the proposed robust identification approach and shown in tables 6.2 and 6.3. In each table, the second column contains the results of the proposed robust identification approach, the third lists the results of subspace identification algorithm, the last those of eigensystem realization algorithm combined with observer/Kalman filter identification. Note that as the rank number r increases to 12, all approaches give an excellent

estimate of the phugoid mode. However, the proposed approach gives excellent estimates even for low rank numbers.

Table 6.2: Frequencies, rad/sec, extracted by different approaches.

Rank	Robust ID	Subspace ID	ERA-OKID
2	0.46362	0.48686	11.20400
3	0.46377	0.47097	11.20000
6	0.46353	0.46350	0.47174
12	0.46353	0.46358	0.46353
15	0.46353	0.46345	0.46353

Table 6.3: Damping rates, in %, extracted by different approaches.

Rank	Robust ID	Subspace ID	ERA-OKID
2	10.509	0.703	6.536
3	10.649	10.671	6.307
6	10.648	10.418	9.190
12	10.649	10.413	10.625
15	10.637	10.518	10.625

6.7.2 Reconstruction of Flutter of a Rectangular Planform Wing

The second example deals with the identification of the flutter of a rectangular planform wing [40]. The proposed system identification algorithm is applied to identify a subspace model to capture the physical properties of the system. The details of the configurations of the system and the aerodynamic modeling have been described in section 5.2.

Two cases were studied for system identification: the first case, denoted *case 1*, the far flow velocity was $U_f = 480$ ft/sec; the second case, denoted *case 2*, the far flow velocity $U_f = 590$ ft/sec. For *case 1*, the control input was selected as the wing angle of attack, described by a impulse, $\theta(t) = a_0 - a_0 \cos(10\pi t)$ for $t \in [0, 0.2]$ sec, where the amplitude was $a_0 = 0.0175$ rad. The dynamic response under this

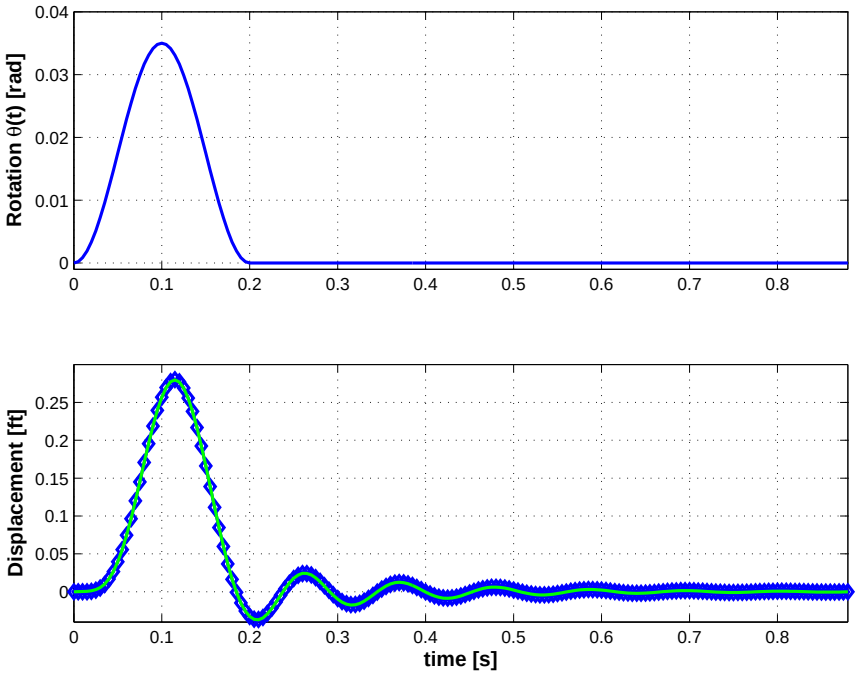

Figure 6.4: The input-output data; top figure, control input; bottom figure, measured output and its reconstruction; measured output: $\diamond$; reconstruction: solid line.

input was computed by using the finite element based multibody formulation [8, 9] for a total period of 0.88 seconds, using a constant time step $\Delta t = 1$ msec. The transverse displacement at the tip of the wing was selected as the control output. When the rank of the outputs block Hankel matrices was predetermined, $r = 4$, the Hankel matrices were assembled and factorized by singular value decomposition. The associated singular energy ratio, eq. (A.3), was computed, $E_{r_{\mathbb{O}_0}} = 99.9733\%$, and the 4^{th} order forward innovation model would be identified

$$A_s = \begin{bmatrix} 0.9969 & -0.0448 & -0.0011 & -0.0001 \\ 0.0754 & 0.9871 & -0.0046 & -0.0005 \\ 0.0099 & -0.0050 & 0.9386 & -0.0270 \\ -0.0063 & 0.0024 & 0.0541 & 0.9970 \end{bmatrix}, \; B_s = \begin{bmatrix} 0.4981 \\ -0.6238 \\ 0.3646 \\ -0.2706 \end{bmatrix},$$

$$C = [0.6568, 1.2199, 0.2478, 0.0248]\,, D = [1.6654]\,, K = \begin{bmatrix} 0.0036 \\ -0.0043 \\ 0.0346 \\ -0.2372 \end{bmatrix}.$$

Finally, the control output was evaluated by this model, and compared with the measured output, see the lower part of figs. 6.4. Clearly, a good correlation was found.

Table 6.4: Identified torsional mode by proposed identification approach.

Rank	Frequencies (rad/s)	Damping(%)	Mode SV	Modal AC
4	71.664	-62.077	0.07783	1.000
6	71.459	-61.373	0.04125	0.999
8	72.658	-60.486	0.03746	1.000
12	71.408	-71.116	0.04555	1.000
16	70.712	-72.141	0.13848	1.000
20	72.360	-71.085	0.07949	1.000

Table 6.5: Identified bending mode by proposed identification approach.

Rank	Frequencies (rad/s)	Damping(%)	Mode SV	Modal AC
4	63.314	1.660	1.00000	1.000
6	63.312	1.661	1.00000	1.000
8	63.313	1.666	1.00000	1.000
12	63.387	1.682	1.00000	1.000
16	63.351	1.582	0.96487	1.000
20	63.346	1.575	0.98252	1.000

For *case 2*, the same control input as that of *case 1* was used. The dynamic simulation was run for a total period of 0.88 seconds, using the time step $\Delta t = 1$ msec. Two sensors were selected as control outputs: the transverse displacement and the torsional moment at the tip of the wing. It has been extracted in section 5.2 the flutter speed was $U_F = 585$ ft/sec, and the lowest bending and torsional modes nearly coalesce. For different rank r, these two lowest modes were evaluated by proposed

identification algorithm; the associated frequencies and damping rates were shown in tables 6.4 and 6.5.

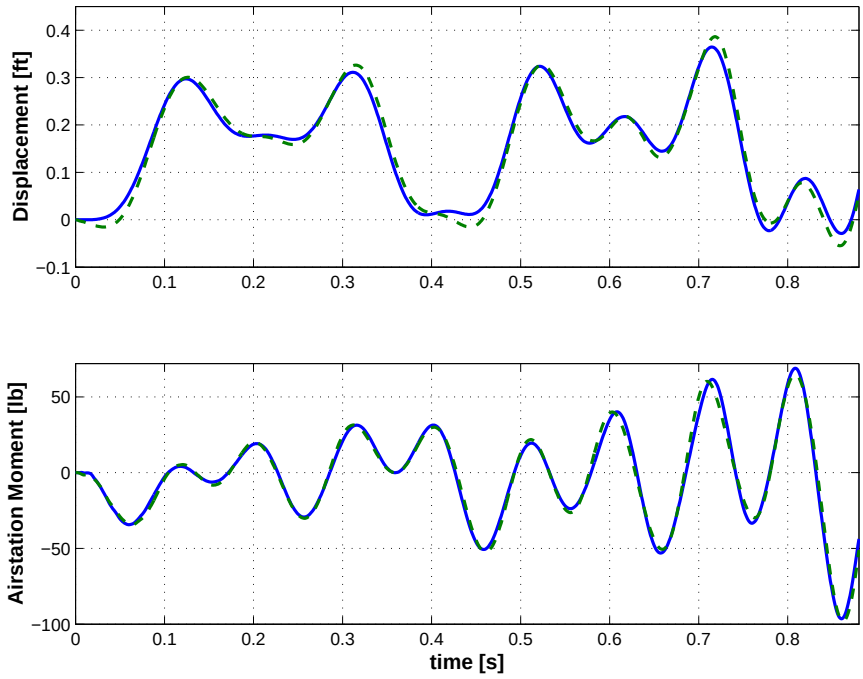

Figure 6.5: The outputs and associated reconstructions; top figure, the transverse displacement; bottom figure, the torsional moment; measured output: solid line; reconstruction: dashed line.

These results were checked by testing the input-output behavior. For the rank $r = 16$, the control input was defined, $\theta(t) = a_0 - a_0/2(\cos(10\pi t) + \cos(5\pi t))$ for $t \in [0,\ 0.88]$ sec and $a_0 = 0.015$ rad; the dynamic response was simulated again by the finite element based dynamic simulation code [8, 9], and compared with the estimates evaluated from the identified model, see figs. 6.5. The amplitude of torsional moment is much larger than that of the transverse displacement. It means that the torsional moment is "easily" excited and "easily" observed. It explains why the curve fitting of torsional moment, in figs. 6.5, was better than the other.

6.7.3 Reconstruction of Flutter of a Wing-Aileron System

The second aeroelastic problem considers the flutter of a wing-aileron system, fig. 6.6. The configurations of the rectangular planform wing and the aerodynamic modeling have been described in section 5.2. Due to symmetry, a half configuration was modeled and proper symmetry conditions were applied. The half wing has a rectangular planform of length $L_w = 20$ ft and chord length $c = 6$ ft. The trailing edge flap of length $L_f = 3$ ft extends over the half wing along the axial axes from 15 ft to 18 ft.

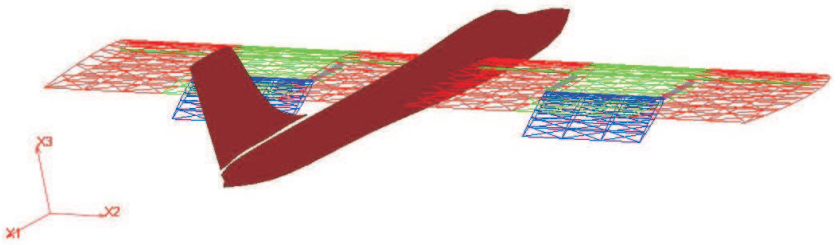

Figure 6.6: Configuration of the wing-aileron system.

The structural properties of the flap are described as follow: bending stiffness, $EI_f = 4.7\ 10^5$ lbs·ft^2, torsional stiffness, $GJ_f = 2.4\ 10^4$ lbs·ft^2, mass per unit span, $m_f = 0.75$ slugs/ft, polar moment of inertia, $I_f = 1.95$ slugs·ft. The flap is attached to the wing by means of two brackets of length $L_b = 3.1$ ft; the associated flap hinge is located at 85% chord. On the inboard side, the flap is attached to the bracket by means of a revolute joint followed by a flexible joint and a universal joint consequently. The flexible joint defines a torsional spring with stiffness, $k_\theta = 5\ 10^6$ lbs·ft^2, to describe the relative rotation of the flap. On the outboard side, the flap is attached to the wing with a prismatic joint followed by a spherical joint. These joints allow the deformations of the wing and flap are independent. The wing-aileron system was discretized by finite element based multibody formulation [8, 9], and a numerical model with 536 degrees of freedom was constructed, in which 28 aerodynamic inflow states are involved.

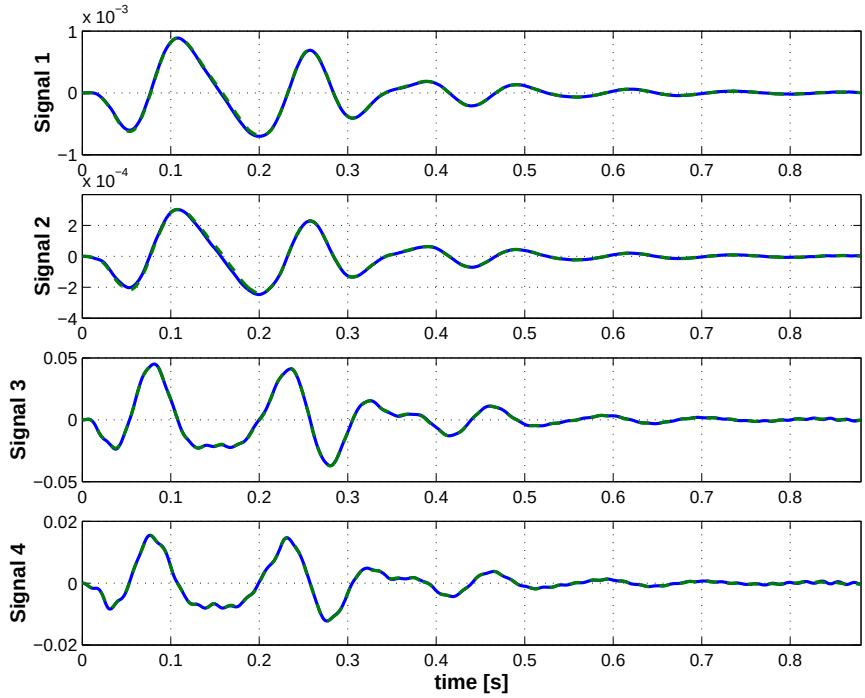

Figure 6.7: The control outputs; measured sensors: solid line; reconstructions: dashed line.

Two cases were studied for system identification: the first case, denoted *case 1*, the far flow velocity was $U_f = 480$ ft/sec; the second case, denoted *case 2*, the far flow velocity $U_f = 590$ ft/sec. For *case 1*, the relative rotation of flap was selected as the control input, and defined as impulse, $\theta_f(t) = b_0 - b_0 \cos(10\pi t)$ for $t \in [0,\ 0.2]$, with amplitude $b_0 = \pi/12$ rad. The dynamic simulation under this control input was run for a total period of 0.88 seconds, using a constant time step $\Delta t = 1$ msec. Four sensors: the transverse displacements and velocities at the tip of and in the middle of the wing, labeled signal 1, 2, 3, and 4, respectively, were selected as control outputs. When the rank of the outputs block Hankel matrix was predetermined, $r = 24$, a subspace model was constructed by using the proposed identification approach. The outputs have been evaluated from the identified plant and shown in figs. 6.7, and a good correlation was found.

For *case 2*, the wing angle of attack, θ_w, and the rotation of flap, θ_f, were used as

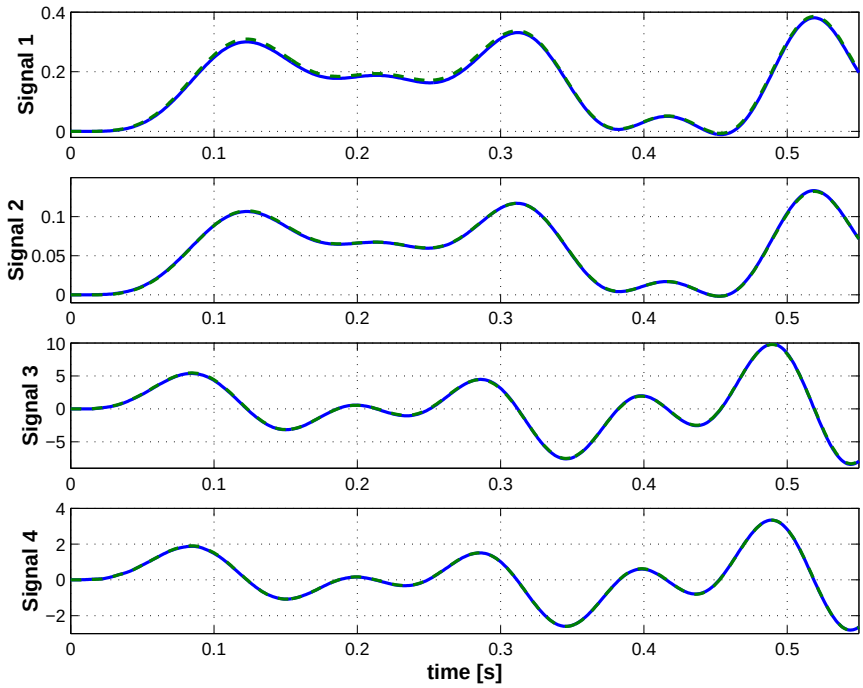

Figure 6.8: The control outputs; measured sensors: solid line; reconstructions: dashed line.

the control inputs; the definition of θ_f was the same as that of *case 1*, θ_w was defined as $\theta_w(t) = a_0 - a_0 \cos(10\pi t)$ for $t \in [0,\ 0.2]$ sec, with amplitude $a_0 = 1$ degree. Due to the flutter, the dynamic simulation under these two control inputs was run for a short period of 0.55 sec, using a constant time step $\Delta t = 1$ msec. The same control outputs as those of *case 1* were used. When the rank number was predetermined, $r = 24$, the proposed identification approach was used to identify a subspace plant model, and the estimated input-output behavior was tested. Two different control inputs were defined

$$\begin{cases} \theta_f(t) = b_0 - b_0 \cos(10\pi t) - b_0 \cos(5\pi t); \\ \theta_w(t) = a_0 - a_0 \cos(10\pi t) - a_0 \cos(5\pi t), \end{cases}$$

for $t \in [0,\ 0.55]$ sec. The dynamic simulation was run again, and the response was measured, and compared with its subspace plant reconstructions. The measured outputs and associated reconstructions were shown in figs. 6.8. Here again, a good

curve fitting was found.

6.8 Chapter Summary

System identification methodologies were investigated in this chapter. A robust approach was proposed, which inherited the merits of both minimum realization algorithms and subspace system identification approaches. First, the system truncation concepts were introduced, including the modal truncation and balanced truncation. Second, minimum realization algorithms, including the observer/Kalman filter identification, the Ho-Kalman algorithm, the eigensystem realization algorithm and its extension were reviewed. Third, subspace approaches, another branch of system identification methods, were briefly discussed. The basic issues and the procedure of the deterministic system identification were introduced. Fourth, the entire procedure for the determination of Kalman filters was described. Finally, a robust system identification approach was developed and implemented. Three examples were presented to validate the proposed approach. It shows that this approach accurately constructs subspace plant models of minimum order that capture the system physical properties.

CHAPTER VII

REALIZATION OF OPTIMAL CONTROL

The linearized optimal control, valid for small perturbations about an equilibrium configuration of the nonlinear system, is the focus of this chapter. Based on the identified subspace plant model discussed in chapter 6, the linear quadratic Gaussian controller is implemented for flexible multibody systems, and applied to practical problems. At first, the dynamic response of the comprehensive multibody systems was computed by using the finite element based numerical simulation tool. Then, the robust system identification algorithm, proposed in chapter 6, is applied to identify a subspace based plant model. Finally, the linear quadratic regulator gain matrix and the Kalman filter gain matrix are computed, and the linear quadratic Gaussian controller and linear feedback are implemented. Note that the robust identification approach is used to construct a forward innovation model, which eases the design of the linear quadratic controller. If a deterministic model was identified, the Kalman filter gain matrix will be computed based on user defined noise covariances. The determinations of linear quadratic regulator and Kalman filter rely on the solution of discrete time algebraic Riccati equations. The most general approaches are Schur-type algorithms [70, 2], which convert the problem to the generalized eigenvalue decomposition [82, 51, 71]. The process is further refined by using a Newton iteration technique [45, 2, 18] and the scaling procedure [43]. Practical implementation have shown that these approaches are very suitable for solving modest sized problems, *i.e.* problems of order less than about 100.

In this chapter, basic issues associated with optimal control and its application, including the linear quadratic regulator and the linear quadratic Gaussian controller,

are introduced. The Schur-type approach for solving the discrete time algebraic Riccati equations and associated refinements are also developed. The implementation of the linear quadratic Gaussian controller is discussed in details. Finally, three examples are presented to validate the proposed optimal control approach.

7.1 Optimization for Dynamic Systems

A general class of optimization problems for dynamical systems modeled by the deterministic equations (2.15) involves finding the values of N_c control parameters, $\underline{f}_k$, that minimize a performance index, $J(\underline{f}_k, \underline{u}_k)$, a scalar function of $2N + N_c$ parameters, $\underline{f}_k$ and $\underline{u}_k$. The performance index can be explicitly expressed in the following form

$$J = \frac{1}{2}\underline{u}_n^T C^T Q_n C \underline{u}_n + \sum_{k=0}^{n-1} \left(\frac{1}{2}\underline{y}_k^T Q_k \underline{y}_k + \underline{y}_k^T \hat{S}_k \underline{f}_k + \frac{1}{2}\underline{f}_k^T \hat{R}_k \underline{f}_k \right), \tag{7.1}$$

or alternatively,

$$J = \frac{1}{2}\underline{u}_n^T C^T Q_n C \underline{u}_n + \sum_{k=0}^{n-1} \left(\frac{1}{2}\underline{u}_k^T C^T Q_k C \underline{u}_k + \underline{u}_k^T C^T S_k \underline{f}_k + \frac{1}{2}\underline{f}_k^T R_k \underline{f}_k \right), \tag{7.2}$$

where Q_k and Q_n are positive semi-definite symmetric matrices, $Q_k = Q_k^T$ and $Q_n = Q_n^T$; $\hat{R}_k$ or R_k positive definite symmetric matrices, $\hat{R}_k = \hat{R}_k^T$ or $R_k = R_k^T$; furthermore, $Q_k - C^T S_k R_k^{-1} S_k^T C$ is positive semi-definite. The relationship between eqs. (7.1) and (7.2), together with the definitions of S_k and R_k can be found in Appendix C.

The optimal problem consists of finding the control inputs, $\underline{f}_k$, that minimize J. The dynamical system characterized by eqs. (2.15) must be driven from an initial state, $\underline{u}_0$, to a terminal state, $\underline{u}_n$, by using "acceptable" levels of control inputs, $\underline{f}_k$, and without exceeding "acceptable" amplitudes of state variables, $\underline{u}_k$. Since the equations of motion, eqs. (2.15), must be satisfied, they can be viewed as constraints, and the optimization problem is, in fact, a constrained optimization problem, which can be transformed into an unconstrained optimization problem with the help of the

Lagrange multiplier technique

$$\begin{aligned}\bar{J} &= \sum_{k=0}^{n-1}\left[\frac{1}{2}\underline{u}_k^T C^T Q_k C\underline{u}_k + \underline{u}_k^T C^T S_k \underline{f}_k + \frac{1}{2}\underline{f}_k^T R_k \underline{f}_k + \underline{\lambda}_{k+1}^T\left(A_s\underline{u}_k + B_s\underline{f}_k - \underline{u}_{k+1}\right)\right] \\ &+ \frac{1}{2}\underline{u}_n^T C^T Q_n C\underline{u}_n, \end{aligned} \tag{7.3}$$

where $\underline{\lambda}_{k+1}$ is a sequence of Lagrange multipliers. Defining a scalar sequence, $\mathcal{N}_k$,

$$\mathcal{N}_k = \frac{1}{2}\underline{u}_k^T C^T Q_k C\underline{u}_k + \underline{u}_k^T C^T S_k \underline{f}_k + \frac{1}{2}\underline{f}_k^T R_k \underline{f}_k + \underline{\lambda}_{k+1}^T\left(A_s\underline{u}_k + B_s\underline{f}_k\right), \tag{7.4}$$

the cost function $\bar{J}$ reduces to

$$\bar{J} = \frac{1}{2}\underline{u}_n^T C^T Q_n C\underline{u}_n + \sum_{k=0}^{n-1}\left(\mathcal{N}_k - \underline{\lambda}_{k+1}^T\underline{u}_{k+1}\right). \tag{7.5}$$

Furthermore, it is reformulated by changing the indices of the last term's summation to find

$$\bar{J} = \frac{1}{2}\underline{u}_n^T C^T Q_n C\underline{u}_n - \underline{\lambda}_n^T\underline{u}_n + \sum_{k=1}^{n-1}\left(\mathcal{N}_k - \underline{\lambda}_k^T\underline{u}_k\right) + \mathcal{N}_0. \tag{7.6}$$

To minimize the performance index, consider infinitesimal changes in $\bar{J}$ due to infinitesimal changes in $\underline{u}_k$, $\underline{f}_k$ and $\underline{u}_n$,

$$\begin{aligned}\mathrm{d}\bar{J} &= \left(\underline{u}_n^T C^T Q_n C - \underline{\lambda}_n^T\right)\mathrm{d}\underline{u}_n + \sum_{k=1}^{n-1}\left[\left(\frac{\partial\mathcal{N}_k}{\partial\underline{u}_k} - \underline{\lambda}_k^T\right)\mathrm{d}\underline{u}_k + \frac{\partial\mathcal{N}_k}{\partial\underline{f}_k}\mathrm{d}\underline{f}_k\right] \\ &+ \frac{\partial\mathcal{N}_0}{\partial\underline{u}_0}\mathrm{d}\underline{u}_0 + \frac{\partial\mathcal{N}_0}{\partial\underline{f}_0}\mathrm{d}\underline{f}_0. \end{aligned} \tag{7.7}$$

It is tedious to determine the differential changes $\mathrm{d}\underline{u}_k$ produced by given $\mathrm{d}\underline{f}_k$. Hence, the following choices are made to decouple $\mathrm{d}\underline{u}_k$ and $\mathrm{d}\underline{f}_k$ for $k = 0, 1, \ldots, n-1$

$$\underline{\lambda}_k^T = \frac{\partial\mathcal{N}_k}{\partial\underline{u}_k} \quad \text{or} \quad \underline{\lambda}_k^T = \underline{u}_k^T C^T Q_k C + \underline{f}_k^T S_k^T C + \underline{\lambda}_{k+1}^T A_s, \tag{7.8}$$

with the boundary conditions $\underline{\lambda}_n^T = \underline{u}_n^T C^T Q_n C$. The infinitesimal changes in $\bar{J}$ is simplified to

$$\mathrm{d}\bar{J} = \sum_{k=1}^{n-1}\frac{\partial\mathcal{N}_k}{\partial\underline{f}_k}\mathrm{d}\underline{f}_k + \frac{\partial\mathcal{N}_0}{\partial\underline{u}_0}\mathrm{d}\underline{u}_0 + \frac{\partial\mathcal{N}_0}{\partial\underline{f}_0}\mathrm{d}\underline{f}_0. \tag{7.9}$$

Imposing the constraint, $\underline{\lambda}_0^T = \partial \mathcal{N}_0 / \partial \underline{u}_0$, $\mathrm{d}\bar{J}$ becomes

$$\mathrm{d}\bar{J} = \sum_{k=0}^{n-1} \frac{\partial \mathcal{N}_k}{\partial \underline{f}_k} \mathrm{d}\underline{f}_k + \underline{\lambda}_0^T \mathrm{d}\underline{u}_0. \tag{7.10}$$

It is clear that $\partial \mathcal{N}_k / \partial \underline{f}_k$ becomes the gradient of $\bar{J}$ with respect to the control inputs, when the initial conditions, $\underline{u}_0$, are given and the Lagrange multipliers λ_k satisfying the constraints, eqs. (7.8) and associated boundary conditions. For an extremum, $\mathrm{d}\bar{J}$ must be zero for arbitrary $\mathrm{d}\underline{f}_k$, this is true if and only if

$$\frac{\partial \mathcal{N}_k}{\partial \underline{f}_k} = 0 \quad \text{or} \quad \underline{u}_k^T C^T S_k + \underline{f}_k^T R_k + \underline{\lambda}_{k+1}^T B_s = 0, \tag{7.11}$$

for $k = 0, 1, \ldots, n-1$. Because Q_k is positive semi-definite and R_k positive definite, the stationary values of $\bar{J}$ and J should be minima, see ref. [26]. In summary, finding a control sequence, $\underline{f}_k$, that minimizes the performance index J leads to the following two-point boundary-value problem

$$\underline{u}_{k+1} = A_s \underline{u}_k + B_s \underline{f}_k; \tag{7.12a}$$

$$\underline{u}_k^T C^T S_k + \underline{f}_k^T R_k + \underline{\lambda}_{k+1}^T B_s = 0; \tag{7.12b}$$

$$\underline{\lambda}_k^T = \underline{u}_k^T C^T Q_k C + \underline{f}_k^T S_k^T C + \underline{\lambda}_{k+1}^T A_s, \tag{7.12c}$$

with boundary conditions $\underline{\lambda}_n^T = \underline{u}_n^T C^T Q_n C$. It is difficult to find the unique solution of this two-point boundary-value problem. A general procedure for solving this problem is the sweep method [26], in which the solutions to Lagrange multipliers, $\underline{\lambda}_k$, can be assumed as $\underline{\lambda}_k = X_k \underline{u}_k$, for $k = 0, 1, \ldots, n-1$, where X_k is a symmetric matrix. When k is shifted by one step, the same solution applies, $\underline{\lambda}_{k+1} = X_{k+1} \underline{u}_{k+1}$. In view of eq. (7.12a), the Lagrange multipliers now become

$$\underline{\lambda}_{k+1} = X_{k+1} A_s \underline{u}_k + X_{k+1} B_s \underline{f}_k. \tag{7.13}$$

Substituting this expression into eq. (7.12b), the control inputs are found as

$$\underline{f}_k = -\left(B_s^T X_{k+1} B_s + R_k\right)^{-1} \left(B_s^T X_{k+1} A_s + S_k^T C\right) \underline{u}_k. \tag{7.14}$$

The Lagrange multipliers, $\underline{\lambda}_k$, are then found by substituting eqs. (7.13) and (7.14) into eq. (7.12c)

$$\begin{aligned}\underline{\lambda}_k &= C^T Q_k C \underline{u}_k - \left(A_s^T X_{k+1} B_s + C^T S_k\right)\left(B_s^T X_{k+1} B_s + R_k\right)^{-1}\left(B_s^T X_{k+1} A_s + S_k^T C\right)\underline{u}_k \\ &+ A_s^T X_{k+1} A_s \underline{u}_k. \end{aligned} \tag{7.15}$$

Because $\underline{\lambda}_k$ is unique, the coefficients of solution $\underline{\lambda}_k = X_k \underline{u}_k$ and eqs. (7.15) must be identical, leading to the following discrete time algebraic Riccati equations

$$\begin{aligned}X_k &= A_s^T X_{k+1} A_s - \left(A_s^T X_{k+1} B_s + C^T S_k\right)\left(B_s^T X_{k+1} B_s + R_k\right)^{-1}\left(B_s^T X_{k+1} A_s + S_k^T C\right) \\ &+ C^T Q_k C. \end{aligned} \tag{7.16}$$

Once the solutions for X_k have been found from the above Riccati equations, the optimal control inputs are found from the following equations

$$\begin{cases} \underline{u}_{k+1} = A_s \underline{u}_k + B_s \underline{f}_k; \\ \underline{y}_k = C \underline{u}_k + D \underline{f}_k, \quad \text{and} \quad \underline{f}_k = -G_k \underline{u}_k, \end{cases} \tag{7.17}$$

where G_k is the feedback gain matrix

$$G_k = \left(B_s^T X_{k+1} B_s + R_k\right)^{-1}\left(B_s^T X_{k+1} A_s + S_k^T C\right). \tag{7.18}$$

7.2 Linear Quadratic Regulator

A regulator [31] is a feedback controller designed to keep a stationary system within an acceptable deviation from a reference condition using acceptable amounts of control. In general, the object of the linear quadratic regulator control is to maintain the state close to the zero state.

Linear quadratic regulator determines a state-feedback control law, which minimize the quadratic performance index J for a linear model, eqs. (2.15). J can be obtained from eq. (7.2) as n increases to infinity

$$J = \sum_{k=0}^{\infty}\left(\frac{1}{2}\underline{u}_k^T C^T Q C \underline{u}_k + \underline{u}_k^T C^T S \underline{f}_k + \frac{1}{2}\underline{f}_k^T R \underline{f}_k\right), \tag{7.19}$$

where the parameter matrices, Q, S and R, are the steady state formulation of matrices Q_k, S_k and R_k; the state vector, $\underline{u}_k$, and the control inputs, $\underline{f}_k$, satisfy the linear model, eqs. (2.15). The unique solution to this problem, a state-feedback control law, can be obtained by using the optimal procedure described in section 7.1. When k goes to infinity, the steady state formulation of eq. (7.16) is obtained

$$X = A_s^T X A_s - \left(A_s^T X B_s + C^T S\right)\left(B_s^T X B_s + R\right)^{-1}\left(B_s^T X A_s + S^T C\right) + C^T Q C, \quad (7.20)$$

the alternative formulation is

$$X = \bar{A}_s^T X \bar{A}_s - \bar{A}_s^T X B_s \left(B_s^T X B_s + R\right)^{-1} B_s^T X \bar{A}_s + C^T Q C - C^T S R^{-1} S^T C, \quad (7.21)$$

where $\bar{A}_s = A_s - B_s R^{-1} S^T C$. Finally, the optimal feedback control law is determined, $\underline{f}_k = -G\underline{u}_k$, where the feedback gain matrix, G, is computed as

$$G = \left(B_s^T X B_s + R\right)^{-1}\left(B_s^T X A_s + S^T C\right). \quad (7.22)$$

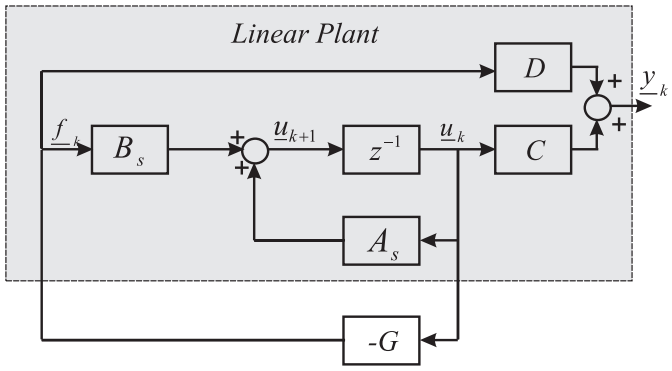

Figure 7.1: The configuration of linear quadratic regulator.

Fig. 7.1 shows the state-feedback configuration of linear quadratic regulator for a linear time invariant plant. Obviously, the state-feedback configuration forms a closed loop control; it is a process of optimal control to the initial value problem.

7.3 Linear Quadratic Gaussian Controller

The name "linear quadratic Gaussian" controller arises from the use of a linear model, an integral quadratic performance function J and Gaussian white noise processes

to model disturbance signals and noise. The process of linear quadratic Gaussian controller consists of first determining the optimal control to a deterministic linear quadratic regulator problem and second finding an optimal estimation of the state, $\underline{\bar{u}}_k$, so that the state covariance is minimized. The details of the linear quadratic Gaussian controller can be found in refs. [101, 32]. Note that the linear quadratic Gaussian controller is generally referred to as H_2 norm optimal control [32].

The linear quadratic Gaussian controller assumes that the combined deterministic-stochastic plant, eqs. (6.82), is given, and the measurement noise and disturbance outputs are stochastic with known statistical properties. The first step in the derivation of linear quadratic Gaussian controllers is to determine the optimal control, $\underline{f}_k$, which minimize the performance index J, eq. (7.19). Namely it is the linear quadratic regulator problem for the linear deterministic plant, eqs. (2.15), without considering the noise components, $\underline{w}_k$ and $\underline{v}_k$. The solution to this problem is $\underline{f}_k = -G\underline{u}_k$, where the feedback gain matrix, G, defined by eq. (7.22), is clearly independent of $\underline{w}_k$ and $\underline{v}_k$.

The second step of the procedure is to evaluate an estimate, $\underline{\bar{u}}_k$, of the state vector, $\underline{u}_k$, that minimizes the noise covariance. $\underline{\bar{u}}_k$ is determined by the Kalman filter, as discussed in section 6.4, and satisfies the innovation model, eqs. (6.96). It is obvious $\underline{\bar{u}}_k$ is independent of Q and R. The solution of the linear quadratic Gaussian problem is then found by replacing $\underline{u}_k$ by its estimate, $\underline{\bar{u}}_k$, to find $\underline{f}_k = -G\underline{\bar{u}}_k$. The flow chart of the linear quadratic Gaussian controller, described in fig. 7.2, clearly shows the linear quadratic Gaussian controller is the combination of the state feedback regulator and of the Kalman filter. Two discrete time algebraic Riccati equations (6.94) and (7.20) need to be solved. Note that if the solution to the linear quadratic Gaussian controller exists, the stabilizability conditions of system pair (A_s, B_s) and detectability conditions of pair (C, A_s) must be satisfied.

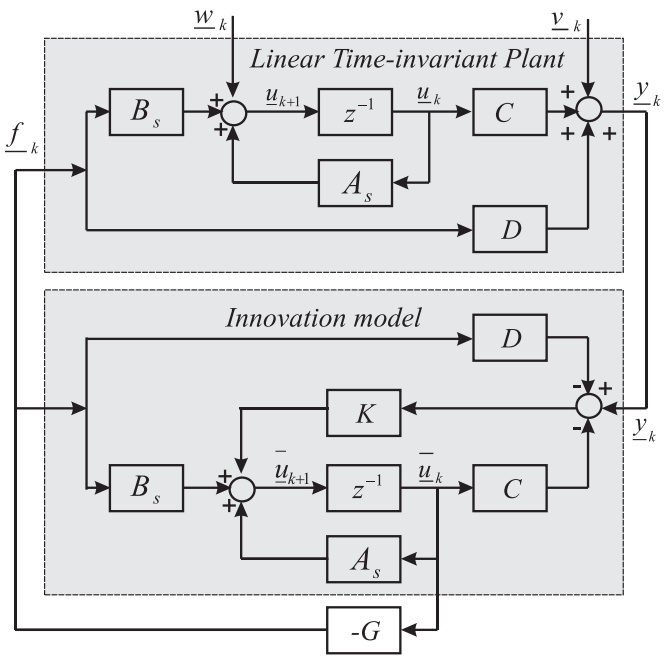

Figure 7.2: The configuration of linear quadratic Gaussian controller.

7.4 Linear Feedback to Achieve a Desired Output

If the desired output functions, $\underline{y}(t)$, are given, the outputs of dynamical system, eqs. (2.15), to follow $\underline{y}(t)$ can be obtained by the optimal control. In this section, the desired output is assumed to be a constant, $\underline{y}(t) = \underline{y}_d$. The associated performance index is defined as

$$\begin{aligned} J &= \frac{1}{2}\sum_{k=0}^{n-1}\left[\left(C\underline{u}_k - \underline{y}_d\right)^T Q_k \left(C\underline{u}_k - \underline{y}_d\right) + 2\left(C\underline{u}_k - \underline{y}_d\right)^T S_k \underline{f}_k + \underline{f}_k^T R_k \underline{f}_k\right] \\ &+ \underline{v}^T\left(C\underline{u}_n + D\underline{f}_n - \underline{y}_d\right). \end{aligned} \tag{7.23}$$

The minimum of this performance index clearly implies that the system outputs converge to the target values $\underline{y}_d$. With the help of the Lagrange multiplier method, the procedure of minimizing J can be started from adjoining the system equations to J as the constraints with the help of a sequence of Lagrange multipliers, $\underline{\lambda}_k$. The

performance index, $\bar{J}$, now becomes

$$\bar{J} = \underline{v}^T \left(C\underline{u}_n + D\underline{f}_n - \underline{y}_d \right) + \sum_{k=0}^{n-1} \left(\bar{\mathcal{N}}_k - \underline{\lambda}_{k+1}^T \underline{u}_{k+1} \right), \tag{7.24}$$

where

$$\begin{aligned} \bar{\mathcal{N}}_k &= \frac{1}{2} \left(C\underline{u}_k - \underline{y}_d \right)^T Q_k \left(C\underline{u}_k - \underline{y}_d \right) + \left(C\underline{u}_k - \underline{y}_d \right)^T S_k \underline{f}_k + \frac{1}{2} \underline{f}_k^T R_k \underline{f}_k \\ &+ \underline{\lambda}_{k+1}^T \left(A_s \underline{u}_k + B_s \underline{f}_k \right). \end{aligned} \tag{7.25}$$

After changing the indices of the summation on the last term, $\bar{J}$ is reformulated as

$$\bar{J} = \underline{v}^T \left(C\underline{u}_n + D\underline{f}_n - \underline{y}_d \right) - \underline{\lambda}_n^T \underline{u}_n + \sum_{k=1}^{n-1} \left(\bar{\mathcal{N}}_k - \underline{\lambda}_k^T \underline{u}_k \right) + \bar{\mathcal{N}}_0. \tag{7.26}$$

It is true that when $\bar{J}$ is minimum, the differential changes of $\bar{J}$ should be zero. When the parameter matrix Q_k is positive semi-definite and R_k positive definite, the stationary value of $\bar{J}$ determined by setting $\mathrm{d}\bar{J} = 0$ should be the minimum. So it is straightforward to compute the differential changes of $\bar{J}$ related to the differential changes of $\underline{u}_k$ and $\underline{f}_k$ in order to determining the minimum value of $\bar{J}$,

$$\begin{aligned} \mathrm{d}\bar{J} &= \left(\underline{v}^T C - \underline{\lambda}_n^T \right) \mathrm{d}\underline{u}_n + \underline{v}^T D \mathrm{d}\underline{f}_n \\ &+ \sum_{k=1}^{n-1} \left[\left(\frac{\partial \bar{\mathcal{N}}_k}{\partial \underline{u}_k} - \underline{\lambda}_k^T \right) \mathrm{d}\underline{u}_k + \frac{\partial \bar{\mathcal{N}}_k}{\partial \underline{f}_k} \mathrm{d}\underline{f}_k \right] + \frac{\partial \bar{\mathcal{N}}_0}{\partial \underline{u}_0} \mathrm{d}\underline{u}_0 + \frac{\partial \bar{\mathcal{N}}_0}{\partial \underline{f}_0} \mathrm{d}\underline{f}_0. \end{aligned} \tag{7.27}$$

When the following constraints are satisfied for $k = 0, 1 \ldots, n-1$,

$$\underline{\lambda}_n^T = \underline{v}^T C, \quad \underline{v}^T D = 0, \quad \underline{\lambda}_k^T = \frac{\partial \bar{\mathcal{N}}_k}{\partial \underline{u}_k}, \tag{7.28}$$

and $\mathrm{d}\underline{u}_0 = 0$ for $\underline{u}_0$ given, $\mathrm{d}\bar{J}$ becomes function of $\mathrm{d}\underline{f}_k$ only

$$\mathrm{d}\bar{J} = \sum_{k=0}^{n-1} \frac{\partial \bar{\mathcal{N}}_k}{\partial \underline{f}_k} \mathrm{d}\underline{f}_k. \tag{7.29}$$

For arbitrary $\mathrm{d}\underline{f}_k$, $\mathrm{d}\bar{J} = 0$ is equivalent to

$$\frac{\partial \bar{\mathcal{N}}_k}{\partial \underline{f}_k} = 0, \tag{7.30}$$

which satisfies the constraints (7.28). In view of eq. (7.25), it is not difficult to find that

$$\begin{aligned}\frac{\partial \bar{\mathcal{N}}_k}{\partial \underline{u}_k} &= \left(C\underline{u}_k - \underline{y}_d\right)^T Q_k C + \underline{f}_k^T S_k^T C + \underline{\lambda}_{k+1}^T A_s,\\ \frac{\partial \bar{\mathcal{N}}_k}{\partial \underline{f}_k} &= \left(C\underline{u}_n - \underline{y}_d\right)^T S_k + \underline{f}_k^T R_k + \underline{\lambda}_{k+1}^T B_s. \end{aligned} \tag{7.31}$$

Finally, the linear feedback of the sensed outputs of linear plant, eqs. (2.15), to follow the desired outputs forms the two-point boundary-value problem

$$\underline{u}_{k+1} = A_s\underline{u}_k + B_s\underline{f}_k; \tag{7.32a}$$

$$S_k^T\left(C\underline{u}_n - \underline{y}_d\right) + R_k\underline{f}_k + B_s^T\underline{\lambda}_{k+1} = 0; \tag{7.32b}$$

$$\underline{\lambda}_k = C^T Q_k\left(C\underline{u}_k - \underline{y}_d\right) + C^T S_k\underline{f}_k + A_s^T\underline{\lambda}_{k+1}, \tag{7.32c}$$

with boundary conditions $\underline{\lambda}_n^T = \underline{v}^T C$ and $\underline{v}^T D = 0$. Here again, the problem was solved by the sweep method. The Lagrange multipliers are assumed to depend on the state vectors according to the following linear equations

$$\underline{\lambda}_k = X_k\underline{u}_k + \underline{q}_k, \tag{7.33}$$

where X_k is a symmetric matrix of unknown coefficients, and $\underline{q}_k$ unknown vector. At a generic time step $k+1$, the solutions become $\underline{\lambda}_{k+1} = X_{k+1}\underline{u}_{k+1} + \underline{q}_{k+1}$. In view of eq. (7.32a), $\underline{\lambda}_{k+1}$ are rewritten as

$$\underline{\lambda}_{k+1} = \underline{X}_{k+1}A_s\underline{u}_k + \underline{X}_{k+1}B_s\underline{f}_k + \underline{q}_{k+1}. \tag{7.34}$$

Consequently, with the help of eqs. (7.34) and (7.32b), the optimal control sequence is found as

$$\underline{f}_k = -\left(B_s^T X_{k+1}B_s + R_k\right)^{-1}\left[\left(B_s^T X_{k+1}A_s + S_k^T C\right)\underline{u}_k - S_k^T\underline{y}_d + B_s^T\underline{q}_{k+1}\right]. \tag{7.35}$$

Substituting eqs. (7.34) and (7.35) into eq. (7.32c), the Lagrange multipliers become

$$\begin{aligned}\underline{\lambda}_k &= C^T Q_k C\underline{u}_k - \left(A_s^T X_{k+1}B_s + C^T S_k\right)\left(B_s^T X_{k+1}B_s + R_k\right)^{-1}\left(B_s^T X_{k+1}A_s + S_k^T C\right)\underline{u}_k\\ &+ A_s^T X_{k+1}A_s\underline{u}_k + \left[A_s^T - \left(A_s^T X_{k+1}B_s + C^T S_k\right)\left(B_s^T X_{k+1}B_s + R_k\right)^{-1}B_s^T\right]\underline{q}_{k+1}\\ &+ \left[\left(A_s^T X_{k+1}B_s + C^T S_k\right)\left(B_s^T X_{k+1}B_s + R_k\right)^{-1}S_k^T - C^T Q_k\right]\underline{y}_d. \end{aligned} \tag{7.36}$$

Comparing eqs. (7.33) and (7.36), the coefficients of the state vector should be identical, leading to the discrete time algebraic Riccati equations (7.16), together with the following equations

$$\begin{aligned} \underline{q}_k &= \left[A_s^T - \left(A_s^T X_{k+1} B_s + C^T S_k\right)\left(B_s^T X_{k+1} B_s + R_k\right)^{-1} B_s^T\right] \underline{q}_{k+1} \\ &+ \left[\left(A_s^T X_{k+1} B_s + C^T S_k\right)\left(B_s^T X_{k+1} B_s + R_k\right)^{-1} S_k^T - C^T Q_k\right] \underline{y}_d. \end{aligned} \tag{7.37}$$

In the case of steady state, when k goes to infinity, X_k and $\underline{q}_k$ converge to constants, X and $\underline{q}$, respectively. The control parameters Q_k, S_k and R_k become constant matrices Q, S and R, respectively. The associated discrete time algebraic Riccati equation is given by eq. (7.20), and $\underline{q}$ is the solution of the following linear equations

$$\begin{aligned} \underline{q} &= \left[A_s^T - \left(A_s^T X B_s + C^T S\right)\left(B_s^T X B_s + R\right)^{-1} B_s^T\right] \underline{q} \\ &+ \left[\left(A_s^T X B_s + C^T S\right)\left(B_s^T X B_s + R\right)^{-1} S^T - C^T Q\right] \underline{y}_d, \end{aligned} \tag{7.38}$$

where X is the solution of eq. (7.20). In summary, the linear feedback to follow the desired targets is represented as

$$\begin{cases} \underline{u}_{k+1} = A_s \underline{u}_k + B_s \underline{f}_k; \\ \underline{y}_k = C \underline{u}_k + D \underline{f}_k, \quad \text{and} \quad \underline{f}_k = -G \underline{u}_k - \underline{f}_q, \end{cases} \tag{7.39}$$

where the feedback gain matrix G and constants $\underline{f}_q$ are given by

$$G = \left(B_s^T X B_s + R\right)^{-1}\left(B_s^T X A_s + S^T C\right), \ \underline{f}_q = \left(B_s^T X B_s + R\right)^{-1}\left(B_s^T \underline{q} - S^T \underline{y}_d\right). \tag{7.40}$$

7.5 Solving Discrete-Time Algebraic Riccati Equation

The computational solutions of the discrete time algebraic Riccati equations can be computed by using several different approaches. In this section, the Schur-type approach [2] combined with a Newton iteration method are implemented to solve the Riccati equations.

7.5.1 Generalized Eigenvalue Problem Algorithm

The Schur-type approach, a generalized eigenvalue problem algorithm, is used to solve the discrete time algebraic Riccati equation based on the fact that each Riccati equation has an associated Hamiltonian matrix or matrix pencil. Arnold and Laub [2] proposed that the solutions of the Riccati equation can be computed by the eigenvalue decomposition of the Hamiltonian matrix pencil. This generalized eigenvalue problem is solved for the orthogonal eigenvectors or Schur vectors. The solutions of the discrete time algebraic Riccati equations are evaluated from the Schur vectors associated with stable eigenvalues.

Note that whether a matrix is said to be *Hamiltonian* if and only if $J_H^{-1} H_H^T J_H = -H_H$, where matrix J_H is defined as

$$J_H = \begin{bmatrix} 0 & I \\ -I & 0 \end{bmatrix}. \tag{7.41}$$

Let L_P and M_P be two $2r \times 2r$ matrices. The set of all matrices of the form $\lambda L_p - M_P$ where λ is a complex number is said to be a matrix pencil. The eigenvalues of the pencil are elements of the set $\lambda(L_P, M_P)$ defined by $\lambda(L_P, M_P) = \{z \text{ complex} \mid \det(zL_P - M_P) = 0\}$.

The first step of Schur-type approach is assembling the associated Hamiltonian matrix pencil. If the solution of eq. (7.20) has the properties $X \geq 0$ and $X = X^T$, the $2r \times 2r$ matrix pencil, $\lambda L_p - M_P$, r order of the system, is assembled

$$\lambda \begin{bmatrix} I & B_s R^{-1} B_s^T \\ 0 & \left(A_s - B_s R^{-1} S^T C\right)^T \end{bmatrix} - \begin{bmatrix} A_s - B_s R^{-1} S^T C & 0 \\ C^T S R^{-1} S^T C - C^T Q C & I \end{bmatrix}. \tag{7.42}$$

When R is singular, an alternative form is

$$\lambda \begin{bmatrix} I & 0 & 0 \\ 0 & A_s^T & 0 \\ 0 & -B_s^T & 0 \end{bmatrix} - \begin{bmatrix} A_s & 0 & B_s \\ -C^T Q C & I & -C^T S \\ S^T C & 0 & R \end{bmatrix}. \tag{7.43}$$

The second step of the Schur-type approach is solving the generalized eigenvalue problem for eigenvectors or Schur vectors U_o. The resulting generalized eigenvalue problem is then transformed by unitary orthogonal matrices V_o and U_o to the form $V_o(\lambda L_P - M_P)U_o = \lambda\hat{L}_P - \hat{M}_P$, where $\hat{L}_P$ is upper triangular and $\hat{M}_P$ quasi-upper-triangular (upper triangular except for 2×2 diagonal blocks corresponding to complex conjugate eigenvalue pairs) and the stable generalized eigenvalues are determined by the upper left $r \times r$ blocks of $\hat{L}_P$ and $\hat{M}_P$. Accordingly, the orthogonal matrix U_o is partitioned. For first pencil, the partition is

$$U_o = \begin{bmatrix} U_{11} & U_{12} \\ U_{21} & U_{22} \end{bmatrix}; \tag{7.44}$$

for second pencil, the partition

$$U_o = \begin{bmatrix} U_{11} & U_{12} & U_{13} \\ U_{21} & U_{22} & U_{23} \\ U_{31} & U_{32} & U_{33} \end{bmatrix}. \tag{7.45}$$

Laub [70] proved that the r "Schur vectors" comprising, $\begin{bmatrix} U_{11}^T & U_{21}^T \end{bmatrix}^T$ for the first partition, $\begin{bmatrix} U_{11}^T & U_{21}^T & U_{31}^T \end{bmatrix}^T$ for the second one, span the stable invariant subspace and the solution of eq. (7.20) is given by

$$X = U_{21}U_{11}^{-1}. \tag{7.46}$$

In general, the QZ algorithm is used to compute the Schur vectors U_o. Details of the QZ algorithm can be found in refs. [41, 74].

7.5.2 Newton Iterations

Numerical implementation of the Schur-type approach described in section 7.5.1 is relatively straightforward. However, the Riccati problem may be ill-conditioned, and the resulting numerical solution may not be as accurate as desired. The Newton's iteration is used to refine the Schur-type solution. Newton's method for iteratively

solving discrete time algebraic Riccati equations was proposed in ref. [45] at first and extended to the generalized equations in refs. [2, 18]. A discussion of the convergence properties can be found in textbooks [68].

In this section, Newton's iterative procedure is presented only for discrete time algebraic Riccati equation based on the algorithm proposed by Hewer [45]. When the feedback gain G_k is defined by eq. (7.18), the discrete time algebraic Riccati equations can be modified to

$$X_k = (A_s - B_s G_k)^T X_k (A_s - B_s G_k) + G_k^T R G_k + C^T Q C - C^T S G_k - \left(C^T S G_k\right)^T. \tag{7.47}$$

If G_0 is chosen such that the closed loop matrix $A_s - B_s G_0$ is stable, then it has been proven [45] that $\lim_{k\to\infty} X_k = X$ with a convergence rate $\|X_{k+1} - X\| \leq C_2 \|X_k - X\|^2$, where C_2 is a finite constant. When the initial value G_0 is a stabilizing state-feedback matrix, this procedure shows monotonic convergence to the non-negative definite solution to eq. (7.20), when it exists. Numerical experience shows that the convergence is quadratic when it is applied to an initial solution value produced by the direct Schur-type method.

When G_k is computed from the previous iteration, eq. (7.47) becomes the discrete matrix Lyapunov equation, with X_k as unknown

$$A_\ell^T X_k A_\ell - X_k + Q_\ell = 0, \tag{7.48}$$

where $A_\ell = (A_s - B_s G_k)^T$ and $Q_\ell = G_k^T R G_k + C^T Q C - C^T S G_k - \left(C^T S G_k\right)^T$. If the order of the system is r, the Lyapunov equation consists of r^2 scalar equations in r^2 unknowns. The solution is unique if and only if eigenvalues of A_ℓ satisfy $\lambda_i + \lambda_j \neq 0$ for $i, j = 1, 2, \ldots, r$. The Lyapunov equation can be solved by building a large $r^2 \times r^2$ matrix, leading to an expensive solution process. The better choice is the Schur-type approach [7], which is a computationally cheaper procedure to solve the matrix Lyapunov equation, involving a system of size $r \times r$. At first, Schur-type approach

transforms matrices A_ℓ and A_ℓ^T into upper triangular matrices. Then, it exploits triangular structure to solve Lyapunov equations using back-substitution.

When the coefficient matrices A_s, B_s, C, Q, S and R are given, the entire procedure to solve the discrete time algebraic Riccati equation involves the following steps.

1. Assemble the matrix pencil $\lambda L_p - M_P$ based on eq. (7.42) or eq. (7.43).

2. Use the QZ algorithm to solve the generalized eigenvalue problem $\lambda L_p - M_P$ for eigenvalues λ and Schur vectors U_o. Reorder the eigenvalues and eigenvectors in the same order and make sure that the stable generalized eigenvalues are determined by the upper left $r \times r$ blocks.

3. Partition the associated unitary Schur vectors U_o, eq. (7.44) or eq. (7.45). Solve eqs. (7.46) for X.

4. Compute the feedback gain matrix G, eq. (7.22), as the initial value for Newton refinement procedure.

5. Perform Newton iterations. At k^{th} iteration ($k = 1, 2, \ldots$), solve the discrete time Lyapunov equation (7.47) for X_k, then compute G_k as the initial values for the next step iteration. Continue iterations till X_k converged.

7.6 Implementation of Linear Quadratic Gaussian Controller

Designing controllers for comprehensive flexible multibody systems is a big challenge. To be effective in the optimal control of large multibody systems, the details of the implementation of the linear quadratic Gaussian controller must be carefully considered. The starting point of the procedure is the determination of a reduced order model for the large-scale dynamical system. Next, the linear quadratic regulator gain matrix and Kalman filter gain matrix are computed from the reduced order

model. Finally, the real-time control is implemented. The process can be thought of as a "reduce-then-design" approach. The linearized minimum realization can be constructed by using the robust identification approach, developed in section 6.5, and is valid for small perturbations about an equilibrium configuration of the nonlinear system. The Schur-type algorithm combined with Newton refinement procedure are used to solve two discrete time algebraic Riccati equations to compute the feedback gain matrix, G, of the linear quadratic regulator and the Kalman filter gain matrix, K, respectively.

When computing the linear quadratic regulator gain matrix, eq. (7.22), from the Riccati eq. (7.20), the system matrices, A_s, B_s and C, are identified plant models, and the control parameters, Q, S and R, are user defined matrices. An appropriate choice of these parameters must be made to obtain "acceptable" levels of state vector $\underline{u}_k$ and control inputs $\underline{f}_k$. For example, a possible choice is: S is set to zero, $Q = \text{diag}(q_i)$ and $R = \text{diag}(r_i)$, where

$$\frac{1}{q_i} = n\ u_i^2 \quad \text{and} \quad \frac{1}{r_i} = n\ f_i^2, \tag{7.49}$$

where n is the data length, u_i^2 the square of the maximum acceptable value of the i^{th} element of $\underline{u}_k$, and f_i^2 the square of the maximum acceptable value of the i^{th} element of $\underline{f}_k$.

The entire procedure for the off-line design of the controller is described in fig. 7.3 and involves the following steps.

1. Construct the finite element based model of the nonlinear system, compute the steady state response of the nonlinear system about its equilibrium configuration.

2. Perturb the nonlinear system by using the wide band excitation. Compute the difference between the perturbed response and the steady state response. The

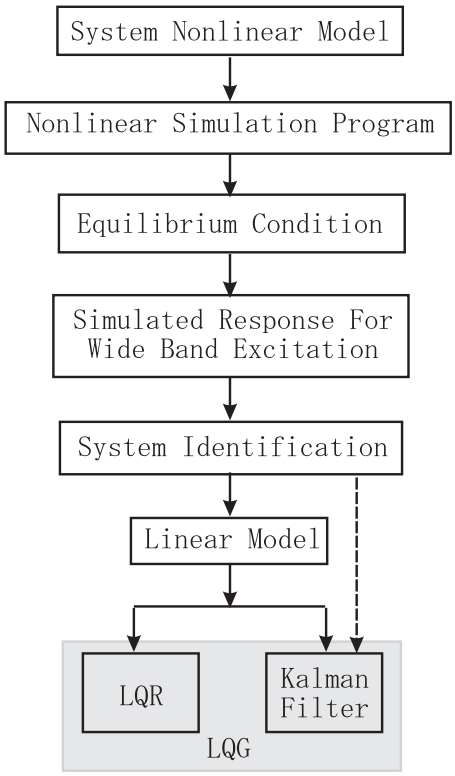

Figure 7.3: The diagram of the off-line implementation of linear quadratic Gaussian controller.

external excitations and the differences are sampled with constant time step size Δt, archived and used as input-output data.

3. Construct the subspace deterministic model, eqs. (2.15) or the forward innovation model, eqs. (6.96), from the computed input-output data by using the proposed robust identification algorithm.

4. Apply Schur-type algorithm combined with Newton refinement procedure to solve the discrete time algebraic Riccati equations. The linear quadratic regulator gain matrix, G, and the Kalman filter gain matrix, K, are then computed if a deterministic model was used in step 3.

The online control realization becomes a simple procedure, depicted in fig. 7.4, which requires the solutions of the nonlinear equations at each discrete time step. The

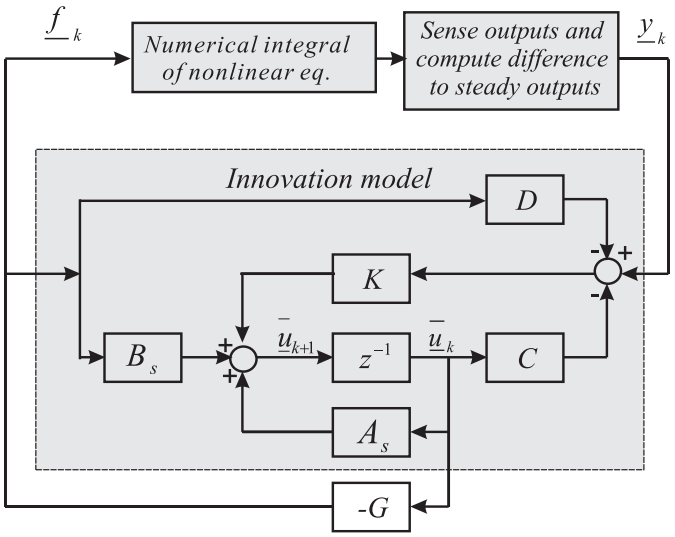

Figure 7.4: The diagrams of the online controller of linear quadratic Gaussian.

finite element based multibody formulation [8, 9] is used to simulate the dynamic response of the nonlinear system. At k^{th} step, the sensors, $\underline{s}_k$, are extracted from the computed response, and if the equilibrium solutions associated with the steady state, $\underline{s}_{k0}$, are available, the differences, $\underline{y}_k = \underline{s}_k - \underline{s}_{k0}$, are evaluated. Next, the state estimates, $\bar{\underline{u}}_{k+1}$, are determined to update the control inputs, $\underline{f}_{k+1}$, for the next discrete time step simulation, $\underline{f}_{k+1} = -G\bar{\underline{u}}_{k+1}$. The measured sensors, $\underline{s}_k$, of the nonlinear system will converge to the reference values, $\underline{s}_{k0}$.

Note that if the linear feedback procedure is used to achieve a set of user specified outputs, $\underline{y}_d$, the procedure described above is still valid, except for the fact that the feedback law now becomes, $\underline{f}_{k+1} = -G\bar{\underline{u}}_{k+1} - \underline{f}_q$, where G and $\underline{f}_q$ are defined by eqs. (7.40).

7.7 Numerical Example of Linear Quadratic Gaussian Controller

Four examples are presented to validate the linear quadratic Gaussian controller.

7.7.1 Control of Transverse Beam Vibration

The transverse vibration of the clamped thin wall beam was simulated and controlled by the linear quadratic Gaussian controller. The results were compared with those of the experimental control implementation [6].

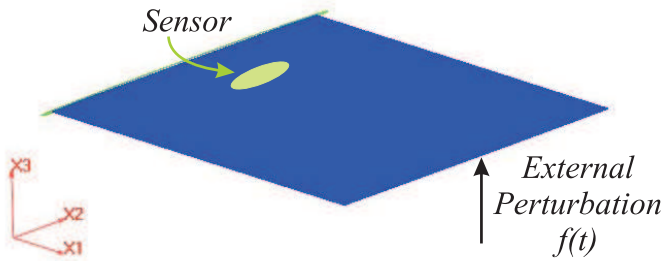

Figure 7.5: The configuration of the thin wall beam.

The geometric configurations and material properties of the cantilevered Euler-Bernoulli beam are as follow: beam length $\ell = 0.286$ m, width $b = 0.001$ m, thickness $h = 0.2543$ m, density $\rho = 3.438\ 10^3$ kg/m^3, Young's modulus $E = 7.062\ 10^{10}$ N/m^2. The physical properties of the beam: bending stiffness, $EI = 1.50$ N·m^2, mass per unit span, $m = 0.87$ kg/m, polar moment of inertia, $I = 0.0047$ N·m. The structural damping is modeled by viscous forces F_d^* proportional to the strain rates, $F_d^* = \mu_s C^* \dot{\underline{e}}^*$, where μ_s is the damping coefficient, $\underline{e}^*$ the 6 strain components, and C^* the cross-sectional stiffness matrix. The damping coefficient is selected as $\mu_s = 0.001$. In experimental setting, a pair of identical piezoceramic patches are bonded on opposite sides of the beam with edges located at $x_1 = 0.02041$ m and $x_2 = 0.04592$ m along the axial axes, and used as control inputs. In the numerical implementation, these control inputs are replaced by an external force, $f(t)$, located at the tip of the beam, see fig. 7.5. A sensor located at $\hat{x} = 0.11076$ m along the axes of the beam is used to measure the transverse displacement and used as control output.

In the off-line design procedure, the control input was defined as $f(t) = f_0 \sin(2\pi t)$,

$f_0 = 20$ N, for $t \in [0, 1]$ sec, and $f(t) = 0$ for $t > 1$ sec. The dynamic simulation was run for a total period of 2 seconds using a constant time step $\Delta t = 1$ msec. A subspace plant model of order $r = 4$ was identified, and the frequency and damping rate of the first bending mode were found to be $\omega_1 = 56.23$ rad/sec and $\zeta = -2.85\%$. The linear quadratic regulator feedback gain matrix, G, and the Kalman filter gain matrix, K, were computed by solving the discrete time algebraic Riccati equations. The error covariance matrices, E_w and E_v, were user defined diagonal matrices, all the diagonal elements were equally set to 50 and 10 respectively, E_s was zero. The effects of matrix Q to control efficiency were studied by setting different values, and matrix R was set as diagonal matrix, $R = \text{diag}(0.01)$.

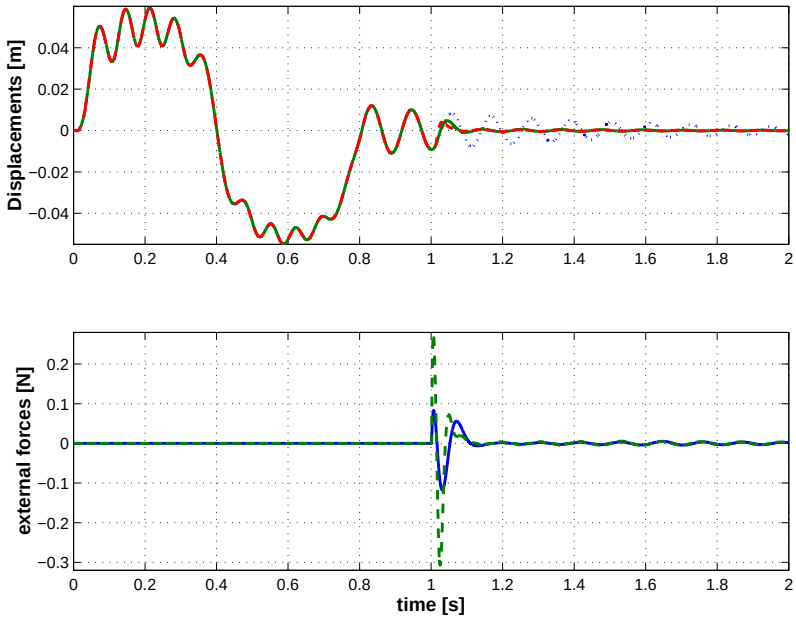

Figure 7.6: The control input and output. Top figure, the transverse displacement; bottom figure, external force; no control: dotted line; $q = 10$: solid line; $q = 100$: dashed line.

For real-time online control, the perturbation, $f(t) = 100 \sin(2.5\pi t)$ N, was applied for 0.8 seconds to excite the beam. The linear quadratic Gaussian controller was activated at $t = 1.0$ sec. The time histories of control input and output, shown in figs. 7.6, indicated that even when the diagonal elements of $Q = \text{diag}(q)$ were set to

a small value, the controller worked well.

7.7.2 Flutter Control of a Rectangular Planform Wing

The flutter of a rectangular planform wing is a typical aeroelastic problem and is used to illustrate the proposed optimal control process. The geometric configurations and the physical properties of the rectangular planform wing, defined in section 5.2, keep unchanged.

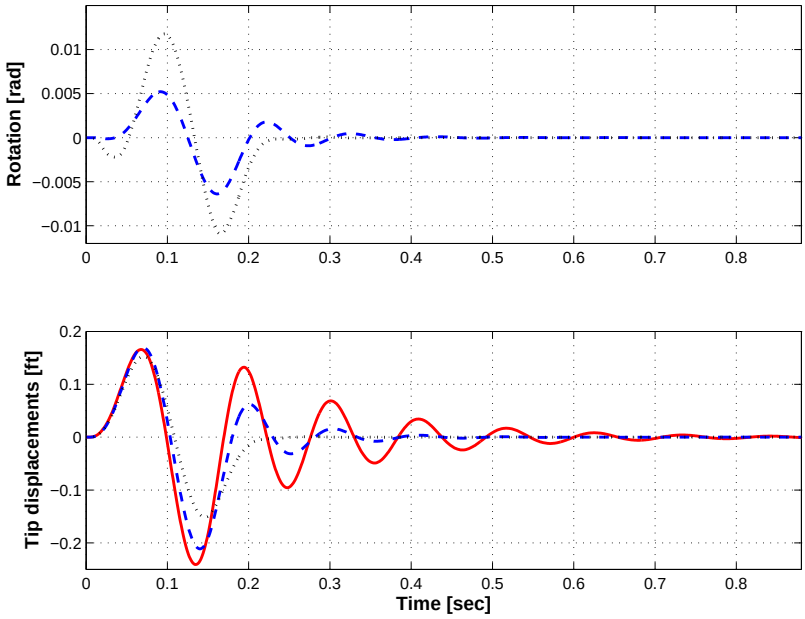

Figure 7.7: Top figure: computed control input; dashed line: $q = 0.005$, dotted line: $q = 0.1$. Bottom figure: wing tip transverse displacement. The uncontrolled response of the system is shown in solid lines.

The minimum realization of this problem has been discussed in section 6.7.2. Correspondingly, two cases for optimal control problem were studied: the first case, denoted *case 1*, the far flow velocity was $U_f = 480$ ft/sec; the second case, denoted *case 2*, the far flow velocity $U_f = 590$ ft/sec. For *case 1*, the innovation model, identified in section 6.7.2, was used for the off-line design of the linear quadratic Gaussian controller; the control input and output were selected the same as those of system identification: the wing angle of attack was used as control input, the wing

tip transverse displacement was selected as control output.

Based on reduced order model, the feedback control law was computed using the following control parameters: $S = 0$, $R = \text{diag}(1.0)$, $Q = \text{diag}(q)$. The error covariance matrices were selected as $E_w = \text{diag}(0.1)$, $E_v = \text{diag}(0.1)$, and $E_s = 0$. To test the performance of the controller, an additional perturbation was added to the system in the form of an upward gust of velocity profile $v_g(t) = 10.0 \ \sin(42t)$ ft/sec for $t \in [0.0, \ 0.15]$ sec. The controller starts to work at time $t = 0$ sec. While the controller has little effect on the forced response of the system, it rapidly eliminates the unstable flutter response for $t > 0.15$ sec, as shown in figs. 7.7 that presents the response of the system with and without application of the linear quadratic Gaussian controller. Two different values of diagonal elements of diagonal matrix Q has been used, $q = 0.005$ and $q = 0.1$. Note that Q will determine the converging rate, it can be observed from figs. 7.7, the wing tip displacement is smaller when $q = 0.1$.

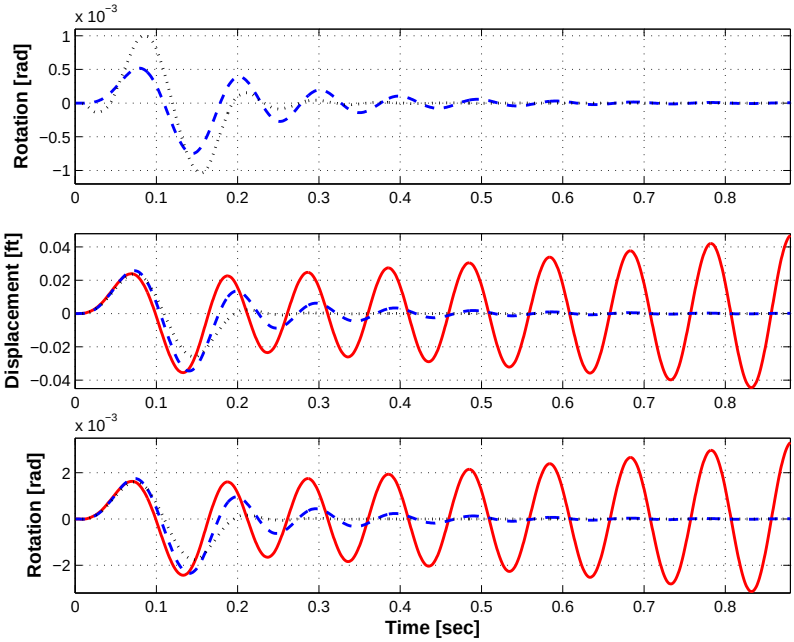

Figure 7.8: Top figure: computed control input; dashed line: $q = 0.001$, dotted line: $q = 0.1$. Middle figure: wing tip transverse displacement; bottom figure: wing tip twist. The uncontrolled response of the system is shown in solid lines.

For *case 2*, the control input keeps the same as that in *case 1*; two sensors, the wing tip transverse displacement and twist, were selected as control outputs. The proposed robust system identification approach was used to construct a subspace plant with order $r = 4$. Based on reduced order model, the feedback control law was computed using the following control parameters: $S = 0$, $R = \text{diag}(1.0)$, $Q = \text{diag}(q)$. The error covariance matrices were selected as $E_w = \text{diag}(10.0)$, $E_v = \text{diag}(10.0)$, and $E_s = 0$. Here again, to test the performance of the controller an additional perturbation was added to the system in the form of an upward gust of velocity profile $v_g(t) = \sin(42t)$ ft/sec for $t \in [0.0,\ 0.15]$ sec. While the controller has little effect on the forced response of the system, it rapidly eliminates the unstable flutter response for $t > 0.15$ sec, as shown in figs. 7.8 that presents the response of the system with and without application of the linear quadratic Gaussian controller. When $q = 0.1$, the controller minimizes the deformations of the wing more quickly than the other case.

7.7.3 Flutter Control of a Wing-Aileron System

The second aeroelastic problem deals with the flutter behavior of the wing-aileron system. The geometric configurations and physical properties of the wing-aileron system are the same as those defined in section 6.7.3.

Similar to the process of system identification, two cases were studied: the first case, denoted *case 1*, far flow velocity was $U_f = 480$ ft/sec; the second case, denoted *case 2*, far flow velocity $U_f = 590$ ft/sec. For both cases, the flap rotation was selected as control input; the mid- and tip transverse displacements of the wing were selected as control outputs. For *case 1*, the plant model with order $r = 4$ was identified at first; the linear quadratic regulator featured the following parameters: $S = 0$, $R = 1$, $Q = \text{diag}(q)$; the Kalman filter gain matrix, K, was computed with the user-defined error covariance matrices: $E_w = \text{diag}(20),\ E_s = 0,\ E_v = 10.0$.

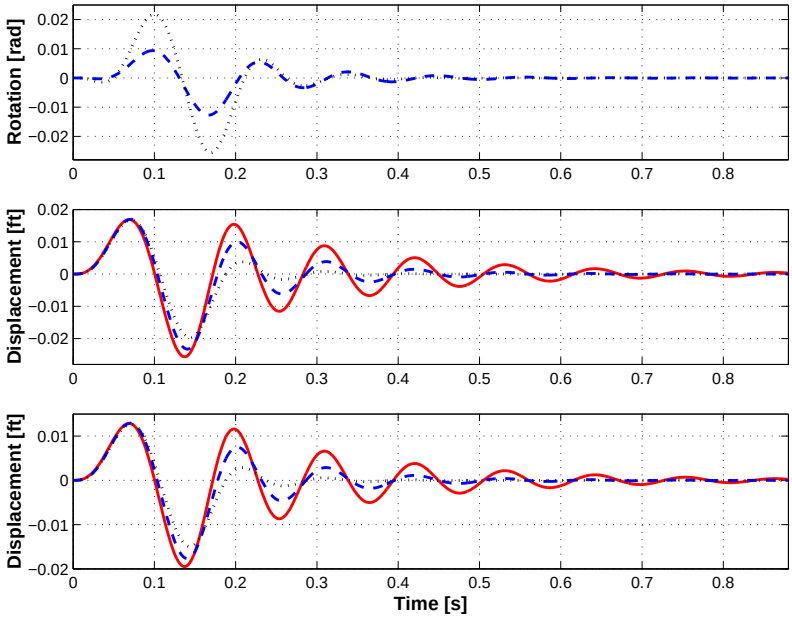

Figure 7.9: Top figure: computed control input; dashed line: $q = 1$, dotted line: $q = 5$. Middle figure: wing tip transverse displacement; bottom figure: wing mid displacement. The uncontrolled response of the system is shown in solid lines.

The linear quadratic Gaussian controller was then used to minimize the tip deflection of the wing when the system was subjected to a gust with an upward velocity $v_g(t) = 2 \sin(42t)$ ft/sec for $t \in [0, 0.15]$ sec. When the dynamic simulation was run for 0.88 seconds with the constant time step $\Delta t = 1$ msec, the deformations were controlled and the results were compared with the uncontrolled deformations in figs. 7.9. The control parameter, q, was set to a small value to obtain an effective control performance before controller reached the saturation constraint.

For *case 2*, the similar procedure was performed: a minimum order plant was constructed with order $r = 4$; the linear quadratic regulator was determined by using the parameters, S was zero, $R = 1$, $Q = \text{diag}(q)$, where $q = 1$ and 20, respectively; the Kalman filter gain matrix, K, was determined directly from the identified innovation model. The linear quadratic Gaussian controller was applied to minimize the unstable deformation of the wing when the gust of upward speed was subjected,

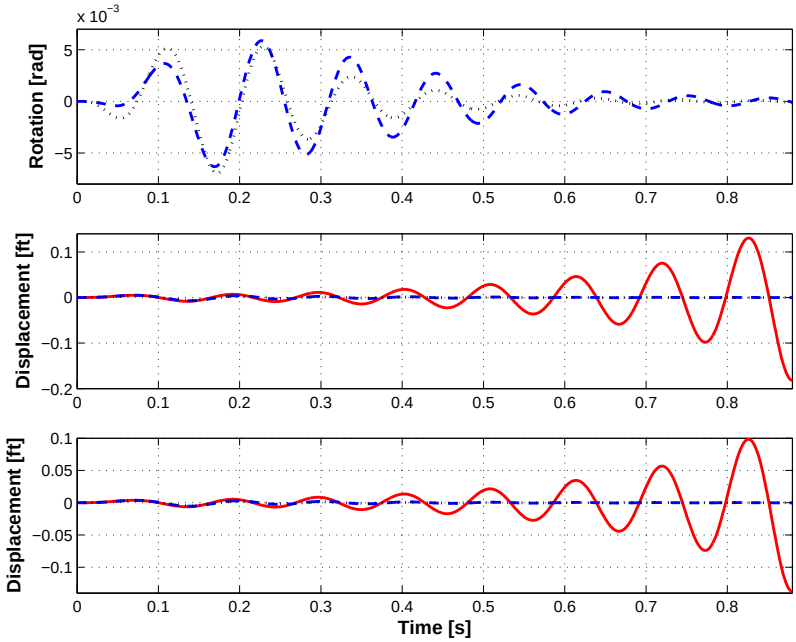

Figure 7.10: Top figure: computed control input; dashed line: $q = 1$, dotted line: $q = 20$. Middle figure: wing tip transverse displacement; bottom figure: wing mid displacement. The uncontrolled response of the system is shown in solid lines.

$v_g(t) = 0.1 \sin(42t)$ ft/sec for $t \in [0, 0.15]$ sec. The uncontrolled and controlled responses of the system were shown in figs. 7.10: clearly, the controller was able to inhibit flutter of the wing-aileron system.

7.7.4 Trim Analysis of the Helicopter Rotor System

The last example deals with a complex aeroelastic representation of a helicopter rotor system. The analysis of the system uses the finite element based multibody dynamics formulation described in ref. [9]. The system includes the four rotor blades and control actuators. The description of the physical properties of each blade can be found in ref. [22]. The four blades are connected to the hub through the blade root retention structures and lead-lag dampers. The configurations of the blade were described in section 5.7.

To simplify the trimming procedure, the rotor was fixed to the ground at the center of the hub. The rotor collective angle of attack was selected as the control

input, whereas the rotor thrust was the control output. Two methods, auto-pilot method [78, 86] and linear quadratic Gaussian controller were applied and compared. The auto-pilot method is characterized by the following control law

$$\underline{f}_{k+1} = \underline{f}_k + \Delta t A_t^{-1} G_t \left(\underline{y}_d - \underline{y}_m \right), \tag{7.50}$$

where Δt is the time step size, $\underline{y}_d$ the array of desired control outputs, $\underline{y}_m$ the array of mean values of measured control outputs at current time step k, A_t the trimmability matrix, and G_t the gain matrix. The trimmability matrix A_t was evaluated numerically as

$$A_{t(N_s \times N_c)} = \begin{bmatrix} \Delta y_1/\Delta f_1 & \Delta y_1/\Delta f_2 & \dots & \Delta y_1/\Delta f_{N_c} \\ \Delta y_2/\Delta f_1 & \Delta y_2/\Delta f_2 & \dots & \Delta y_2/\Delta f_{N_c} \\ \vdots & \vdots & \ddots & \vdots \\ \Delta y_{N_s}/\Delta f_1 & \Delta y_{N_s}/\Delta f_2 & \dots & \Delta y_{N_s}/\Delta f_{N_c} \end{bmatrix}, \tag{7.51}$$

where Δf_i is the perturbation of i^{th} control input, and Δy_i the resulting perturbation of i^{th} control output. On the other hand, the gain matrix, G_t, affects the convergence characteristics of the auto-pilot trimming, and is selected as $G_t = gI_{(N_s \times N_s)}$, where $I_{(N_s \times N_s)}$ is an identity matrix and g the gain value that was adjusted manually to obtain the best convergence characteristics

$$g = g_0 \begin{cases} 1, & \text{if} \Delta > \Delta_{ref}; \\ \tanh(4\Delta/\Delta_{ref}), & \text{otherwise}, \end{cases} \tag{7.52}$$

where g_0 is the initial gain value, and Δ the differences between the measured and desired values of the controlled variables, Δ_{ref} the preset reference differences.

In this study, the auto-pilot trimming was performed in three steps: reference run, perturbation run and simulation run. First, in the reference run, the finite element based multibody code was run till the target values stabilized using a set of prescribed pitch settings. Then, the perturbation run was performed in which

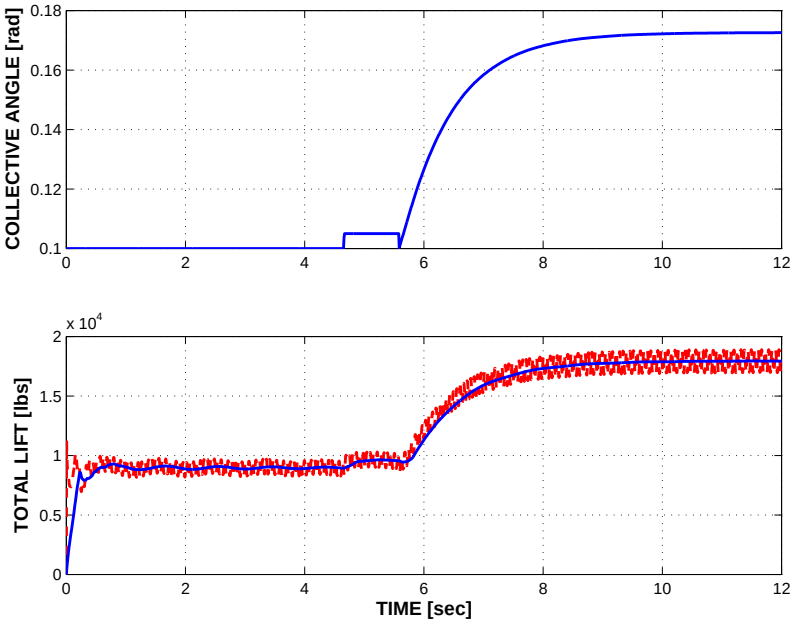

Figure 7.11: Time histories of control input and output for the auto-pilot method. Top figure, control input; bottom figure, control output; response: dashed line; mean value: solid line.

the control input was perturbed; the trimmability matrix A_t was evaluated by finite differences. Finally, in the simulation run, the control input was updated for dynamic simulation based on the auto-pilot control law, eq. (7.50), till the output converged to desired value. During the entire procedure, the dynamic simulation was run using a constant time step $\Delta t = 1.8167$ msec for a total period of 12 seconds: 4.65 sec for reference run, 0.93 sec for perturbation run, and 6.42 sec for simulation run. The collective angle of attack, θ, and lift L, were selected as control input and output, respectively. The initial value of collective angle was $\theta_0 = 0.1$ rad; the target value of lift was $L_t = 17,944$ lbs. During the perturbation run, the collective angle was perturbed, $\theta_0 = 0.1 + \Delta\theta$, $\Delta\theta = 0.005$ rad, for $t \in [4.65,\ 5.58]$ sec. The time histories of lift and associated control input were shown in figs. 7.11. At convergence, lift mean value was $17,934$ lbs, compared to the target value of $17,944$ lbs. Note that a long simulation period was required to achieve convergence.

Next, the proposed control approach was applied to the same problem. At first,

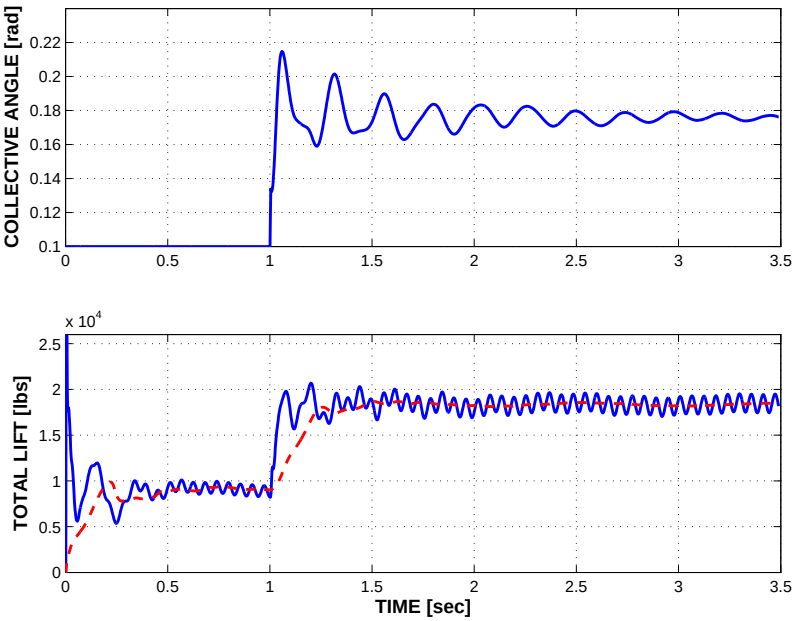

Figure 7.12: Time histories of control input and output based on linear quadratic Gaussian controller. Top figure, control input; bottom figure, control output; response: solid line; mean value: dashed line.

the dynamic simulation was run for a total period of 3.488 seconds using the same time step size and collective angle as those used with the auto-pilot reference run. The resulting lift was $L_0(t)$, and had a mean value $L_m = 8,960.20$ lbs. Then, the collective angle was perturbed by $\Delta\theta$ for a period of 0.5 sec, where $\Delta\theta = \pi/20\ (1 - \cos(4\pi(t - 1.0)))$ for $t \in [1.0,\ 1.5]$ sec and $\Delta\theta = 0$ for $t > 1.5$ sec. The perturbation run was performed and the difference between the perturbed lift and its reference counterpart was computed. The system identification algorithm was applied to the response of the system over the time window of size $t \in [1.0,\ 3.44]$ sec to construct a 12^{th} order forward innovation model. The system desired output was $y_d = L_t - L_m = 8,983.8$ lbs. Figs. 7.12 show the time histories of the control input and output. Clearly, the proposed approach quickly identified the control settings, although a low frequency oscillation remains in the output signal. This is probably due to the fact that the identification was performed over too short a window, which did not allow proper identification of the slowest modes of the system.

7.8 Chapter Summary

The basic concepts associated with optimal control were presented in this chapter. In the case of steady state, the regulator for discrete time model was defined. As a combination of the linear quadratic regulator and the Kalmam filter, the linear quadratic Gaussian controller was constructed and applied to solve the real time control problem. The Schur-type approach with the Newton refinement procedure were implemented to solve the discrete time algebraic Riccati equations. Next, the details of the practical implementation of linear quadratic Gaussian controller were discussed. Finally, four numerical examples were presented to validate the linear quadratic Gaussian controller and the linear feedback to follow the desired outputs.

CHAPTER VIII

CONCLUSIONS AND FUTURE WORK

8.1 Conclusions

Linearized stability analysis methodologies, system identification algorithms and optimal control that are applicable to large scale, multi-physics problems were presented in this thesis.

For stability analysis, the first contribution is the development of two classes of closely related stability analysis algorithms based on a partial Floquet and on an autoregressive approach, respectively. Second, a number of other stability analysis approaches, such as Prony's method or Poincaré mapping, have been shown to be identical to those proposed here. The common foundation of all these approaches was emphasized. Third, the robustness of the approach was improved by using optimized signals that are derived from the proper orthogonal modes of the system, a set of orthogonal modes capturing the dominant motion of the system in an energy norm. Even for large systems, proper orthogonal modes can be effectively extracted from very large sets of response data at all degrees of freedom of the system using the Lanczos algorithm. Visualization of the proper orthogonal modes provides valuable insight into the physical phenomena that cause the instability. Finally, signal synthesis based on the identified frequencies and damping rates was shown to be an important tool for assessing the accuracy of the identified parameters; furthermore, it provides a means of resolving the frequency indeterminacy associated with the eigenvalues of the transition matrix for periodic systems. Unlike classical stability analysis methodologies, the linearization of the equations of motion of the system is not required. In the proposed implementation, the singular value decomposition is

systematically used as a means of dealing with noisy, highly redundant data sets.

System identification algorithms, which shares a common basis with the proposed stability evaluation approaches, are investigated next. The proposed system identification algorithm uniquely combines the methods of minimum realization and subspace identification. For minimum realization, the computation of Markov parameters remains complex and determines the accuracy of the system realization. The proposed approach bypasses the computation of Markov parameters because the free impulse response of the system can be directly computed in the present computational environment. Minimum realization concepts were applied to identify the stability and output matrices. On the other hand, subspace identification algorithms construct a state space plant model of linear system by using computational expensive oblique matrix projection operations. The proposed algorithm avoids this burden by computing the Kalman filter gain matrix and model dependency on external inputs in a small sized subspace. The robustness of this algorithm was improved by the application of the singular value decomposition and least squares regression techniques. The proposed approach to system identification is flexible, since both forward innovation models, or deterministic models can be constructed. Finally, the output sensors were reconstructed from the identified plant and shown to be important accuracy indicators together with modal amplitude coherence and mode singular value. The proposed stability analysis approaches and system identification algorithm are computationally inexpensive and consist of purely post processing steps that can be used with any multi-physics computational tool or with experimental data.

Finally, optimal control for high-dimensional systems was implemented by coupling system identification algorithms and the linear quadratic Gaussian controller, a combination of the linear quadratic regulator and Kalman filter techniques. A Schur-type solver and a refinement procedure based on Newton iterations were implemented

to solve the resulting discrete time algebraic Riccati equations. This approach is efficient because it is applied to low dimensional, reduced order models. The accuracy of optimal control is greatly improved due to the fact the effect of noise on the identified plant model has been minimized. Application of the proposed approach to large-scale multibody systems was successfully demonstrated. The proposed optimal control approach was applied to the minimization of the unstable deflections of a nonlinear flexible multibody systems, and to the trim a complex rotorcraft system.

8.2 Future Work

Robust approaches for stability analysis, system identification and linear control have been implemented. Numerical examples have demonstrated the robustness of the methodologies and their applicability to large-scale multibody systems. However, the various steps of the procedure are presently user driven. Further work could be done to automate the procedure, resulting in an adaptive control methodology, as depicted in fig. 8.1. It should be noted that adaptive control is expected to be more robust because the feedback control laws are updated at each iteration.

In the present implementation, control laws were developed to reach a given, constant target. This was the case for the trimming problem presented as an example in this thesis. If the desired outputs are time dependent, controllers should be designed that are capable of achieving a given trajectory. This extension of the present work to handle this problem could be achieved rather simply. Additionally, system identification and optimal control algorithms were implemented for constant coefficient systems. Extending the proposed approaches to periodic coefficient systems would be a worthy effort.

Proper orthogonal decomposition is widely used in the fields of fluid, solid mechanics, and signal processing etc. In the framework of the present thesis, it was implemented to condense large amounts of data and compute optimized signals. Proper

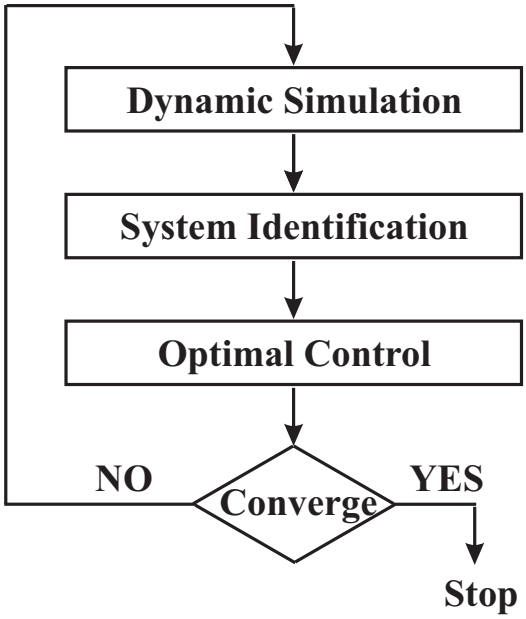

Figure 8.1: The diagram of the adaptive control.

orthogonal decomposition could also be applied to other important problems. For aeroelastic simulations, proper orthogonal decomposition could be applied to fluids problems. For instance, identifying reduced order free wake models would be a powerful tool for reducing the computational cost of rotorcraft aeroelastic analysis.

APPENDIX A

THE SINGULAR VALUE DECOMPOSITION

The present work requires the manipulation of large data sets that are highly redundant and noisy. The main tool for extracting reliable information from these data sets is the singular value decomposition (SVD) [41]. The singular value decomposition of a real rectangular matrix $S \in \mathbb{R}^{m\times n}$, $m > n$, of rank n is

$$S_{m\times n} = \begin{bmatrix} U_{m\times n} & \Gamma_{m\times(m-n)} \end{bmatrix} \begin{bmatrix} \Sigma_{n\times n} \\ 0_{(m-n)\times n} \end{bmatrix} V^T_{n\times n}, \tag{A.1}$$

where $\Sigma = \mathrm{diag}(\sigma_i)$ is a unique diagonal matrix of nonnegative singular values σ_i; $[U\ \Gamma]$ an orthogonal matrix, implying $U^TU = I$, $\Gamma^T\Gamma = I$, $U^T\Gamma = 0$ and $\Gamma^TU = 0$; V an orthogonal matrix, implying $V^TV = VV^T = I$, and Γ forms the *null space* of S^T, *i.e.* $S^T\Gamma = 0$. The compact form of the singular value decomposition is $S = U\Sigma V^T$.

When dealing with highly redundant data sets, many of the singular values of S will be nearly zero. Typically, if the singular values are ordered in descending order, the following situation is encountered

$$\frac{\sigma_1}{\sigma_1} \geq \frac{\sigma_2}{\sigma_1} \geq \ldots \geq \frac{\sigma_r}{\sigma_1} \geq \frac{\sigma_{r+1}}{\sigma_1} \approx \frac{\sigma_{r+2}}{\sigma_1} \approx \ldots \approx \frac{\sigma_n}{\sigma_1} \approx 0. \tag{A.2}$$

In practice, this situation is met when $\sigma_{r+1}/\sigma_1 < \varepsilon$, $i = r+1, r+2, \ldots, n$, where ε is a small number. In effect, it follows that $\mathrm{rank}(S) = r < n$. Matrix S can now be approximated as $S \approx S_r = U_r\Sigma_rV_r^T$, where matrices U_r and V_r consist of the first r columns of U and V, respectively, and Σ_r is the $r \times r$ principal minor of Σ; it can be shown that S_r is the rank r matrix that is closest to S in the Frobenius norm. This approximation is based on the selection of the small quantity, ε; a more physically

meaningful criterion to determine the rank of S is the following energy ratio criterion

$$E_r = \left(\sum_{i=1}^{r} \sigma_i \right) / \left(\sum_{i=1}^{n} \sigma_i \right), \tag{A.3}$$

that indicates the amount of energy captured in the retained modes as a fraction of the total amount of energy contained in the signal.

APPENDIX B

THE FOURIER TRANSFORM

The Fourier transform $F(s)$ for a continuous function $f(t)$ is defined as

$$F(s) = \int_{-\infty}^{\infty} f(\tau) e^{-\mathbf{i}2\pi s\tau} \mathrm{d}\tau, \tag{B.1}$$

and the formulation of inverse transform is

$$f(t) = \int_{-\infty}^{\infty} F(s) e^{\mathbf{i}2\pi ts} \mathrm{d}s, \tag{B.2}$$

where $\mathbf{i} = \sqrt{-1}$.

When the Fourier transform was applied to a discrete complex valued series, it is called as Discrete Fourier Transform (DFT). Given a complex series $x(j)$ with n samples x_j, where x_j are complex numbers

$$x_j = x_j^{re} + \mathbf{i}x_j^{im}, \quad j = 0, 1, \ldots, n-1, \tag{B.3}$$

the discrete Fourier transform works with the assumptions that x_j has the period $T = n\Delta t$, where Δt the sampling time step size, and the periodic properties, $x_j = x_{j+n}$, hold for all j. Denoting X_k as the Fourier transform of x_j, it can be presented by the sum of exponentials

$$X(k) = \frac{1}{n} \sum_{j=0}^{n-1} x(j) e^{-\mathbf{i}2\pi jk/n}, \quad k = 0, 1, \ldots, n-1. \tag{B.4}$$

Accordingly, the inverse transform is written as

$$x(j) = \sum_{k=0}^{n-1} X(k) e^{\mathbf{i}2\pi kj/n}, \quad j = 0, 1, \ldots, n-1. \tag{B.5}$$

When the exponential components are represented by the sinusoidal and cosinoidal functions

$$e^{\mathbf{i}2\pi kj/n} = \cos(2\pi kj/n) + \mathbf{i}\sin(2\pi kj/n), \tag{B.6}$$

the forward Fourier transform can be recast of

$$X(k) = \frac{1}{n}\sum_{j=0}^{n-1}\left[x_j^{re}\cos(2\pi k\frac{j}{n}) + x_j^{im}\sin(2\pi k\frac{j}{n})\right] - \mathbf{i}\left[x_j^{re}\sin(2\pi k\frac{j}{n}) - x_j^{im}\cos(2\pi k\frac{j}{n})\right] \tag{B.7}$$

for $k = 0, 1, \ldots, n-1$. In general, $X(k)$ is a complex valued function in frequency domain. It can be rewritten as real part and imaginary part explicitly

$$X_k = X_k^{re} + \mathbf{i}X_k^{im}, \quad k = 1, 2, \ldots, n-1, \tag{B.8}$$

or in exponential, $X(k) = r_k e^{\mathbf{i}\phi_k}$, the magnitude r_k and phase angle ϕ_k are defined as

$$r_k = \sqrt{X_k^{re2} + X_k^{im2}}, \quad \phi_k = \text{atan2}(X_k^{re}, X_k^{im}), \quad k = 0, 1, \ldots, n-1. \tag{B.9}$$

Similarly, with the help of eqs. (B.8) and (B.6), the inverse Fourier transform can be rewritten as a summation of sinusoidal and cosinoidal functions also

$$x(j) = \sum_{k=0}^{n-1}\left[X_k^{re}\cos(2\pi k\frac{j}{n}) - X_k^{im}\sin(2\pi k\frac{j}{n})\right] + \mathbf{i}\left[X_k^{re}\sin(2\pi k\frac{j}{n}) + X_k^{im}\cos(2\pi k\frac{j}{n})\right] \tag{B.10}$$

for $j = 0, 1, \ldots, n-1$.

It is necessary to address some important properties of discrete Fourier transform. First, for $k = 0$, the first sample of the transformed series $X(0)$ is computed from eq. (B.4) as

$$X(0) = \frac{1}{n}\sum_{j=0}^{n-1} x(j). \tag{B.11}$$

Apparently, the quantity $X(0)$ is the average of the input series. Second, the measured data in time domain is always a real series. However, the discrete Fourier transform is always a complex series in frequency domain. So the complex series must be a symmetric series so as to represent the real one. It has been proved that

$$X_0^{im} = 0, \quad X(k) = X(n-k), \quad X_k^{re} = X_{n-k}^{re}, \quad X_k^{im} = -X_{n-k}^{im}, \quad k = 1, 2, \ldots, \frac{n}{2}. \tag{B.12}$$

Consequently, the Fourier transforms of a real series is simplified to

$$\begin{aligned} X(k) &= \frac{1}{n}\sum_{j=0}^{n-1} x_j \cos(2\pi k\frac{j}{n}) - \mathbf{i}\ x_j \sin(2\pi k\frac{j}{n}), \\ X_k^{re} &= \frac{1}{n}\sum_{j=0}^{n-1} x_j \cos(2\pi k\frac{j}{n}), \\ X_k^{im} &= \frac{1}{n}\sum_{j=0}^{n-1} \mathbf{i}\ x_j \sin(-2\pi k\frac{j}{n}),\ k = 1, 2, \ldots, n-1. \end{aligned} \tag{B.13}$$

The inverse Fourier transform $x(j)$ is formulated as,

$$x(j) = X_0^{re} + \sum_{k=1}^{n/2} 2\left[X_k^{re}\cos(2\pi k\frac{j}{n}) - X_k^{im}\sin(2\pi k\frac{j}{n})\right], \quad j = 0, 1, \ldots, n-1. \tag{B.14}$$

Finally, it is concluded if there are no frequencies above the Nyquist frequency, the highest positive frequency sample $X(n/2)$, the signal, $x(j)$, can be exactly reconstructed from the discrete Fourier transform series $X(k)$.

APPENDIX C

THE PERFORMANCE INDEX

The performance index of a general class of parameter optimization problem for dynamic system is defined as

$$J = \frac{1}{2}\underline{u}_n^T C^T Q_n C \underline{u}_n + \sum_{k=0}^{n-1} \frac{1}{2} \begin{bmatrix} \underline{y}_k^T & \underline{f}_k^T \end{bmatrix} \begin{bmatrix} Q_k & \hat{S}_k \\ \hat{S}_k^T & \hat{R}_k \end{bmatrix} \begin{bmatrix} \underline{y}_k \\ \underline{f}_k \end{bmatrix}, \tag{C.1}$$

which subjected to a linear time-invariant model (2.15). Alternatively, J can be reformulated as

$$J = \frac{1}{2}\underline{u}_n^T C^T Q_n C \underline{u}_n + \sum_{k=0}^{n-1} \left(\frac{1}{2}\underline{y}_k^T Q_k \underline{y}_k + \underline{y}_k^T \hat{S}_k \underline{f}_k + \frac{1}{2}\underline{f}_k^T \hat{R}_k \underline{f}_k \right), \tag{C.2}$$

where the property of vector inner product, $\underline{y}_k^T \hat{S}_k \underline{f}_k = \underline{f}_k^T \hat{S}_k^T \underline{y}_k$, was applied. The control parameter matrices, Q_k and $\hat{S}_k$, are positive semidefinite, $\hat{R}_k$ positive definite. The symmetric properties are applied, $Q_k = Q_k^T$ and $\hat{R}_k = \hat{R}_k^T$. In view of second equation of linear model (2.15), $\underline{y}_k = C\underline{u}_k + D\underline{f}_k$, the following equations are formulated

$$\begin{aligned} \underline{y}_k^T Q_k \underline{y}_k &= \underline{u}_k^T C^T Q_k C \underline{u}_k + 2\underline{u}_k^T C^T Q_k D \underline{f}_k + \underline{f}_k^T D^T Q_k D \underline{f}_k, \\ \underline{y}_k^T \hat{S}_k \underline{f}_k &= \underline{u}_k^T C^T \hat{S}_k \underline{f}_k + \underline{f}_k^T D^T \hat{S} \underline{f}_k, \\ \underline{f}_k^T \hat{S}_k^T \underline{y}_k &= \underline{f}_k^T \hat{S}_k^T C \underline{u}_k + \underline{f}_k^T \hat{S}^T D \underline{f}_k. \end{aligned} \tag{C.3}$$

Finally, the performance index J can be rewritten as

$$J = \frac{1}{2}\underline{u}_n^T C^T Q_n C \underline{u}_n + \sum_{k=0}^{n-1} \left(\frac{1}{2}\underline{u}_k^T C^T Q_k C \underline{u}_k + \underline{u}_k^T C^T S_k \underline{f}_k + \frac{1}{2}\underline{f}_k^T R_k \underline{f}_k \right), \tag{C.4}$$

with the help of following notations

$$S_k = Q_k D + \hat{S}_k, \quad R_k = D^T Q_k D + D^T \hat{S}_k + \hat{S}_k^T D + \hat{R}_k. \tag{C.5}$$

REFERENCES

[1] Antoulas, A., Sorensen, D., and Gugercin, S., "A survey of model reduction methods for large scale systems," *Contemporary Mathematics, AMS Publication*, vol. 280, pp. 193–219, 2001.

[2] Arnold, W. and Laub, A., "Generalized eigenproblem algorithms and software for algebraic Riccati equations," *Proceedings of the IEEE*, vol. 72, no. 12, pp. 1746–1754, 1984.

[3] Åström, K. and Wittenmark, B., *Computer Controlled Systems: theory and design*. Upper Saddle River, NJ: Prentice-Hall Inc., third ed., 1997.

[4] Atwell, J., *Proper Orthogonal Decomposition for Reduced Order Feedback Control of Partial Differential Equations*. PhD thesis, Virginia Polytechnic Institute and State University, 2000.

[5] Azeez, M. and Vakakis, A., "Proper orthogonal decomposition (POD) of a class of vibroimpact oscillations," *Journal of Sound and Vibration*, vol. 240, no. 5, pp. 859–889, 2001.

[6] Banks, H., del Rosario, R., and H.T., T., "Proper orthogonal decomposition-based control of transverse beam vibrations: Experimental implementation," *IEEE Transactions on Control System Technology*, vol. 10, no. 5, pp. 717–726, 2002.

[7] Barraud, A., "A numerical algorithm to solve $A^{\mathsf{T}}XA - X = Q$," *IEEE Transactions on Automatic Control*, vol. AC-22, no. 5, pp. 883–885, 1977.

[8] Bauchau, O., "Computational schemes for flexible, nonlinear multi-body systems," *Multibody System Dynamics*, vol. 2, no. 2, pp. 169–225, 1998.

[9] Bauchau, O., Bottasso, C., and Nikishkov, Y., "Modeling rotorcraft dynamics with finite element multibody procedures," *Mathematical and Computer Modeling*, vol. 33, no. 10-11, pp. 1113–1137, 2001.

[10] Bauchau, O. and Liu, H., "On the modeling of hydraulic components in rotorcraft systems," *Journal of the American Helicopter Society*, vol. 51, pp. 175–184, April 2006.

[11] Bauchau, O. and Nikishkov, Y., "An implicit Floquet analysis for rotorcraft stability evaluation," *Journal of the American Helicopter Society*, vol. 46, pp. 200–209, 2001.

[12] Bauchau, O. and Nikishkov, Y., "An implicit transition matrix approach to stability analysis of flexible multibody systems," *Multibody System Dynamics*, vol. 5, pp. 279–301, 2001.

[13] Bauchau, O. and Rodriguez, J., "Modeling of joints with clearance in flexible multibody systems," *International Journal of Solids and Structures*, vol. 39, pp. 41–63, 2002.

[14] Bauchau, O., Rodriguez, J., and Bottasso, C., "Modeling of unilateral contact conditions with application to aerospace systems involving backlash, freeplay and friction," *Mechanics Research Communications*, vol. 28, no. 5, pp. 571–599, 2001.

[15] Bauchau, O., van Weddingen, Y., and Agarwal, S., "Semi-active Coulomb friction lead-lag dampers," *Journal of the American Helicopter Society*, 2008. Submitted for publication.

[16] Bauchau, O. and Wang, J., "Stability analysis of complex multibody systems," *ASME Journal of Computational and Nonlinear Dynamics*, vol. 1, no. 1, 2006.

[17] Bauchau, O. and Wang, J., "Efficient and robust approaches to the stability analysis of large multibody systems," *ASME Journal of Computational and Nonlinear Dynamics*, 2007. To appear.

[18] Benner, P., "Accelerating Newton's method for discrete-time algebraic Riccati equations," in *Proceedings of the MTNS-98 Symposium, Padova, Italy*, pp. 569–572, 1998.

[19] Bialecki, R., Kassab, A., and Fic, A., "Proper orthogonal decomposition and modal analysis for acceleration of transient FEM thermal analysis," *International Journal for Numerical Methods in Engineering*, vol. 62, no. 6, pp. 774–797, 2005.

[20] Bisplinghoff, R., Ashley, H., and Halfman, R., *Aeroelasticity*. Reading, Massachusetts: Addison-Wesley Publishing Company, second ed., 1955.

[21] Bolotin, V., *Nonconservative Problems of the Theory of Elastic Stability*. Oxford, England: Pergamon Press Limited, 1963.

[22] Bousman, W. and Maier, T., "An investigation of helicopter rotor blade flap vibraory loads," in *American Helicopter Society 48th Annual Fourm Proceedings*, (Washington, D.C.), June 1992.

[23] Bousman, W. and Winkler, D., "Application of the moving-block analysis," in *Proceedings of the 22th Structures, Structural Dynamics, and Materials Conference, Dallas, TX, April 17-20*, 1981.

[24] Brewer, J., "Kronecker products and matrix calculus in system theory," *IEEE Transaction on Circuits and Systems*, vol. 25, no. 9, pp. 772–781, 1978.

[25] Bryson, A. and Mills, R., "Linear-quadratic-Gaussian controllers with special parameter robustness," *Journal of Guidance, Control, and Dynamics*, vol. 21, no. 1, pp. 11–18, 1998.

[26] Bryson, A. and Yuchi, H., *Applied Optimal Control*. Washington, D.C., New York: Hemisphere Publishing Corporation, 1975.

[27] Cardona, A., *An Integrated Approach to Mechanism Analysis*. PhD thesis, Université de Liège, 1989.

[28] Cardona, A. and Géradin, M., "Time integration of the equations of motion in mechanism analysis," *Computers and Structures*, vol. 33, no. 3, pp. 801–820, 1989.

[29] Dahlquist, G. and Björck, A., *Numerical Methods*. Englewood Cliffs, New Jersey: Prentice Hall, Inc., 1974.

[30] Demmel, J., *Applied Numerical Linear Algebra*. Philadelphia: SIAM, 1997.

[31] Dorato, P., Abdallah, C., and V., C., *Linear Quadratic Control: An Introduction*. Englewood Cliffs, New Jersey: Prentice-Hall, Inc., 1995.

[32] Dullerud, G. and F., P., *A Course in Roubst Control Theory: a Convex Approach*. New York: Springer, 2000.

[33] Durbin, J., "Efficient estimation of parameter in moving average models," *Biometrica*, vol. 46, pp. 306–316, 1959.

[34] Ewins, D., *Modal testing: theory and practice*. New York: Wiley, 1984.

[35] Feeny, B. and Kappagantu, R., "On the physical interpretation of proper orthogonal modes in vibrations," *Journal of Sound and Vibration*, vol. 211, no. 4, pp. 607–611, 1998.

[36] Fierro, R. and Jiang, E., "Lanczos and the Riemannian SVD in information retrieval applications," *Numerical Linear Algebra With Applications*, vol. 12, pp. 355–372, 2005.

[37] Friedmann, P., Hammond, C., and Woo, T., "Efficient numerical treatment of periodic systems with application to stability problems," *International Journal for Numerical Methods in Engineering*, vol. 11, pp. 1171–1136, 1977.

[38] Gautier, P., Gontier, C., and Smail, M., "Robustness of an ARMA identification method for modal analysis of mechanical systems in the presence of noise," *Journal of Sound and Vibration*, vol. 179, no. 2, pp. 227–242, 1995.

[39] Glover, K., "All optimal Hankel-norm approximations of linear multivariable systems and their L inf-error bounds," *International Journal of Control*, vol. 39, no. 4, pp. 1115–1193, 1984.

[40] Goland, M., "The flutter of a uniform cantilever wing," *Applied Mechanics*, vol. 12, no. 4, pp. A197–A208, 1945.

[41] Golub, G. and Van Loan, C., *Matrix Computations*. Baltimore, MD: Johns Hopkins University Press, second ed., 1989.

[42] Goodwin, M., *Dynamics of Rotor-Bearing Systems*. London: Unwinm Hyman, 1989.

[43] Gudmundsson, T., Kenney, C., and Laub, A., "Scaling of the discrete-time algebraic Riccati equation to enhance stability of the Schur solution method," *IEEE Transaction on Automatic Cotrol*, vol. 37, no. 4, pp. 513–518, 1992.

[44] Hammond, C. and Doggett, R.V., J., "Determination of subcritical damping by moving-block/randomdec applications," in *NASA Symposium on Flutter Testing Techniques, NASA SP-415*, pp. 59–76, 1975.

[45] Hewer, G., "An iterative technique for the computation of steady state gains for the discrete optimal regulator," *IEEE Transactions on Automatic Control*, vol. AC-16, pp. 382–384, 1971.

[46] Ho, B. and Kalman, R., "Efficient construction of linear state variable models from input/output functions," *Regelungstechnik*, vol. 14, pp. 545–548, 1966.

[47] Hochstadt, H., *Differential Equations*. New York: Dover Publications, Inc., 1964.

[48] Hsu, C., "Impulsive parametric excitation: Theory," *Journal of Applied Mechanics*, vol. 39, pp. 551–558, 1972.

[49] Hsu, C., "On approximating a general linear periodic system," *Journal of Mathematical Analysis and Applications*, vol. 45, pp. 234–251, 1974.

[50] Ibrahim, S. and Mikulcik, E., "A method for the direct identification of vibration parameters from the free response," *Shock Vibration Bulletin*, vol. 47, pp. 183–198, 1977.

[51] Ionescu, V., Oară, C., and Weiss, M., "General matrix pencil techniques for the solution of algebraic Riccati equation: A unified approach," *IEEE Transactions on Automatic Control*, vol. 42, no. 8, pp. 1085–1097, 1997.

[52] Jong, P. and Penzer, J., "The ARMA model in state space form," *Statistics Probability Letters*, vol. 70, pp. 119–125, 2004.

[53] Juang, J., *Applied System Identification*. Englewood Cliffs, New Jersey: Prentice-Hall, Inc., 1994.

[54] Juang, J., *Optimized System Identification.* NASA Technical Paper 209711, 1999.

[55] Juang, J. and Pappa, R., "An eigensystem realization algorithm for modal parameter identification and model reduction," *Journal of Guidance, Control, and Dynamics*, vol. 8, no. 5, pp. 620–627, 1985.

[56] Kalman, E., "A new approach to linear filtering and prediction problem," *Transactions of the ASME-Journal of Basic Engineering*, vol. 82(Series D), pp. 35–45, 1960.

[57] Kalman, E., "Mathematical description of linear dynamical systems," *SIAM Journal on Control*, vol. 1, no. 2, pp. 152–192, 1963.

[58] Kannan, S., *Adaptive Control of Systems in Cascade With Saturation.* PhD thesis, Georgia Institute of Technology, 2005.

[59] Kay, S. and Nagesha, V., "Maximum likelihood estimation of signals in autoregressive noise," *IEEE Transactions on Signal Processing*, vol. 42, no. 1, pp. 88–101, 1994.

[60] Kepler, G., Tran, H., and Banks, H., "Compensator control for chemical vapor deposition film growth using reduced-order design models," *IEEE Transactions on Semiconductor Manufacturing*, vol. 14, no. 3, pp. 231–241, 2001.

[61] Kim, C. and Arora, J., "Nonlinear dynamic system identification for automotive crash using optimization: A review," *Structural and Multidisciplinary Optimization*, vol. 25, no. 1, pp. 2–18, 2003.

[62] Kokiopoulou, E., Bekas, C., and Gallopoulos, E., "Computing smallest singular triplets with implicitly restarted Lanczos bidiagonalization," *Applied Numerical Mathematics*, vol. 49, pp. 39–61, 2004.

[63] Kunisch, K., Volkwein, S., and Xie, L., "HJB-POD-Based feedback design for the optimal control of evolution problems," *SIAM Journal of Applied Dynamical Systems*, vol. 3, no. 4, pp. 701–722, 2004.

[64] Kuo, B., *Automatic Control Systems.* Englewood Cliffs, New Jersey: Prentice-Hall, Inc., sixth ed., 1991.

[65] Lalane, M. and Ferraris, G., *Rotordynamics Prediction in Engineering.* New York: John Wiley & Sons, 1990.

[66] Lall, S., Marsden, J., and Glavaśki, S., "Empirical model reduction of controlled nonlinear systems," in *Proceedings of the IFAC World Congress*, pp. 473–478, 1999.

[67] Lall, S., Marsden, J., and Glavaški, S., "A subspace approach to balanced truncation for model reduction of nonlinear control systems," *International Journal of Robust and Nonlinear Control*, vol. 12, no. 5, pp. 519–535, 2002.

[68] Lancaster, P. and Rodman, L., *Algebraic Riccati Equation*. Walton Street, Oxford: Oxford University Press, 1995.

[69] Lathrop, D. and Kostelich, E., "Characterization of an experimental strange attractor by periodic orbits," *Physical Review A*, vol. 40, no. 7, pp. 4028–4031, 1989.

[70] Laub, A., "A Schur method for solving algebraic Riccati equations," *IEEE Transactions on Automatic Control*, vol. AC-24, no. 6, pp. 913–921, 1979.

[71] Laub, A. and Willems, J., *The Riccati Equations*. Berlin Heidelberg, New York: Springer-Verlag, 1991.

[72] Lieu, T., Farhat, C., and Lesoinne, M., "Reduced-order fluid/structure modeling of a complete aircraft configuration," *Computer methods in applied mechanics and engineering*, vol. to appear, 2006.

[73] Lus, H., Betti, R., and R.W., L., "Obtaining refined first-order predictive models of linear structural systems," *Earthquake Engineering & Structural Dynamics*, vol. 31, pp. 1413–1440, 2002.

[74] Moler, C. and G.W., S., "An algorithm for generalized matrix eigenvalue problems," *SIAM Journal on Numerical Analysis*, vol. 10, no. 2, pp. 241–256, 1973.

[75] Moore, B., "Principal component analysis in linear systems: Controllability, observability, and model reduction," *IEEE Transaction on Automatic Control*, vol. AC-26, no. 1, pp. 17–32, 1981.

[76] Murphy, K., Bayly, P., Virgin, L., and Gottwald, J., "Measuring the stability of periodic attractors using perturbation induced transients: Applications to two nonlinear oscillators," *Journal of Sound and Vibration*, vol. 172, pp. 85–102, 1994.

[77] Nayfeh, A. and Mook, D., *Nonlinear Oscillations*. New York: John Wiley & Sons, 1979.

[78] Nikishkov, Y., *Computational Stability Analysis of Dynamical Systems*. PhD thesis, Georgia Institute Of Technology, 2001.

[79] Nixon, M., Langston, C., Singleton, J., Piatak, D., Kvaternik, R., Corso, L., and Brown, R., "Aeroelastic stability of a four-bladed semi-articulated soft-inplane tiltrotor model," in *American Helicopter Society 59th Annual Forum Proceedings*, (Phoenix, AZ), May 6-8 2003.

[80] Overschee, P. and De Moor, B., *Subspace Identification for Linear Systems: Theory-Implementation-Applications*. New York, NY: Springer, 1996.

[81] Papadopoulos, M. and Garciat, E., "Global-local observer Markov parameter identification for system realization," *Journal of Guidance, Control and Dynamics*, vol. 19, no. 6, pp. 1221–1225, 1996.

[82] Pappas, T., Laub, A., and Jr., N., "On the numerical solution of the discrete-time algebraic Riccati equation," *IEEE Transactions on Automatic Control*, vol. AC-25, no. 4, pp. 631–641, 1980.

[83] Pearson, K., "On lines and planes of closest fit to points in space," *Philosophical Magazine*, vol. 2, pp. 609–629, 1901.

[84] Peeters, B. and De Roeck, G., "Reference-based stochastic subspace identification for output-only modal analysis," *Mechanical Systems and Signal Processing*, vol. 13, no. 6, pp. 855–878, 1999.

[85] Peeters, B. and De Roeck, G., "Stochastic system identification for operational modal analysis: A review," *Journal of Dynamic Systems, Measurement, and Control*, vol. 123, pp. 659–667, 2001.

[86] Peters, D. and Barwey, D., "A general theory of rotorcraft trim," *MPE*, vol. 2, pp. 1–34, 1996.

[87] Peters, D. and He, C., "Finite state induced flow models. Part II: Three-dimensional rotor disk," *Journal of Aircraft*, vol. 32, pp. 323–333, 1995.

[88] Peters, D. and Hohenemser, K., "Application of the Floquet transition matrix to problems of lifting rotor stability," *Journal of the American Helicopter Society*, vol. 16, pp. 25–33, 1971.

[89] Peters, D., Karunamoorthy, S., and Cao, W., "Finite state induced flow models. Part I: Two-dimensional thin airfoil," *Journal of Aircraft*, vol. 32, pp. 313–322, 1995.

[90] Peters, D. and Wang, X., "Generalized Floquet theory for analysis of numerical or experimental rotor response data," in *Proceedings of the 24th European Rotorcraft Forum*, (Marseilles, France), September 1998.

[91] Poincaré, H., *Les Méthodes Nouvelles de la Mécanique Céleste*. Paris: Gauthier-Villars, 1892.

[92] Prandini, M., *Adaptive Linear Quadratic Gaussian Control: Optimality Analysis and Robust Controller Design*. PhD thesis, University of Brescia, 1998.

[93] Press, W., Flannery, B., Teutolsky, S., and Vetterling, W., *Numerical Recipes. The Art of Scientific Computing*. Cambridge: Cambridge University Press, 1990.

[94] Quaranta, G., Mantegazza, P., and Masarati, P., "Assessing the local stability of periodic motions for large multibody non-linear systems using proper orthogonal decomposition," *Journal of Sound and Vibration*, vol. 271, pp. 1015–1038, 2004.

[95] Rao, B. and Arun, K., "Model based processing of signals: A state space approach," *Proceedings of the IEEE*, vol. 80, pp. 283–309, 1992.

[96] Ravindran, S., "Reduced-order adaptive controllers for fluid flows using POD," *Journal of Scientific Computing*, vol. 15, no. 4, pp. 457–478, 2000.

[97] Rowley, C., "Model reduction for fluids, using balanced proper orthogonal decomposition," *International Journal of Bifurcation and Chaos*, vol. 15, no. 3, pp. 997–1013, 2005.

[98] Rowley, C. and Juttijudata, V., "Model-based control and estimation of cavity flow oscillations," in *Decision and Control, 2005 and 2005 European Control Conference. CDC-ECC '05. 44th IEEE Conference on, Seville, Spain, December 12-15*, pp. 512–517, 2005.

[99] Schuster, H., *Deterministic Chaos: an Introduction*. Weinheim, Germany: VCH Verlagsgesellschaft mbH, third augmented ed., 1995.

[100] Shin, K., Hammon, J., and White, P., "Iterative SVD method for noise reduction of low-dimensional chaotic time series," *Mechanical Systems and Signal Processing*, vol. 13, no. 1, pp. 115–124, 1999.

[101] Skogestad, S. and Postlethwaite, I., *Multivariable Feedback Control : Analysis and Design*. Chichester, New York: John Wiley, 1996.

[102] Stol, K., Bir, G., and Balas, M., "Linearized dynamics and operating modes of a simple wind turbine model," in *Proceedings of the 37th AIAA Aerospace Sciences Meeting and Exhibit, Jan. 11-14, Reno, Nevada*, pp. 135–142, 1999. NICH Report No. 32548.

[103] Szabo1, Z., Heuberger, P., Bokor, J., and den Hof, P., "Extended Ho-Kalman algorithm for systems represented in generalized orthonormal bases," *Automatica*, vol. 36, no. 12, pp. 1809–1818, 2000.

[104] Trefethen, L. and Bau, D., *III. Numerical Linear Algebra*. Philadelphia: SIAM, 1997.

[105] Trickey, S., Virgin, L., and Dowell, E., "The stability of limit cycle oscillations in a nonlinear aeroelastic system," *Proceedings of the Royal Society of London*, vol. 458, pp. 2203–2226, 2002.

[106] Unger, J., *System Identification and Damage Detection in Civil Engineering*. PhD thesis, Katholieke Universiteit Leuven, 2002.

[107] Van Der Veen, A.-J., Deprettere, E., and Swindlehurst, A., "Subspace-based signal analysis using singular value decomposition," *Proceedings of the IEEE*, vol. 81, pp. 1277–1308, 1993.

[108] Viberg, M., "Subspace-based methods for the identification of linear time-invariant systems," *Automatica*, vol. 31, no. 12, pp. 1835–1851, 1995.

[109] Wang, X. and Peters, D., "Floquet analysis in the absence of complete information on states and perturbations," in *Proceedings of the Seventh International Workshop on Dynamics and Aeroelasticity Stability Modeling, St. Louis, October 14-16*, pp. 237–248, 1997.

[110] Willcox, K. and Peraire, J., "Balanced model reduction via the proper orhtogonal decomposition," *AIAA Journal*, vol. 40, no. 11, pp. 2323–2330, 2002.

VITA

Jielong Wang was born in Tangshan City, Hebei Province of the peoples republic of China, in 1974. Jielong Wang graduated from Tsinghua University, at Beijing of China, in June of 2001, majoring in general mechanics and mechanics fundamental for his Master degree. During the next two years, he worked for a telecommunication technology company as a software engineer. Jielong Wang started his graduate study at the Department of Aerospace Engineering of Georgia Institute of Technology, Atlanta, GA in January 2003. He became the PhD. candidate after passing the qualify examinations in Spring 2005. His major research at Georgia Tech was the stability analysis and optimal control of large-scale multibody dynamics presented in this thesis. He also finished the coding work of Herting reduction to afford one flexible interface among different finite element based dynamic simulation codes, and of trim analysis based on auto-pilot method using C language.